Cation and Anion Doping of ZnO Thin Films by Spray Pyrolysis

Nazanin Rashidi

St. Catherine's College, University of Oxford

A thesis submitted to the University of Oxford for the degree of Doctor of Philosophy

Supervisor

Prof. Peter P. Edwards FRS

Inorganic Chemistry Laboratory

The work described in this thesis was carried out in the Inorganic Chemistry Laboratory, University of Oxford from October 2010 until September 2014, under supervision of Professor Peter P. Edwards. All of the work is my own unless otherwise stated, and has not been submitted previously for any degree at this or any other University.

Nazanin Rashidi

September 2014

Acknowledgements

I would never have been able to finish my thesis without the help and support of the kind people around me, to only some of whom it is possible to give particular mention here.

Above all, I would like to express appreciation to my beloved husband and best friend Payam who spent sleepless nights with and was always my greatest support in the moments when there was no one to answer my queries. Words cannot express how grateful I am to my parents who raised me with a love of science and supported me in all my pursuits, my parents-in law, my brother Babak, my sisters- and brothers-in-law, Shabnam, Leila, Sara, and Mehran, for their love, encouragement, and unequivocal support throughout, and most of all to my supportive and caring brother-in-law Pedram and his lovely son Arvin whose presence enriched and delighted our life in Oxford.

I would like to express my sincere gratitude to my supervisor, Prof. Peter Edwards, for his aspiring guidance and providing me with an excellent atmosphere for doing research. The great advice, support and friendship of my co-supervisor, Prof. Jonathan Dilworth, has been invaluable on both an academic and a personal level, for which I am extremely grateful. My heartfelt thanks goes to Dr. Vladimir Kuznetsov, for the assistance he provided at all levels of the research project. I appreciate his vast knowledge and skill in many areas and his guidance and assistance in writing reports and this thesis. A very special thanks to Linda Webb whose kind, genuine and generous help and advice as well as her key role in the group made everyone's life easier.

I would like to thank Dr. Robert Jacobs and Mrs Gabriella Chapman for their assistance with the atomic force microscopy and scanning electron microscopy. I would also like to thank Dr. Richard Cooper for letting me use thermal analysis facilities in their group.

I would love to thank Alex Vai for his help in collecting scanning electron microscopy data and reading this thesis for submission, and more importantly for all his helpful comments and discussions on data and results.

The members of the Edwards group have contributed immensely to my personal and professional time at Oxford. The group has been a source of friendships as well as good advice and collaboration. Past and present group members that I have had the pleasure to work with or alongside are Josh Makepeace, Michael Jones, Andrew Seel, Kate Ryan, Liang Kong, Katie Hore, Nurul Che Lah, Philippe Aeberhard, Henry Lai, Liam France; and the numerous DPhil and Part II students who have come through the lab.

My time at Oxford was made enjoyable in large part due to the many friends that became a part of my life. I am grateful for time spent with friends, for Golnaz, Afrah, Sneha and Agata, and for many other people and memories.

I would like to acknowledge the financial, academic and technical support of the University of Oxford and St. Catherine's College, and their kind, friendly and helpful staff.

Last, but by no means least, I thank all my friends and family members in Iran, and elsewhere for their support and encouragement throughout, some of whom have already been named.

Cation and Anion Doping of ZnO Thin Films by Spray Pyrolysis

Nazanin Rashidi

A thesis submitted to the department of Chemistry of the University of Oxford for the degree of Doctor of Philosophy in Inorganic Chemistry

Abstract

ZnO is an n-type semiconducting material with high optical transparency in the visible range (400 - 750 nm) of the electromagnetic spectrum. When doped with group 13 or 14 metal oxides, ZnO exhibits almost metallic electrical conductivity. ZnO thin films have been recognised as promising alternative material for the currently widely-used but expensive indium oxide in the form of indium tin oxide (ITO), in terms of their low cost and the high abundance of zinc. At the moment, even the best solution-processed ZnO films still can not compete for ITO replacement especially in solar energy utilization and OLED lighting applications, and the performance of ZnO films needs to be further improved. The objective of this work was to enhance the electrical and optical properties of spray pyrolysed ZnO thin films by simultaneous cation and anion doping. This was achieved by growing several series of undoped, single-doped, and co-doped ZnO thin films over a wide range of conditions, in order to understand the growth behaviour of undoped and doped ZnO, and to establish the optimum growth procedure. Spray pyrolysis process has advantages over vacuum-based techniques in terms of its low-cost, high deposition rate, simple procedure and can be applied for the production of large area thin films. Various techniques were employed to characterize the properties of the prepared thin films, and thus determine the optimum growth conditions (*i.e.* X-ray diffraction (XRD), X-ray photoelectron spectroscopy (XPS), atomic force microscopy (AFM), scanning electron microscopy (SEM), UV-Vis-NIR spectroscopy and Hall effect measurement).

The growth of doped ZnO on glass substrates using Si and F as dopants, yielded highly conducting and transparent thin films. The co-doped thin films exhibited distinct widening of band gap upon increasing deposition temperature and doping concentration as a result of increasing electron concentration up to 4.8×10^{20} cm^{-3} upon doping with Si and F at the same time. The resistivity of the films deposited from $Zn(acac)_2 \cdot xH_2O$ solutions and at the optimum temperature of 450 °C, was found to decrease from 4.6×10^{-2} Ω cm for the best undoped ZnO film to 3.7×10^{-3} Ω cm, upon doping with 3% Si. The films co-doped with Si and F in the ratios of [Si] / [Zn]= 3 - 4 mol% and [F] / [Zn]=30 - 40 mol% were the most conducting ($\rho \sim 2.0 \times 10^{-3}$ Ω cm). The associated optical transmittance of co-doped ZnO was above 85% in the whole visible range. Results compare favourably with In-doped ZnO deposited under similar conditions. Si+F co-doped ZnO films offer a suitable replacement for ITO in many applications such as LCD and touch screen displays.

Publications

Publications arising from this thesis

Rashidi N., Kuznetsov V. L., Dilworth J. R., Pepper M., Dobson P. J., Edwards P. P. "Highly Conducting and Optically Transparent Si-Doped ZnO Thin Films Prepared by Spray Pyrolysis", *J. Mater. Chem. C*, **1**, 2013, 6960-6969.

Vai A. T., Kuznetsov V. L., Jain H., Slocombe D., Rashidi N., Pepper M., Edwards P. P. "The Transition to the Metallic State in Polycrystalline n-type Doped ZnO Thin Films", *Z. Anorg. Allg. Chem.* **40** (6), 2014, 1054-1062.

Rashidi N., Vai A. T., Kuznetsov V. L., Dilworth J. R., Edwards P. P. "Fluoride-Enhanced Silicon Doping in ZnO Films" (Submitted to Chem. Commun., February 2015)

Contents

1 Introduction **1**

1.1 Aim of this study 1

1.2 Strategy 2

1.3 Transparent Conducting Materials 2

1.4 Applications of TCO materials 5

1.5 Thin Film Deposition Techniques 8

1.6 ZnO 15

1.6.1 Precursors to ZnO 16

1.7 Doping of ZnO 18

1.7.1 Ability to dope 18

1.7.2 Doping of ZnO 20

1.7.2.1 P-type doping 22

1.7.2.2 N-type doping 23

1.7.2.3 Co-doping method 25

1.8 Structural properties of ZnO 27

1.9 Optical properties of ZnO 29

1.10 Electrical properties of ZnO 33

1.11 Correlation of optical and electrical properties 38

1.12 Defect structures of Si, F, or Cl doped ZnO (First-principles electronic structure calculations) 39
1.12.1 Zn and O defect models 39
1.12.2 Si defect models 41
1.12.3 F defect models 43
1.12.4 Cl defect models 43

2 Experimental Techniques and Data Acquisition 45
2.1 X-ray diffraction (XRD) 46
2.1.1 Introduction 46
2.1.2 Principles of the technique 46
2.1.3 Applications of XRD 48
2.1.3.1 Phase determination by fingerprinting 48
2.1.3.2 Quantitative phase analysis 49
2.1.3.3 Calculation of lattice parameters 50
2.1.3.4 Analysis of crystallite size and strain 50
2.1.4 Instrumentation 51
2.2 Atomic Force Microscopy (AFM) 51
2.2.1 Introduction and principle of the technique 51
2.2.2 Applications of AFM 53
2.2.3 Instrumentation 55
2.3 X-ray Photoelectron Spectroscopy (XPS) 55
2.3.1 Introduction 55
2.3.2 Principles of the technique 56
2.3.3 Applications of XPS and data analysis 61
2.3.3.1 Qualitative analysis 61
2.3.3.2 Quantitative analysis 61
2.3.3.3 Chemical states and chemical shifts 62

2.3.3.4 Spin-orbit splitting 63
2.3.4 Instrumentation 64
2.4 Ultraviolet, visible and near-infrared (UV-Vis-NIR) absorption spectroscopy 65
2.4.1 Introduction 65
2.4.2 Basic principles of the technique 66
2.4.3 Applications of UV-Vis-NIR spectroscopy and data analysis 68
2.4.3.1 Qualitative analysis 68
2.4.3.2 Quantitative analysis 69
2.4.3.3 Materials properties measurable by UV-Vis-NIR spectroscopy 69
2.4.4 Instrumentation 72
2.5 Hall effect measurement 72
2.5.1 Introduction 72
2.5.2 Theory of Hall effect 73
2.5.2.1 The van der Pauw technique 75
2.5.3 Instrumentation 78
2.6 Scanning electron microscopy (SEM) 78
2.6.1 Principles of the technique 79
2.6.2 Instrumentation 80

3 Study of the Thermal Decomposition of Potential Zinc Oxide Precursors 82
3.1 Introduction and overview 82
3.2 Experimental 86
3.3 Results and discussion 87
3.3.1 Thermogravimetric analysis-differential scanning calorimetry (TGA-DSC) technique 87
3.3.2 Precursor decomposition analysis 88
3.4 Conclusions 100

4 Preparation and Characterisation of Silicon-doped ZnO (SiZO) Thin Films 101

4.1 Introduction and overview 101

4.2 Experimental 103

4.3 Results and discussion 106

4.3.1 Structural studies of ZnO and SiZO thin films 106

4.3.1.1 Effect of deposition temperature 106

4.3.1.2 Effect of Si concentration 112

4.3.2 AFM and SEM studies of ZnO and SiZO thin films 114

4.3.2.1 Effect of deposition temperature 114

4.3.2.2 Effect of Si concentration 116

4.3.3 Optical studies of ZnO and SiZO thin films 119

4.3.4 Electrical transport properties of ZnO and SiZO thin films 122

4.4 The conduction mechanism and the insulator-conductor transition in ZnO, SiZO and FSZO polycrystalline thin films 126

4.5 Conclusions 136

5 Preparation and Characterisation of Fluorine-doped ZnO (FZO) and Chlorine-doped ZnO (ZnO:Cl) Thin Films 137

5.1 Introduction and overview 137

5.2 Experimental 140

5.3 Results and discussion 141

5.3.1 Structural and morphological properties 141

5.3.2 Optical properties 146

5.3.3 Electrical properties 148

5.4 Conclusions 151

6 Preparation and Characterisation of Fluorine and Silicon Co-doped ZnO (FSZO) Thin Films 152

6.1 Introduction and overview 152
6.1.1 Donor-acceptor dopants 153
6.1.2 Two donor dopants 154
6.2 Experimental 156
6.3 Results and discussion 158
6.3.1 Effect of deposition temperature 158
6.3.1.1 Structural characterisation 158
6.3.1.2 XPS Analysis 164
6.3.1.3 Morphology 173
6.3.1.4 Optical properties 176
6.3.1.5 Electrical properties 180
6.3.2 Effect of F concentration 183
6.3.2.1 Structural characterisation 183
6.3.2.2 XPS analysis 186
6.3.2.3 Morphology 194
6.3.2.4 Optical properties 197
6.3.2.5 Electrical properties 200
6.3.3 Effect of silicon concentration 202
6.3.3.1 Structural characterisation 202
6.3.3.2 Surface analysis 205
6.3.3.3 Morphology 209
6.3.3.4 Optical properties 211
6.3.3.5 Electrical properties 214
6.3.4 Effect of type of the precursor solution container 216
6.3.4.1 Structural characterisation 216
6.3.4.2 Surface analysis 218
6.3.4.3 Morphology 221

6.3.4.4 Optical properties 222
6.3.4.5 Electrical properties 224
6.4 Conclusions 227

7 Summary and Conclusions 229

7.1 Conclusions 229
7.2 Future work 231

References 233

Chapter 1

Introduction

1.1 Aim of this study

Recently, transparent conducting oxides (TCOs) that contain a reduced amount of or no indium have attracted much attention as substitute for indium-based semiconductor materials for a variety of optoelectronic applications. [1] The main goal of this project is to introduce a low-cost highly-abundant ZnO-based TCO material as a potential alternative for the currently widely-used but expensive indium tin oxide (In_2O_3:Sn, ITO) materials for large area optoelectronic and photovoltaic applications. Developing alternatives to ITO is desirable because of the high cost and low abundance of indium. ZnO is lower in cost and also more abundant than ITO, so it may replace ITO as a front electrode in some future displays, such as flat-panel displays. In order to develop such optoelectronic devices, one important issue that must be resolved is the fabrication of low-resistivity ZnO thin films.

To achieve this goal, production of highly transparent and conducting ZnO thin films at the lowest possible temperature, using a solution-based deposition technique was attempted. Different zinc compounds have been selected and their decomposition temperatures were studied. Dopants which have not been thoroughly studied yet such as silicon and fluorine have been explored, and comparisons of the optical and electrical properties of undoped,

Si-doped, F-doped, Cl-doped, and Si+F co-doped ZnO thin films have been made.

1.2 Strategy

In the present study we report, for the first time, the preparation of highly conducting and transparent Si-doped and Si+F co-doped ZnO thin films deposited on glass substrates by the spray pyrolysis technique. Zinc acetylacetonate, which had the lowest decomposition temperature amongst the precursor compounds studied, was used as the Zn precursor. Silicon tetraacetate and/or ammonium fluoride were added to the zinc precursor solution as dopants. We find that Si doping and Si+F co-doping of ZnO thin films lead to a significant improvement in the electrical and optical properties as compared to undoped ZnO prepared under similar conditions. The variations in the structural, electrical and optical properties of t he films as a function of critical parameters such as deposition temperature and dopant concentration are investigated and reported. These results provide a potential solution-based route for the production of highly conducting ZnO thin films for low cost and large area optoelectronic applications.

1.3 Transparent Conducting Materials

In recent years, there have been rapid and significant advances in the field of material science, especially in semiconductor physics. One of the most important fields of current interest centres on the fundamental aspects and applications of Transparent Conducting Materials (TCMs), which are both optically transparent and electrically conducting and introduce completely new areas of applications. Generally materials that combine optical transparency in the visible spectrum with reasonable electrical conductivity fall into three classes: very thin pure metals, highly doped conjugated organic polymers, and degenerately doped wide band gap post-transition metal oxide semiconductors. [2]

According to the Electromagnetic Theory (Maxwell's equations), [3] optically transpar-

ent materials tend to be electrical insulators because of their large electronic band gaps ($E_g > 3.1$ eV). The absolute limit to the resistivity would be 3.0×10^{-5} Ω cm for the TCOs and the corresponding carrier concentration would be about 9.0×10^{21} cm^{-3}. [4] At higher concentrations, the reflectivity due to the carriers would be very high and the film can no longer be used as a transparent conductor. However, transparent conductors - of which TCOs are a prototypical class of materials - exhibit a remarkable combination of properties whereby they transmit light and conduct electric current simultaneously, [5, 6] and despite their large band gaps, show high electrical conductivity, of the order of $> 10^3$ Ω^{-1} cm^{-1}. TCOs have been known for a century, with the first discovered in 1907 by the German scientist Bädeker, who used a simple vapour deposition system to deposit Cd metal thin films, which could be to be oxidised to optically transparent CdO after heating in air, while remaining electrically conducting. [7] In the 1960s, it was recognized that thin films composed of other binary compounds such as ZnO, SnO_2, In_2O_3 and their alloys were also TCOs. [8] In addition to binary compounds, the ternary compounds such as Cd_2SnO_4, $CdSnO_3$ and $CdIn_2O_4$ were developed as TCO materials prior to 1980, but their TCO films have not been used widely. [9] Impurity-doped ZnO thin films such as ZnO:Al (AZO), ZnO:Ga (GZO), ZnO:Si (SiZO) and ZnO:In (IZO) along with the abundance of binary compounds previously mentioned were developed in the 1980s by Minami *et.al* using magnetron sputtering techniques. [10–12] In the 1990s, new TCO materials consisting of combinations of ZnO, CdO, In_2O_3 and SnO_2, such as Zn_2SnO_4, Cd_2SnO_4, $Zn_2In_2O_5$, and $In_4Sn_3O_{12}$ were developed. [9] Over the last fifty to sixty years, the most utilised TCO materials have been undoped, doped and multicomponent indium oxide (In_2O_3), tin oxide (SnO_2) and zinc oxide (ZnO) because they offer the best available performance in terms of electrical conductivity and optical transparency.

Transparent conducting tin-doped indium oxide (In_2O_3:Sn or ITO), which was the first of the modern TCO materials, was prepared using spray pyrolysis technique for the first time by Mochel in 1951. [13] A few years later in 1954, ITO was developed by Rupprecht [14] for

window coating. In the subsequent half-century, ITO has been the most widely used TCO for optoelectronic device applications. Recently, TCOs that contain a reduced amount of indium have attracted much attention as substitute materials for ITO in transparent electrode applications, [15] due to the fact that the ITO thin films are very expensive for device applications and a stable supply of ITO cannot be assured. [16] Impurity-doped ZnO, In_2O_3 and SnO_2 and multicomponent oxides composed of combinations of these binary compounds such as ZnO-In_2O_3, In_2O_3-SnO_2 and ZnO-In_2O_3-SnO_2 are examples of reduced-indium TCO materials. [9, 15] Figure 1.1 shows the TCO composition space in which individual oxides are located at the corners, edges are lines of mixing between two oxides (binary systems), and faces are areas of mixing between three oxides (ternary systems). [17] Moreover, the continued depletion of raw materials and concerns about the environmental impact of, particularly, Sn, make it increasingly important to employ more abundant and less toxic elements in the fabrication of high performance TCO materials. In these regards, zinc oxide and doped ZnO thin films continue to attract considerable interest, [18] owing to their high performance along with lower costs, reasonably adequate stability and reproducibility.

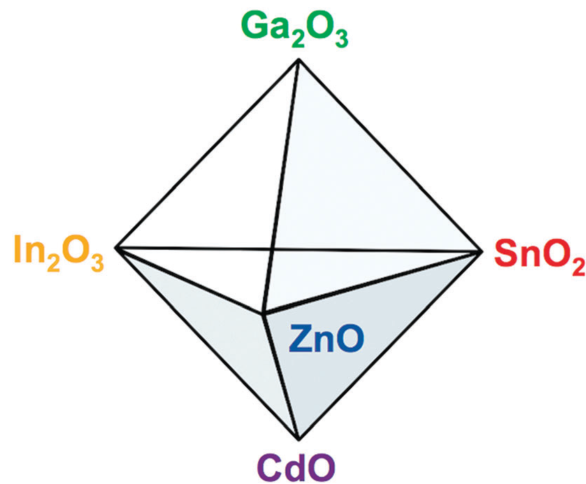

Figure 1.1: The hexahedron represents the conventional TCO composition space and their multiple combinations (adapted from [17])

TCOs are employed in a diverse range of applications for solar energy utilization [19] and optoelectronic devices [20], and critical research is needed for these applications. [21] TCO thin films need to encompass high optical transmission (mostly in the visible spectral range), low electrical resistivity, low surface roughness and good thermal and chemical stability. In addition, the development of low-cost and energy-efficient thin film deposition processes to these advanced energy materials are needed, particularly for large area applications.

1.4 Applications of TCO materials

Owing to unique combined electrical and optical properties, TCO thin films are an essential part of technologies that require both large-area electrical conduction and optical transparency in the visible portion of the light spectrum. A wide range of optical and electrical properties are needed for various industrial uses of TCOs (Figure 1.2), and optimisation of these properties will depend on the application, but in most cases, both parameters should be as large as possible. [5]

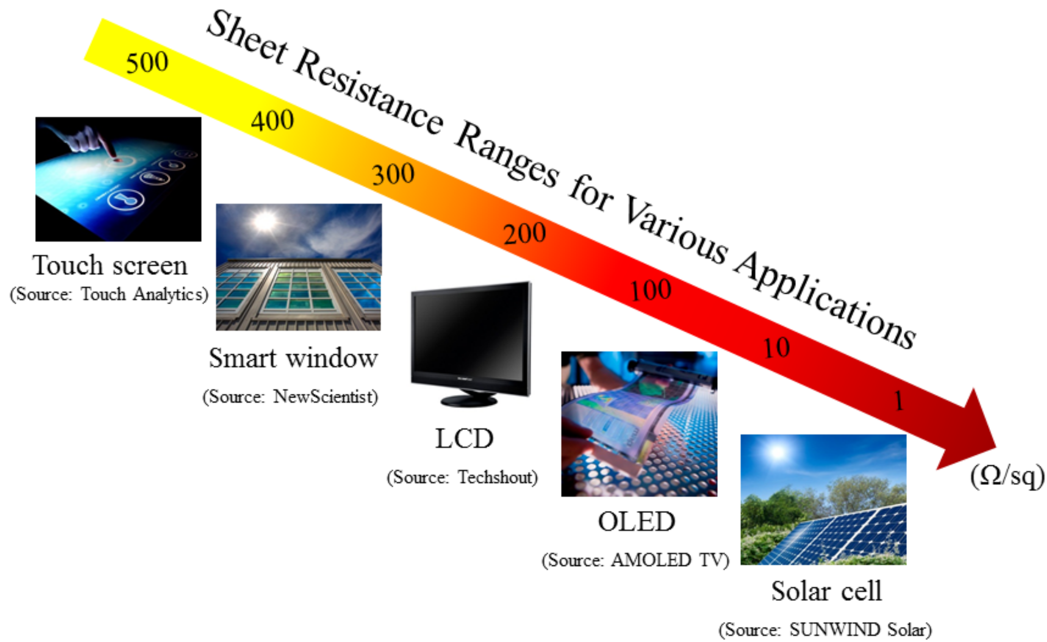

Figure 1.2: Sheet resistance range required for various TCO applications (Figure adapted from [22]), Sheet resistance, R_s, of TCO thin films is calculated from: $R_s = \frac{\rho}{t}$, where ρ is the bulk resistivity and t is the film thickness

The major applications of TCOs are photovoltaic solar cells, [19, 23] transparent electrodes in touch screen and flat panel display technologies, [2] energy efficient windows, [24, 25] organic light emitting dioeds (OLEDs) [26, 27] and transparent thin film transistors (TFTs). [28]

A solar cell is a solid-state electrical device which converts the energy of sun directly into electricity using the photoelectric effect. A solar cell is a multi-layered device including p-type (acceptor) and n-type (donor) semiconductor materials (a so-called p-n junction). The process of conversion first requires a donor material to absorb the solar energy (photon), whereupon an electron is excited from the valence band to the conduction band. The flow of high-energy electron will be transferred to the acceptor material at an interface and finally to the cathode and an external circuit for charge collection. [29] TCOs have attracted considerable interest in recent years towards the development of TCO-based solar cells.

[19, 30, 31]

An organic light emitting diode (OLED), which is widely used in the display industry, is a semiconductor device made by placing a series of organic thin films between two conductors (electrode) one of which must be transparent. A typical OLED display consists of a number of layers including a cathode, an emissive layer, a conductive layer and a transparent anode. When an external voltage (typically a few volts) is applied to the device, electrons and holes are injected from the cathode and the anode, respectively, and drift towards each other. When the initially free electrons and holes meet, they form strongly bound electron–hole pairs, which then may decay and emit photons. [32] TCO coatings have been used in various display devices such as liquid crystal displays (LCDs) [33] and OLEDs as transparent electrodes, where the efficiency of the devices is increasing with the transparency and optical properties. [34]

There are four main touch screen technologies; 1) resistive, 2) capacitive, 3) surface acoustic wave, and 4) infrared (IR). [35] TCO materials such as ITO are fundamental components of resistive and capacitive touch screen displays, where the highest possible optical transparency is vital and relatively high electrical conductivity is also a necessity.

One of major tasks of energy saving windows (also called smart or energy efficient windows) is to minimise of radiative heat losses. The reduction of heat losses through glass can be achieved by applying special coatings. TCO thin film coatings deposited on the glass serve as mirrors for long-wave infrared radiation and thus, reduce radiative heat losses. [25] High conductivity of TCOs, when it arises from high carrier concentrations, is usually accompanied by high reflectance in the near-infrared region (NIR), due to the Plasmon Resonance effect. [36] This high reflectance in the NIR region, allows the window to remain highly transparent in the visible region, while keeping infrared energy inside the buildings or cars, etc. The function of TCOs in energy efficient windows is mainly derived from their optical transparency rather than their electrical conductivity.

1.5 Thin Film Deposition Techniques

Deposition of high quality, uniform thin films is an intensive area of research which has yielded many varied deposition techniques. The methods employed for thin oxide film deposition can be divided into two broad categories based on the nature of the deposition process: physical deposition methods and chemical deposition methods. The physical methods include physical vapour deposition and sputtering while the chemical methods comprise gas phase deposition methods and solution techniques. Some of the most common methods in each category are shown in Figure 1.3. Physical vapour deposition technology consists of a variety of vacuum deposition processes such as evaporation and sputtering techniques, which can result in the production of a high-quality thin film.

As mentioned above, the chemical deposition techniques can be divided into two subcategories, based on the precursor initial phase; gas and solution phase techniques. The most widely-used gas phase methods include chemical vapour deposition (CVD) [37, 38] and atomic layer deposition (ALD) [39], while spray pyrolysis, [40] sol-gel, [41] spin-coating, [42, 43] and dip-coating [42] methods employ precursor solutions. Depending on the material being deposited and the final application of the thin film, some methods might be more effective than others.

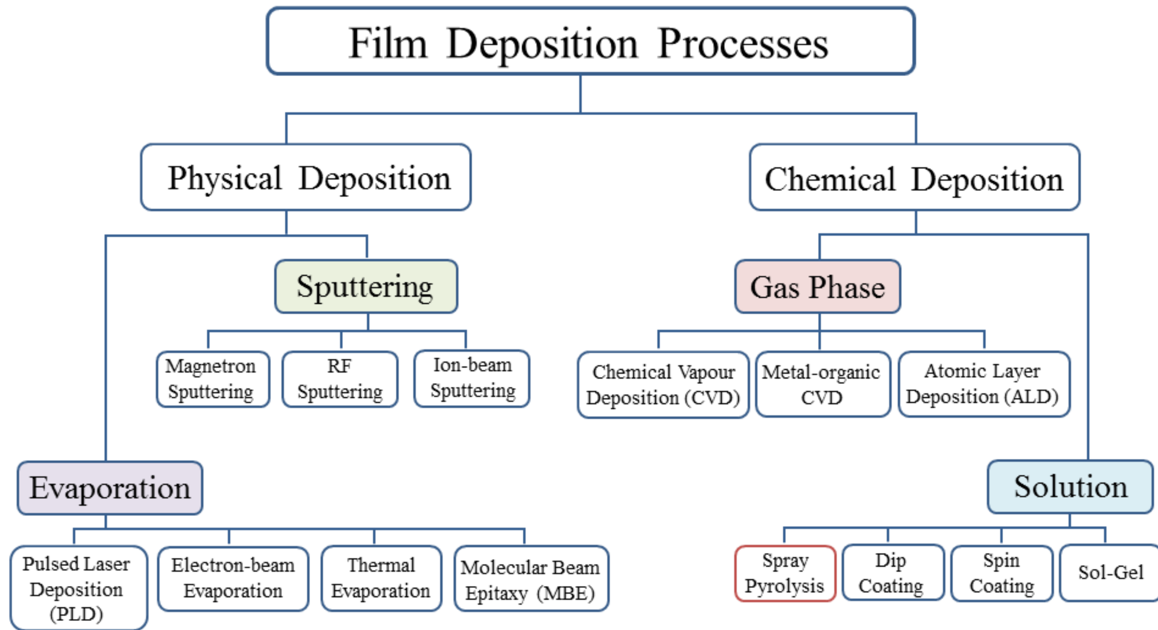

Figure 1.3: Classification of the most common thin film deposition techniques

Some properties of the thin films such as crystallinity (polycrystalline or amorphous) and morphology, depend strongly on the growth process. These properties can directly influence the other properties of the thin films such as optical and electrical properties, and thus, an appropriate control over the properties of the thin films can be achieved by careful selection of the deposition technique. [44] Each of the categories and a range of common individual techniques are very briefly described as follows.

❶ Physical deposition methods:

In **evaporation** techniques a hot source of the pure material is evaporated in a high vacuum. In high vacuum, evaporated particles can travel ballistically to the deposition substrate, where they condense back to a solid state. There are many different types of evaporation methods characterised by the use of different evaporation sources such as thermal, electron-beam, flash, and resistive evaporation methods. [45] **Pulsed laser deposition** (PLD), which is one of the most popular techniques for the deposition of semiconductor materials, [46, 47] uses a high-power pulsed laser beam to strike a target of the material

to be deposited. As a result the material is vaporized from the target and deposited as a thin film on a substrate. PLD deposition allows controlled chemical composition of the deposited compounds. This process may occur in ultra high vacuum or can be done in the presence of a background gas, such as oxygen. [48] A schematic of a typical PLD system is shown in Figure 1.4 (a).

Sputtering processes involve ejecting atoms or molecules from a "target" (or cathode) plate consisting of the material being deposited onto a substrate in a vacuum chamber. This effect is caused by the bombardment of the target by plasma, which is usually formed from an inert gas such as argon. The ejected particles are then directed toward the substrate and a thin film is deposited as seen in Figure 1.4 (b). [49, 50]

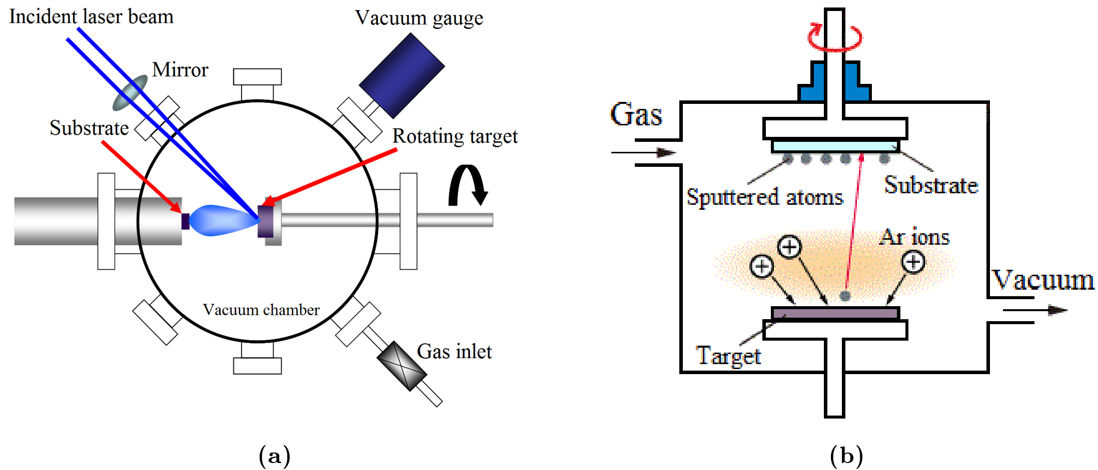

Figure 1.4: Schematics of (a) PLD (adapted from [51]) and (b) sputtering (adapted from www.en.rigaku-mechatronics.com website) systems

❷ Chemical deposition methods:

Chemical vapour deposition (CVD) is a generic name for a group of processes that involve depositing a solid material from a gaseous phase. In these processes precursor gases (often diluted in carrier gases) are delivered into the reaction chamber at approximately ambient temperatures. As they pass over or come into contact with a heated substrate, they react or decompose forming a solid phase that is deposited onto the substrate. [37] Different

types of CVD methods are in wide use and are frequently referenced in the literature. These processes differ in the means by which chemical reactions are initiated and the process conditions. Some of the most important types of CVD processes are: atmospheric pressure chemical vapour deposition (APCVD), low pressure chemical vapour deposition (LPCVD), and metal-organic chemical vapour deposition (MOCVD). [38] **Atomic layer deposition** (ALD) is a special variant of the CVD technique with a self-limiting nature which allows a very precise (atomic level) thickness control. [39, 52]

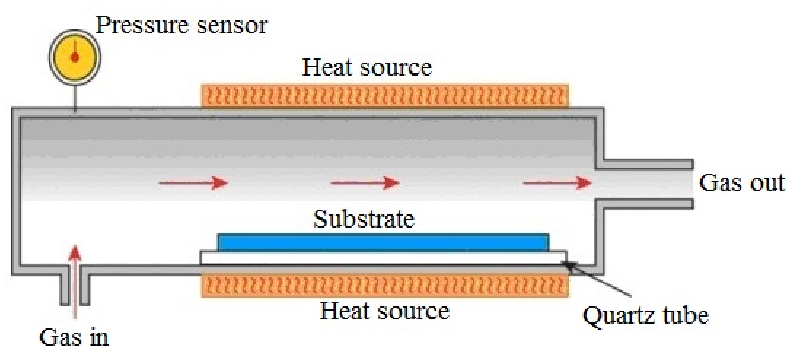

Figure 1.5: Typical CVD reactor (Figure adapted from www.AzoNano.com website)

Sol-gel techniques, consist of coating a substrate with prepared polymeric or colloidal inorganic precursor solution (sol) by dip-coating [53] (or spin-coating [54]), followed by gravitational draining, solvent evaporation (drying), and further condensation reactions, which result in the deposition of a film (solid gel) on the substrate surface. Afterwards, a thermal treatment, or annealing process (usually at quite high temperatures), is often necessary in order to enhance the properties and stability of the films. The structure of the film deposited depends on the size and the structure of the precursor, relative rates of condensation, evaporation, drying, substrate withdrawal speed and drying temperature. [41]

Spin coating deposition techniques involves depositing a small solution puddle (coating material) onto a centre of a flat substrate and then rotating the substrate at relatively high speed in order to spread the solution, accompanied by a drying step to eliminate excess

solvents from the resulting film. [42] In this method, finding a balance between centrifugal forces controlled by spin speed and solution viscosity is extremely important. Final film thickness and other properties will highly depend on the nature of the solution material such as viscosity, drying rate, concentration and surface tension. The spin process parameters such as acceleration and rotation speed, drying temperature and drying atmosphere will also affect the properties of the thin films. [43]

As mentioned previously, thin film samples in this thesis were prepared on glass substrates using spray pyrolysis. Among all the deposition methods, **spray pyrolysis,** which was first introduced and developed as a low cost thin film deposition technique in the 1940s for the preparation of transparent oxide films (TCOs), [55] is one of the simplest, most effective and low cost routes to continuous and scalable deposition of thin films with easy compositional control. [40] One of the early applications of the spray pyrolysis technique was the deposition of a sulfide thin film by Chamberlin, *et al.* [56]. The technique attracted great interest after they extended their studies and published the first paper on preparation of CdS films for solar cells using the spray pyrolysis deposition technique. [57] A few years later, Bube and co-workers applied the spray pyrolysis method to prepare a complete range of solid solution films of (Cd, Zn)S and Cd(S, Se) using the technique [58] and later on in 1979 investigated the spray pyrolysis of ZnO films onto glass for solar cell applications. [59] Owing to its simplicity and inexpensiveness, spray pyrolysis technique has been studied extensively for the preparation of thin films of numerous metal oxides. [60]

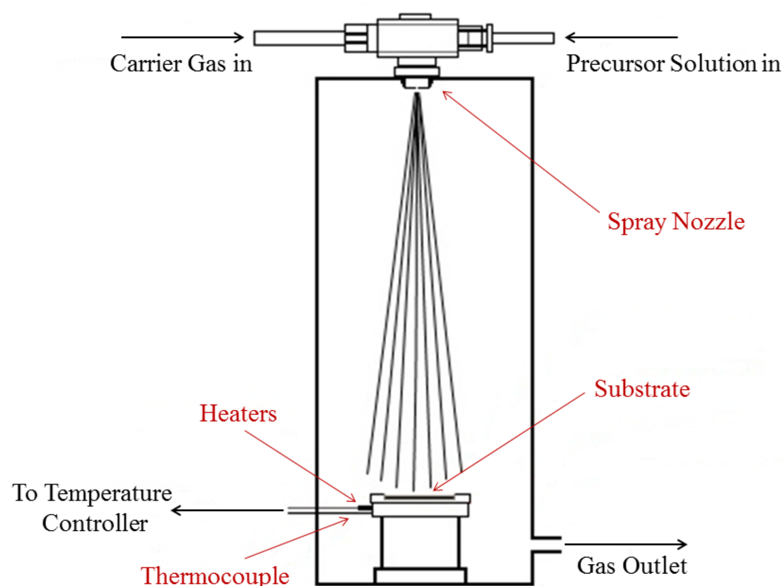

Figure 1.6: Schematic diagram of a spray pyrolysis system

Spray pyrolysis involves the generation of a fine mist of a dilute solution of an appropriate metal precursor using a nebulising technique and carrying this mist in a gas flow to a preheated substrate where the precursor thermally decomposes on the substrate surface and gives rise to continuous film growth. The process is carried out at atmospheric pressure using argon, nitrogen or air as the carrier gas to transport the precursor mist. The precursor solutions are usually made by dissolving suitable chemicals in solvents such as ethanol, butyl acetate, isopropanol, aqueous HCl or H_2O. Doping is achieved by adding proper amount of dopant compound to the spray solution. [61] A schematic-like drawing of an experimental apparatus used for spray pyrolysis is shown in Figure 1.6.

In this process, the important variables that should be taken into consideration in order to obtain uniform and good quality films are the chemical composition of the carrier gas, the precursor solution composition, and most importantly, the substrate temperature. To this list one should add the carrier gas flow rate, nozzle-to-substrate distance, droplets

radii, solution concentration, and solution flow rate. The chemical reactants are selected such that the products other than the desired compound are volatile at the temperature of deposition, and are easily removed from the system. The ease and scalability of the spray pyrolysis technique makes it particularly suitable for the preparation of large area thin films. [62] Some other advantages of the spray pyrolysis process are:

- Doping of the films can be easily done almost with any element or compound, at almost any molar ratio, by adding the correct quantity of dopant to the precursor solution.
- The thickness of the coating can be easily controlled by changing either the precursor solution volume or the precursor solution concentration.
- The precursor solution components can be changed in the middle of the process, therefore production of the layered films is possible.
- The process is very cheap and diverse types of precursor compounds and substrates can be used.
- The technique can be used for large area deposition using low-cost materials and thus, it can be extrapolated to an industrial scale.

The substrate can also have a significant influence on the properties of the films, depending on the deposition technique. [63] Substrate such as glass (borosilicate and soda-lime), alumina (sapphire and Al_2O_3), SiO_2 (quartz and silica), silicon (Si), and gallium nitride (GaN) are commonly used for thin film deposition. [64, 65] Glass substrates are the most commonly used substrates, but in processes which involve high deposition temperatures, the effect of the diffusion of alkali ions from the glass substrate to the film is extremely important. The problem is most severe in the case of soda-lime glass substrates, which have a high sodium content, or for very thin coatings. [44, 66–68] In contrast the low temperature processes such as sputtering or PLD techniques allow the deposition of the TCO films onto plastic substrates. [69–72]

1.6 ZnO

The low cost and high abundance of ZnO, as well as good optical and electrical properties, reasonable chemical and mechanical stability make ZnO thin films a cost-effective alternative and one of the most promising TCO materials to the currently used indium tin oxide (ITO) coatings, particularly for large scale applications. Zinc oxide and doped ZnO thin films continue to attract considerable interest because of their potential use in many current and emerging opto-electronic applications. [18, 73] Zinc oxide itself is an n-type semiconductor material with a direct optical band gap of 3.28 eV, [74] which is large enough to transmit most of the visible spectrum. In addition to oxygen vacancies and Zn interstitials, electron doping is accomplished either by substitutionally adding a higher valent metal, or by replacing some oxygen with fluorine or chlorine, etc. When doped with group 13 or 14 metal oxides above a certain critical doping level, ZnO thin films exhibit metal-like electrical resistivity. A combination of high optical transparency and good electrical transport properties therefore, makes doped ZnO one of the most promising transparent conducting oxides (TCOs) in a number of applications such as TFTs (Thin Film Transistors) and flat panel displays, [75, 76] OLEDs (Organic Light Emitting Diodes), [27, 77] LCD (Liquid Crystal Display) panels, [78] energy-efficient windows, [79] photovoltaics, [80, 81] touch screen displays, [82] as well as an active material in the developing area of transparent electronics/optoelectronics. [20, 83, 84]

Several synthetic methods have been applied to prepare ZnO thin films including chemical vapour deposition (CVD), [85] metal organic CVD (MOCVD), [86, 87] pulsed laser deposition (PLD), [88] magnetron sputtering, [89] radio frequency (RF) sputtering, [90] atomic layer deposition (ALD), [91] sol-gel, [92, 93] spin coating, and [94, 95] spray pyrolysis. [61, 96–99]

1.6.1 Precursors to ZnO

As explained in section 1.5, spray pyrolysis uses a precursor solution, which is atomised and sprayed onto a heated substrate, where it thermally decomposes to the desired products and gives rise to a thin film growth. Therefore, the use of the spray pyrolysis technique for the preparation of ZnO thin film requires a soluble zinc compound which can thermally decompose into ZnO after being sprayed onto a hot substrate. An ideal precursor should have relatively low decomposition temperature, and by-products of the decomposition reaction should be volatile gases which can easily escape and not leave any residue behind in the deposited material. [100] A number of zinc precursors are already used to prepare ZnO thin films by spray pyrolysis including zinc chloride, [101, 102] zinc nitrate, [61, 100, 103] zinc acetate, [96, 97, 104] and zinc acetylacetonate. [98, 99, 105]

During the last decade or so, much attention has been devoted to low temperature routes that are compatible with plastic substrates, which is particularly relevant for specific applications such as flexible displays. [106] In general, optimal thin film deposition temperature is highly dependent on the identity of the precursor compound and the details of preparation. Although the decomposition temperature of most of the common zinc compounds to ZnO is not very high, in order to improve optical and electrical properties, high deposition or annealing (post treatment) temperatures have been usually applied for preparation of thin oxide films by solution-based techniques. [93, 97] As mentioned earlier, all thin film samples in this thesis were prepared from solutions of zinc acetylacetonate, because among several Zn salts studied (Chapter 3), thermal decomposition of zinc acetylacetonate occurred at lower temperature temperature and through a one-step process.

Zinc acetylacetonate hydrate, $Zn(C_5H_7O_2)_2 \cdot xH_2O$ ($Zn(acac)_2$) is a white crystalline powder with solubility of 12 g L^{-1} in water (95 g L^{-1} in ethanol, 70 g L^{-1} in isopropanol, and 160 g L^{-1} in methanol) at room temperature. In the solid state, both oxygen atoms of the acetylacetonate ligand are bound to the zinc, forming a six-membered ring. [107]

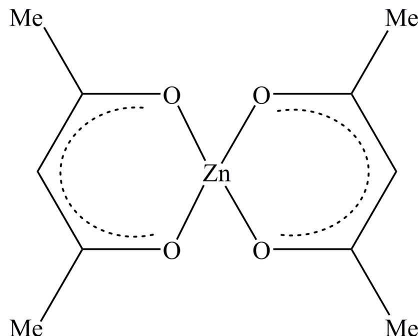

Figure 1.7: Molecular structure of $Zn(acac)_2$

Several researchers have studied the decomposition reaction of $Zn(acac)_2$ to ZnO. Figure 1.8 shows the schematic of decomposition reaction mechanism of $Zn(acac)_2$ to ZnO nanoparticles proposed by Ambrožič *et al.*, [108, 109] in agreement with the literature report on the alcoholysis of 1,3-diketones in an acidic medium into acetone and the corresponding ester. [110]

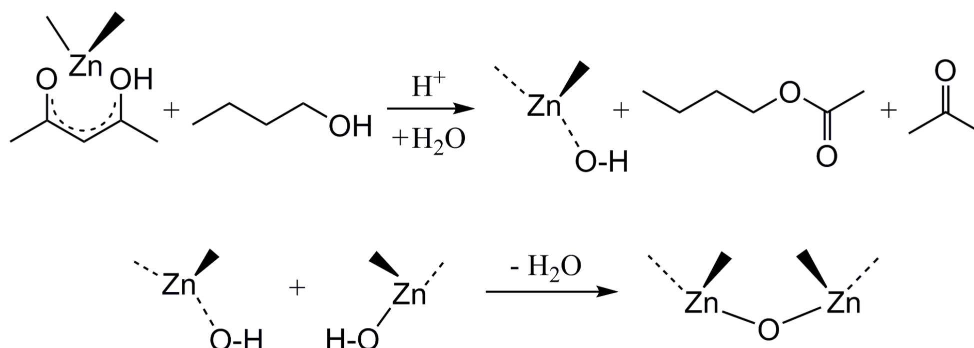

Figure 1.8: Schematic of decomposition of $Zn(acac)_2$ to ZnO in alcoholic-acidic medium (adapted from [108])

The thermal decomposition of $Zn(acac)_2$ has been studied using different techniques such as thermogravimetric analysis (TGA), differential thermal analysis (DTA), infrared spectroscopy (IR) and X-ray diffraction (XRD). Charles and co-workers carried out a comparative study on heat stabilities of some other metal acetylacetonates (including $Zn(acac)_2$) at 191 °C as a function of heating time, but the nature of the products was not reported. [111] Although mass spectrometer studies of thermal decomposition of some

metal acetylacetonates had been done earlier, [112] one of the first detailed thermal decomposition studies of Zn(acac)$_2$ was conducted by Rudolph, *et al.* in 1964. Their results indicated that it decomposes at 130 °C in an inert solvent, such as toluene and xylene. [113] Hussein thoroughly studied the thermal decomposition products of Zn(acac)$_2 \cdot$ xH$_2$O to ZnO using XRD and IR and proposed a mechanism for this route. He concluded that the formation of ZnO from Zn(acac)$_2$ occurred in six stages. [114] In another work, Arii, *et al.* proposed a simplified decomposition mechanism in controlled humidity atmospheres, as shown below in Equation 1.1:

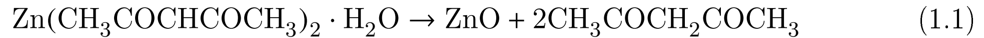

$$\mathrm{Zn(CH_3COCHCOCH_3)_2 \cdot H_2O \rightarrow ZnO + 2CH_3COCH_2COCH_3} \qquad (1.1)$$

They also claimed that at high partial pressure of water, synthesis of crystalline ZnO from Zn(acac)$_2$ can be achieved at low temperatures below 100 °C. [115]

1.7 Doping of ZnO

1.7.1 Ability to dope

Substitutional doping is a key requirement for a semiconductor to be used in practical devices. There are three factors can limit the ability to dope a material effectively [116, 117]:

- Lack of solubility of the dopant in the lattice
- Deepness of the dopant level
- Compensation of the dopant by native defects

Point 1 is usually easily satisfied and point 2 becomes more important when designing the p-type TCOs, but compensation (point 3) is the the key limitation. This occurs if moving the Fermi energy, E_F, to a band edge causes the formation of compensating defects because the formation energy of that defect has fallen to zero at that Fermi energy. In that case, if there is thermal equilibrium, the donor action is completely compensated by the defect. In the other words, the creation energy of the intrinsic defect (say the vacancy)

depends on the Fermi energy. So, there will be some Fermi energy at which the cost of the vacancy creation is zero. If a dopant would move the Fermi level to this energy, called the dopant pinning energy, then vacancies will be spontaneously created at no cost. There will be two pinning energies, one for n- and one for p-type doping. Thus, if equilibrium holds, it will be impossible to shift the Fermi level beyond these two pinning energies $E_{pin,n}$ and $E_{pin,p}$. Practical doping will only occur if these pinning energies lie in the conduction or valence band, respectively, and not in the gap. If for example, $E_{pin,p}$ lies above the valence band edge VB, then there will be no p-type doping, because it will not be possible to shift E_F to the valence band edge.

The dopability of oxides can be viewed in terms of the valence band maximum and the conduction band minimum on an absolute energy scale or with respect to a common alignment energy such as the charge neutrality level (CNL) derived from their band structures. The well-known n-type oxides (ZnO, In_2O_3, and SnO_2) are found to have conduction band edges deep below the vacuum level, while the known p-type oxides (NiO, Cu_2O, $CuAlO_2$, $CuGaO_2$, and $CuCrO_2$) have high-lying valence band edges. N-type and p-type pinning-limit energies are plotted in Figure 1.9.

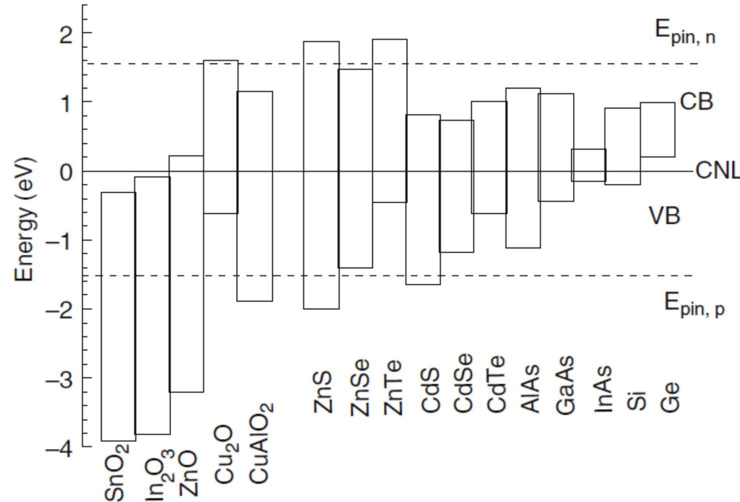

Figure 1.9: Band diagrams of various oxides semiconductors aligned according to their charge neutrality levels, with dopant pinning levels indicated (Figure adapted from [116])

The pinning-limit energies set the range over which E_F can be varied, without causing the formation of compensating defects that stop doping. If the n-type limit lies above CB of that oxide, E_F can be shifted to CB without defect formation and it can be doped n-type. If the p-type limit is below VB, then that oxide can be doped p-type without defect formation. Figure 1.9 says that the criterion is that the CNL should lie in midgap or the upper gap for n-type dopability, or at midgap or in the lower gap for p-type dopability. SnO_2, In_2O_3 are very unusual in that their CNLs actually lie above the conduction band edge [118, 119], rather than in the gap as normal. In ZnO, the CNL lies close to the conduction band edge. This accounts for their ease of n-type doping. On the other hand, that the CNL is so far above the valence band edge in SnO_2, In_2O_3 and ZnO accounts for why these oxides are difficult to dope p-type. [116]

The position of the CNL relative to the band extrema also has implications for the bulk electronic properties of the oxides. Native defects tend to drive the Fermi level in the bulk towards the CNL. For example, as the CNL lies well above the CBM in In_2O_3, native defects favourably form as donors, increasing the Fermi level, while compensating acceptor defects will have higher formation energies. This, therefore, provides an overriding band-structure explanation of the propensity for In_2O_3 to have a high background electron density even when nominally undoped. [119]

1.7.2 Doping of ZnO

Extrinsic doping is the process of addition of foreign atoms (impurities or dopants) into the crystal structure of the semiconductor materials, by which more electrons are inserted into or removed from the lattice. There are two different types of doping; **n-type** and **p-type** doping. N-type doping (n for negative charge carriers or electrons) involves substituting semiconductor atoms by elements that contribute excess free electrons. For example, small amounts of Al, In or Si can substitute for Zn (or F can substitute for O), and donate their extra valence electrons to the ZnO lattice (also called donor dopants). In n-type

semiconductors, the doping atoms form a set of energy states that lie in the band gap between the valence and conduction bands. Because the impurity atoms have more electrons than the semiconductor material atoms, these energy states are filled. Since electrons are present close to the bottom of the conduction band and can easily be excited into the conduction band, the conductivity of the material is increased (Figure 1.10 (a)).

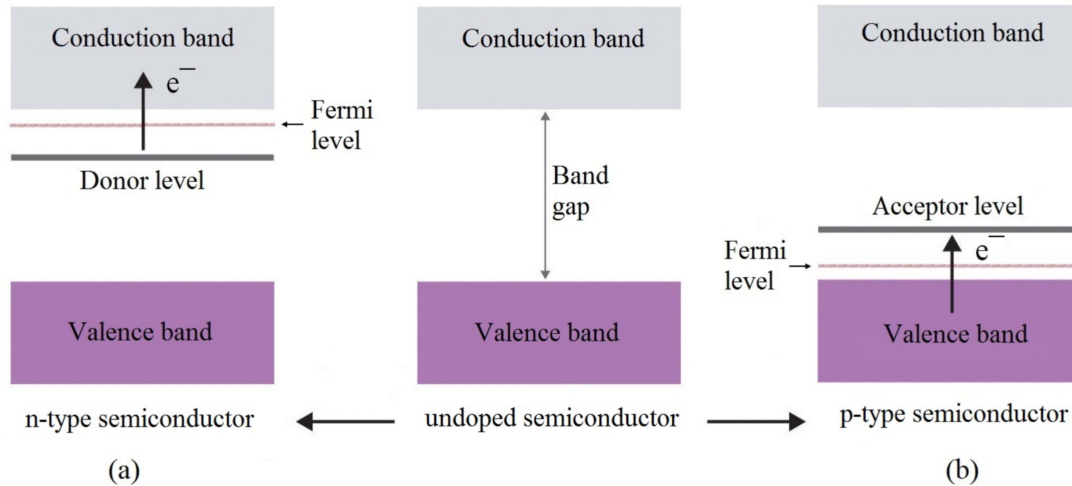

Figure 1.10: Schematic band diagrams of undoped, n-type and p-type semiconductors. (a) Elements with more valence electrons result in a new filled state between the valence and conduction bands of the host. (b) Elements with fewer valence electrons result in a new empty level between the valence and conduction bands of the host

In extrinsic p-type doping (p for positive charge carriers or holes), semiconductor atoms are replaced by impurity atoms with fewer valence electrons, such as, Li for Zn, or N for O in ZnO. These impurity atoms can accept electrons from the host atoms, in order to compensate for their deficiency of valence electrons (they are also called acceptor atoms). Therefore, for every host atom replaced by impurity atom, there is an electron missing from the valence band. A semiconductor like this is called p-type semiconductor because its conductivity is related to the number of the positive holes produced by the impurity atoms. Figure 1.10 (b) depicts energy band in p-type semiconductors.

ZnO is naturally an n-type semiconductor material, as a result of non-stoichiometry

from intrinsic lattice defects such as O vacancies and Zn interstitials. The optical and electrical properties of solution-processed undoped ZnO thin films can be further improved without extrinsic dopants by annealing the thin films at low partial pressure of oxygen and relatively high temperatures to increase the concentration of donor defects in ZnO lattice such as O vacancies or Zn interstitial atoms, [120, 121] extrinsically through doping with a variety of chemical elements, [122–124] or by combination of both strategies.

1.7.2.1 P-type doping

P-type doping of wide band gap semiconductor materials such as ZnO is very difficult for several reasons. Generally, three main factors can lead to low efficiency of p-type doping; (1) low solubility of dopants, (2) self-compensation, and (3) the formation of deep impurity levels. [125, 126] One of the major issues is a self-compensation effect, in which p-type dopants may be compensated for, by low energy native n-type defects such as Zn interstitial or O vacancy. [122, 127] As mentioned previously ZnO is naturally only n-type due to the presence of native n-type defects associated with deviations from perfect stoichiometry, making the acceptor doping of ZnO difficult.

Known p-type (acceptor) dopants in ZnO are group 1 (IA) elements such as Li, Na, and K substituting at Zn sites and group 15 (VA) elements such as N, P, and As substituting at O sites. [125] However, group 1 elements may occupy interstitial sites rather than substitutional sites, because of their small ionic radii, and therefore behave as donor dopants. Among group 15 elements, N is the most promising and commonly used p-type dopant in ZnO, as N has close ionic radius to O, thus can substitute for O with minimal lattice distortion ($r_{N^{-3}}$ = 1.46 Å and $r_{O^{2-}}$ = 1.38 Å). [128] Other group 15 elements such as P, As, Sb have much larger ionic radii than O ion. Their large size causes low solubility and large lattice distortions. [125]

1.7.2.2 N-type doping

N-type doping of ZnO is easier than p-type doping. Among all known n-type dopants for ZnO, group 13 and 14 (IIIA and IVA) elements such as Al, Ga, In, Si and Sn as substitutional elements for Zn, and group 17 (VII A) elements such as F and Cl as substitutional elements for O, have been most widely investigated. [129–134] Doping with group 13 elements (Al, Ga, and In) usually results in highly conducting and transparent ZnO thin films. The ionic radius of Al^{3+} is 0.39 Å, which is smaller than that of Zn^{2+} (0.60 Å), so the Al^{3+} can occupy the place of Zn^{2+} in lattice, leading to a reduction of the lattice parameters. [135] Ga^{3+} in comparison with Al^{3+}, has closer ionic radius (0.47 Å) to Zn^{2+} ions, which minimises the ZnO lattice deformations even at higher doping concentrations. [136, 137] Aktaruzzaman *et al.* reported a low resistivity of 2.0×10^{-3} Ω cm for spray pyrolysed Al-doped ZnO films deposited at 425 °C. [131] Major *et al.* grew In-doped ZnO films by spray pyrolysis technique at 450 °C with a minimum electrical resistivity of 8.0 - 9.0×10^{-4} Ω cm. [138] Reddy *et al.* succeeded in Ga doping of ZnO thin films grown on glass substrates by spray pyrolysis at temperature of 350 °C, and they reported resistivities as low as 1.5×10^{-3} Ω cm. [133] In has been used as the most prominent and efficient n-type dopant in ZnO probably due to its almost identical ionic radius to Zn ($r_{In^{3+}} = 0.62$ Å and $r_{Zn^{2+}} = 0.60$ Å). Doping with Sn and Si has been less thoroughly investigated and literature review results show that doping with group 14 elements is less efficient than that with group 13 elements, particularly if solution-based techniques are applied for thin film deposition. Cheng *et al.* studied the optoelectronic characteristics of Sn-doped ZnO thin films prepared on flexible PET substrates at room temperature by pulsed laser deposition (PLD) technique. The lowest electrical resistivity of their ZnO:Sn films was 3.8×10^{-2} Ω cm. [134]

Minami *et al.* pioneered the first Si-doped ZnO thin films using RF magnetron sputtering, reporting resistivities as low as 3.8×10^{-4} Ω cm in 1986. [12] Afterwards, various groups have reported that Si acts as an n-type dopant in ZnO films prepared by magnetron

sputtering, [139, 140] PLD, [141, 142] ALD, [143] and sol-gel spin-coating deposition. [144] Das *et al.* deposited thin films on sapphire substrates using PLD at a substrate temperature of 600 °C. They found the resistivity decreased from $\sim 3.0 \times 10^{-2}$ to 6.2×10^{-4} Ω cm, while the carrier density of the films increased to a maximum value of 3.25×10^{20} cm^{-3} upon increasing Si concentration up to 6.5 at.%. [141] Sato *et al.* obtained very low resistivity of 4.7×10^{-4} Ω cm and an average transmittance above 85% for Si-doped ZnO films prepared by magnetron sputtering at a substrate temperature below 140 °C. [139] Yuan grew Si-doped ZnO thin films at 300 °C using ALD method. They reported a minimum resistivity value of 9.2×10^{-4} Ω cm, with a carrier concentration of 4.3×10^{20} cm^{-3} and a mobility of 15.8 cm^2 V^{-1} s^{-1} for the films deposited at Si concentration of 2.1 at.%. [143] In another study, Sorar *et al.* reported the preparation of Si-doped ZnO thin films using the sol-gel spin-coating method. However, they only investigated the optical and structural properties of the films after heat treatment of the samples at 550 °C. [144]

The first preparation of Si-doped ZnO by spray pyrolysis was reported by Kuznetsov and Edwards in 2011. [145] ZnO thin films were deposited on glass substrates at 400 °C from precursor solutions containing zinc acetate and 2 mol.% silicon tetraacetate. A minimum electrical resistivity of 5.6×10^{-3} Ω cm was obtained for the Si-doped ZnO samples.

N-type doping of ZnO with anion impurities to substitute for O such as F and Cl, seems to be effective particularly if the films are deposited by vacuum-based techniques. However, there are many reports available on solution processed F-doped ZnO. [146–149] Unlike elements which substitute for Zn^{2+}, the effect of F^- is less discussed. Fluorine incorporates into the lattice by substituting oxygen atoms due to the comparability of ionic radius ($r_{F^-} = 1.31$ Å and $r_{O^{2-}} = 1.38$ Å [150]). For the first time, Hu and Gordon reported F doping of ZnO films in 1991. They deposited F-doped ZnO thin films on soda lime glasses using atmospheric pressure CVD at temperatures between 350 °C and 470 °C. The lowest resistivity of about 6.0×10^{-4} Ω cm, was achieved at [F] / [Zn] at.% of 0.5 for the films deposited at 400 °C. [151] Choi *et al.* fabricated F-doped ZnO (FZO) thin

films by ALD deposition technique at 140 °C. The lowest resistivity was 1.8×10^{-3} Ω cm for the ZnO film doped with 1.0 at.% F. [152] Cao et al. prepared FZO thin films via PLD, getting a resistivity of 4.8×10^{-4} Ω cm, carrier concentration of 5.4×10^{20} cm^{-3}, and Hall mobility of 23.8 cm^2 V^{-1} s^{-1}. The average optical transmittance in the visible wavelength was reportedly higher than 90%. [153] Bhachu *et al.* deposited FZO thin films on a glass substrate at temperature of 450 °C by aerosol assisted chemical vapour deposition technique. The resistivity of obtained films was 3.7×10^{-4} Ω cm. [154] F-doped ZnO thin films were synthesized at 400 °C substrate temperature using chemical spray pyrolysis technique by Shinde *et al.* Films with [F] / [Zn] ratio of 15.0 at.%, annealed at 200 °C showed the lowest resistivity, about 0.9×10^{-4} Ω cm. The reported transmittance of their films was of the order of 90%. [146] The lowest resistivity value in the order of 10^{-2} Ω cm was obtained for F-doped ZnO thin films deposited at 475 °C by chemical spray pyrolysis technique using zinc acetylacetonate and ammonium fluoride as precursors in a work by Guillén-Santiago *et al.* [147]

Only a few studies have been conducted on Cl substitution for O over the past few years, and in all those studies Cl-doped ZnO films prepared using vacuum deposition processes. [155–157] The Cl doping of ZnO is not as successful as F doping, presumably because of significant difference between ionic radii of O and Cl ($r_{Cl^{-1}}$ = 1.81 Å and $r_{O^{2-}}$ = 1.38 Å). Chikoidze *et al.* grew the Cl-doped ZnO films by MOCVD on sapphire substrates. They obtained the lowest resistivity $\rho = 3.6 \times 10^{-3}$ Ω cm for layers deposited at growth temperature of 425 °C. [155]

1.7.2.3 Co-doping method

In addition to doping with a single dopant, co-doping with more than one doant at the same time, for achieving enhanced properties in ZnO has also been investigated. Differences of radii between doping ions and Zn^{2+} or O^{2-} ions will result in variation of lattice constants and degradation of crystallinity in ZnO. This issue can be partially resolved by

co-doping methods, which have seen heightened interest in recent years. [135] Co-doping techniques were first introduced in order to improve the p-type doping of wide band gap semiconductors, using two potential acceptor dopants (A-A, such as N and As), [128] or with both donor and acceptor dopants (A-D, such as Al and N). These co-doping methods are mainly used to reduce the acceptor energy level, while leaving the valence band structure of the matrix unchanged. [158] In the A-D co-doping method, it has been suggested that the dopant solubility can be enhanced by attractive interactions between acceptors and donors and that the activation energy of dopants can be lowered by the level repulsion between donor and acceptor levels. [159, 160] Co-doping with both donor and acceptor impurities has been realized to result in p-type doping of ZnO. [159, 161] Ga+N, [161, 162], Al+As, [163], Al+N, [164] and Ga+Cu [165] co-doped ZnO thin films are some examples of donor-acceptor co-doping. Co-doping with two acceptor impurities such as Li+N co-doped ZnO films has been also demonstrated. [166]

Interestingly, besides the afore mentioned co-doping technique, another type of co-doping has also developed for further improvement in the electrical properties of n-type TCOs. This type of co-doping method involves using two donor dopants (D-D) simultaneously. One class of D-D co-doping applies two different cations which can substitute for the metal atom in TCO materials (**cation-cation co-doping**). Doping of Zn with two dopants such as Al, Ga, In or Si falls into this category. For example, preparation of Al+Ga co-doped ZnO thin films, [167] Al+Ga co-doped ZnO films [168] and Si+Al co-doped ZnO thin films [169] using vaccum-based techniques such as the RF sputtering method has been reported by various researchers.

In the other class of D-D co-doping, the lattice metal ion (Zn) is substituted by a cation, while the lattice oxygen is replaced by an anion (**cation-anion co-doping**). Obviously both cation and anion should have more valence electrons than Zn and O, respectively. Based on this assumption, the simultaneous doping of TCO materials with both cation and anion can be an interesting way to decrease the electrical resistivity values. In the case

of ZnO, different combinations of cationic and anionic elements such as In, Al, Cl, and F have been studied previously. In fact, co-doping with Al+F in ZnO thin films deposited by sol-gel [170] or RF magnetron sputtering, [171] with In+F in ZnO thin films prepared by chemical spray pyrolysis [172–174] or sol-gel, [175] and with Al+Cl in ZnO thin films grown by the spray pyrolysis technique [176] have been previously studied.

In the present work, we studied the properties of Si+F co-doped ZnO thin films deposition by spray pyrolysis technique for the first time. Afterwards, Si-doping, F-doping and Cl-doping of ZnO thin films was also investigated.

1.8 Structural properties of ZnO

TCO materials can structurally be classified into three main categories [177] as summarised in table 1.1.

Structural feature	Carrier type	Examples
Tetrahedrally-coordinated cations	n-type	ZnO, BeO
Octahedrally-coordinated cations	n-type	CdO, In_2O_3, SnO_2, Cd_2SnO_4, etc.
Linearly-coordinated cations	p-type	$CuAlO_2$, $SrCu_2O_2$, etc.

Table 1.1: Structural categories of TCOs (Adapted form [177])

The first category has n-type character and includes cations tetrahedrally coordinated by oxygen. ZnO and BeO are the only known metal oxides which crystallise in this type of coordination. The second category, which is the largest category and includes most of the best n-type metal oxide materials, has cations in octahedral coordination. The third category with p-type character has cations in linear coordination with oxygen. [177]

ZnO crystallises in three forms; hexagonal wurtzite, cubic zinc blende, and cubic rock-salt. [122] The hexagonal wurtzite structure is the most stable under ambient conditions, and therefore, is the predominant form of ZnO. In the hexagonal wurtzite structure, each anion is surrounded by four cations at the corner of a tetrahedron, and vice versa. Thus, both Zn^{2+} and O^{2-} have the coordination number of four. The various crystal structures

of ZnO are shown in Figure 1.11.

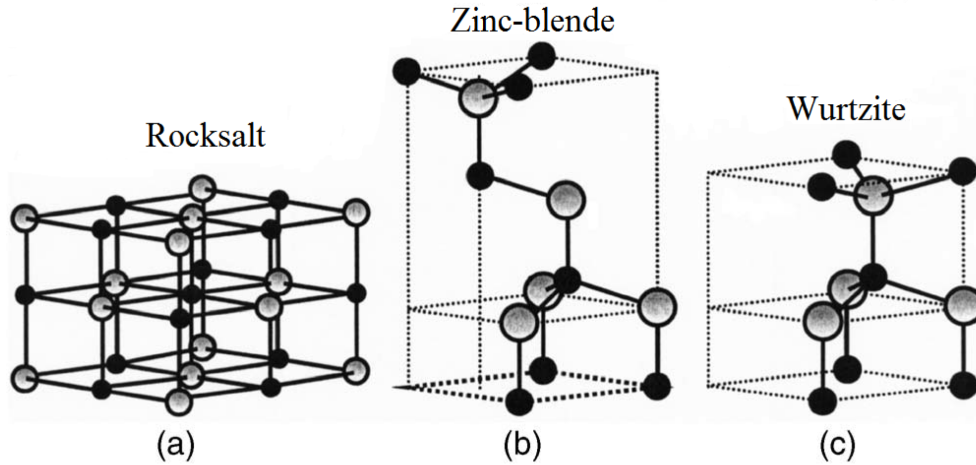

Figure 1.11: ZnO crystal structures: (a) cubic rocksalt, (b) cubic zinc blende, and (c) hexagonal wurtzite. The shaded grey and black spheres denote Zn and O atoms, respectively (Figure adapted from Özgür *et al.* [122])

The lattice parameters of a semiconductor material can be affected by several parameters; 1) free-electron concentration which occupy and deform the potential of the conduction band, [178] 2) difference between ionic radii of impurity atoms and substituted host ions, [179] 3) external strain, and 4) temperature. [122] One of the first X-ray diffraction (XRD) studies on the crystal structure of wurtzite ZnO was carried out by Bragg in 1920. [180] The hexagonal wurtzite structure has two lattice parameters a ($a = b$) and c in the ratio of $c/a = \sqrt{8/3}$ =1.633 (in an ideal wurtzite structure) and belongs to the space group C^4_{6v} in the Schoenflies notation and $P6_3mc$ in the Hermann–Mauguin notation. In a real ZnO crystal, the wurtzite structure deviates from the ideal arrangement, by changing the c/a ratio. The experimentally c/a observed ratios are smaller than ideal, where it has been suggested that not being so, would lead to zinc blende phase. [181] The lattice constants mostly range from 3.2475 to 3.2501 Å for the a-parameter and from 5.2042 to 5.2075 Å for the c-parameter. Lattice parameters a and b are at 120° in the horizontal plane, while lattice parameter c is in the vertical plane parallel to the z-axis and 90° from both a and b. [123, 182]

At extremely high pressures (~ 10 GPa), ZnO can be transformed to the rocksalt structure. [183] The reason for this is that the reduction of the lattice dimensions causes the interionic Coulomb interaction to favour the ionicity more over the covalent nature. [181] The rocksalt structure is a cubic crystal structure with cation and anion coordination numbers of six. In the unit cell of the rocksalt structure anions arranged on the face centred and corners of the cube while one cation is in the centre of the cube and there are another 12 cations on each of the cube edges.

The zinc blende structure is a metastable structure that can only be stabilised by growth on cubic substrates, such as ZnS [184] or Pt/Ti/SiO_2/Si, using topological compatibility to overcome the intrinsic tendency of forming the wurtzite phase. In the case of highly mismatched substrates, there is usually a certain amount of zinc blende phase of ZnO separated by crystallographic defects from the wurtzite phase. [181, 185] Zinc blende is a cubic structure with coordination number of four and there are four atoms per unit cell in zinc blende structure, and each cation is tetrahedrally coordinated by four anions, and vice versa. In the zinc blende unit cell anions occupy the face centred and corners of the cube and cations occupy half of the tetrahedral sites.

1.9 Optical properties of ZnO

Optical measurement constitutes the most-important means of determining the band structures of semiconductors. Photon-induced electronic transitions can occur between different bands, which lead to the determination of the energy band gap, or within a single band such as the free-carrier absorption. [186]

Several deposition parameters such as microstructure, impurity content and growth technique can influence the optical properties of TCOs. [187] Typical transmission, reflection, and absorption spectra of TCO materials is shown in Figure 1.12. The optical properties of TCO materials are closely related to its electrical properties, as the electric field component of light can interact with the electrons of the material according to the

Drude free electron model. [17]

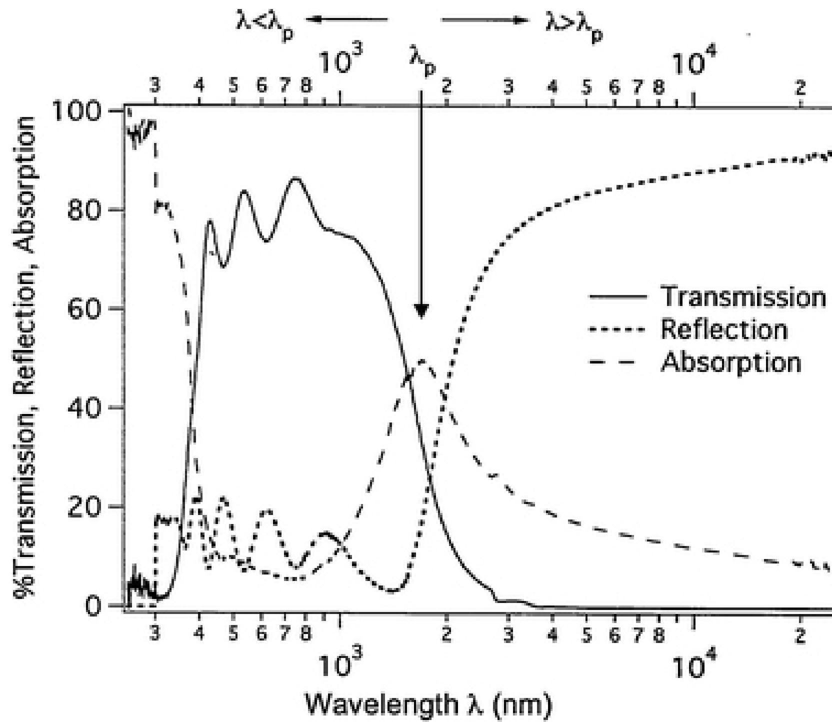

Figure 1.12: Typical transmission, reflection, and absorption spectra of a typical TCO thin films (Figure adapted from [17])

The transmission spectrum shows that for wavelengths longer than plasma wavelength the TCO reflects radiation while for shorter wavelengths TCO is transparent. There are three characteristic regions in the spectra. First, a transparent conducting oxide must be transparent in the visible region of the spectrum, typically defined as λ = 400 - 750 nm ($h\nu$ = 3.1 - 1.7 eV). Second, light with energy above the band gap is absorbed in band transitions. This occurs as an abrupt drop in transmission and increase in absorption at shorter wavelengths ($<$ 350 nm or 3.5 eV - UV region). Lastly, a second decrease in transmission and increase in reflection is observed at longer wavelengths ($>$ 1500 nm - IR region). The optical phenomenon in the IR range, corresponding to a maximum in absorption, can be understood on the basis of Drude's theory of free electrons. [188] This transition is defined by the plasma wavelength (λ_p), where the frequency of the light is the

same as the frequency of the collective oscillation of free electrons in the material. For most TCO materials, λ_p falls in the near-infrared (NIR) part of the spectrum. The electrons oscillating in phase with the electric field component of the light results in absorption. At wavelength below the λ_p ($\lambda < \lambda_p$) the wavefunction is oscillatory and radiation can propagate, resulting in a transparent material, while at $\lambda > \lambda_p$ the wavefunction decays and no radiation can propagate, resulting in reflection. [17] The validity of Drude's theory has been tested by several researchers and shown to be in good agreement with experimental results for higher wavelengths (IR region). [189–191] Hu and Gordon showed that the values of carrier density and mobility for ZnO films determined from Hall measurement and from optical analysis are in quite good agreement. [189]

In heavily doped semiconductors, there are two competing effects which can affect the absorption edge; Burstein-Moss (BM) band-filling effect and band-gap narrowing (BGN) effect (Figure 1.13). [192, 193] The well-known optical band-gap blue shift in heavily doped semiconductors occurs because the lower states in the conduction band are blocked, thus increasing the effective size of the band gap. [135] The second effect is due to the change in the nature and interaction potentials between donors and host materials, and impact the optical absorption edge with increasing donor density. This phenomenon increases the tailing of the absorption edge and therefore, results in band gap shrinkage. [194, 195] For very high carrier concentrations the band gap narrowing ($\triangle E_g$) is proportional to $n^{1/3}$.

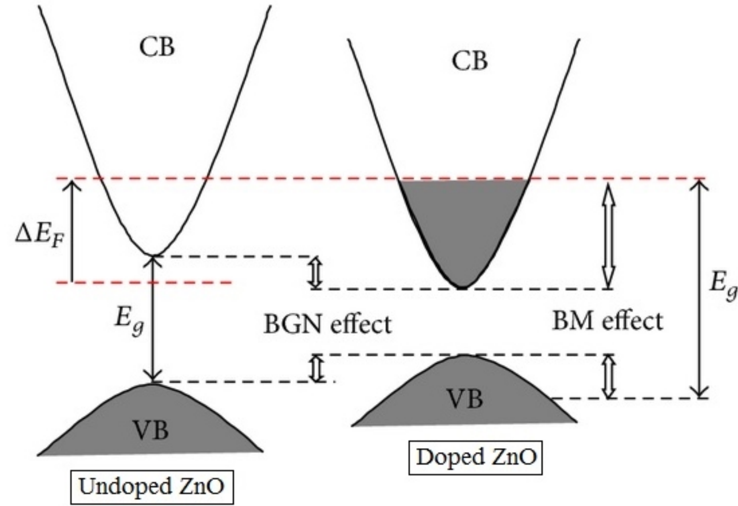

Figure 1.13: Burstein-Moss (BM) band-filling and band-gap narrowing (BGN) effects contributions to the E_g (Figure adapted from [135])

Thin films of ZnO have a sharp UV transmission cut-off at around λ = 380 nm. ZnO thin films are, in general, transparent in the wavelength range 400 - 2500 nm, and the plasma edge, depending upon the carrier concentration, lies in the range 2000 - 4000 nm. Normally as carrier concentration increases, the band edge shifts towards lower wavelengths (blue shift). The band gap varies approximately linearly with $n^{2/3}$. [187] This variation of band gap with carrier concentration can be explained by Burstein-Moss band-filling model. Both oxygen partial pressure and substrate temperature play an important role in determining the optical properties of ZnO thin films. The optical transmission of ZnO thin films grown under optimum conditions can reach greater than 80%. Films are highly transparent, but poorly conducting when the oxygen concentration is $>$ 2%. On the other hand, the films are conducting but opaque up to a substrate temperature ~ 200 °C. The films are conducting and more transparent at substrate temperature about 300 °C and higher. The reflectance of ZnO thin films in IR region depends strongly on the carrier concentration, the higher the carrier concentration, the greater the value of reflectance. Therefore, even in doped ZnO thin films the reflectance is significantly lower than other materials such as ITO.

In general, the optical properties of ZnO have been studied using various experimental techniques such as optical absorption, transmission, reflection, photoreflection, spectroscopic ellipsometry, photoluminescence, cathodoluminescence, calorimetric spectroscopy, etc. [122]

1.10 Electrical properties of ZnO

Electrical conductivity is a vital property of TCOs. Therefore, a general understanding of electronic properties is necessary. Numerous investigations have been made on the electrical properties of TCO films to understand their electrical conductivity. Various parameters such as type and temperature of substrate, film thickness, growth rate, post-deposition treatments, dopants and their concentrations, etc. can affect the electrical properties of TCO films. [60] Optimisation of the growth conditions of the metal oxide films depends on the thorough study of these parameters.

Most of TCO materials have n-type conductivity and the high conductivity in undoped TCOs mainly results from non-stoichiometry. [44] Electronic carriers are generated both intrinsically and extrinsically. The conduction electrons in undoped TCO films are supplied from donor sites associated with thermal introduction of defects such as oxygen vacancies or excess interstitial metal ions. [187] Such a process for oxides can be illustrated with the following equilibrium reaction: [17]

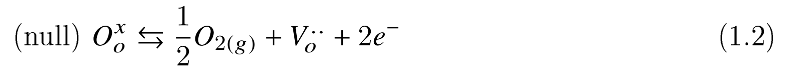

$$\text{(null)}\ O_o^x \leftrightarrows \frac{1}{2}O_{2(g)} + V_o^{\cdot\cdot} + 2e^- \quad (1.2)$$

where $V_o^{\cdot\cdot}$ is an oxygen vacancy and e^- is a free electron. Thus, the resulting material is non-stoichiometric. Intentional doping, for example with Sn in In_2O_3, F in SnO_2, or Al in ZnO will increase the conductivity of TCO films via extra free electrons donating by dopant atoms.

The electrical conductivity of a material comes from the results of various resistance

forces when electrons are in motion under the action of internal or external fields. [4] Conductivity is given by the relation:

$$\sigma = \frac{1}{\rho} = ne\mu \tag{1.3}$$

where n is the carrier concentration, e is the electronic charge, and μ is the mobility of the charge carriers. The fundamental charge of an electron is 1.602×10^{-19} C. The reciprocal of electrical conductivity is known as electrical resistivity, ρ. For a rectangular-shaped sample the resistance, R, is given by:

$$R = \rho(\frac{l}{bt}) \tag{1.4}$$

where l is the length, b is the width and t is the thickness of the sample. If $l \approx b$, equation 1.4 becomes:

$$R = \frac{\rho}{t} = R_s \tag{1.5}$$

R_s is known as the sheet resistance. Sheet resistance is independent of the actual size of the thin film, and useful parameter for describing thin films of uniform thickness. R_s is expressed in Ω/square. The conductivity of the thin films is significantly influenced by the thickness of the films. The conduction of the charge carriers might be affected by scattering at the surface of the thin films. Any surface is by definition a defect and will scatter carriers and thus, result in a decrease in conductivity of the thin films. The charge carrier might be either scattered or reflected on such a surfaces. In addition, other factors such as lattice impurities, and structural defects in the films can also influence the conductivity.

Mobility can be described as the ability of carriers to move freely and easily through the material. It is defined in terms of the average scattering time (τ) and the charge carrier effective mass (m_e^*) as: [17]

$$\mu = \frac{e\tau}{m_e^*} \tag{1.6}$$

According to the Equation 1.6, in order to increase the mobility, the scattering time

must be increased or the effective mass must be decreased. Charge transfer mobility is a major factor governing the conductivity of TCO films. Mobility of the carriers in the crystalline films is dependent on the mechanism by which carriers are scattered by lattice imperfections. The various scattering mechanisms involved in semiconducting thin films are lattice scattering (including acoustic deformation potential scattering and optical phonon scattering), neutral impurity scattering, ionised impurity scattering, and electron-electron scattering. [187] Among all the scattering mechanisms, ionised impurity scattering has the greatest impact on the scattering of the carriers, mainly because the electrostatic field due to ionised impurities is still effective at large distance. Other scattering mechanisms, such as neutral impurity scattering that was proved to play a role at low temperatures and electron-electron scattering, have been assumed to have little effect on the total scattering mechanisms. [4] In addition, grain boundary scattering is another important scattering mechanism in polycrystalline semiconductors. [196, 197] In polycrystalline thin films, depending on their mean grain size, the conduction mechanism is dominated by the inter-crystalline boundaries (grain boundaries) rather than the intra-crystalline features. Grain boundaries usually have very high densities of interface states which can trap the free carriers from the bulk of the grains and result in charge regions. These charge regions can cause band bending, resulting in the formation of potential barriers to charge transport. Minami *et al.* found that the mobility of Al-doped ZnO films with a carrier concentration in the range of 10^{20} - 10^{21} cm^{-3} was mainly dominated by ionized impurity scattering, and that of ZnO films with a carrier concentration in the range of 10^{19} - 10^{20} cm^{-3} was mainly dominated by grain boundary scattering. [198]

With respect to the application of ZnO as a transparent electrode, the aim is to achieve a resistance as low as possible with the constraint of a high transparency, both by increasing the carrier concentration and the mobility. At high deposition temperatures, polycrystalline ZnO films usually grow with the c-axes of the crystallites oriented approximately perpendicular to the film plane. [199, 200] Therefore, the electrical transport in polycrystalline films

occurs in almost all cases perpendicular to the c-axes of the crystallites. [201] The electrical properties of ZnO thin films are mainly controlled by the deposition method, thermal treatment and oxygen species chemisorption. As mentioned previously, conductivity in undoped ZnO is due to deviation from stoichiometry. In the 1930s, Wagner investigated the dependence of the electrical properties of oxides on their stoichiometry. Wagner and Schottky could show that the oxygen content of the crystals, varied by annealing at different oxygen partial pressures, strongly determines the electrical carrier concentration and hence the conductivity due to a reaction balance between oxygen vacancies (Equation 1.7) or interstitial zinc atoms (Equation 1.8) and electrons in the conduction band according to: [201]

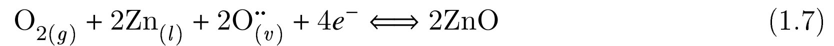

$$O_{2(g)} + 2Zn_{(l)} + 2O^{\cdot\cdot}_{(v)} + 4e^{-} \Longleftrightarrow 2ZnO \tag{1.7}$$

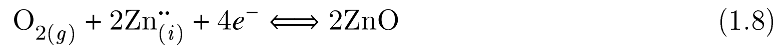

$$O_{2(g)} + 2Zn^{\cdot\cdot}_{(i)} + 4e^{-} \Longleftrightarrow 2ZnO \tag{1.8}$$

where l, v, and i are lattice place, vacancy, and interstitial position, respectively. The electrical properties of the ZnO are unstable in long term, and this instability is associated to the change in conduction of the surface of ZnO thin films due to the oxygen chemisorption and desorption. It is apparent from Equation 1.3 that the conductivity is a function of two parameters: mobility and carrier concentration. Typical carrier concentrations for doped ZnO are 10^{19} - 10^{21} cm^{-3} compared to 10^{22} - 10^{23} cm^{-3} for metals. Electron mobility in highly conductive ZnO is typically in the range of 10 - 50 cm^{2} V^{-1} s^{-1}. [17]

◆ **Effect of substrate temperature**; The variation of resistivity with substrate temperature has been studied by many researchers and results are in good agreement. Generally in the case of substrate temperatures higher than 350 °C, the increase in electrical conductivity arises from an increase in carrier concentration, and decrease in electrical conductivity at lower substrate temperatures is consistent with the decrease in carrier concentration. Webb *et al.*, [202] and Natsume and co-workers [203, 204] reported this behaviour for undoped ZnO. This can probably attributed to more complete oxidation

of organic products on the substrate surface at higher temperatures, resulting in better stoichiometry. However, mobility is usually increasing with substrate temperature. This might be because of better crystallisation, larger grain size, and reduced grain boundaries barrier potential of ZnO films. [205]

◆ **Effect of doping**; Doping of ZnO films not only improves their electrical properties, but also enhances their thermal and chemical stability in various ambients. Major *et al.* showed the films doped with 3 wt.% indium exhibit thermal stability up to 375 °C in vacuum and up to 175 °C in oxygen atmosphere. [206] In most cases, doped ZnO films have higher carrier concentration and lower mobility compared with undoped ZnO films. The higher carrier concentration is attributed to the contribution from dopant ions on substitutional sites of Zn^{2+} or O^{2-} ions, or interstitial dopant ions in the ZnO lattice, which can provide a large number of free electrons in the film. For very high dopant concentration, the conductivity is expected to to decrease due to the phase segregation of large amount of non-conductive dopant atom oxides, such as SiO_2 or Al_2O_3 when Si or Al is used as dopant, respectively, in the films. [131] As the dopant atoms in the films produce not only conduction electrons, but also ionised impurity scattering centres, the mobility generally decreases with increasing in dopant content. [1]

◆ **Effect of film thickness**; Resistivity of the films decreases with an increase of film thickness for thicknesses less than 2500 Å. After that, resistivity is almost independent of film thickness. Surface scattering is the main reason for the resistivity variations in very thin films. [187] This behaviour has been reported by Minami *et al.* for Al-doped ZnO [164, 207] and by Major *et al.* for In-doped ZnO. [206]

◆ **Post-deposition annealing effect**; Appropriate post-deposition heat treatment improves the conductivity and transparency of the ZnO thin films. Excess oxygen concentration increases the electrical resistivity, while too low an oxygen content makes the films more metallic and deteriorates the transparency. Therefore, optimisation of oxygen concentration seems to be necessary in order to obtain highly conducting, transparent ZnO

films. Annealing in reducing atmosphere such as H_2 can reduce the resistivity of highly resistive films, by lower the oxygen content of the film. Many researchers have studied the annealing effect on properties of ZnO thin films. [208–210]

1.11 Correlation of optical and electrical properties

The resistivity, ρ, of a semiconductor is related to the charge carrier density, n, and the carrier mobility, μ, by the relation in Equation 1.3. If n is increased to reduce ρ, the TCO film transmission especially in the near-infrared (NIR) region is reduced as a result of absorption by free carriers or by metal-like reflection. It is therefore important that reductions in the TCO resistivity must not adversely reduce the optical transparency of the film. However, ρ of a TCO film may be decreased without reducing the NIR transmission by increasing μ rather than n. [211]

Drude's theory which is based on the interaction between radiation and free electrons, correlates the optical constants with the electrical quantities n and μ. According to Drude's theory, for free electrons in metals, the plasma resonance frequency, ω_p, can be expressed as: [187]

$$\omega_p = (\frac{4\pi ne^2}{\varepsilon_0 m_e^*})^{1/2} \tag{1.9}$$

where n is the carrier concentration, e is the electronic charge, ε_0 is the dielectric constants of the free space, and m_e^* is the effective mass of the charge carriers. On the other hand, the carrier concentration is inversely related to the plasma wavelength as $\lambda_p \propto 1/\sqrt{n}$. Thus, the higher the carrier concentration, the lower will be the plasma wavelength. Plasma wavelength is not directly influenced by the change in mobility, and therefore as mentioned previously, one approach to improving conductivity without adversely impacting visual transmission is to increase the mobility instead of the carrier concentration, which can be done by eliminating scattering mechanisms or by choosing a different material with improved mobility. [17]

1.12 Defect structures of Si, F, or Cl doped ZnO (First-principles electronic structure calculations)

1.12.1 Zn and O defect models

Few possible types of Zn and O native point defects in ZnO are vacancies (V_{Zn}, V_{O}), interstitials (Zn_i, O_i), and anti-site defects (Zn_O, O_{Zn}). The O vacancy, Zn interstitial and Zn anti-site, which are associated with O defficiency or Zn excess (Zn-rich/O-poor conditions), are donor-type defects. The Zn vacancy, O interstitial and O anti-site are acceptor-type defects associated with Zn deficiency or oxygen excess (O-rich/Zn-poor conditions). [212, 213]

Zn vacancies, which have been suggested to be the dominant acceptor-type defect in ZnO, introduce partially occupied sites in the band gap. These states are derived from the broken bonds of the four oxygen nearest neighbours and lie close to the valence band maximum (VBM). They are partially filled and can accept additional electrons, thus causing V_{Zn} to act as an acceptor. In n-type ZnO, zinc vacancies have the lowest formation energy among the native point defects under the O-rich limit. [213] Among the native donor-type defects, oxygen vacancies have the lowest formation energy under O-poor conditions. Oxygen vacancy has a deep donor level and has been proposed to be the source of non-stoichiometry in ZnO. In contrast, in another local density approximation (LDA) analysis by Janotti and Van de Walle, the formation energy of V_{O} was reported quite high in n-type materials. They claimed that V_{O} concentration will always be very low, even under extreme Zn-rich conditions. [213, 214]

There are two distinct types interstitial sites in the wurtzite structure: the tetrahedral (tet) sites and the octahedral (oct) sites, as shown in Figure 1.14. The difference between the tetrahedral and octahedral interstitial sites can be understood by considering a view of the wurtzite structure along the hexagonal axes. There are open, six-member channels in the structure, and a location within one such channel approximately equidistant from six oxygen sites is the octahedral interstitial location. In contrast, the tetrahedral site can be viewed

as a site along the c-axis projected from a host site away from the associated host bond, such that it is approximately equidistant from four host oxygen atoms at lower distance. [215] Therefore, Zn atom placed at the tetrahedral site will be dynamically unstable, [213] and Zn interstitial prefers the octahedral site where the geometrical constraints are less severe. [212] A Zn interstitial will always donate electrons to the conduction band, thus Zn_i is suggested to be a shallow donor. With regard to the high formation energy of Zn_i (even at O-poor limit), the concentration of the Zn_i is expected to be very low in n-type ZnO under thermal equilibrium. However, Kim *et al.* has found by means of local density approximation (LDA) calculations, that the Zn interstitial may be stabilized in the presence of a high concentration of the O vacancy. [216]

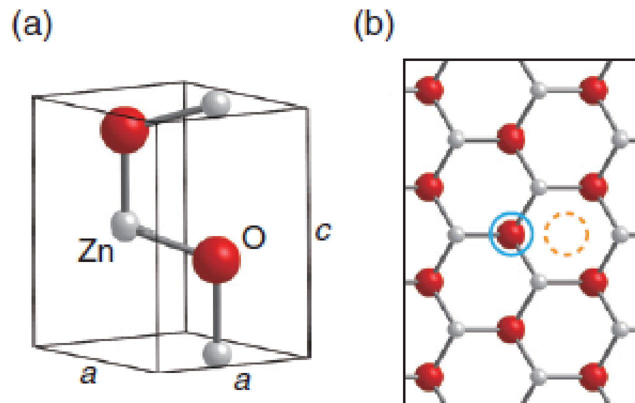

Figure 1.14: (a) Unit cell of ZnO. Smaller (grey) and larger (red) circles denote Zn and O atoms, respectively. (b) Crystal structure of ZnO viewed from the [0001] direction. Octahedral and tetrahedral interstitial sites are denoted by dashed and solid circles, respectively (Figure adapted from Oba *et al.* [212])

Excess oxygen atoms in the ZnO lattice can be incorporated in the form of oxygen interstitials. The oxygen atoms can also occupy the octahedral or tetrahedral sites or from split interstitials ($O_{i(split)}$). A split interstitial is a configuration in which oxygen shares a lattice site with one of the nearest neighbour substitutional oxygen atoms. The O_i at the tetrahedral site is unstable and spontaneously relaxes into a split interstitial. Interstitial

oxygen can exist either as electrically inactive split interstitials $O^0_{i(split)}$ in p-type materials or as deep acceptors at the octahedral interstitial site $O^{-2}_{i(oct)}$ in n-type materials. However, the formation energies of both forms are very high except under extreme O-rich conditions, and oxygen interstitials are not expected to be present in significant concentrations under equilibrium conditions. [124]

Zn anti-site defects consist of a Zn atom located at the O site (Zn_O), and oxygen anti-site defect is an O atom that wrongly occupies a site on the Zn sub-lattice (O_{Zn}). Zn anti-sites behave as shallow donors, but first principle calculations showed that Zn_O defects have higher formation energy than the other donor-type native defects (Zn_i and V_O). Thus, Zn_O is unlikely to form at substantial concentration in n-type ZnO. [213, 214, 217] O_{Zn} is an acceptor-type point defect with a very high formation energy, even higher than O_i, even under O-rich conditions. This makes it very unlikely that O_{Zn} would be present at thermal equilibrium.

Since the native defects possibly cannot explain the observed n-type conductivity in ZnO, it was proposed that other impurities may be present in different growth environments and act as donors. Among the possible impurities, hydrogen is a likely candidate. First principles calculation showed that hydrogen can substitute on an oxygen site and form a multi-centre bond with the four nearest neighbour Zn atoms. [124, 213, 218] Substitutional hydrogen (H_O) has a low formation energy, acts as a shallow donor, and can explain the variation of conductivity with oxygen partial pressure, consistent with a wide range of experimental results. [219, 220]

1.12.2 Si defect models

Doping of the ZnO films is achieved by introducing dopant atoms to the lattice. The ideal ZnO structure is a hexagonal wurtzite structure with two Zn and two O atoms in each primitive cell. For a dopant such as Si acting as an electron donor, three possible defect models can be considered: A substitutional Si ($Si_{s(Zn)}$) which is created by substituting

one Zn atom with one Si atom, and interstitial Si, where one Si atom is embedded into a interstitial space. [221] The potential doping sites of Si atoms, including $Si_{s(Zn)}$, $Si_{i(oct)}$ and $Si_{i(tet)}$), are indicated as 1, 2, and 3, respectively, in Figure 1.15.

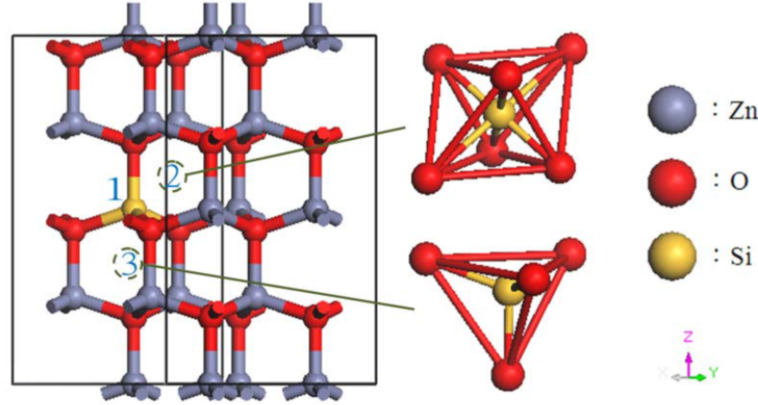

Figure 1.15: A 2 × 2 × 2 ZnO supercell model containing substitutional and interstitial Si atoms. 1, 2, 1nd 3 show substitutional, octahedral interstitial site, and tetrahedral interstitial site, respectively (adapted from Wu *et al.* [221])

Results of density functional theory (DFT) analyses demonstrate that $Si_{s(Zn)}$ defect exhibited the lowest formation energy, indicating that substitutional Si defects are formed more easily than interstitial defects. [221] For all Si defects, the Fermi level shift upward into the conduction band with typical n-type conductive characteristics. Substitutional Si defect creates shallow levels near the conduction band minimum (CBM), which can serve as donor levels and improve the conductivity. In both interstitial models, the larger effective masses of electrons obtained from the calculations are related to a reduction in carrier mobility and electrical conductivity. Additionally, the calculations have shown that the presence of interstitial Si atoms can generate resonant levels within the conduction band but also deep levels below the CBM of ZnO. These levels can lead to a reduction of the optical transparency of Si-doped ZnO. According to DFT calculations, Si acts as a double donor. [221] However, in experiments, Si apparently does not act as an fully effective double donor. A possible reason for the reduction of free electrons has been claimed to be the presence of native intrinsic acceptors like the zinc vacancies which can trap electrons and

thus reduce the effective number of free charge carriers related to $Si_{s(Zn)}$. DFT calculations suggest that the formation energies of the Si substituting O states (Si_O) is much higher than Si on Zn site and Si_O defect is very unlikely to form. [222]

1.12.3 F defect models

F has one more electron than O and, when inserted on the O site (F_O), can act as a shallow donor in ZnO. [124, 214] As discussed earlier, oxygen vacancy has the lowest formation energy under O-poor conditions. [213, 214] Therefore, less energy is required for a fluorine atom entering into the site where the oxygen vacancy forms. F ions at oxygen sites could result in a reduction in oxygen vacancy concentration. The formation energy of F_O is much lower in p-type ZnO than that in n-type ZnO, where F_O is assumed to be in 1+ charge state. [223] At high fluorine doping concentration, F_i could appear, where fluorine atoms could occupy the tetrahedral or octahedral interstitial sites ($F_{i(tet)}$ and $F_{i(oct)}$), but only octahedral interstitial site could be stably occupied. The results of DFT calculations of formation energies by Liu *et al.* indicated that for ZnO:F under O-poor condition, F_O has lower formation energy than F_i, and the formation energies for F_i defects are relatively high, even under the F-rich condition. [223] In polycrystalline ZnO thin films, a considerable amount of surface dangling bonds can trap free carriers and decrease the mobility of carriers. Fluorine ions at grain boundaries could cause surface passivation effect by saturating these dangling bonds and thus increase carrier concentration and mobility. [224]

1.12.4 Cl defect models

Figure 1.16 shows the structure of wurtzite ZnO:Cl, with Cl substituted for oxygen. Doping of ZnO with Cl produces a structural distortion around the dopant site. These distortions arise from the larger ionic radius of Cl^- (1.81 Å) compared to the ionic radius of oxygen anion (1.38 Å). Calculation results showed that in stoichiometric ZnO, the Zn–O distances are 1.97 Å, while with Cl-doping, the Zn–Cl bond distances range from 2.38 - 2.43 Å. [155]

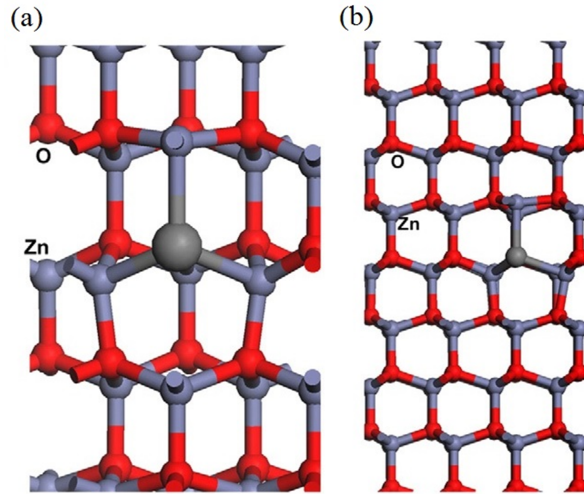

Figure 1.16: (a) (2 × 2 × 2) and (b) (4 × 4 × 4) supercells of ZnO, each with one Cl dopant substituting for a lattice oxygen. Zn and O atoms are indicated in the figure and the dopant is the large grey sphere (Figure adapted from Chikoidze *et al.* [155])

The calculated formation energies from the density functional theory (DFT) calculations performed by Liu *et al.*, indicated that interstitial site Cl_i has relatively high formation energy and is unlikely to form during the growth. The calculation results also showed that although the Cl^- ion may occupy the tetrahedral or octahedral interstitial sites in the ZnO structure, but only octahedral interstitial site could be stably occupied. However, they suggested that Cl when inserted on the O site, Cl_O, has lower formation energy in the O-poor condition and therefore, is energetically more favourable. [225] They also found that the formation energies of Cl_O and Cl_i are higher than those of F_O and F_i in ZnO:F [223] and they correlated that to the radii of Cl^- and F^- ions, and to the fact that the radius of F^- is closer to the radius of O^{2-}. They calculated the Zn−O, Zn−F, and Zn−Cl bond distances to be 1.95 Å, 2.11 Å, and 2.33 Å, respectively, and thus the higher formation energy of Cl_O and Cl_i might be due to the considerable lattice distortion caused by the large radius Cl^-.

Chapter 2

Experimental Techniques and Data Acquisition

Characterisation techniques such as X-ray diffraction (XRD), atomic force microscopy (AFM), X-ray photoelectron spectroscopy (XPS), ultraviolet, visible and near-infrared (UV-Vis-NIR) absorption spectroscopy, Hall effect measurement and scanning electron microscopy (SEM) are widely used to understand and determine the structural, optical and electrical properties of the semiconductor thin films. A brief introduction to the background and applications of these techniques and different types of data that can be achieved from each of them will be presented in this chapter.

2.1 X-ray diffraction (XRD)

2.1.1 Introduction

X-ray scattering and spectroscopy methods can provide useful information concerning the physical and electronic structure of crystalline and non-crystalline materials. X-ray Diffraction (XRD) is generally the first and most commonly used technique for investigating the atomic and crystal structure of crystalline materials. The technique is non-destructive and can be applied to any polycrystalline phase such as powders, cast solids and films grown on a substrate. Extensive amounts of information can be extracted from an XRD pattern. The key applications of this technique can be summarised as: [226]

- Identification an unknown material by comparing the positions and intensities of the the observed peaks in the XRD spectrum to a database of known materials.

- Determination of the crystal structure.

- Detection of lattice vacancies, texture analysis and determination of the preferred orientations.

- Measurement of internal strain and crystallite size.

- Quantitative phase analysis of a mixture of two or more crystalline phases.

Some of these objectives can only be achieved with high-resolution data and high sample quality.

2.1.2 Principles of the technique

The technique involves generating electrons by heating a filament (usually tungsten) electrically in vacuum and accelerating the electrons by a high voltage power (20 - 50 kV) toward a metal target (copper, molybdenum, etc.). The collision of the electrons with the anode material results in emission of a continuous spectrum of X-rays.

When an X-ray strikes an atom, it will be scattered in all directions. A crystal is made up of a families of lattice planes (*hkl*, called Miller indices) and the X-rays reflected by each

plane will only emerge as a single beam of a reasonable intensity if they reinforce and arrive at the detector in-phase with one another. For constructive interference to take place, the path length of the incident beams must differ by an integral number of wavelengths.

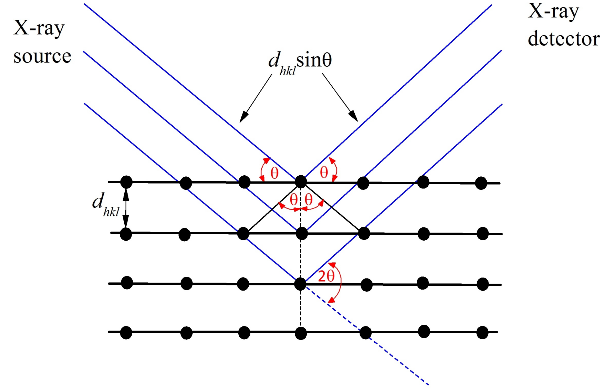

Figure 2.1: Bragg reflection from a set of crystal planes with a spacing d_{hkl}

This results in a relationship between the X-ray wavelength λ, the spacing d between lattice (hkl) planes, and the angle of incidence θ, as shown in Figure 2.1 and known as the Bragg's law: [227]

$$n\lambda = 2d_{hkl}sin\theta \tag{2.1}$$

where n is an integer and when $n = 1$, the reflections are called first order, and when $n = 2$ the reflections are second order, and so on. However, the Bragg equation for a second order reflection from set of planes hkl is:

$$2\lambda = 2d_{hkl}sin\theta \tag{2.2}$$

which can be written as:

$$\lambda = 2\frac{d_{hkl}}{2}sin\theta \tag{2.3}$$

Equation 2.3 represents a first order reflection from a set of planes with inter-planar spacing $\frac{d_{hkl}}{2}$. The set of planes with inter-planar spacing $\frac{d_{hkl}}{2}$ has Miller indices $2h2k2l$. Therefore,

the second order reflection from *hkl* is indistinguishable from the first order reflection from $2h2k2l$, and the Bragg equation may be written more simply as:

$$\lambda = 2d_{hkl} sin\theta \tag{2.4}$$

From the Bragg equation, each set of lattice planes with a unique d-spacing will give rise to a distinct diffraction peak in the XRD pattern and the lowest angle peaks will come from crystal planes with the largest spacing. The characteristic set of d-spacings and their intensity generated in a X-ray scan provides a unique fingerprint of the planes present in a sample. d-spacing can be calculated from cell constants (a, b, c) and Miller indices (hkl). As an example, d-spacing for cubic crystal structure, is calculated from the equation below:

$$\frac{1}{d_{hkl^2}} = \frac{h^2 + k^2 + l^2}{a^2} \tag{2.5}$$

2.1.3 Applications of XRD

2.1.3.1 Phase determination by fingerprinting

Any crystalline material produces a diffraction pattern that is characteristic of its constituent compounds or phases. In order to identify the contents of a sample and to determine the presence or absence of any particular phase, the position and approximate relative intensities of a set of peaks in an XRD pattern can be compared to a database of patterns for known materials. International Centre for Diffraction Data (ICDD) is one of the world's largest centres which has provided a large set of diffraction and related data from almost every known inorganic and many organic crystalline substances. Generally, to have a valid match, all expected reflections should be seen in the reference data. If the measured pattern contains more reflections than the reference, more than one phase might be present in the sample.

2.1.3.2 Quantitative phase analysis

A mixture of two or more crystalline phases can be analysed in terms of its phase fractions. The relative proportions of crystalline phases present in a sample can be determined with a high quality XRD data. [226]

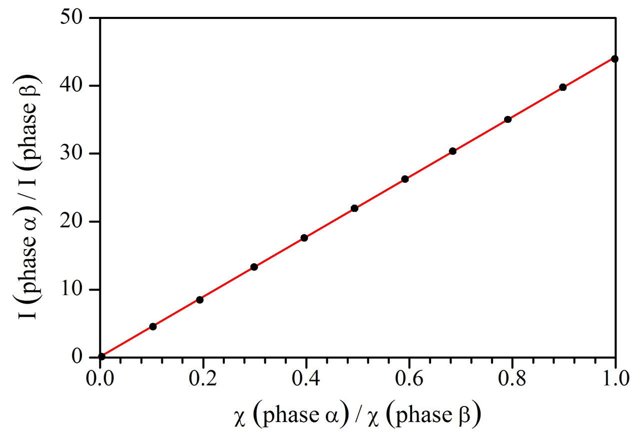

Figure 2.2: Peaks intensities as a function of weight fractions for a mixture of two phases (adapted from [228])

The ratio of peak intensities varies linearly as a function of weight fractions for any two phases in a mixture as shown in Figure 2.2. [228]

$$\frac{I_\alpha}{I_\beta} = K\frac{\chi_\alpha}{\chi_\beta} \tag{2.6}$$

where $I_\alpha$and I_β are the intensities of 100% peak, and χ_α and χ_β are the weight fractions of phases α and β respectively, and K is calibration constant which can be determined by:

- Empirical measurements of known standards
- Calculating from published reference intensity ratio (RIR) values ($K = \frac{RIR_\alpha}{RIR_\beta}$)
- Calculating by whole pattern fitting/Rietveld refinement

RIR method gives semi-quantitative results, whereas quantification by using Rietveld method is more accurate but more complicated.

2.1.3.3 Calculation of lattice parameters

Alloying, substitutional doping, temperature and pressure, etc. can create changes in lattice parameters. The unit cell lattice parameters of phases in a sample can be determined by accurately measuring peak positions over a wide range in 2theta. The observed peak positions are converted to corresponding d_{hkl} values using Bragg equation (Eq. 2.1) and the Miller indices (hkl) of the diffraction peaks are identified from published reference patterns. Once d_{hkl} and hkl values are determined, the lattice parameters can be calculated by replacing them in the d-spacing equation. For example, in cubic crystal structure $a = b = c$ is calculated from the equation below: [227]

$$d_{hkl} = \frac{a}{\sqrt{(h^2 + k^2 + l^2)}} \tag{2.7}$$

Using many peaks over a long range of 2theta will help to identify and correct the peak position (angle) errors arises from mechanical faults or instability of the instrument or from displacement of the sample from the axis of the diffractometer. Moreover, the unit cell volume can easily be calculated from lattice constants. The cell volume V for cubic crystal structure is given by:

$$V = a^3 \tag{2.8}$$

2.1.3.4 Analysis of crystallite size and strain

As the crystallite size decreases, the width of the diffraction peak increases. Therefore, crystallites smaller than ~ 100 nm create broadening of the peaks. This peak broadening can be used to calculate the average crystallite size using Scherrer equation: [227]

$$\tau = \frac{K\lambda}{\beta cos\theta} \tag{2.9}$$

where τ is the mean crystallite size, K is Scherrer constant (~ 0.94, dependent on crystallite shape and crystallite-size distribution), λ is the wavelength of the radiation, β is the full-width at the half-maximum (FWHM, also known as additional broadening, in radians) and θ is the Bragg angle.

Peak broadening may also be caused by non-uniform lattice strain and defects. In the cases where both stress and finite crystallite size lead to broadening of the diffraction peaks, a more comprehensive method must be used to separate the contributions.

2.1.4 Instrumentation

The X-ray diffraction (XRD) measurement of all samples was carried out on a PANalytical X'Pert PRO diffractometer, operating in the Bragg-Brentano geometry with a fixed X-ray source, at the emission current of 40 mA and the anode voltage of 45 kV. The divergence slit is automatically adjusted to maintain a fixed sample irradiation area during the scan. The spectra were recorded using high intensity, monochromated Cu-$K_{\alpha 1}$ radiation (λ = 1.54059 Å) from 5° to 80° scanning angle (2θ) with a step size of 0.0084°. Samples in form of fine powders or thin films were placed on spinner sample holder and to improve the averaging the crystallite orientation, the spinner stage was rotated at 60 rpm during the measurement. XRD spectra and structural properties of the samples are studied in Chapters 6, 4, and 5.

2.2 Atomic Force Microscopy (AFM)

2.2.1 Introduction and principle of the technique

Atomic force microscopy (AFM) is a powerful analytical technique capable of imaging almost any type of surface, including polymers, ceramics, composites, coatings, glass and biological samples, the operation of which does not require any particular environmental conditions. Imaging can be performed in vacuum, at high pressure (air), and in liquids.

An atomic force microscope is atype of Scanning Probe Microscope (SPM), which works by measuring a local property such as height, optical absorption, or magnetism, with a probe (tip) mounted on a very flexible cantilever and maintained very close to the sample. The physical characteristics of the cantilever and tip can affect the performance of an AFM. The cantilever-tip assemblies in use today are produced by etching single chips of silicon, silicon oxide, or silicon nitride replacing early metal foil AFM cantilevers cut with manually glued tips made from crushed diamond particles. Three modes are commonly used in AFMs: contact mode, non-contact mode, and tapping mode. [229] In contact mode the tip is in constant contact with the surface of the sample. This can lead to frictional forces as the tip moves over the sample, which dull the tip and damage the sample. In tapping mode, the tip periodically contacts the surface for only a short time and then is removed which can effectively overcome the problem of surface damage. The non-contact mode is the least common mode of operation, in which the tip hovers a few nanometres above the sample surface. In this mode attractive van der Waals forces between the tips and the sample are detected as the tips scans over the surface. These forces are weaker than those detected in contact mode AFMs. Hence, tip oscillation and ac detection techniques are required to recover the small signals.

The amount of deflection of the cantilever, caused by the forces developed between the tip and the sample, is measured by reflecting light from a laser diode off the back of the cantilever, onto an array of position-sensitive photodetectors. This signal is used to generate an image of the surface as shown in Figure 2.3.

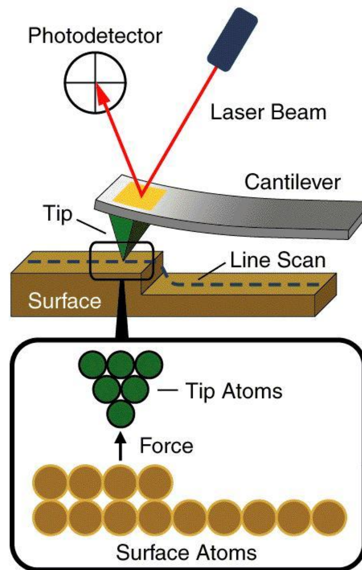

Figure 2.3: Schematic description of the underlying principles of Atomic Force Microscopy (AFM) [230]

The force is not measured directly, but can be calculated using Hooke's law, by measuring a deflection of the cantilever, of known stiffness:

$$F = -kz \tag{2.10}$$

where F is the force, k is the stiffness of the lever and is a constant, and z is the distance the lever is bent. Depending on the sharpness of the tip, AFM can generate high-resolution (1 - 20 nm) topographical images of the surface of a sample. [226]

2.2.2 Applications of AFM

The ability of AFM to provide nanometer-scale three-dimensional images, as well as studying the topography of the surface of the samples with little or no sample preparation in the sample's native environment, makes this technique extremely useful in materials science. Some possible applications of AFM are:

- Determination of surface roughness

- Analysis of grain size

- Analysis of force curves to obtain information regarding the chemical and mechanical properties of the surface such as adhesion, elasticity, hardness and rupture bond lengths

Force curves measure the amount of force felt by cantilever as the tip is brought close to the sample surface and then pulled away. In a force curve analysis the probe is repeatedly brought towards the surface and then retracted, as shown in Figure 2.4. The slope of the the deflection (C in Figure 2.4) provides information on the hardness of the sample and the adhesion (D in Figure 2.4) provides information on the interaction between the probes and samples surface.

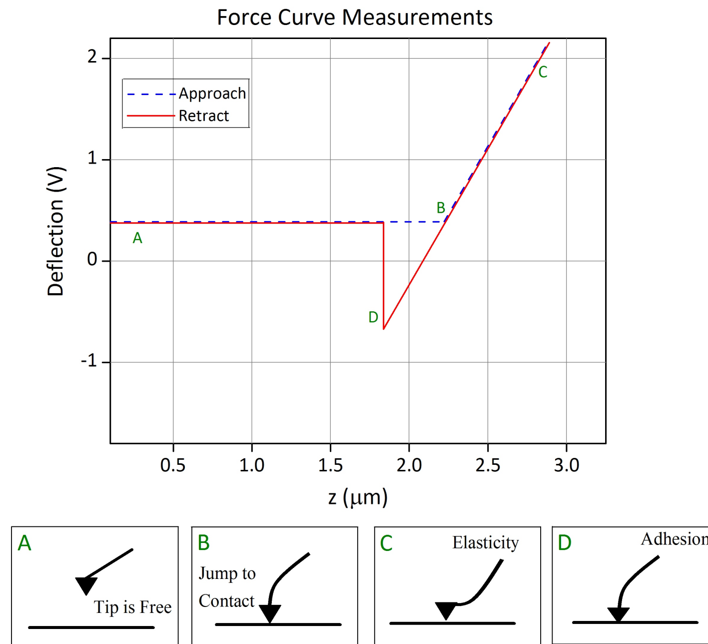

Figure 2.4: A typical force curve showing the various probe-sample interactions [231]

AFM can be used alone or can be combined with other optical and spectroscopic techniques to provide complementary information.

2.2.3 Instrumentation

AFM images were recorded on a Digital MultiMode scanning probe microscope, using a Nascatec GmbH (model NST NCHFR) silicon probe with resonant frequencies of approximately 320 kHz, and in conjugation with a NanoScope IIIA controller which provides 16-bit resolution on three dimensions. The MultiMode allows both conductive and non-conductive samples to be studied. The measurements were carried out in tapping mode, in air across the surface of the sample, and tip velocities were chosen 2, 5, and 10 μm s^{-1} for the scan size of 2, 5, and 10 μm, respectively. AFM images are illustrated in Chapters 6 and 4.

Nanoscope 5.12r3 software was used to analyse the AFM data. Using this software the Images can be displayed in two- or three-dimensional representations, and analysed with a wide variety of functions including cross sectional analysis, roughness measurement, grain size analysis, and depth analysis.

2.3 X-ray Photoelectron Spectroscopy (XPS)

2.3.1 Introduction

X-ray photoelectron spectroscopy (XPS) is a non-destructive analytical method which is applied to all types of solids, including metals, ceramics, semiconductors and polymers in many forms, including foils, fibres and powders. It has also been used to study gas phase compounds. XPS is a surface-sensitive technique with a nominal analysis depth of about 1 - 10 nm. XPS quantitatively measures the elemental composition, atomic concentration and chemical states of elements, including oxidation states or hybridisation states for the chemical bonds of the elements present at surface of a sample. All elements with atomic number greater than 3 can be detected, detection limits for most of the elements are in the parts per thousand range, and the detection sensitivity varies for each element. XPS is also known as ESCA (Electron Spectroscopy for Chemical Analysis).

2.3.2 Principles of the technique

XPS involves irradiating a sample with soft X-rays (usually Al-K_α= 1.4866 keV or Mg-K_α=1.2536 keV) of characteristic energy in high vacuum ($\sim 10^{-8}$ - 10^{-10} torr) and measuring the flux of escaping electrons (photoelectrons) leaving the surface. Therefore, the fundamental event associated with XPS measurements is photoemission precess. A X-ray photon of frequency $\nu = c/\lambda$, where λ is its wavelength, has a kinetic energy of $h\nu$. Interaction and absorption of the X-ray photon with the electrons in the material can lead to an electronic excitation of the atom. The kinetic energy (E_K) of the ejected electron from an atomic orbital is equal to the energy of the primary X-ray photon less the initial binding energy (E_B) of the electron according to the following equation:

$$E_K = h\nu - E_B - w \tag{2.11}$$

In this equation, w is the work function of the spectrometer, which corrects for the electrostatic environment in which the electron is formed and measured. [229] The binding energy of an electron is characteristic of the atom and orbital that emit the electron and can be determined from the kinetic energy of the electron which is experimentally measured using electrostatic, time-of-flight, or magnetic analysers. Figure 2.5 illustrates a schematic diagram of the emission of an electron from the 1s atomic orbital of an atom.

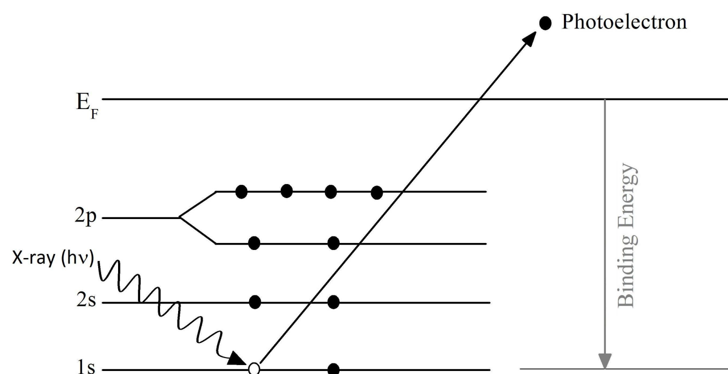

Figure 2.5: Schematic of the excitation process leading to photoemission (E_F is the position of the Fermi energy, solid circles and open circles are core-level electrons and holes, respectively)

The number of electrons that arrive at the detector is counted for a certain time interval, and the electron counting is repeated at a new E_K value, or alternatively the number of electrons at the detector is counted concurrently while sweeping the energy selection range of the analyser. Typical output from XPS measurements is a spectrum of number of electrons emitted from the sample per unit time (electron counts per time, or I_i^e) as a function of electron binding energy or the E_K of the electron. Since core level electrons in solid-state atoms are quantised, the resulting energy spectra exhibit resonance peaks characteristics of the electronic structure for atoms at the sample surface, thus peaks appear in the spectrum at energies where electronic excitation has occurred.

As can be seen in Figure 2.5 the primary ionisation of an electron leaves behind a site of positive charge (hole) which can be filled with a secondary ionisation process, of which the Auger process is one of the important relaxation processes can occur. The Auger process is shown in Figure 2.6.

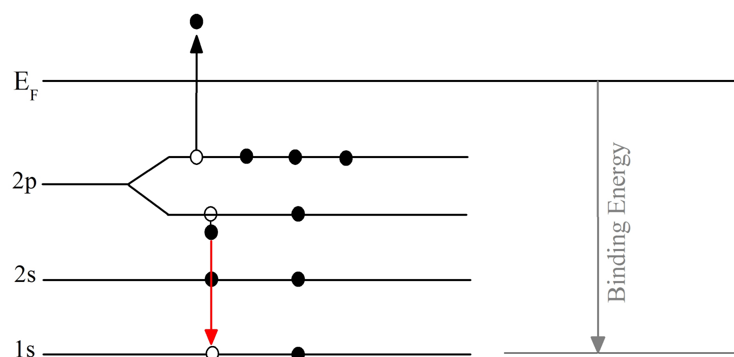

Figure 2.6: Schematic of the Auger relaxation process

An upper lying (lower E_B) electron drops into the hole, and the energy available from this transition is sufficient to cause ejection of a second electron (called Auger electron) from an upper energy level. Because Auger process is an internal ionisation process, the kinetic energy for a particular Auger process is independent of the X-ray photon energy and how the initial hole was created. Auger electron peaks will also appear in XPS spectra and are more difficult to characterise than XPS peaks.

Figure 2.7 shows a XPS survey spectrum of ZnO consisting of a plot of electron-counting rate (CPS) as a function of binding energy E_B. It is evident that XPS provides a means of qualitative identification of the elements present on the surface of solids. ZnO is made up of two elements and well-separated peaks for each of the elements can be observed. In addition, a small peak for carbon is present, suggesting that some surface carbon contamination from the ambient atmosphere had occurred. It can be noted that the binding energies for 1s electrons increase with atomic number due to the increased positive charge of the nucleus. Moreover, more than one peak for a given element can be observed; therefore, peaks for $3d$, $3p$, $3s$ and $2p$ electrons for Zn can be seen.

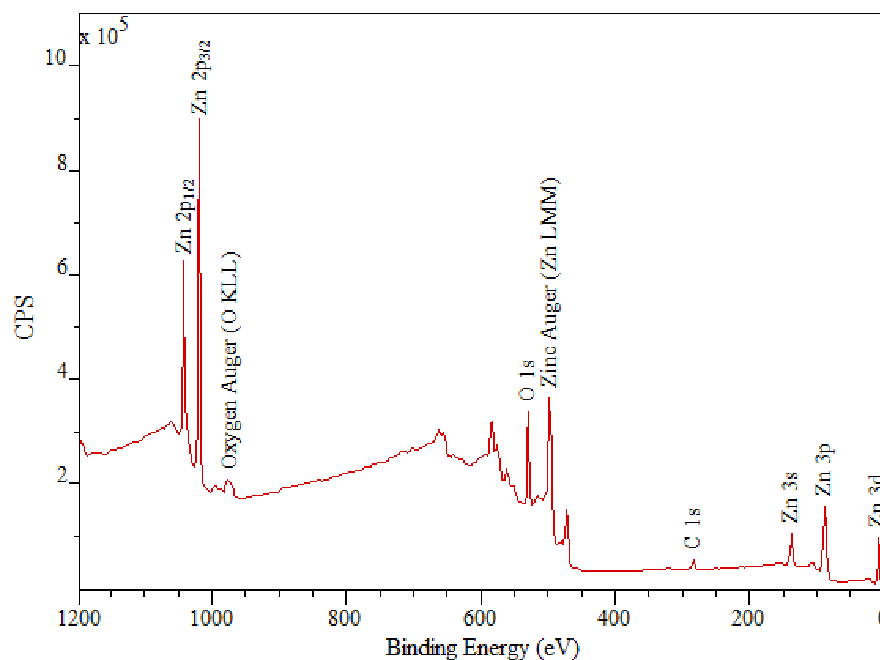

Figure 2.7: X-ray photoelectron survey spectrum of ZnO. The peaks are labelled according to the element and orbital from which the emitted electrons originate

The typical components of an XPS instrument are shown in Figure 2.8. The components include an X-ray source, a sample holder, an analyser, a detector, and a signal processor and read out. When X-rays irradiate a sample, surface electrons with a range of energies are ejected in different directions. A proportion of the emitted electrons which can be transferred through the apertures and focused onto the analyser entrance slit, are collected by the electron optics consisting of set of electrostatic and/or magnetic lens units.

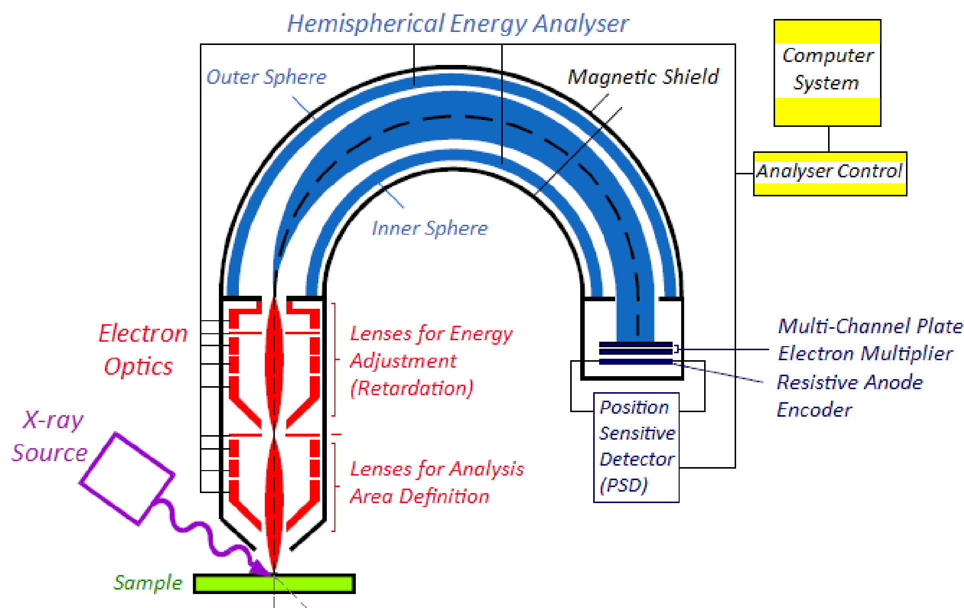

Figure 2.8: Schematic of X-ray photoelectron spectroscopy instrumentation

The photoelectrons can be put into a small orbit by placing a negative charge on the outer plate and a positive charge on the inner plate of the hemispherical analyser (HSA). Electrostatic fields within the hemispherical analyser are established to only allow electrons of a given energy (the so called Pass Energy PE) to arrive at the detector slits and onto the detectors themselves. Electrons of a specific initial kinetic energy are measured by setting voltages for the lens system that both focus onto the entrance slit the electrons of the required initial energy and retards their velocity so that their kinetic energy after passing through the transfer lenses matches the pass energy of the hemispherical analyser. Hence, it is possible to set the potential between the two plates such that only electrons of a known kinetic energy will produce a signal at the electron detector. By sweeping a range of different potentials, an XPS spectrum is obtained.

2.3.3 Applications of XPS and data analysis

XPS provides qualitative and quantitative information about the elemental composition of solid surfaces. It can also provide useful structural information. [232]

2.3.3.1 Qualitative analysis

A survey spectrum such as that shown in the Figure 2.7 is used as a basis for the determination of the elemental composition of samples. Generally, a survey spectrum includes a kinetic energy range of 250 eV to 1500 eV, which corresponds to binding energies of about 0 eV to 1250 eV. Every element in the periodic table except hydrogen and helium has one or more energy levels with characteristic binding energies that will result in the appearance of peaks in this region. In most cases, for the elements with concentrations more than 0.1%, the peaks are well resolved and can be explicitly identified. Problems such as peak overlap can be solved by investigating other spectral regions for additional peaks.

2.3.3.2 Quantitative analysis

There has been increasing use of XPS for determining the chemical composition of the surface of solids over the last few years. [233] There are two different approaches to quantitative analysis with XPS: a) using sensitivity factors and b) calculations from first principles. [234]

- **Sensitivity factors:** When quantifying XPS spectra, Relative Sensitivity Factors (RSF) are used to scale the measured peak areas so that variations in the peak areas are representative of the amount of material in the sample surface. By having RSF, the atomic fractional concentration of element x, C_x, can be calculated by:

$$C_x = \frac{\frac{I_x}{RSF_x}}{\sum \frac{I_i}{RSF_i}} \tag{2.12}$$

where I_x is the measured signal area of element x in the unknown and the summation is over one term for each element, i, in the unknown. Equation 2.12 can be improved by

including corrections for atom size and electron inelastic mean free path.

- **First principles:** If the solid is homogeneous to a depth of several electron mean free paths, the photoelectron current, I, can be calculated from the following equation: [229]

$$I = n\phi\sigma\varepsilon\eta ATl \tag{2.13}$$

where:

n : number of atoms of element per unit volume;

ϕ : flux of the incident X-ray beam;

σ : total phoionisation cross-section;

ε : angular efficiency factor for the instrument;

η : efficiency of producing photoelectrons (photoelectrons/photon);

A : area of the sample from which photoelectrons are detected;

T : efficiency of detector;

l : total inelastic mean free path of the photoelectron in the sample;

Many unknowns in Equation 2.13 make it difficult to use for quantitative analysis and in practice, ratios are taken for pairs of elements.

2.3.3.3 Chemical states and chemical shifts

Obtaining chemical state information from an XPS spectrum is as important as determination of elemental composition, particularly in applications that should investigate the relative amounts of different oxides, valence, or hybridisation states of an element. The chemical state of an atom depends on the number of valence electrons and the type of bond it forms: metallic, covalent, or ionic. In metals, atoms are neutral (oxidation state of zero) and in covalent materials, atoms can have partial charges due to electronegativity differences. Although bonding occurs through valence electrons, the E_B of all core levels are also affected by the chemical state of the element. Therefore, in atoms with a partial negative charge, the core levels will shift to lower E_B because biding energies decrease as

the oxidation state becomes more negative and less work is needed. Correspondingly, the core levels in positively charged atoms shift to higher E_B. This chemical shift can be explained by assuming that the attraction of the nucleus for a core electron is changed by the presence or absence of outer electrons. For example, when one of these electrons is removed, the effective charge sensed for the core electron is increased and, results in an increase in binding energy. A peak shift to higher or lower E_B cannot always be interpreted as arising only from a change in chemical (oxidation) states, as other factors such as structure and various functional groups (local chemical and physical environment) can influence it.

2.3.3.4 Spin-orbit splitting

Closer inspection of the spectrum in Figure 2.7 shows that emission from some core levels (most obviously zinc $2p$) does not give rise to a single photoemission peak, but a closely spaced doublet. This is called splitting of the orbitals and arises from coupling between the electron spin and orbital angular momenta for the orbitals. Either j-j coupling or L-S (Russell-Sanders) coupling methods can be applied to determine the magnitude of spin-orbit coupling.

- In j-j coupling, the magnitude of total angular momentum for a given electron is the vector sum of its spin and orbital angular momenta. The s orbitals do not split because they have no orbital angular momentum and electrons in spin-up or spin-down configurations have the same magnitude of total angular momentum. In p orbitals, vector coupling of spin-up or spin-down states with the ± 1 orbital angular momentum vectors gives total angular momentum of either $1/2$ (from $|1 - 1/2|$ or $|-1 + 1/2|$) or $3/2$ (from $|1 + 1/2|$ or $|-1 - 1/2|$). These two spin-orbit couplings have different binding energies, resulting in the splitting of the levels.

- In L-S coupling, the total angular momentum is determined by summing the total spin angular momentum (S) and the total orbital angular momentum (L) after removal of the electron ($J = L + S$). Similar splitting of orbitals is obtained.

The ground state electron configuration of Zn is:

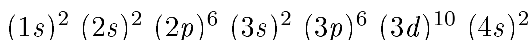

$(1s)^2$ $(2s)^2$ $(2p)^6$ $(3s)^2$ $(3p)^6$ $(3d)^{10}$ $(4s)^2$

The removal of an electron from the $2p$ level leads to a $(2p)^5$ configuration for the final state. Since the p orbitals have non-zero orbital angular momentum ($l = 1$), there will be coupling between the unpaired spin and orbital angular momenta. Thus, the $(2p)^5$ configuration gives rise to two states of $2p_{1/2}$ and $2p_{3/2}$. These two states arise from the coupling of the $L = 1$ and $S = 1/2$ to give permitted J values of 1/2 and 3/2. Since the shell is more than half full, hence $J = 3/2$ is the lower binding energy peak. The width of the spin-orbit splitting depends on the magnitude between electron spins and orbital angular momentum and is proportional to $< 1/r^3 >$, where r is the radius of the orbital. Therefore, the width of the spin-orbit splitting for a given element decreases with increasing principal quantum number ($2p$ levels are split more than $3p$ levels) and with increasing angular momentum quantum number ($3p$ levels are split more than $3f$ levels). The strength of the spin-orbit splitting also increases with increasing atomic number due to an increase in nuclear charge. The spin-orbit split levels have different relative intensities ($g_J = 2J + 1$), proportion to the degeneracies of the levels. Thus, p 1:2, d 2:3, and f 3:4.

2.3.4 Instrumentation

X-ray photoelectron spectroscopy (XPS) was carried out at the National EPSRC XPS User's service (NEXUS) located at Newcastle University (Newcastle upon Tyne, UK). Spectra were collected on an AXIS Nova (Kratos Analytical, Manchester, UK) using a monochromatic Al-K$_\alpha$ X-ray source (1486.6 eV) operating with an anode voltage of 15 kV and emission current of 15 mA (a power of 225 W). The Nova utilises a 180° hemispherical analyser (165 mm mean radius) with survey spectra collected with 160 eV pass energy and high resolution (narrow scan) spectra collected with 20 eV pass energy. Multiple sweeps were averaged for each chosen region; 3 sweeps for survey spectra, 10 sweeps for narrow scans, and 25 sweeps for XPS valence band spectra. Charge neutralisation was

used throughout the analysis and achieved through low energy electrons directed at the surface. The spectrometer was calibrated using standard silver, copper and gold reference materials. Cleaning of the surface of the samples was achieved *in-situ* via a 15 second ion etch by argon ions at 5 keV (5 mA ion current). XPS data will be shown and analysed in Chapter 6.

CasaXPS 2.3.16 Pre-rel 1.4 software was used to analyse the XPS spectra. The software suite as a whole may be regarded as being structured from five interacting components; data display and browser, element library, graph annotation, data processing and quantification.

2.4 Ultraviolet, visible and near-infrared (UV-Vis-NIR) absorption spectroscopy

2.4.1 Introduction

Ultraviolet, visible and near-infrared (UV-Vis-NIR) absorption spectroscopy is the measurement of attenuation of a beam of light as it passes through a sample or by reflection from a sample surface. A variety of absorbance, transmittance, and reflectance measurements in the ultraviolet (UV), visible, and near-infrared (NIR) spectral regions are included in the term UV-Vis-NIR spectroscopy. The UV-Vis-NIR spectral range is approximately 200 nm to 3300 nm. Ultraviolet-visible-near-infrared spectroscopy is one the important analytical and characterisation techniques which is used to study a variety of technologically important materials including semiconductors for electronics, lasers, and detectors; transparent or partially transparent optical component; solid-state laser hosts; optical fibres, waveguides, and amplifiers for communications; and materials for solar energy conversion. The use of UV-Vis-NIR spectroscopy in materials research can be divided into two main categories:

- Quantitative measurements of a sample in the gas, liquid, or solid phase, which often needs the measurement of absorption and reflectance at a single wavelength. This category is most useful as a tool for the preparation of the materials or as a process method to

monitor the concentration of reactants and products during reaction.

- Characterisation of the optical and electronic properties of a material, which is a more qualitative application and usually requires recording a portion of the UV-Vis-NIR spectrum for characterisation of the properties of materials.

2.4.2 Basic principles of the technique

UV-Vis-NIR spectroscopy measures the attenuation of light when it interacts with a sample. Attenuation of the light may occur as a result of absorption, reflection, scattering, or interference of the light by atoms or molecules in the sample as shown in Figure 2.9.

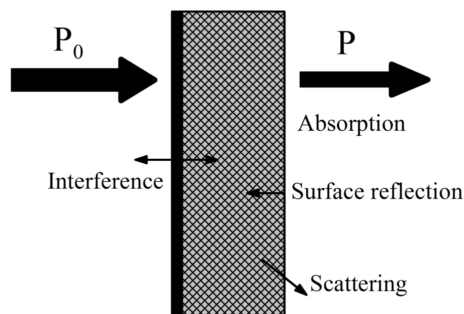

Figure 2.9: Schematic of transmittance measurement of a dielectric coating on a substrate

Accurate quantification requires that the measurement record only the absorption (or transmittance) by the sample, and to compensate for the loss of light from other mechanisms, the power of beam transmitted by the sample is usually compared with power of the beam transmitted by a blank sample (blank sample have everything the same as the sample minus analyte compound). Experimental transmittance T and absorption A values are obtained with the equations:

$$T = \frac{P}{P_0} \tag{2.14}$$

$$A = -logT = log\frac{P_0}{P} \tag{2.15}$$

where P refers to the power of radiation after it passes through the sample and P_0 is the initial power of the radiation. T and A are both unitless and absorption data and spectra are often presented using A, T, $\%T$, or 1-T versus wavelength.

Instruments for measuring the absorption of ultraviolet, visible, and near-infrared irradiation are made up of (1) light sources; (2) sample container; (3) wavelength selector, which isolates a restricted region of the spectrum for measurement; (4) radiation detectors, which convert radiant energy to a usable electrical signal; and (5) signal processor and readout, which displays the transduced signal on a meter scale, a computer screen, a digital meter, or another recording device. A diagram of the components of a typical dual-beam spectrometer is illustrated in Figure 2.10.

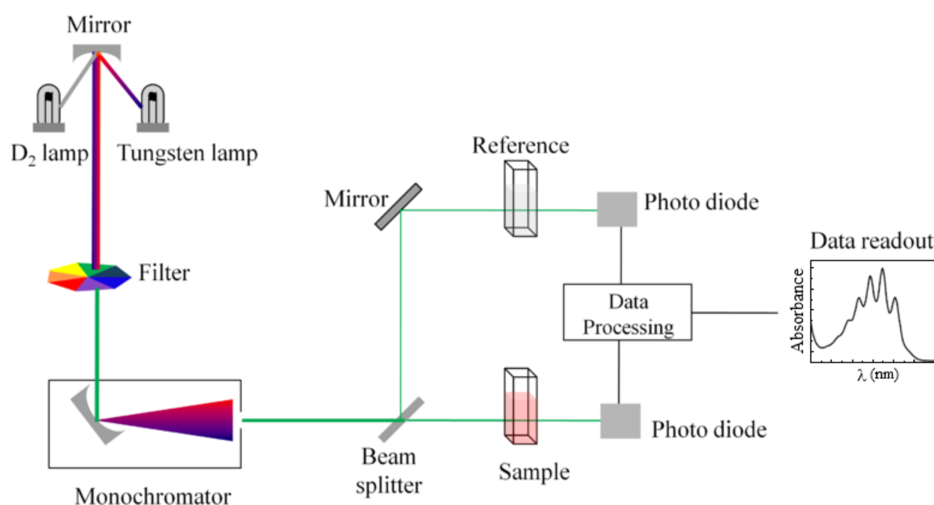

Figure 2.10: Instrumental design for a UV-Vis-NIR spectrometer

A beam of light from a visible and near-infrared (tungsten filament lamp, 350 - 2500 nm) or UV (deuterium discharge lamp, 190 - 400 nm) light source passes into the wavelength selector (filter or monochromator) where the beam is split into its component wavelengths,

and then through the sample. The instruments automatically swap lamps when scanning between the UV and visible regions. The UV-Vis-NIR spectrometers utilise a combination of different types of detectors for different regions. The light beam is redirected automatically to the appropriate detector when scanning between the visible and NIR regions.

2.4.3 Applications of UV-Vis-NIR spectroscopy and data analysis

UV-Vis spectroscopy can be used for chemical analysis of different organic and inorganic compounds, such as transition metal ions, highly conjugated organic compounds, and biological macromolecules.

2.4.3.1 Qualitative analysis

UV-Vis-NIR spectroscopy measurements are useful for detecting choromophoric groups (molecular groups containing unsaturated π bonds). Due to the transparency of most complex organic compounds in wavelength region higher than 180 nm, the appearance of one or more peaks in the region from 200 nm to 400 nm is a clear indication of the presence of unsaturated groups. Although UV-Vis-NIR spectra do not enable absolute identification of an unknown, the identity of the absorbing groups can be determined by comparing the spectrum of an analyte with those of simple molecules containing various choromophoric groups. [235]

The colour can be exploited as the basis of simple and highly specific spectrophotometric determinations. Many transition metal ions form highly coloured complexes and absorption by these compounds involves transition of electrons between the filled and unfilled d orbitals, and thus the wavelength at which absorption occurs depends on the atomic number, the oxidation state of the metal, and the ligand to which it is bonded.

Many inorganic and organic compounds absorb UV or visible radiation due to charge-transfer process, and are thus known as charge-transfer complexes. Molar absorptivity values are very large (ε > 10,000), which leads to high sensitivity for these compounds

even at very low concentration. A charge transfer complex consists of an electron donor group together with an acceptor group. When such a compound absorbs light, an electron from the donor is transferred to an orbital that is largely associated with the acceptor. In many examples, a metal ion acts as the electron acceptor. Charge transfer bands can occur from the UV to the NIR.

2.4.3.2 Quantitative analysis

The absorption of light by a sample is directly proportional to the concentration of the absorbing species and to the distance the light travels through the sample. This linear relationship is known as the Beer-Lambert law (or simply Beer's law) and makes UV-Vis-NIR spectroscopy especially attractive for making quantitative measurements. Beer's law allows accurate concentration measurement of the absorbing species in the sample and is usually represented as:

$$A = \varepsilon bc \tag{2.16}$$

where A is the measured absorption, ε is the molar absorptivity (also called molar extinction coefficient), b is the path length, and c is the concentration of the absorber. It is important to note that ε is wavelength-dependent and so the Beer's law is valid only if the incident radiation is monochromatic (has a single wavelength).

2.4.3.3 Materials properties measurable by UV-Vis-NIR spectroscopy

The band gap of a semiconductor depends on the identity and physical dimensions of the material and can correspond to photon energies ranging from UV to NIR. The optical band gap (E_g) of semiconductors can be calculated from the UV-Vis-NIR spectrum according to Tauc relation: [236]

$$\alpha h\nu = c(h\nu - E_g)^{\gamma} \tag{2.17}$$

where α is the absorption coefficient, $h\nu$ is photon energy (h is Planck's constant and ν is the photon frequency), c is proportionality constant, and γ is an index which can assume values of 2, 3, $\frac{1}{2}$, and $\frac{3}{2}$ depending on the nature of electronic transitions responsible for the absorption (2 for indirect allowed transitions, 3 for indirect forbidden transitions, $\frac{1}{2}$ for direct allowed transitions, and $\frac{3}{2}$ for direct forbidden transitions). [237] The absorption coefficient per unit length is defined as: [186]

$$\alpha \equiv \frac{4\pi k}{\lambda} \tag{2.18}$$

where k is called the extinction coefficient. Near the absorption edge the absorption coefficient can be expressed as:

$$\alpha \propto (h\nu - E_g)^{\gamma} \tag{2.19}$$

For $k = 0$ at which the direct band gap is defined, only direct allowed transitions ($\gamma = 1/2$) occur and thus this relation can be used in determining the band gap experimentally. A plot of $(\alpha h\nu)^2$ *vs* $h\nu$ when the linear portion of the curves extrapolated to $\alpha h\nu = 0$ gives the value of the direct band gap, E_g. The band edge of the semiconductor materials will be shifted to shorter or longer wavelengths with structural changes in the material such as the size or dimensions of the particles and presence of impurities (dopants) and defects.

When semiconductor thin films have good surface quality and homogeneity, their thickness (t) can be estimated from the interference fringes related to reflections of the transmission spectrum using "envelope method" originally proposed by Manifacier *et al.* [238] and developed by Swanepoel whereby: [239]

$$t = \frac{M\lambda_1\lambda_2}{2(\lambda_1 n_2 - \lambda_2 n_1)} \tag{2.20}$$

where M is the number of oscillations between the two extrema ($M = 1$ between two consecutive maxima or minima), n_1 and n_2 are the refractive indices at two adjacent extrema

(maxima or minima) at wavelengths λ_1 and λ_2, respectively. The refraction indices n at various wavelengths are calculated using the envelope curves for T_{max} (T_M) and T_{min} (T_m) in the transmission spectra by the expression:

$$n = \left[N + (N^2 - n_s^2)^{1/2}\right]^{1/2} \tag{2.21}$$

where

$$N = 2n_s \frac{T_M - T_m}{T_M T_m} + \frac{n_s^2 + 1}{2} \tag{2.22}$$

and n_s is the refractive index of substrate (n_s =1.470 for borosilicate glass). The envelopes of the maxima, $T_{max}(\lambda)$, and the minima, $T_{max}(\lambda)$, are shown in Figure 6.17.

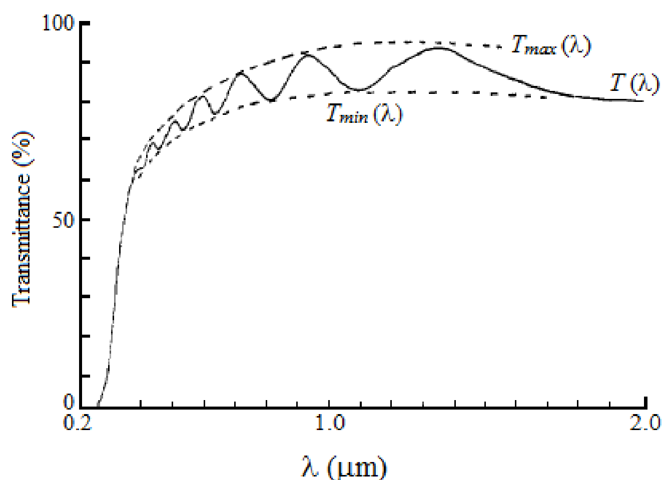

Figure 2.11: Typical transmission spectrum for thin films of uniform thickness, illustrating the envelope curves for T_{max} and T_{min} (Figure adapted from [238])

For inorganic complexes, the UV-Vis-NIR spectrum can provide information about oxidation states, electronic structure, and metal-ligand interactions. For solid materials, the UV-Vis-NIR spectrum can measure the band gap and identify any localised excitations or impurities. Collective excitations that determine the absorption or reflectivity of a material will also occur in this range. For example, the peak absorption of the plasmon

resonance absorption of thin films of aluminium, gold and semiconductors occurs in the ultraviolet, visible, and near-infrared regions, respectively. [226]

2.4.4 Instrumentation

UV-Vis-NIR spectroscopy was carried out on two different spectrometers; a Varian Cary 5000 UV-Vis-NIR spectrometer and a Perkin Elmer Lambda 19. Both instruments are dual-beam, ultraviolet, visible and near-infrared spectrometers, that can record from about 175 nm to 3300 nm. The spectrometers are equipped with a tungsten halogen Vis-NIR source, a deuterium arc UV source, a photomultiplier tube UV-Vis detector, and a cooled PbS photocell NIR detector. Spectra were collected at room temperature from 2500 nm to 250 nm with data collection interval of 1.0 nm on Cary 5000 and 3.0 nm on Lambda 19. Data from the Varian Cary 5000 UV-Vis-NIR spectrometer will be illustrated and discussed in Chapter 4, and data from Perkin Elmer Lambda 19 will be presented in Chapters 6 and 5.

2.5 Hall effect measurement

2.5.1 Introduction

Hall effect measurement has been an important diagnostic and valuable tool for the characterisation of electrical transport properties of materials, particularly semiconductors. The discovery of Hall effect enabled a direct determination of both the type of the charge carriers (electron or holes) and their density in a given sample. Hall effect measurement is used in many phases of the electronics industry, from basic materials research and device development to device manufacturing. Hall effect measurement can actually be used to determine quite few material parameters, but the primary one is the Hall voltage (V_H). Other important parameters such as carrier mobility (μ), carrier concentration (n), Hall coefficient (R_H), resistivity (ρ), and the conductivity type are all derived from the Hall

voltage measurement.

2.5.2 Theory of Hall effect

The fundamental physical principle underlying the Hall effect is the Lorentz force (illustrated in the upper panel of Figure 2.12) which is a combination of two separated forces: the electrical force and the magnetic force. Essentially, the Hall effect can be observed when the combination of a magnetic field through a sample and a current along the length of the sample creates a transverse voltage (potential difference) perpendicular to both the magnetic field and the current. When an electron moves along the electric field direction perpendicular to an applied magnetic field, it experiences a magnetic force, $\vec{F}$, ($\vec{F} = -q\vec{v}\vec{B}$, where q is the charge of particle, $\vec{v}$ is the velocity of the particle, and $\vec{B}$ is the magnetic field) acting normal to both directions, and moves in response to this force. The direction of this magnetic force can be determined by using the right hand rule convention. For an n-type semiconductor such as that shown in Figure 2.12, the free carriers are electrons of bulk density, n.

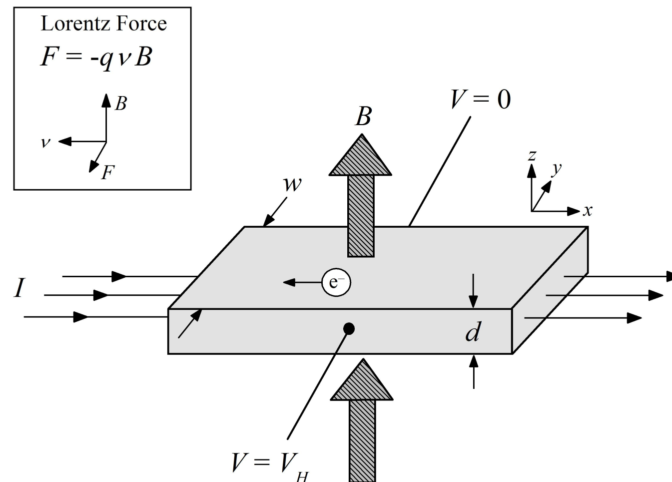

Figure 2.12: The Hall effect and Lorentz force (diagram adapted from the National Institute of Standards and Technology, NIST, website)

If a constant current I flows along the x-axis from left to right in the presence of a

magnetic filled B along z-axis, electrons subject to the Lorentz force will initially drift away from the current flow line toward the negative y-axis direction, thus resulting in an excess surface electrical charge on that side of the sample. This excess surface charge results in the Hall voltage, V_H, a potential drop across the two sides of the sample. Hall voltage magnitude is equal to:

$$V_H = \frac{IB}{ned} \tag{2.23}$$

where I is the applied current, B is the applied magnetic field , d is the sample thickness , and e is the elementary charge (1.602×10^{-19} C). Equation 2.23 is remarkable in two ways. First, the only sample dimension appearing in the equation is the thickness (the dimension in the direction of the magnetic field). Second, the Hall voltage yields a direct measurement of carrier concentration. Therefore, by measuring the Hall voltage and from the known values of I, B, and e, one can obtain the density of charge carriers in semiconductors, n:

$$n = \frac{IB}{edV_H} \tag{2.24}$$

Sometimes it is more convenient to use sheet density n_S ($n_S = nd$) instead of bulk density, n.

Hall mobility, μ, can be easily calculated from the equation below:

$$\mu = \frac{V_H}{R_S IB} = \frac{1}{(en_S R_S)} \tag{2.25}$$

where R_S (in $\Omega/\square$) is the sheet resistance of the semiconductor material and is determined by use of van der Pauw resistivity measurement technique. If the thickness, d, of the conducting layer is known, the bulk resistivity, ρ, can be determined using sheet resistance from:

$$\rho = R_S d \tag{2.26}$$

Changing the sign of the charge carriers changes the sign of the Hall voltage. Considering this, the Hall coefficient can be determined from Hall voltage using:

$$R_H = \frac{V_H d}{IB} = \frac{1}{nq} \tag{2.27}$$

where $q = e$ for positive carriers and $q = -e$ for negative carriers. The hall coefficient is characteristic of the material being measured. The simple relationship between carrier concentration and mobility, and Hall coefficient can then be defined as:

$$n = \frac{1}{R_H e}$$
$$\mu = \frac{R_H}{\rho} \tag{2.28}$$

2.5.2.1 The van der Pauw technique

A combination of resistivity measurement and Hall effect measurement allows both the mobility μ and the sheet density n_S to be determined. The van der Pauw technique is the most convenient technique to determine the resistivity of uniform thin film samples, and thus is widely used in the semiconductor industry. [240] The van der Pauw technique's power lies in its ability to accurately measure the properties of a sample of any arbitrarily shape subject to fairly mild constraints. Thin film samples (approximately two-dimensional) with no holes or non-conducting islands or inclusions, containing four very small ohmic contacts place on the boundaries of the film, are appropriate for the measurement. Some possible van der Pauw configurations, contact placements, and their preference are shown in Figure 2.13. In order to use van der Pauw method, the sample thickness must be negligible compared to the width and length of the sample.

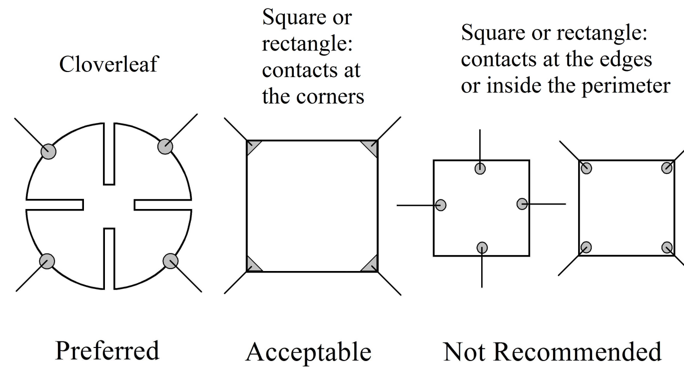

Figure 2.13: Examples of possible sample geometries for van der Pauw measurement and their preferences (diagram adapted from the National Institute of Standards and Technology, NIST, website)

Therefore, the van der Pauw technique assumes the following five conditions hold; 1) the sample must have a flat shape of uniform thickness, 2) the surface of the sample must not have any isolated holes, 3) The sample must be homogeneous and uniform, 4) all four contacts must be placed on the edge of the sample, and 5) the contacts must be sufficiently small compared to the area of the entire sample. In addition, ideally all four contacts should be made of the same material and the same batch of wire.

The conventional technique to measure the resistivity of a certain material involves cutting a bar-shaped sample and making separate current contacts on the short edges and voltage contacts on the surface of the sample. This technique is also called four-point probe resistivity measurement and allows the measurement of the substrate resistivity by passing a current through two outer probes and measuring the voltage through the inner probes. [241] According to four-point probe technique, by using the voltage and current readings from probe, the measurement of the sheet resistance can be obtained using:

$$R_S = \frac{\pi}{ln(2)}(\frac{V}{I}) = 4.523(\frac{V}{I}) \tag{2.29}$$

However, as mentioned before, the van der Pauw technique allows determination of electrical properties of samples of any arbitrary shape without knowing the current pattern.

Using this method, the resistivity can be derived from a total of eight measurement of voltage which are made around the periphery of the sample as shown in Figure 2.14.

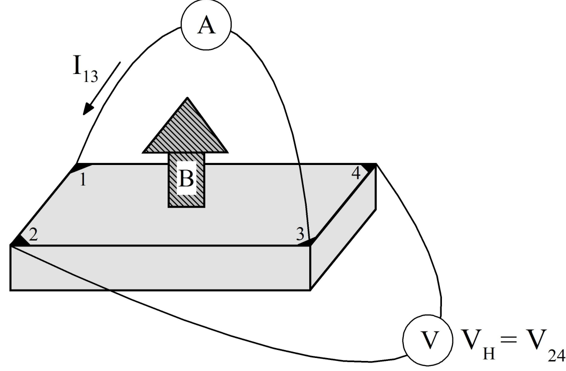

Figure 2.14: Schematic of a van der Pauw configuration used in the determination of the Hall voltage V_H [242]

Once all voltage measurements are taken, two values of horizontal and vertical resistance are derived as follows (the relationship between voltage (V) and current (I) in a circuit of constant resistance (R): $R = \frac{V}{I}$)

$$R_A = (R_{14,23} + R_{23,14} + R_{32,41} + R_{41,32})/4$$
$$R_B = (R_{12,43} + R_{21,34} + R_{34,21} + R_{43,12})/4 \quad (2.30)$$

Therefore, van der Pauw method consists of two characteristic resistance, R_A and R_B, which are related to the sheet resistance R_S through the van der Pauw equation: [243]

$$exp(-\pi \frac{R_A}{R_S}) + exp(-\pi \frac{R_B}{R_S}) = 1 \quad (2.31)$$

In order to simplify Equation 2.31 and reduce errors in the measurements, it is desirable to measure square-shaped symmetrical samples, where $R_A \approx R_B$. In this case, equation 2.31 can be written as:

$$\rho = R_S d = \frac{\pi d}{ln2} \frac{(R_{12,34} + R_{23,41})}{2} f \quad (2.32)$$

where

$$R_{12,34} = \frac{V_{34}}{I_{12}} \text{ and } R_{23,41} = \frac{V_{41}}{I_{23}},$$

d is the thickness of the sample, and f represents the correction factor, which is function of sample symmetry.

2.5.3 Instrumentation

Room temperature electrical characterisations were carried out by the van der Pauw technique using an Ecopia HMS-3000 Hall effect measurement system with a 0.55 T permanent magnet and a custom-built cryogenic cooling system. A small section of the samples (5 mm $\times$ 5 mm) were mounted on a printed circuit boards designed for the Ecopia HMS-3000 system. Depending on the resistance of the sample, input current could be changed in the range between μA to mA. Indium solder on the corner of the samples was used to fabricate ohmic contacts to the thin films. The HMS-3000 includes software with I-V curve capability for checking the ohmic integrity of the user made sample contacts. Hall effect measurement data will be discussed in Chapters 6, 4, and 5. Temperature dependence of the electrical properties was studied over a wide range of temperature from about 350 K to8 K using liquid nitrogen as the cryogen. The HMS-3000 measurement capabilities include the Hall coefficient, the Hall voltage, the sheet resistance from which the resistivity can be inferred for a sample of a given thickness, the sign and the concentration of the carriers, and the mobility of semiconductor materials. Data from temperature dependence studies of the electrical properties are discussed in Chapter 4.

2.6 Scanning electron microscopy (SEM)

Scanning electron microscopy is widely used to analyse the micro-structure of materials and thus is a very important technique to investigations on the processing, properties, and behaviour of materials that involves their micro-structure. The scanning electron

microscope (SEM) permits the observation and characterization of heterogeneous organic and inorganic materials on a nanometre (nm) to micrometre (μm) scale and its popularity stems from its capability of obtaining three-dimensional-like images of the surfaces of a very wide range of materials. [244] The scanning electron microscope uses a tightly focused beam of electrons accelerated to high energy to create an image of the specimen. The SEM images can provide very useful information relating to topographical features, crystal morphology, compositional differences, phase distribution, crystal structure, crystal orientation, particle size, and presence and location of electrical surface defects.

2.6.1 Principles of the technique

The scanning electron microscope produces a magnified image by using electrons instead of light to form an image. A beam of high-energy electrons is produced at the top of the microscope by an electron source. The electron beam follows a vertical path through the microscope, which is held within a vacuum. The beam travels through electromagnetic fields and lenses, which focus the beam down toward the sample. The beam electrons interact with atoms in the sample by a variety of mechanisms such as inelastic interactions, in which energy is transferred to the sample from the beam, and elastic interactions that are defined by a change in direction of the beam without loss of energy. The main signals resulting from these interactions of the primary electrons (PE) of the electron beam and the specimen are secondary electrons (SEs), backscattered electrons (BSEs), X-rays, and Auger electrons. A secondary electron is a low-energy (2 eV to 5 eV) electron ejected from the outer shell of a sample atom upon impact of the incident electron beam and after an inelastic interaction. These low-energy electrons can escape from the surface only if generated near the surface and thus the secondary electrons are influenced more by surface properties than by atomic number. Backscattered electrons are electrons from the incident probe that undergo elastic interactions with the sample, change direction, and escape the sample. These make up the majority of electrons emitted from the sample at high beam

voltage, and their average energy is much higher than that of the SEs.

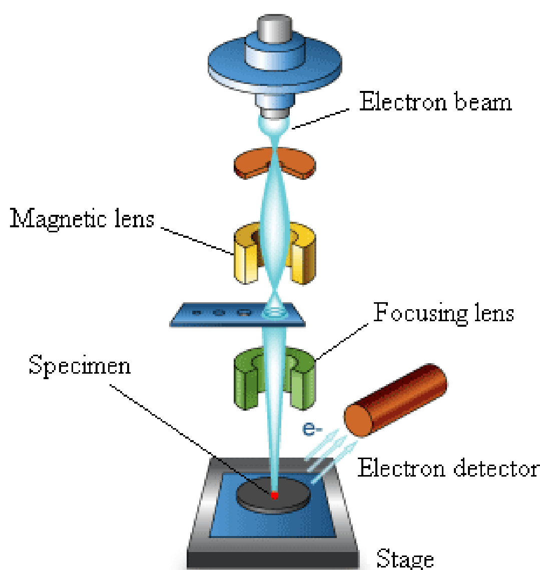

Figure 2.15: Schematic of the scanning electron microscope (Figure adapted from the Australian Microscopy and Microanalysis Research Facility, ammrf, website)

Characteristic X-ray and Auger electrons are generated by inelastic interactions of the probe electron in which an inner shell electron is emitted from a sample atom. Following this ionisation process, the atom undergoes a relaxation process by a transition in which an outer shell electron fills the inner shell. [226] The electrons scattered by the surface of the sample and emitted secondary electrons are collected by detectors to give a map of the surface topography of samples. Image construction in the SEM is performed by mapping intensity of SE and/or BSE signals from the sample onto a viewing screen or film. Key components of a scanning electron microscope are shown in Figure 2.15.

2.6.2 Instrumentation

Scanning electron microscopy (SEM) was carried out at the Oxford Materials Electron Microscopy and Microanalysis Facility located at Oxford University Begbroke Science Park (OUBSP) on two different microscopes. SEM images in Chapter 4 were collected on a JEOL

JSM-6500F low voltage field emission gun scanning electron microscope which operates between 1 and 30 kV with spatial resolution of 3 nm. Samples were mounted on SEM stubs using small amount of conductive carbon adhesive paste, and were examined without platinum or gold coating. The images were obtained at accelerating voltage of 5 kV from secondary electrons (SE) in the magnification range from 10,000× up to 50,000×. SEM images in Chapters 6 and 5 were collected on a JEOL JSM-840F SEM with a cold cathode field emission electron source. The gun emission current was between 8 - 14 μA and probe current was 2×10^{-11} A. Samples were observed in the SEM with sputter coating with platinum. Images were obtained at acceleration voltage of 5 kV and using a secondary electron detector. The DISS 5 digital image acquisition and processing system was used to process for data acquisition.

Chapter 3

Study of the Thermal Decomposition of Potential Zinc Oxide Precursors

3.1 Introduction and overview

Chemical deposition routes start with a precursor and the nature of the precursor used in solution-based techniques can significantly affect the properties of the thin films produced. The selection of a precursor is dependent upon its solubility in appropriate solvents, formulation, and the desired processing route. Several researchers have studied the effect of using different zinc salts on the structural, optical and electrical properties of ZnO thin films deposited by the spray pyrolysis technique. However, the range of zinc precursors investigated has been limited. A list of zinc precursors that have been most used is given in Table 3.1.

Precursor	References
Zinc acetate, $Zn(C_2H_3O_2)_2 \cdot xH_2O$	[96, 97, 104, 245–248]
Zinc nitrate, $Zn(NO_3)_2 \cdot xH_2O$	[61, 100, 103, 245–247]
Zinc acetylacetonate, $Zn(C_5H_7O_2)_2 \cdot xH_2O$	[98, 99, 105]
Zinc chloride, $ZnCl_2$	[101, 102, 245–247]
Diethyl zinc, $Zn(C_2H_5)_2$	[249, 250]

Table 3.1: Common Zn precursors for solution processing of ZnO thin films

For example, in a study carried out by Lehraki *et al.,* ZnO thin films were deposited from three different zinc precursors; zinc chloride, zinc acetate, and zinc nitrate. The films deposited from zinc chloride solutions showed rod-shaped particles on the surface, and these films had better crystallinity compared to the films deposited from acetate and nitrate precursor solutions. However, zinc acetate solution yielded a film with a higher transmittance compared to films prepared with the chloride and nitrate precursors. [245] In different studies Bacaksiz *et al.* and Arca *et al.* also studied the effects of the same range of precursors on the morphology, structural, and optical properties of ZnO thin films deposited by spray pyrolysis technique. [246, 247] Interestingly, they reported very similar results to those reported by Lehraki *et al.*

Zinc acetate has attracted more interest in preparation of ZnO thin films (by solution-based techniques) than other zinc precursors, probably due to its ready availability, high water solubility and low cost. The thermal decomposition of zinc acetate has been widely studied. [251–253] Arii and Kishi investigated the thermal decomposition of zinc acetate dihydrate, $Zn(CH_3CO_2)_2 \cdot 2\,H_2O$, in dry helium and wet nitrogen atmospheres using thermogravimetric analysis (TGA) and analysed the evolved gas using simultaneous mass spectrometry and X-ray diffractometry. [251] They showed that the thermal decomposition of zinc acetate in dry helium atmosphere began with dehydration at ∼ 150 °C followed by the sublimation around 180 °C and then decomposition over 250 °C. They also discovered that ZnO was formed in good yields, only in a humidity-controlled nitrogen atmosphere, where it could be easily synthesized at temperatures below 250 °C. They proposed the formation of ZnO from anhydrous zinc acetate in humid atmosphere occurs according to the reaction:

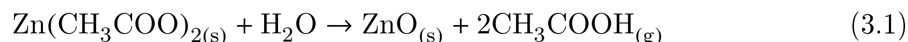

$$Zn(CH_3COO)_{2(s)} + H_2O \rightarrow ZnO_{(s)} + 2CH_3COOH_{(g)} \tag{3.1}$$

McAdie also studied thermal decomposition of zinc acetate dihydrate in a dynamic nitrogen atmosphere and drew the conclusion that the decomposition of zinc acetate might

occurs the following route: [252]

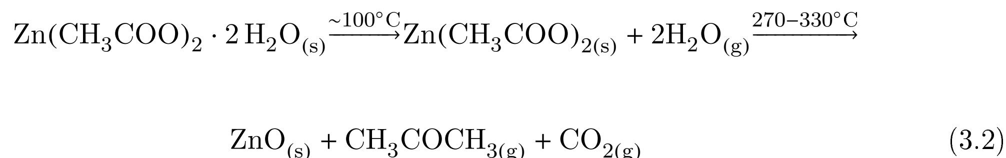

$$Zn(CH_3COO)_2 \cdot 2\,H_2O_{(s)} \xrightarrow{\sim 100^\circ C} Zn(CH_3COO)_{2(s)} + 2H_2O_{(g)} \xrightarrow{270\text{–}330^\circ C}$$

$$ZnO_{(s)} + CH_3COCH_{3(g)} + CO_{2(g)} \qquad (3.2)$$

The thermal decomposition of zinc nitrate hexahydrate is known to lead eventually to zinc oxide. Zinc nitrate thermal decomposition and chemical analysis of the residue has been investigated by Sirina *et al.* in 1970. [254] They observed two distinct endothermic phenomena and accompanied weight losses at 37 °C and 312 °C, due to the loss of the water of crystallisation, and final decomposition to ZnO, respectively. They also described that during this process some NO_2 was evolved. Nikolic *et al.* also showed that thermal decomposition of $Zn(NO_3)_2 \cdot 6\,H_2O$ occurs above 300 °C from TGA/DSC studies. [255] They proposed the following decomposition scheme for decomposition of $Zn(NO_3)_2 \cdot 6\,H_2O$ to ZnO, but non of the gaseous products were identified:

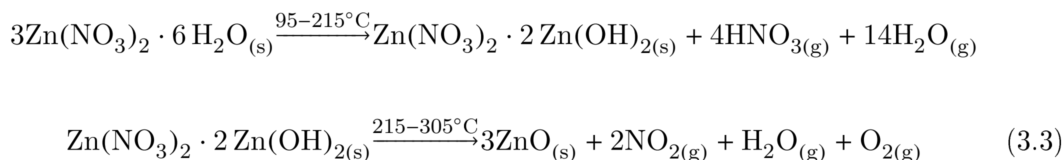

$$3Zn(NO_3)_2 \cdot 6\,H_2O_{(s)} \xrightarrow{95\text{–}215^\circ C} Zn(NO_3)_2 \cdot 2\,Zn(OH)_{2(s)} + 4HNO_{3(g)} + 14H_2O_{(g)}$$

$$Zn(NO_3)_2 \cdot 2\,Zn(OH)_{2(s)} \xrightarrow{215\text{–}305^\circ C} 3ZnO_{(s)} + 2NO_{2(g)} + H_2O_{(g)} + O_{2(g)} \qquad (3.3)$$

Thermal decomposition of diethyl zinc in oxygen-free atmospheres such as He or H_2 will not result in formation of ZnO as reported by Dumont *et al.* [256, 257] However, ZnO can be obtained from heating of diethyl zinc in oxygen containing atmospheres such as air or O_2, and water containing solutions as suggested by Yoshino *et al.* through the reactions below: [249, 250]

$$(C_2H_5)_2Zn_{(s)} + 7O_{2(g)} \rightarrow ZnO_{(s)} + 4CO_{2(g)} + 5H_2O_{(g)} \qquad (3.4)$$

or

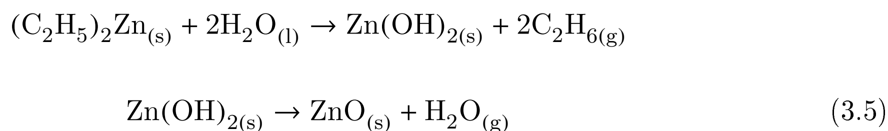

$$(C_2H_5)_2Zn_{(s)} + 2H_2O_{(l)} \rightarrow Zn(OH)_{2(s)} + 2C_2H_{6(g)}$$

$$Zn(OH)_{2(s)} \rightarrow ZnO_{(s)} + H_2O_{(g)} \tag{3.5}$$

Very little work has been reported on the possibility of using other commercially available zinc precursors such as zinc formate and zinc propionate. To the best of our knowledge, there is only one published study by Ryabova and Savitskaya on utilising zinc propionate as a precursor for deposition of ZnO thin films. [258] In their work, ZnO films were deposited onto mica in an oxygen atmosphere by the thermal decomposition of zinc propionate vapour ($Zn(C_3H_5O_2)_2$) at substrate temperature of 450 to 540 °C. Thermal decomposition of zinc propionate in different atmospheres have been studied previously by TGA, and some possible decomposition mechanisms were proposed. [259, 260] For example, Skoršepa *et al.* suggested the following scheme for the thermal decomposition of zinc propionate to ZnO in air and used IR spectroscopy to confirm the intermediate composition: [259]

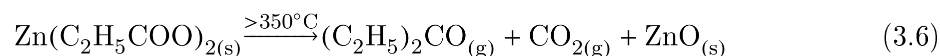

$$Zn(C_2H_5COO)_{2(s)} \xrightarrow{>350°C} (C_2H_5)_2CO_{(g)} + CO_{2(g)} + ZnO_{(s)} \tag{3.6}$$

However, the decomposition mechanism may change as the experimental conditions change.

Thermal decomposition of zinc formate, $Zn(HCO_2)_2$, in various atmospheres has been investigated using several techniques. [261, 262] In 1967 Dollimore and Tonge found by TGA that zinc formate dihydrate was dehydrated at 120 - 180 °C in air and at 100 - 180 °C in nitrogen. The anhydrous salt then decomposed to ZnO at 260 - 350 °C in air and at 270 - 340 °C in nitrogen in a single step. [261] They proposed the following mechanism:

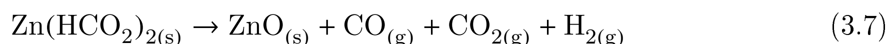

$$Zn(HCO_2)_{2(s)} \rightarrow ZnO_{(s)} + CO_{(g)} + CO_{2(g)} + H_{2(g)} \tag{3.7}$$

Study of the thermal decomposition of zinc formate dihydrate carried out by Zhang *et*

al. under nitrogen atmosphere, showed a two-step mass loss in the temperature range of 25 to 375 °C. The first mass loss in the temperature between 80 - 155 °C, was attributed to the formation of anhydrous zinc formate from zinc formate dihydrate, and decomposition of zinc formate to ZnO was observed to occur in the region of 155 - 375 °C. [262]

Previous studies on thermal decomposition of zinc acetylacetonate have been reviewed and summarised in Section 1.6, Chapter 1.

3.2 Experimental

Zinc bis(acetylacetonate) hydrate ($Zn(acac)_2$, $Zn(C_5H_7O_2)_2 \cdot xH_2O$, ≥ 99.995%, Sigma-Aldrich), zinc propionate ($Zn(prop)_2$, $Zn(C_3H_5O_2)_2$, 97%, Alfa Aesar), zinc formate hydrate ($Zn(form)_2$, $Zn(HCO_2)_2 \cdot xH_2O$, 98%, Alfa Aesar), zinc trifluoroacetate hydrate ($Zn(tfa)_2$, $Zn(CF_3COO)_2 \cdot xH_2O$, Sigma-Aldrich), zinc oxalate hydrate (Zn(ox), $Zn(C_2O_4) \cdot xH_2O$, ≥ 99.99%, Sigma-Aldrich), and zinc acetate hydrate ($Zn(ac)_2$, $Zn(C_2H_3O_2)_2 \cdot xH_2O$, 99.99%, Sigma-Aldrich) were selected as potential candidates for ZnO deposition. Applying thermogravimetric analysis (TGA) and variable temperature X-ray diffraction (VT-XRD), the decomposition temperature of precursor compounds without any purification were studied. Thermogravimetric analysis coupled with differential scanning calorimetry (TGA-DSC) was also carried out on zinc acetylacetonate hydrate and zinc acetate hydrate to confirm the results from X-ray.

TGA measurements was performed using a Perkin Elmer TGA-7 system. The sample mass of *ca.* 15 - 20 mg was weighed into an platinum crucible, and heated up to 500 °C at heating rate of 3.0 °C min^{-1}, in dry air with a flow rate of 30 mL min^{-1}. The decomposition of powdered samples of zinc precursor was studied *in-situ* by VT-XRD using a SIEMENS D5000 X-Ray Diffractometer with Cu-$K_{\alpha 1}$ radiation source (λ = 1.54059 Å) operating at 40 kV and 40 mA. The spectra were recorded from 10° to 70° in 2θ from room temperature up to 500 °C at a heating rate of 1.0 °C min^{-1} and under a static air atmosphere. The temperature was maintained at a constant value during the X-ray measurements.

TGA-DSC analyses of $Zn(acac)_2$ and $Zn(ac)_2$ were performed in an argon atmosphere at a flow rate of 30 mL min^{-1}, from room temperature to 500 °C at heating rate of 5.0 °C min^{-1} using a Perkin Elmer STA 6000 instrument. Thermal analysis was carried out on about 10 - 15 mg of the samples in alumina cups used as sample holders.

3.3 Results and discussion

3.3.1 Thermogravimetric analysis-differential scanning calorimetry (TGA-DSC) technique

Thermogravimetric analysis (TGA) is a technique that monitors accurately the mass change of a sample as a function of time or temperature as the sample specimen is subjected to controlled temperature program and atmosphere. Changes in the structure of the sample, such as loss of water of crystallisation or volatile fragments, as well as the decomposition of the sample are observed as a weight loss, while the oxidation or absorption of gas is seen as a weight gain. A TGA consists of a sample holder that is supported by a precision balance and resides in a furnace, thus it can be heated or cooled during the experiment. The mass of the sample is monitored during the experiment. The sample environment is controlled by an inert or a reactive gas that flows over the sample and exits through an exhaust.

TGA sometimes performed simultaneously with DTA or DSC. Differential scanning calorimetry (DSC) measures the variation of heat flows released (exothermic) or received (endothermic) by a sample as the temperature is increased or decreased. In fact, DSC is a thermal analysis technique that monitors how a material's heat capacity (C_p) is varied with temperature. This allows the investigation of transitions such as melting, glass transitions, phase changes, and chemical reactions.

3.3.2 Precursor decomposition analysis

As mentioned earlier, thermal decomposition of various Zn compounds such as $Zn(ac)_2$, $Zn(acac)_2$, $Zn(prop)_2$, $Zn(form)_2$, and Zn(ox) have been studied by several groups and some possible decomposition mechanisms under different conditions have been also proposed. Due to the differences in experimental procedures of the reported thermal studies (such as the atmosphere and heating rate under which the decomposition was studied) and in order to have comparable thermal decomposition conditions, the thermal analysis of the selected Zn precursors was undertaken again.

The typical TGA curves for selected zinc precursors at a heating rate of 3 °C min^{-1} in dry air flow are shown in Figure 3.1. Small amounts of residue in the crucible was observed after the thermal analysis of each sample. Among all studied samples, $Zn(acac)_2 \cdot xH_2O$ had the lowest decomposition temperature of about 175 °C, while $Zn(ox) \cdot xH_2O$ had the highest decomposition temperature of about 425 °C. Two major mass losses were observed on TGA spectrum of $Zn(acac)_2 \cdot xH_2O$. The first mass loss of about 7%, at about 100 °C, agrees well with the theoretical value corresponding to the thermal dehydration of one water molecule, and the second mass loss attributes to the final thermal decomposition to ZnO.

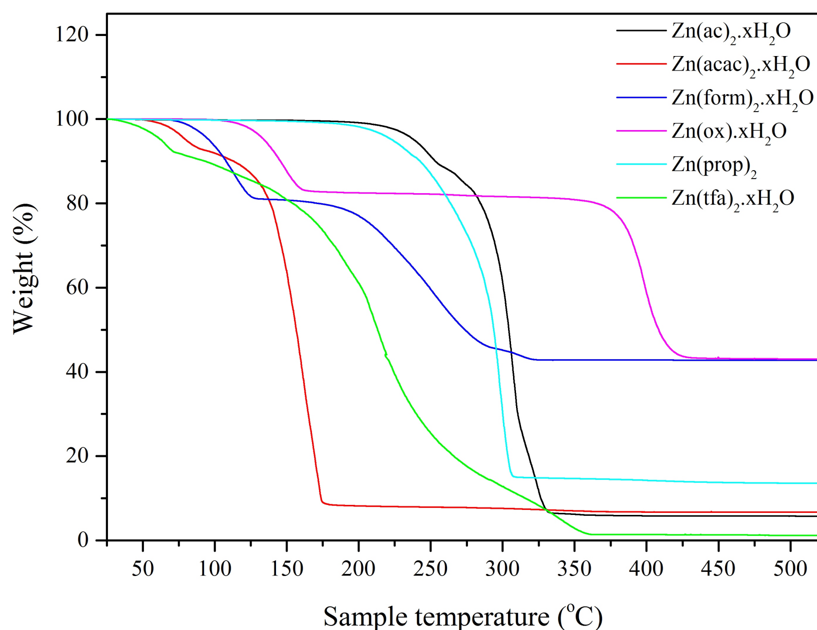

Figure 3.1: TGA results of selected zinc compounds in dry air flow at 3 °C min^{-1}

Additional information can be extracted from calculating theoretical and experimental mass loss percentages, for example to determine whether the Zn compounds entirely decomposes to ZnO, or other thermal processes such as sublimation or evaporation of the samples are also involved. The total theoretical mass loss percentage is the proportion of the molecular weight (in g mol^{-1}) of ZnO to the starting anhydrous Zn compound, since the experimental mass loss percentage is obtained from TGA graph and is the weight of the starting anhydrous material minus final product:

$$\text{Theoretical mass loss percentage} = 100 - \left(\frac{\text{ZnO Molecular Weight}}{\text{Zn precursor Molecular Weight}} \times 100\right) \quad (3.8)$$

Experimental mass loss percentage =

Weight percentage of anhydrous Zn precursor – Final weight percentage

For example the theoretical mass loss ratio for final decomposition of anhydrous $Zn(acac)_2$

and $Zn(ac)_2$ to ZnO is calculated from:

$$\text{Theoretical mass loss percentage for } Zn(acac)_2 \text{ to ZnO conversion } =$$

$$100 - (\frac{81.38}{263.61} \times 100) = 69.1\%$$

$$\text{Theoretical mass loss percentage for } Zn(ac)_2 \text{ to ZnO conversion } =$$

$$100 - (\frac{81.38}{183.48} \times 100) = 55.6\%$$

The theoretical and empirical mass losses of Zn compounds, relevant to dehydration of water of crystallisation and final thermal decomposition to ZnO, are listed in Table 3.2. The correct empirical mass loss percentage equivalent to the second mass loss observed in the TGA graph is: For $Zn(form)_2 \cdot xH_2O$ and $Zn(ox) \cdot xH_2O$ which also show two mass loss steps, the dehydration of their crystallisation water occurred at moderate temperatures of about 125 °C and 175 °C, respectively. The mass loss percentages agree well with theoretical values for loss of two molecules of water. Among the Zn compounds studied, decomposition of $Zn(form)_2$ and Zn(ox) to ZnO did not involve sublimation or evaporation of the specimens during the heating process and the the final empirical mass losses perfectly correlate with the theoretical values.

$Zn(prop)_2$ which was defined to be anhydrous, showed only one step mass loss at about 310 °C, and no mass loss associated to the dehydration of water was observed in the TGA measurement. The only and final mass loss of about 85.0% does not correlate perfectly well with the theoretical mass loss (61.5%) for final decomposition of $Zn(prop)_2$ to ZnO, which suggests that this zinc salt also goes under evaporation or sublimation during heating process but probably not as fast and severe as $Zn(ac)_2$ and $Zn(acac)_2$ compounds.

Zn Compound	Molecular Weight (g mol^{-1}) of anhydrous Zn compound	**Theoretical** mass loss of thermal dehydration of **one** water molecule	**Theoretical** mass loss of thermal dehydration of **two** water molecule	**Experimental** mass loss of thermal dehydration	**Theoretical** mass loss of final thermal decomposition to ZnO	**Experimental** mass loss of final thermal decomposition to ZnO
$Zn(acac)_2$	263.6	12.0%	6.4%	7%	69.1%	Decomposition + sublimation
$Zn(ac)_2$	183.5	16.4%	8.9%	11%	55.6%	Decomposition + sublimation
$Zn(prop)_2$	211.5	14.5%	7.8%	—	61.5%	Decomposition + sublimation
$Zn(tfa)_2$	291.4	11.0%	5.8%	8%	72.1%	Decomposition + sublimation
$Zn(form)_2$	155.4	18.8%	10.4%	19%	47.6%	48.2%
Zn(ox)	153.4	19.0%	10.5%	17%	47.6%	48.2%

Table 3.2: Calculation of theoretical and empirical mass losses of thermal dehydration and decomposition of Zn compounds (experimental values obtained from TGA spectra)

To examine the effect of heating rate on the thermal processing of the zinc compounds, $Zn(form)_2$, which is not sublimed in the temperature range of the experiment, was heated up to 500 °C in air, but with much lower heating rate of 0.5 °C min^{-1}. The TGA curves of the sample in two different regimes, were plotted together in one graph for better comparison (Figure 3.2).

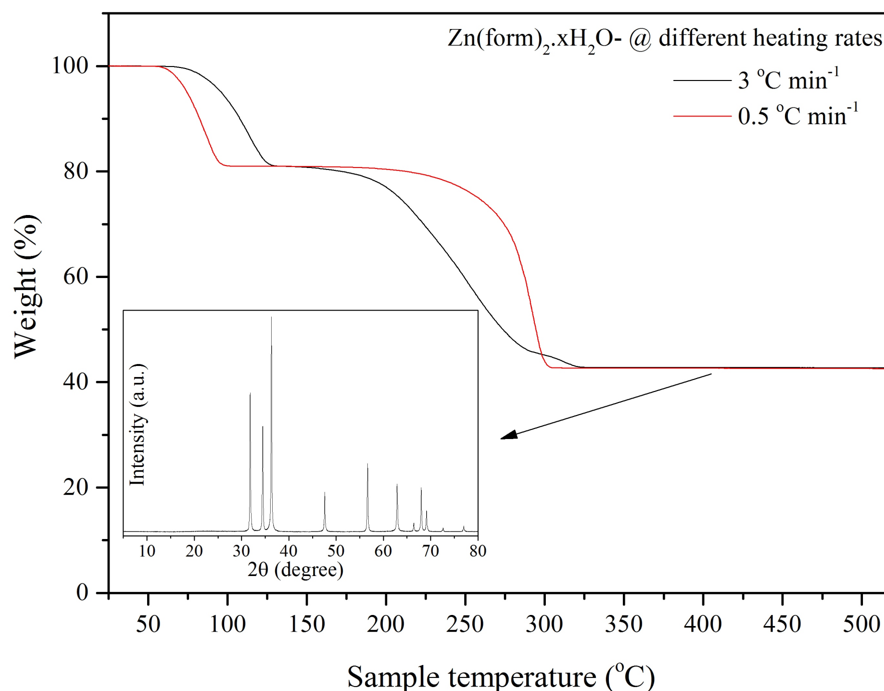

Figure 3.2: Effect of heating rate on the TGA of $Zn(form)_2$. Inset: XRD pattern of the residue after TGA measurement

The TGA curve recorded at lower heating rate includes two neat steps of mass loss, corresponding to the dehydration and decomposition processes. The mass loss percentages are identical in two TGA curves, but in TGA at lower heating rate, dehydration and decomposition of the sample occur at about 50 °C and 25 °C lower temperature, respectively. This supports the effect of the heating rate on the observed results of various thermal processing techniques. Inset in Figure 3.2 displays the XRD pattern of the residue after TGA measurement. Result confirms the full decomposition of $Zn(form)_2$ to ZnO by heating at temperatures higher than ~ 350 °C in air.

In order to confirm the formation of ZnO by thermal decomposition of selected Zn compounds, it is important to identify unequivocally the products formed in the decomposition process. *In-situ* VT-XRD patterns of the Zn compounds were recorded from $2\theta = 7°$ to $2\theta = 70°$ from room temperature to 500 °C in a dry static air atmosphere. Figure 3.3 displays the *in-situ* VT-XRD patterns of $Zn(acac)_2$, $Zn(ac)_2$, $Zn(prop)_2$, $Zn(tfa)_2$, $Zn(form)_2$, and

Zn(ox). The observed lower dehydration and decomposition temperature of Zn compounds in VT-XRD compared with the TGA data may arise of the smaller amount of sample, higher applied heating rate, and the effect static gas *vs* gas flow during heating process. In fact, the heating process in VT-XRD involves a stepped temperature regime in which the sample is held at constant temperature for about an hour while the XRD pattern is recorded, so VT-XRD has much slower heating rate, whereas, in TGA the sample is constantly heated up to the final temperature at higher heating rates. On the other hand, the VT-XRD measurements were carried out under static air, while TGA experiments were performed under a gas flow. This might also influence the observed results from each technique. Although the VT-XRD and TGA data are not directly comparable, the relative differences in thermal reactions, observed for various samples, are still valid.

The VT-XRD data clearly define that among the six zinc compounds, $Zn(acac)_2$ has the lowest decomposition temperature, and in the second step $Zn(prop)_2$ and $Zn(ac)_2$ have the lower decomposition temperatures than other Zn compounds. It can be seen that the conversion of $Zn(prop)_2$ and $Zn(ac)_2$ to ZnO occurs without involvement of any crystalline intermediates. However, $Zn(acac)_2$, $Zn(tfa)_2$, $Zn(form)_2$ and Zn(ox) pass through an intermediate crystalline phase of unknown structure. In XRD patterns of $Zn(tfa)_2$, there is a phase generated at *ca.* 175 °C which shows no distinct diffraction peaks and may be amorphous.

Additional sharp peaks with low intensity observed in the XRD patterns of the Zn compounds (particularly in the XRD patterns of $Zn(tfa)_2$), between 43° and 67° degrees in 2θ (43.5°, 52.5°, 57.5° and 66.5) at temperatures at which ZnO is already formed (200 °C and higher), are caused by the alumina crucible used as a sample holder for these measurements. This might be because of significant evaporation and mass loss of the specimen during the heating process, as was also observed in the TGA measurements (Figure 3.1).

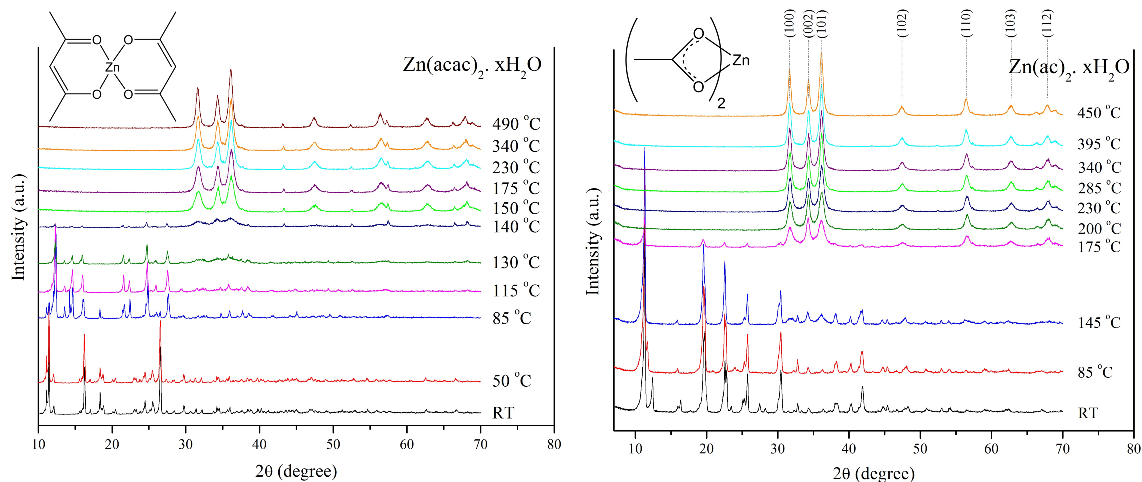

(a)

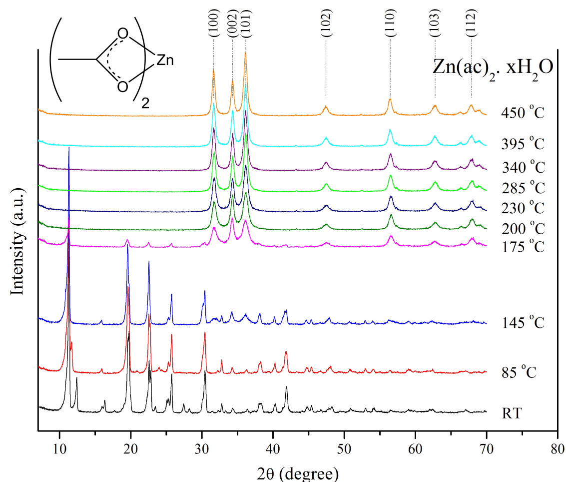

(b)

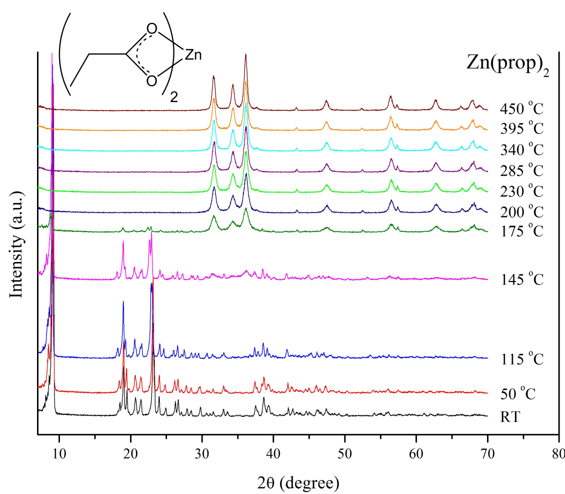

(c)

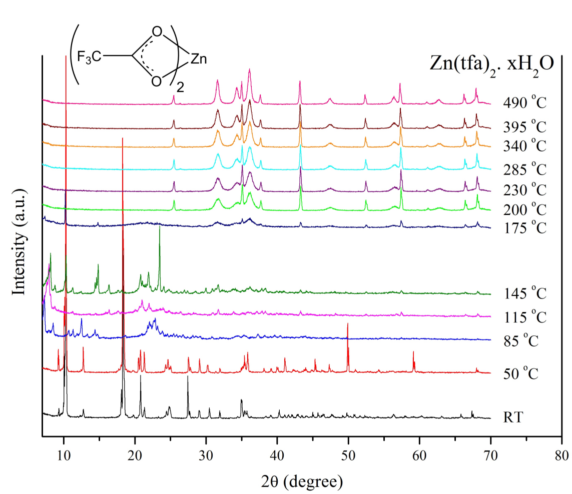

(d)

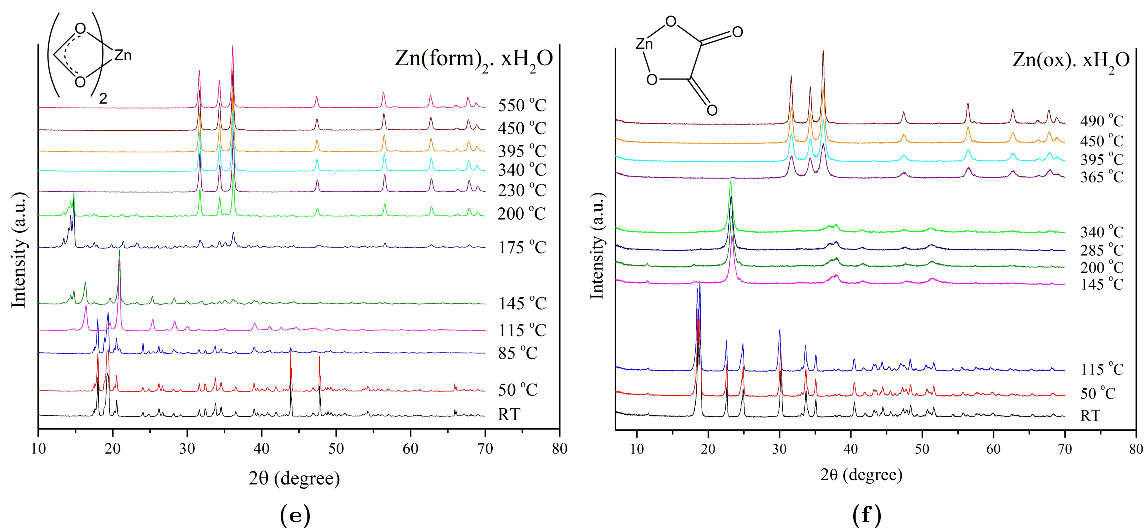

Figure 3.3: VT-XRD patterns for the thermal decomposition of (a) Zn(acac)$_2$, (b) Zn(ac)$_2$, (c) Zn(prop)$_2$, (d) Zn(tfa)$_2$, (e) Zn(form)$_2$, and (f) Zn(ox). ZnO main diffraction peaks are shown in figure (b), the XRD pattern of Zn(ac)$_2$

The decomposition temperature ranges in which fully crystalline ZnO is formed from Zn compounds, obtained from VT-XRD data, are shown in Figure 3.4. The first points correspond to the onset of the formation of the crystalline ZnO phase which in fact might coexist with the Zn compound, and the last points at higher temperature in each range show the temperature in which Zn compounds have been fully decomposed to ZnO. The XRD patterns do not change on further increase of the temperature, although the intensity or width of the diffraction peaks do change because of alteration in the ZnO particle size.

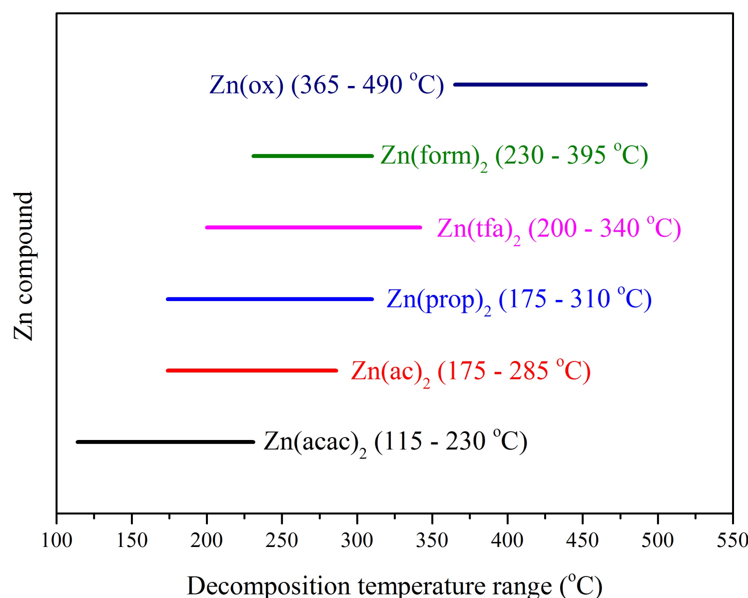

Figure 3.4: The ZnO appearance temperature range for Zn compounds obtained from VT-XRD data

Figure 3.3 (a) shows VT-XRD patterns of $Zn(acac)_2 \cdot xH_2O$. It is seen that the decomposition occurs in two discrete steps, in accordance with TGA-DSC analyses shown in Figure 3.5. An intermediate phase of anhydrous $Zn(acac)_2$ formed at 85 °C decomposes completely to ZnO at temperature of about 150 °C. Very low intensity and broad ZnO diffraction peaks observed at 140 °C indicate a very small (~ 9.5 nm) crystallite size of the initially-formed crystalline ZnO phase. The XRD patterns do not change significantly at temperatures above 150 °C. However, ZnO crystallite sizes calculated using the Scherrer formula increased from 9.6 nm at 150 °C to 30.3 nm at 500 °C.

TGA-DSC measurements were carried out on $Zn(acac)_2$ and $Zn(ac)_2$, in order to confirm the initial data obtained from TGA and VT-XRD and provide some more useful information about thermal decomposition processes. The TGA-DSC data of $Zn(acac)_2 \cdot xH_2O$ clearly indicates that the decomposition begins at around 75 °C and is complete by ~ 220 °C. As can be seen in Figure 3.5, $Zn(acac)_2 \cdot xH_2O$ loses weight in two discrete steps. The first weight loss of ca. 6.5% in the temperature range of 100 - 110 °C is accompanied by a broad

endothermic DSC peak attributed to the removal of one water molecule forming anhydrous Zn(acac)$_2$. A sharp endothermic peak observed at 134 °C does not involve any weight loss and corresponds to melting of Zn(acac)$_2$ (135 - 138 °C). In the second weight loss step, ZnO is formed by the decomposition of the anhydrous Zn(acac)$_2$, which is also endothermic and observed between 210 - 220 °C in DSC. The total weight loss reaches over 94.0% at 220 °C and is significantly larger than the expected weight loss of about 70% for the total decomposition of the precursor into stoichiometric ZnO. Such a large difference indicates that the decomposition of anhydrous Zn(acac)$_2$ is accompanied by a significant evaporation of the specimen during heating in argon flow. [115]

These results demonstrate that the formation of ZnO via thermal decomposition of Zn(acac)$_2 \cdot$ xH_2O precursor in oxygen-containing atmosphere is beneficial as a simple, low temperature synthesis route. ZnO thin films can therefore be successfully grown above a substrate temperature of 200 °C.

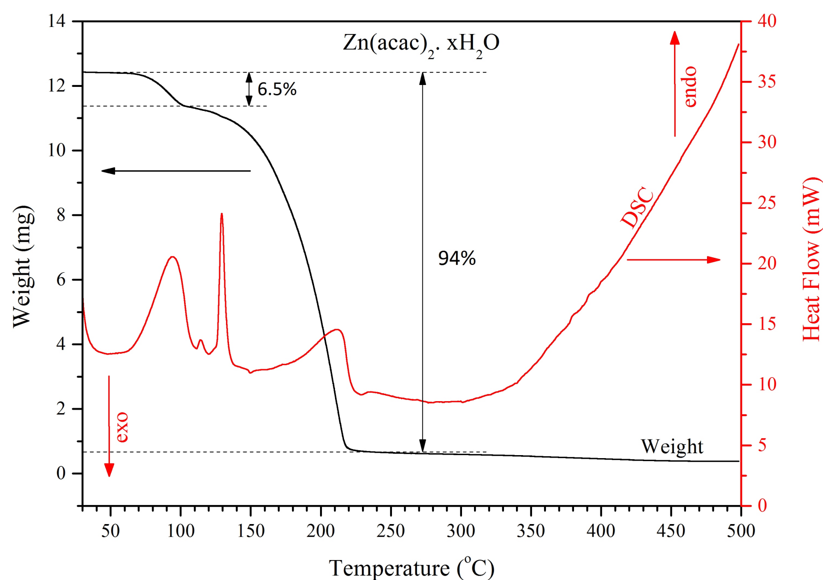

Figure 3.5: Thermogravimetric analysis (black) and differential scanning calorimetry (red) curves for the heating of Zn(acac)$_2 \cdot$ xH_2O

It has been proposed that ZnO is formed from anhydrous Zn(acac)$_2$ on a hot substrate

surface according to the following simplified thermal decomposition scheme [6]:

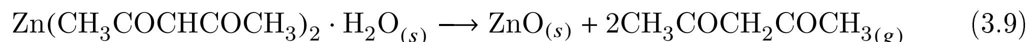

$$Zn(CH_3COCHCOCH_3)_2 \cdot H_2O_{(s)} \longrightarrow ZnO_{(s)} + 2CH_3COCH_2COCH_{3(g)} \tag{3.9}$$

Interestingly, the decomposition reaction demonstrates that ZnO is the only product and there is no organic residue left on the surface.

The VT-XRD patterns of $Zn(ac)_2 \cdot xH_2O$ in dry air atmosphere is shown in Figure 3.3 (b). The XRD profile suggests that the thermal process proceeds via two straightforward reaction steps, as only an existence of two different solid phases revealed by the XRD diagrams. The XRD diagram were changed to anhydrous phase which completed the dehydration at 85 °C, and the resulting phase agreed approximately with the XRD diagram of anhydrous zinc acetate. It can be clearly observed that the main change in XRD patterns attributed to the formation and growth of crystalline zinc oxide gradually starts from around 175 °C, and is completed after 200 °C. The XRD diagrams obtained after 200 °C remained unchanged and had relatively strong crystalline peaks, indicating pure crystalline zinc oxide. Unlike $Zn(acac)_2$, $Zn(ac)_2$, and $Zn(prop)_2$, the VT-XRD patterns of $Zn(tfa)_2$, $Zn(form)_2$, and Zn(ox) show that the thermal decomposition occurs in several complicated reaction steps and different solid phases are involved in the process.

TGA-DSC data clearly indicate that $Zn(ac)_2$ decomposition to ZnO occurs at higher temperature (~ 310 °C) compared to $Zn(acac)_2$ (~ 220 °C) and these results support the VT-XRD measurements shown in Figure 3.3 (a) and (b).

From the simultaneous TGA-DSC curves in Figure 3.6, $Zn(ac)_2$ precursor also loses weight in two major steps. The first step of about 4.5% weight loss, is the endothermic dehydration of the water of crystallisation between 60 - 80 °C, and is attributed to the loss of one water molecule. The major weight loss of 81% on the TGA curve between 310 - 340 °C is ascribed to the exothermic decomposition of the dehydrated $Zn(ac)_2$ to give ZnO as the final product. The endothermic peak at 250 °C corresponds to the melting of $Zn(ac)_2$

(237 °C, from Merck Chemicals website).

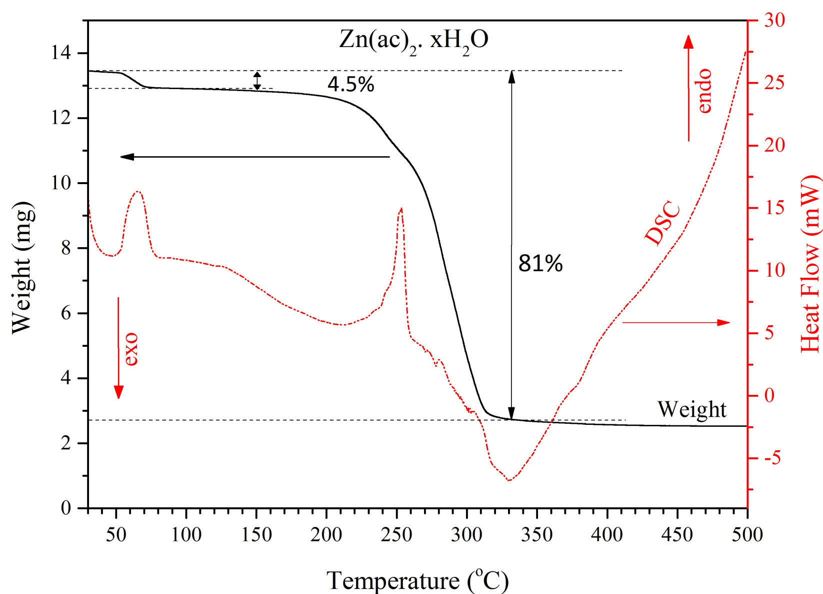

Figure 3.6: Thermogravimetric analysis (black) and differential scanning calorimetry (red) curves for the heating of $Zn(ac)_2 \cdot xH_2O$

For $Zn(ac)_2$ to form ZnO, the experimental mass loss is much higher than the theoretical mass loss. This difference might be due to the sublimation (or evaporation) of $Zn(ac)_2$ as reported to occur above 180 °C in dry atmosphere by other researchers. [251, 252] Arii and Kishi suggested that the humid atmosphere was capable of preventing the sublimation of anhydrous zinc acetate. [251] For $Zn(acac)_2$, as mentioned before, the evaporation of sample during heating is more dramatic, and this makes it a very promising zinc precursor for ZnO thin film deposition using solution-free deposition techniques such as chemical vapour deposition (CVD). This is consistent with the use of zinc acetylacetonate as an agent for atmospheric pressure chemical vapour deposition (APCVD). [263, 264]

At the end it is important to point out that all the experiments presented in this chapter were carried out in dry atmosphere, and therefore, the discussed decomposition temperatures and mechanisms might not be directly extrapolated to the decomposition processes take place in the solution and during the deposition of thin films using spray pyrolysis. Due

to the fundamental differences between investigation of thermal decomposition and spray pyrolysis processes, studied zinc salt might decompose to ZnO through different mechanisms which would lead to different decomposition temperatures. However, based on several experimental observations, we found that zinc precursors which decompose via several complicated steps or have very high decomposition temperatures (from TGA data) do not tend to produce high quality and conductive ZnO thin films using spray pyrolysis technique.

3.4 Conclusions

Thermal processes of various zinc precursors were investigated by TGA, TGA-DSC and VT-XRD in dry atmosphere, and the formation of ZnO from the decomposition of the zinc salts has been confirmed. Among all precursors studied, $Zn(acac)_2 \cdot xH_2O$ had the lowest decomposition temperature. From TGA-DSC results the thermal decomposition of $Zn(acac)_2 \cdot xH_2O$ began with a single-step dehydration at $\sim$ 75 °C, followed by melting and parallel reactions including the sublimation and decomposition of anhydrous zinc acetylacetonate. TGA-DSC clearly indicated that the decomposition of anhydrous zinc acetylacetonate occurred together with evaporation/sublimation of the specimen at temperature of around 220 °C. VT-XRD revealed that formation of anhydrous zinc acetylacetonate occurred at around 85 °C, followed by decomposition around 140 °C, and crystalline ZnO could be identified below 175 °C. Heating rate of thermal processes was found to be responsible for the observed difference in thermal decomposition temperatures from TGA and VT-XRD. On the other hand, thermal analysis of $Zn(ac)_2$ revealed that it decomposes via a two-step process. TGA-DSA revealed that the thermal process of $Zn(ac)_2$ was completed by the sublimation around 300 °C. VT-XRD showed that anhydrous zinc acetate formed at 85 °C, was directly decomposed to crystalline zinc oxide at $\sim$ 200 °C.

Thermal analysis such as TGA-DSC equipped with mass spectrometer (TGA-DSC-MS) is essential for determining the accurate decomposition mechanism in sufficient detail.

Chapter 4

Preparation and Characterisation of Silicon-doped ZnO (SiZO) Thin Films

4.1 Introduction and overview

As discussed in Chapter 1, low resistivity semiconductor thin films can be prepared by the creation of intrinsic atomic defects that act as donors, for example oxygen vacancies and zinc atoms on interstitial lattice sites. An intrinsically-doped semiconductor thin film can be achieved by controlling the oxygen partial pressure [265] and temperature during deposition. On the other hand, an extrinsic semiconductor is a semiconductor with a small amount of impurities added by a process known as doping. Extrinsic doping in ZnO is usually achieved by the substitution of of extrinsic such as In, Al or Si on metal lattice sites or halogens, such as Cl or F on oxygen lattice sites. [147, 157] In real oxide films, both intrinsic and extrinsic doping mechanisms occur simultaneously.

In this and the next chapter, in order to understand the effect of single doping on the properties of ZnO thin films, doping of silicon into ZnO (SiZO, this chapter), and doping of fluorine into ZnO (FZO, next chapter) using spray pyrolysis is explored.

In In-doped, Al-doped or Ga-doed ZnO, In, Al, and Ga atoms on Zn sites act as single

electron donors. Investigation of the effect of tetravalent dopants such as Ge, Sn and Si dopants, which might act as multi electron donors and more efficiently improve the optical and electrical properties of TCOs by increasing the carrier concentration, have attracted a lot of interest. Clatot *et al.* studied Sn, Ge, and Si doping of ZnO using the pulsed laser deposition (PLD) technique. [266] They reported the lowest resistivity for Si-doped ZnO, whereas, Ge-doped ZnO thin films had promising transparency and conductivity and Sn-doped ZnO thin films were non-conductive. Si-doped ZnO prepared by RF Magnetron Sputtering was reported for the first time by Minami *et al.* in 1986. [12] SiZO thin films with minimum resistivity of 3.8×10^{-4} Ω cm and transmittance above 85% were produced at low substrate temperatures of about 250 °C. More recent reinvestigation of Si-doping of ZnO has resulted in a large dispersion in reported resistivity values, which vary from 6.2×10^{-2} Ω cm to 1.3×10^{-4} Ω cm. [12, 141–143, 267] The SiZO thin films deposited by Luo *et al.* at room temperature by reactive magnetron co-sputtering method, using Zn target attached to several Si chips distributed uniformly around the sputtering racetrack, showed a minimum resistivity value of 6.2×10^{-2} Ω cm for the $Zn_{1-x}Si_xO$ (x = 0.02) composition. [267] Yuan reports an optimum Si concentration of 2.1% corresponding to a lowest resistivity of 9.2×10^{-4} Ω cm for SiZO thin films grown on sapphire substrates at 300 °C by atomic layer deposition method. [143] In the work of Rougier *et al.*, transparent (~ 80%) 3% SiZO thin films with a low resistivity of about 7.9×10^{-4} Ω cm were deposited at low substrate temperatures of ≤ 150 °C by PLD. However, this work only used substrate surface area up to 1×1 cm^2. [142] The same group, in a different study, deposited SiZO thin films using co-sputtering from ZnO and SiO_2 targets. [268] A resistivity of 3.2×10^{-3} Ω cm at a [Si] / [Zn] ratio of 3.9 at.% was reported for the thin films grown at ambient temperature under an Ar flow.

4.2 Experimental

All the ZnO thin films presented here and in the next chapters have been extrinsically doped by adding silicon tetraacetate and/or ammonium fluoride to the zinc acetylacetonate ($Zn(acac)_2$) precursor solution.

In the present work, several series of undoped and Si-doped zinc oxide thin films of thickness ~ 500 nm were prepared by the spray pyrolysis technique at deposition temperatures between 250 °C to 500 °C. A 0.15 M zinc precursor solution was prepared by dissolving zinc acetylacetonate hydrate ($Zn(C_5H_7O_2)_2 \cdot xH_2O$, ≥ 99.995% metals basis, Sigma-Aldrich) in a 1:2 (by volume) mixture of distilled water (Ondeo Purite Select Analyst) and isopropanol (99.5%, Sigma-Aldrich). 10 drops (~ 0.5 mL) of glacial acetic acid (99.8%, Fischer Scientific) was added to the precursor solution (10 ml) in order to dissolve and prevent hydrolysis of zinc acetylacetonate monohydrate. After stirring for 30 minutes, a transparent solution with no suspended particles was obtained. The mixture was gravity filtered through qualitative filter paper, resulting in a clear, homogeneous solution. For each deposition run, 10 mL of this solution was used. Silicon tetra acetate ($Si(OCOCH_3)_4$, 98%, Aldrich) was added to the base $Zn(acac)_2$ solution as Si source, respectively. For deposition of doped samples, 10 mL of solution was transferred to a second glass vial equipped with a stirbar. While stirring, dopant was added to the solution, and the solution left stirring for 24 hours before spraying.

32 mm × 24 mm Schott D263T borosilicate glass cover slips (No. 1, 0.13 mm - 0.17 mm thick, Menzel-Gläser) ultrasonically cleaned in acetone and distilled water and dried in the oven at 60 - 70 °C were used as substrates. The substrate was firmly mounted on and heated from below by a stainless steel heating block with two embedded 100 W cartridge heaters. During film deposition the temperature of the block was adjusted and controlled using an Eurotherm PID temperature controller and a Type J thermocouple inserted into the centre of the heating block. The block was held at a constant temperature between 250 °C and 550 °C during deposition. The precursor solution was sprayed through an atomiser

nozzle (0.3 mm diameter, BETE XA PR-050) on to the preheated substrates at at a flow rate of ~ 0.55 mL min^{-1} using a peristaltic pump (Masterflex® Console Drive, Model: 7519-20). The nozzle was located at the top of the chamber and the nozzle to substrate distance was 30 cm. Deposition was carried out inside an acrylic chamber with a positive internal pressure of nitrogen. Dry nitrogen gas was used as the carrier gas at the flow rate of 14 - 15 L min^{-1}. Before commencing each deposition process the chamber was flushed with nitrogen and the system was heated to the operating temperature and held there for approximately 20 minutes. After spraying, the system was held at operating temperature for a further 5 minutes before cooling down. The substrates were heated up to deposition temperature at a rate of 30 °C min^{-1} and cooled down after deposition to room temperature under flowing nitrogen. The effect of Si doping was studied by adding different amounts (0.5 to 5 mol.%) of silicon tetraacetate ($Si(OCOCH_3)_4$, 98%, Sigma-Aldrich) to the zinc precursor solution.

Based upon a series of calibration experiments using an optical pyrometer while no spraying was happening (carried out by Alex T. Vai), it is estimated that the equilibrium temperature at the top surface of glass substrates is ~ 0.76 times the temperature measured in the heater block. It was also found that the substrate temperature is not 100% uniform. In order to avoid any confusion, all deposition temperatures are expressed as the heater setpoint temperature and can be corrected any time using the graph shown in Figure 4.1.

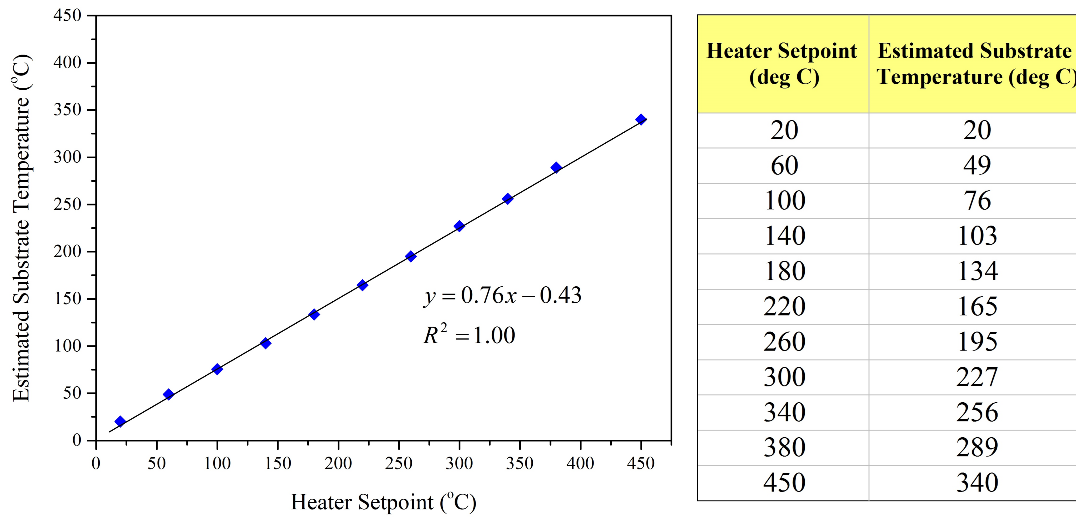

Heater Setpoint (deg C)	Estimated Substrate Temperature (deg C)
20	20
60	49
100	76
140	103
180	134
220	165
260	195
300	227
340	256
380	289
450	340

Figure 4.1: Temperature correction at the surface of the substrate

Structural, optical, electrical, morphological and surface properties of the prepared films were characterised by X-ray diffraction (XRD), UV-Vis-NIR spectroscopy, Hall effect measurement, atomic force microscopy (AFM), and scanning electron microscopy (SEM). X-ray diffraction measurement of samples was performed using a a PANalytical X'Pert PRO Diffractometer (monochromated Cu-$K_{\alpha 1}$ radiation, λ = 1.54059 Å) at an emission current of 40 mA and an anode voltage of 45 kV. The spectra were recorded from 5° to 80° scanning angle (2θ) with a step size of 0.0084°. Samples were placed on a 60 rpm spinner to improve averaging of crystallite orientation. The optical transmission spectra for undoped ZnO and SiZO thin films in this chapter, were recorded at room temperature for wavelengths between 2500 and 200 nm using a Varian Cary 5000 UV-Vis-NIR spectrometer. The optical data were used to calculate the film thickness by modelling the interference fringes of ZnO films observed in the visible part of spectra using the envelope method of Swanepoel. [239] Electrical characterisations were studied by the van der Pauw technique [240] using an Ecopia HMS-3000 Hall effect measurement system with a 0.55 T permanent magnet on a small piece of the samples (5 mm × 5 mm). Indium solder was used to create four ohmic electrical contacts on the corners of the thin films. Electrical Measurements at

temperatures below (to ~ 80 K) and above (to ~ 350 K) were achieved using a custom-designed heating and cryogenic cooling system. Sample temperature was measured with a Type T thermocouple embedded in the sample mount and in contact with the film substrate. AFM images were recorded on a Digital MultiMode scanning probe microscope with a Nanoscope IIIa controller. Nascatec GmbH (model: NST NCHFR) silicon probe with resonant frequencies of approximately 320 kHz were used. The AFM probe was calibrated by scanning a three-dimensional reference from Digital Instruments. The SEM images in this chapter were collected on a JEOL JSM-6500F low voltage field emission gun scanning electron microscope at an accelerating voltage of 5 kV. Samples were examined without any platinum or gold coating.

4.3 Results and discussion

4.3.1 Structural studies of ZnO and SiZO thin films

4.3.1.1 Effect of deposition temperature

The X-ray diffraction patterns of undoped and Si-doped ZnO thin films deposited at temperatures between 250 °C and 500 °C are shown in Figure 4.2 (a) and (b). The XRD patterns show only peaks consistent with the hexagonal wurtzite ZnO phase; no crystalline phase corresponding to either SiO_2 or Zn_2SiO_4 were observed in the XRD patterns. A reference pattern for ZnO is also shown in the figure.

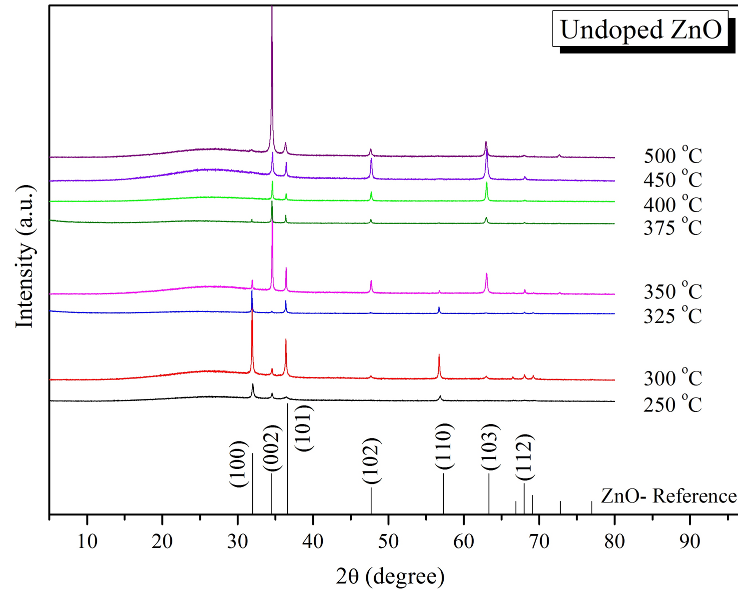

(a)

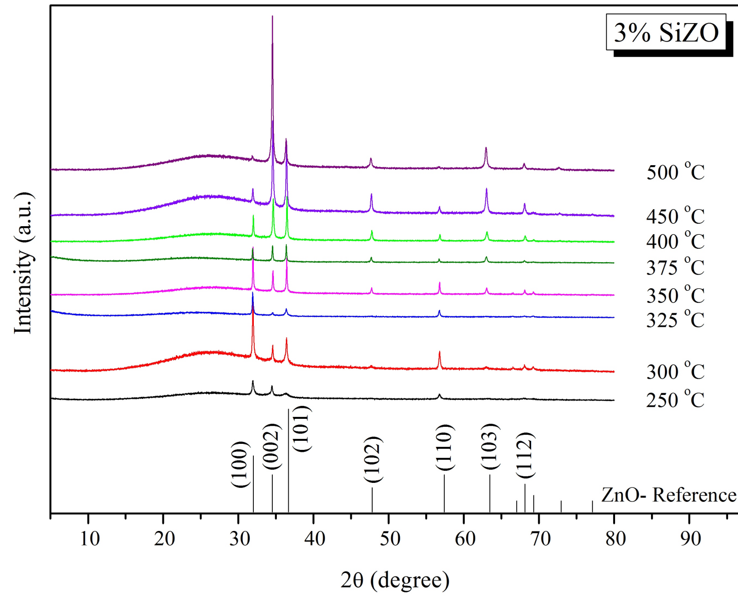

(b)

Figure 4.2: XRD patterns of (a) ZnO and (b) SiZO thin films deposited at temperatures from 250 °C to 500 °C

The substrate temperature plays an important role in determining the preferred orient-

ation of crystallites in the deposited ZnO thin films. The variations in intensity ratios of the (100), (002) and (101) XRD reflections (expressed as texture coefficient, TC), as a function of substrate temperature are shown in Figure 4.3. The preferred orientation of growth of thin films can be determined by the texture coefficient of the (hkl) plane, $TC_{(hkl)}$, using Equation 4.1.

The texture coefficient of the (hkl) plane, $TC_{(hkl)}$, can be used to evaluate the preferred orientation of growth of ZnO thin films, using the following formula introduced by Barret and Massalski in 1980: [269]

$$TC_{(hkl)} = \frac{I_{(hkl)i}/I_{0(hkl)i}}{N^{-1}\sum I_{(hkl)n}/I_{0(hkl)n}} \times 100\% \tag{4.1}$$

where $I_{(hkl)}$ is the measured relative intensity of a plane (hkl), and $I_{0(hkl)}$ is the standard intensity of the corresponding bulk reference plane, taken from the databases (JCPDS). [270] However, the above formula for different planes of one sample differs only by a constant value. Thus, for different planes in the ZnO pattern Equation 4.1 can be rewritten as:

$$TC_{(100)} = \frac{I_{(100)}}{I_{(100)} + I_{(002)} + I_{(101)}} \times 100\%$$

$$TC_{(002)} = \frac{I_{(002)}}{I_{(100)} + I_{(002)} + I_{(101)}} \times 100\%$$

$$TC_{(101)} = \frac{I_{(101)}}{I_{(100)} + I_{(002)} + I_{(101)}} \times 100\% \tag{4.2}$$

where $I_{(100)}$ and $I_{(002)}$ and $I_{(101)}$ are the intensities of each plane. A TC value close to 100% arises from a perfect preferential growth along one plane and lack of growth along other planes.

Both undoped ZnO and SiZO thin films deposited at low temperatures exhibit a polycrystalline structure with a (100) preferred orientation; the relative intensity of the (100)

reflection decreases significantly with an increase of deposition temperature up to 325 °C. As the deposition temperature is raised above 325 °C, the intensity of (002) reflection increases, indicating preferential growth of crystallites with the (002) plane parallel to the substrate surface. Similar observations were also reported by Solookinejad *et al.* for ZnO thin films deposited by the sol-gel technique. [271] It is known that preferred orientation of thin films is affected by surface free energy of each crystal plane and the surface free energy depends strongly on the type of hybridised orbital available at the metal. For example, for materials with sp^2 orbitals the surface of the films have tendency to be (001)-oriented and for those with sp^3 orbitals the (111) plane is preferred in the cubic structure and the (001) direction is preferred in the hexagonal structure, because these planes have minimum surface free energies and the film grows to minimise the surface free energy. ZnO has tetrahedral coordination formed by sp^3 hybridised orbitals and as it has wurtzite structure, the direction of each apex is parallel to the c-axis ((001) plane), and this is why the ZnO films tends to grow in the (001) direction, and the (001) oriented and self textured films are easily obtained. [200]

The behaviour of undoped ZnO and SiZO diverges at higher temperatures. In pure ZnO thin films, the (100) reflection in the XRD spectra is not present at temperatures greater than 400 °C. However, for the SiZO thin films, the (100) reflection is still observed even at high temperatures, indicating that a mixed orientation of crystallites is preserved.

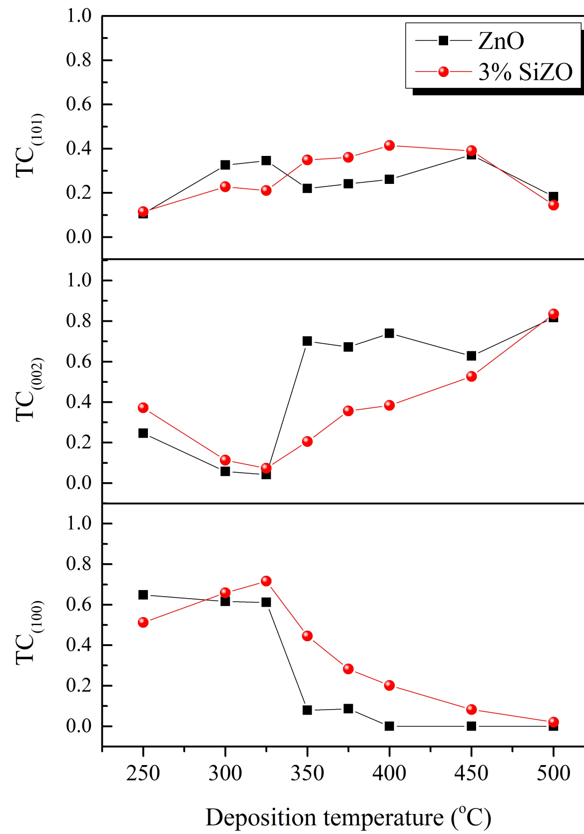

Figure 4.3: Variations in $TC_{(100)}$, $TC_{(002)}$ and $TC_{(101)}$ of ZnO *vs* SiZO as a function of the film deposition temperature

The mean crystallite size in thin films was calculated from the line broadening in the XRD patterns using Scherrer equation (Equation 2.9). The results are presented in Figure 4.4. The crystallite size in both ZnO and 3% SiZO films exhibits a maximum at deposition temperatures of around 325 °C. At deposition temperatures below 350 °C, the crystallite size of the SiZO films deposited is smaller by approximately 10 nm in comparison to that of undoped ZnO films whereas for films deposited above 350 °C, the crystallite sizes of ZnO and SiZO films are very similar. It is also observed that the crystallite size of undoped and SiZO films decreases as the preferred orientation along the *c*-axis and the intensity of the (002) reflection plane increase.

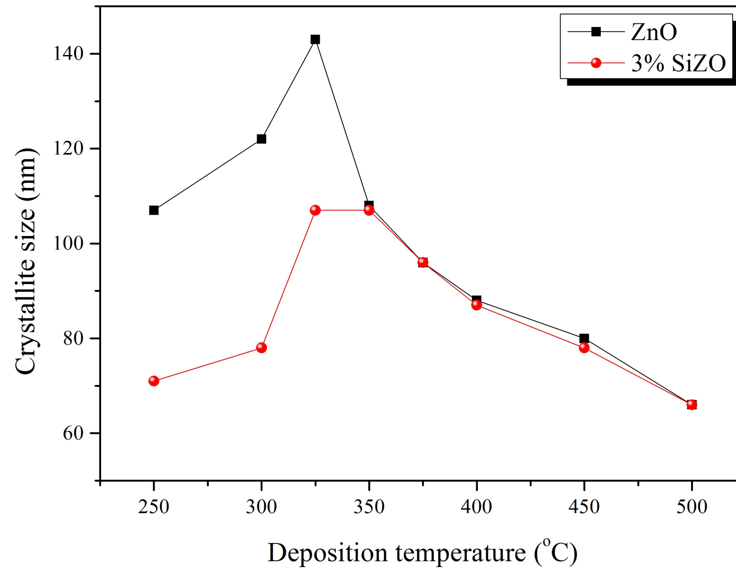

Figure 4.4: Calculated Scherrer crystallite sizes as a function of deposition temperature for ZnO and 3% SiZO thin films

The variation in lattice parameters of ZnO and 3% SiZO thin films as a function of deposition temperature was investigated (Figure 4.5). For both ZnO and SiZO thin films the lattice constant $a = b$ is weakly dependent on the deposition temperature, increasing from 3.245 Å to about 3.252 Åover the range studied. In contrast, the lattice parameter c decreases from 5.217 Å to 5.203 Å with increasing deposition temperature up to 350 - 400 °C and then remains almost constant still at higher temperatures. The unit cell volume for both ZnO and 3% SiZO films follows the trend observed for the c lattice constant. The contraction of the ZnO unit cell at deposition temperatures up to 350 °C can be attributed to increasing solubility of Si in the ZnO structure and substitution of Zn atoms in ZnO lattice by the smaller Si atoms (ionic radii of Zn^{2+} and Si^{4+} under tetrahedral coordination, are 0.60 Å and 0.26 Å, respectively [150]) during the formation of SiZO thin films and also to an increase in concentration of oxygen vacancies in ZnO thin films.

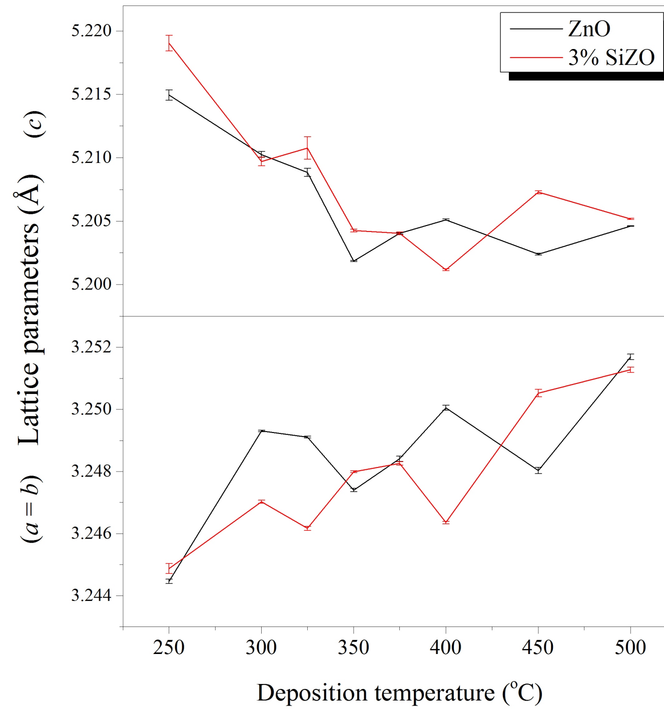

Figure 4.5: Variation of the lattice parameters of ZnO and SiZO thin films deposited at various deposition temperature

It can be proposed that the concentration of substitutional Si defects and the deviation from oxygen stoichiometry in ZnO lattice reach their limits at deposition temperatures of around 400 - 450 °C and do not increase at the higher deposition temperatures. The correlation between the variations in lattice parameters of the films prepared at different temperatures and the degree of Si doping and oxygen non-stoichiometry is also consistent with the results of electrical property measurements which show that electron carrier concentration increases with deposition temperature until it reaches a limiting value above 400 °C, as will be discussed further in Section 4.3.4.

4.3.1.2 Effect of Si concentration

Figure 4.6 (a) shows the resulting XRD patterns for the SiZO thin film deposited at 450 °C with variation of Si concentration. For all the samples, the (002) peak has the highest

intensity, indicating that the as grown SiZO thin films exhibit (002) preferential orientation with c-axis perpendicular to the substrate. No extra peaks related to silicon oxide or silicon zinc oxide were found in the XRD patterns, even at high concentration of Si. This may be due to Si ions substituted into the ZnO lattice or Si segregated to the non-crystalline region in the grain boundary. [143] The position of (002) peak as a function of Si concentrations are shown in Figure 4.6 (b). It can be seen that the position of (002) peak gradually shift to higher 2θ angle with increases Si concentration, which indicated that Si has really doped into the ZnO lattice.

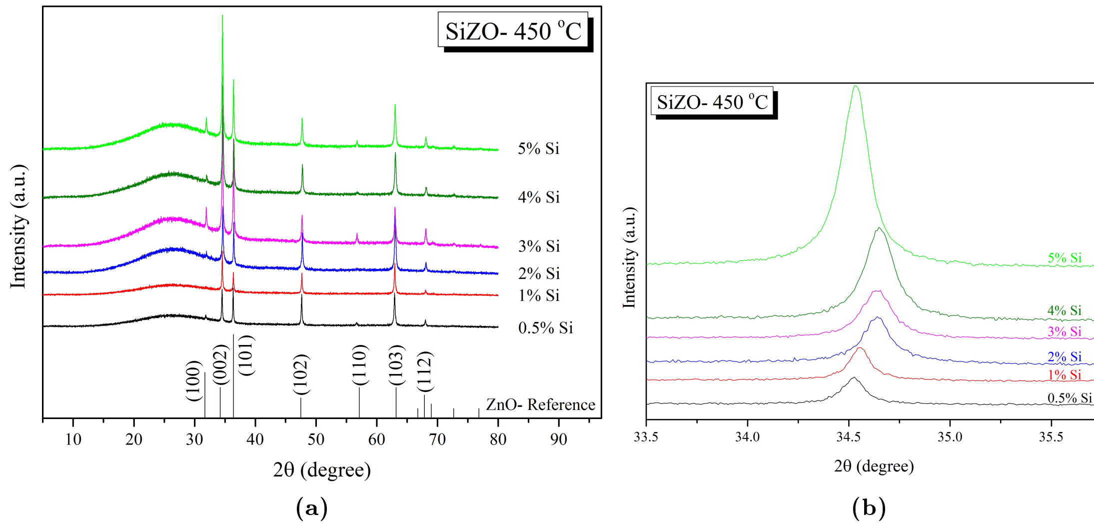

Figure 4.6: (a) XRD patterns and (b) position of the (002) peak of SiZO thin films with various Si concentration deposited at 450 °C

Although, the intensity of the (100) peak increases with increasing Si concentration to 2% and higher, but by looking at variations of the intensity ratios of the (100), (002), and (101) reflections more closely, as seen in Figure 4.7, TC values for SiZO films deposited at 450 °C do not depend on the Si dopant concentration and the $TC_{(100)}$, $TC_{(002)}$, and $TC_{(101)}$ values remain almost invariant with increasing Si doping level. This suggest that the texture of the thin films should not considerably change with increasing doping level.

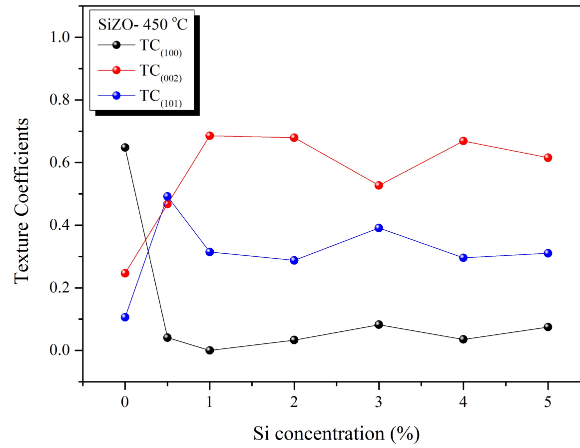

Figure 4.7: Variations in $TC_{(100)}$, $TC_{(002)}$ and $TC_{(101)}$ of SiZO thin films deposited at 450 °C as a function of Si concentration

Using the XRD patterns and the Scherrer equation (Equation 2.9) the influence of Si content on the crystallite size was investigated. The mean crystallite size was found to decrease slightly from around 80.0 nm at 0% Si to around 50.0 nm at Si concentration of 5%. These results agree well with the variation of the particle size obtained from AFM images (Figure 4.9).

4.3.2 AFM and SEM studies of ZnO and SiZO thin films

4.3.2.1 Effect of deposition temperature

Figure 4.8 depicts AFM micrographs of ZnO and 3% SiZO films deposited at different deposition temperatures. As seen in Figure 4.8 (a) to (f), the particle size and the uniformity of the films increase with increasing deposition temperature for both ZnO and 3% SiZO thin films. In general, SiZO films show a smaller particle size than corresponding ZnO films.

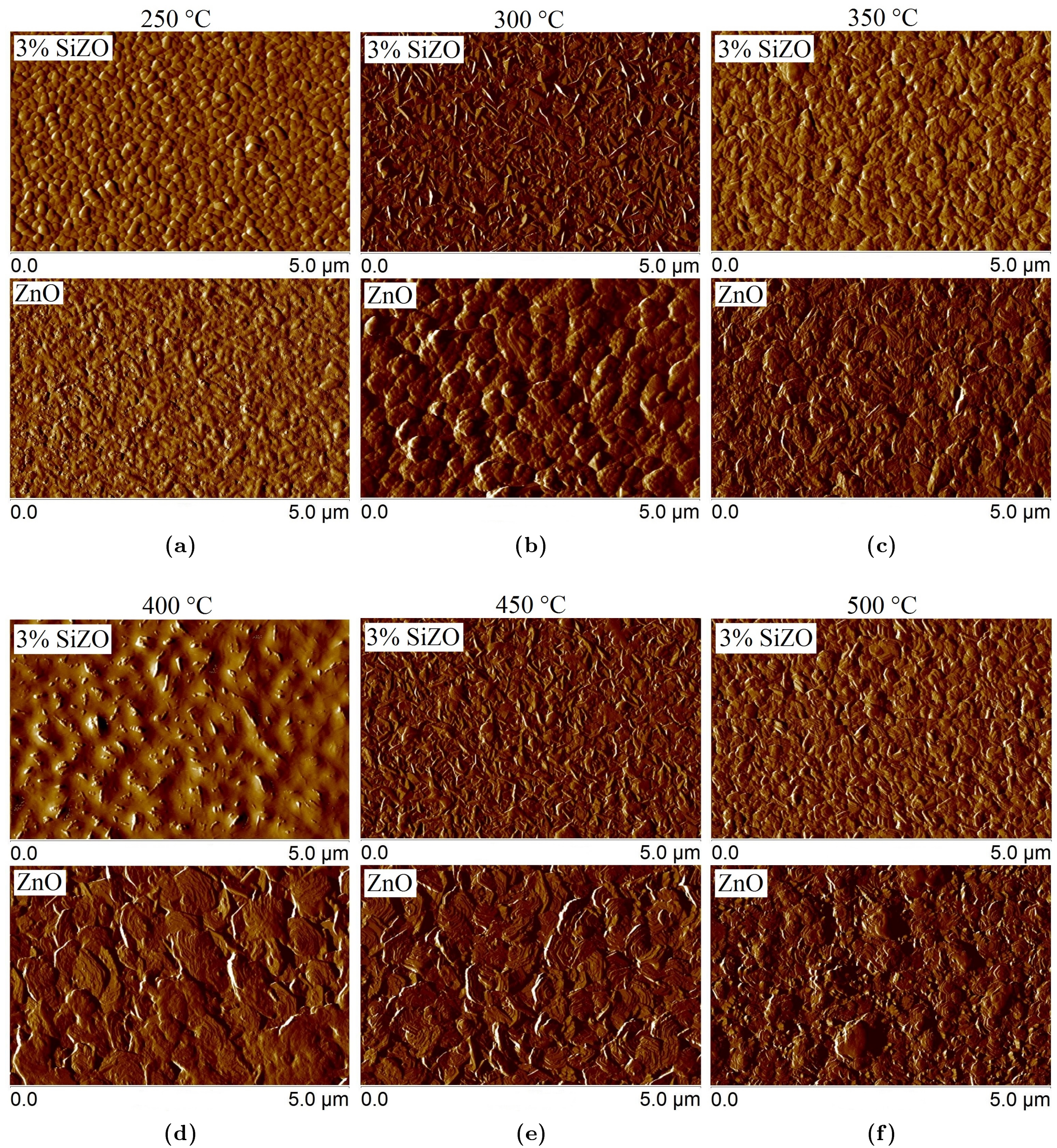

Figure 4.8: AFM images of ZnO and 3% SiZO thin films deposited at different temperatures; (a) 250 °C, (b) 300 °C, (c) 350 °C, (d) 400 °C, (e) 450 °C, and (f) 500 °C

Deposition temperature seems to be a key factor in determining the particle shape and size of ZnO and SiZO thin films. The particle size of undoped ZnO thin films increased from 140.0 ± 25.0 nm for the film deposited at lower 350 °C to about 220.0 ± 30.0 nm

with increasing deposition temperature to 400 °C and above. The mean surface roughness followed the same trend and increased from about 33.4 ± 4.2 nm for the samples deposited at 350 °C and lower to 43.8 ± 2.8 nm for the films deposited at temperatures above 400 °C. SiZO thin films show smaller particle size on the surface comparing to ZnO thin films, but it still increases as the deposition temperature was raised. The particle size grows from about 120.0 nm for the film made at 250 °C to around 150.0 nm for the samples prepared at temperatures higher than 400 °C. The surface roughness was more or less similar for all SiZO and in the range of 21.3 to 27.4 nm.

4.3.2.2 Effect of Si concentration

Figure 4.9 shows the AFM micrographs of SiZO films deposited at constant deposition temperatures and with varying Si dopant concentration at a constant temperature (450 °C). Increasing Si concentration results in smaller particle sizes. These results are in agreement with the variation of the crystallite size obtained from XRD patterns. In addition, the surface roughness of ZnO thin films was found to decrease with increasing Si dopant concentration, in consent with the decrease in particle size. The root-mean square roughness of ZnO and 3% SiZO films deposited at 450 °C was found to be 47.7 nm and 21.3 nm, respectively.

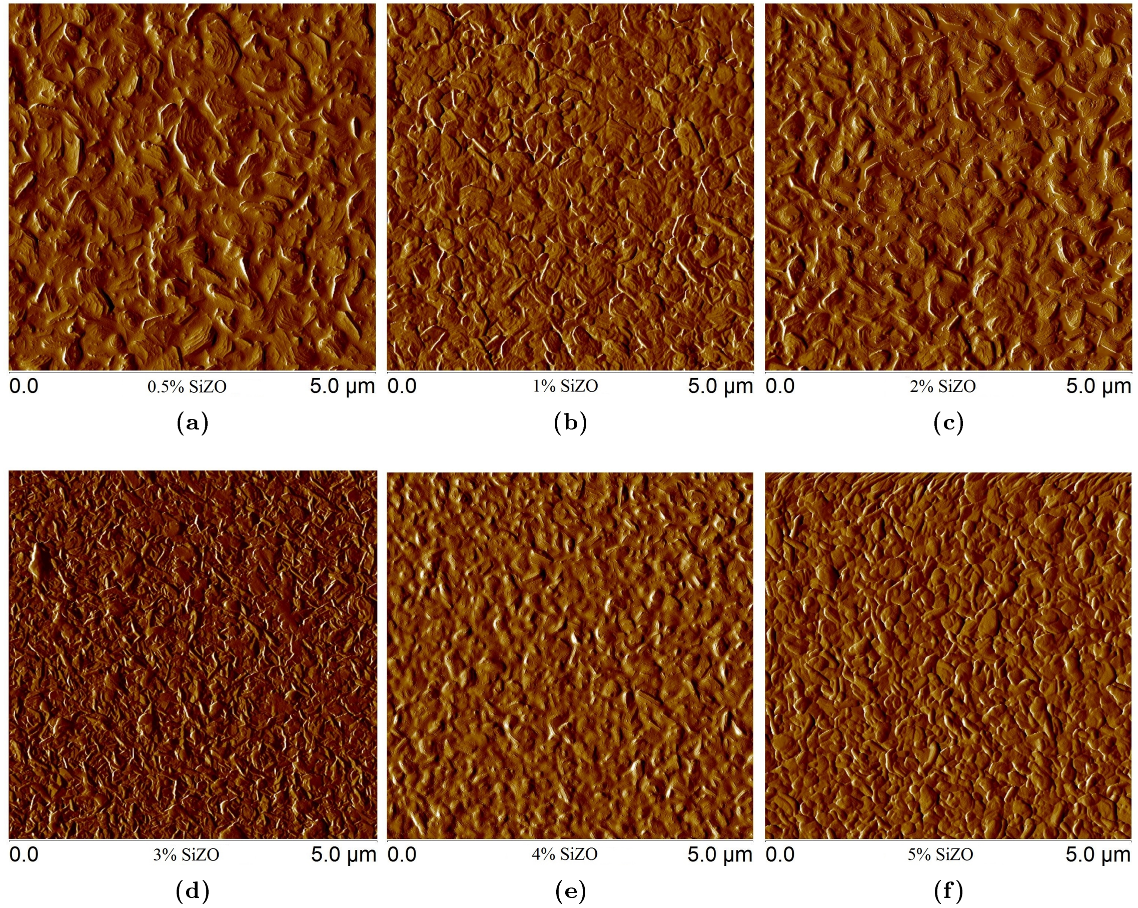

Figure 4.9: AFM images of SiZO thin films deposited with various Si concentration at 450 °C

The SEM micrographs shown in Figure 4.10 illustrate details of the surface morphology for ZnO thin films deposited at 250 °C, 325 °C and 450 °C, and 3% SiZO film deposited at 450 °C. While particle sizes observed in SEM and AFM are larger than crystallite sizes determined from XRD, this simply suggests that the larger particles may be composed of several smaller crystallites. A similar difference between the particle sizes from SEM analysis and the crystallite sizes from XRD has also been observed in doped ZnO thin films reported by other researchers. [272] The small particles of about 50 nm observed in the SEM images of SiZO samples which can be representative of crystallites on the surface of the films.

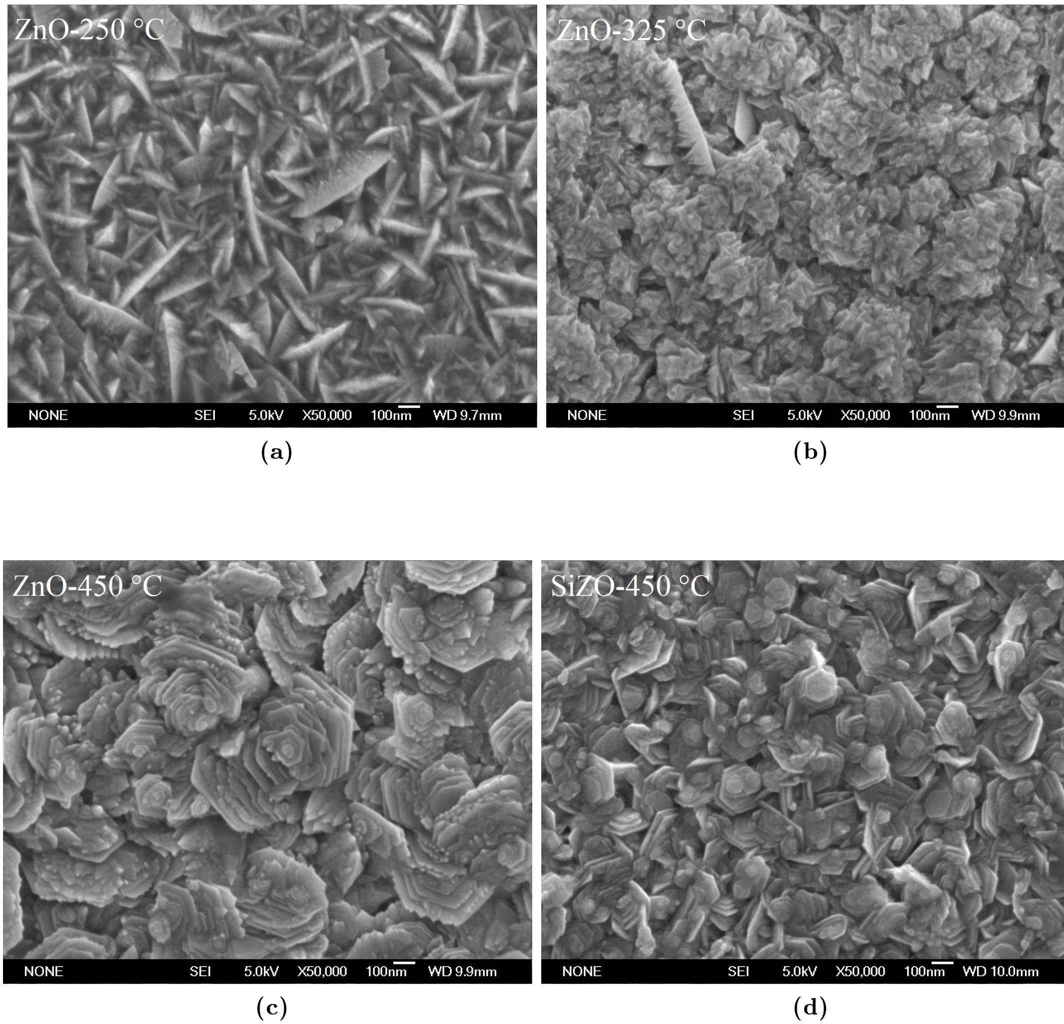

Figure 4.10: SEM images of ZnO thin films deposited at (a) 250 °C , (b) 325 °C, (c) 450 °C, and (d) 3% SiZO thin film deposited at 450 °C

The ZnO thin film deposited at 250 °C shows a structure consisting of small wedge-like particles that are oriented perpendicular to the substrate surface; this correlates with the XRD data which show a (100) preferential orientation for this film. On the other hand, the SEM image of the film deposited at 450 °C revealed a flake-like structure with preferential orientation of two-dimensional particle sheets parallel to the substrate surface in agreement with the XRD results (Figure 4.2 (a)) which show a highly *c*-axis oriented structure. Figure 4.10 (d) displays the SEM image of a 3% SiZO thin film grown at 450 °C. The film shows

similar shaped-particles to that observed in the undoped ZnO film prepared at 450 °C, but with smaller particle size and weaker *c*-axis orientation particles. The differences in particle size, orientation and morphology significantly influence the electrical properties of the thin films, as discussed in Section 4.3.4.

4.3.3 Optical studies of ZnO and SiZO thin films

The effect of deposition temperature and Si doping on the optical transmittance spectra of ZnO thin films in the wavelength range from 250 nm to 2500 nm was studied. The results are presented in Figure 4.11. All of the films show high transparency (~ 65 - 85%) over the visible range of the electromagnetic spectrum. The high frequency interference fringes observed in the infrared (IR) part of the spectra originate from the multiple reflections in ~ 0.15 mm glass substrates.

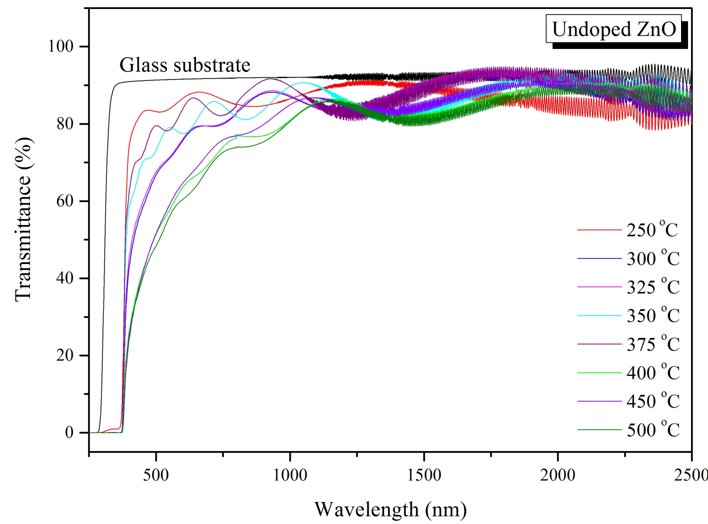

(a)

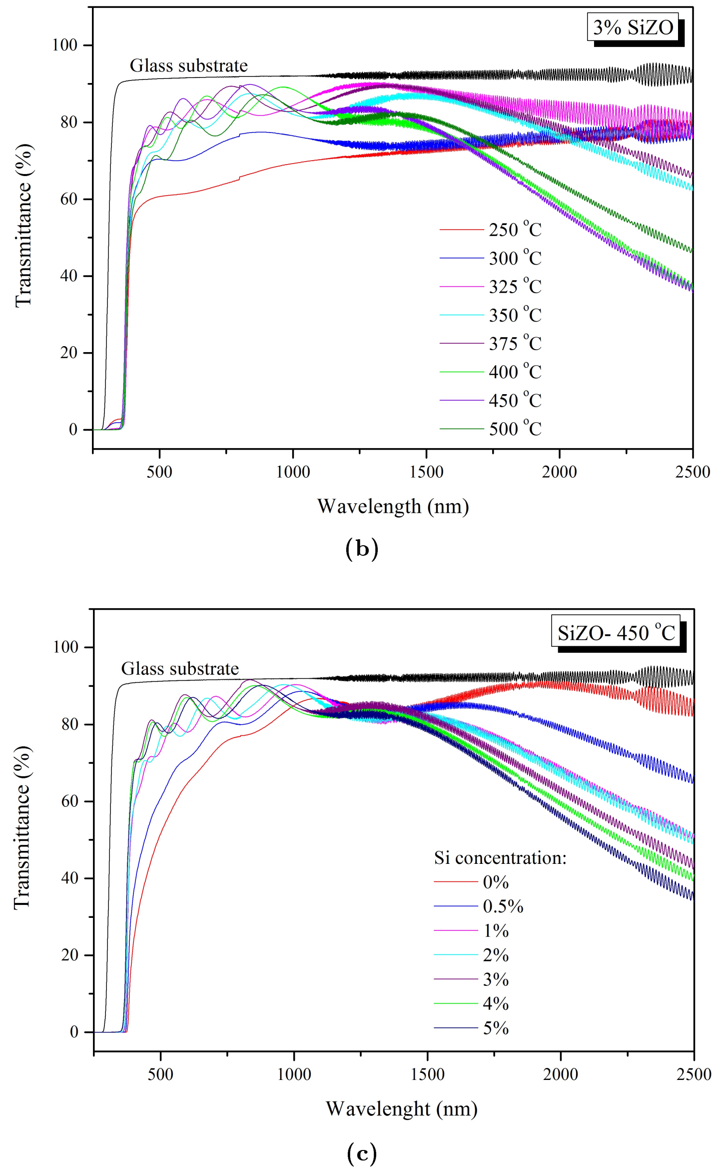

Figure 4.11: Optical transmittance spectra of (a) undoped ZnO and (b) 3% SiZO films deposited at different temperatures, and (c) SiZO films with different Si concentration deposited at 450 °C

As seen in Figure 4.11 (b) and (c), with increasing deposition temperature and doping concentration, SiZO thin films exhibit a decrease in IR transmittance. According to Drude's theory the optical properties in the near-infrared (NIR) are closely linked to the properties of free carriers in the material. [188] A significant decrease in transmittance observed in

the infrared region is associated with the plasma reflectivity of free carriers (Equation 1.9). This is also called Plasmon Resonance effect. The plasma edge for samples with $n < 1 \times 10^{20}$ cm^{-3} usually lies at wavelengths longer than the wavelength range of these measurements. High electron concentration ($n > 1 \times 10^{20}$ cm^{-3}) and low electron effective mass, therefore, lead to the observed increase in the infrared reflectivity. However, in the visible region the SiZO thin films are still highly transparent.

A blue shift in the plasma edge with increasing deposition temperature and Si doping level is consistent with an increase in free carrier concentration in the films. The sharp fundamental absorption edge at about 380 nm observed for all of the films arises from the intrinsic band gap transitions in ZnO. With increasing carrier concentration in the films a blue shift of the onset of the interband absorption edge is observed due to the Burstein-Moss effect.

Figure 4.12 shows the optical band gaps (E_g) of undoped ZnO and SiZO thin films, calculated from the transmittance spectra using the Tauc relation (Equation 2.17) and the method described in the Section 2.4 of the Experimental Chapter.

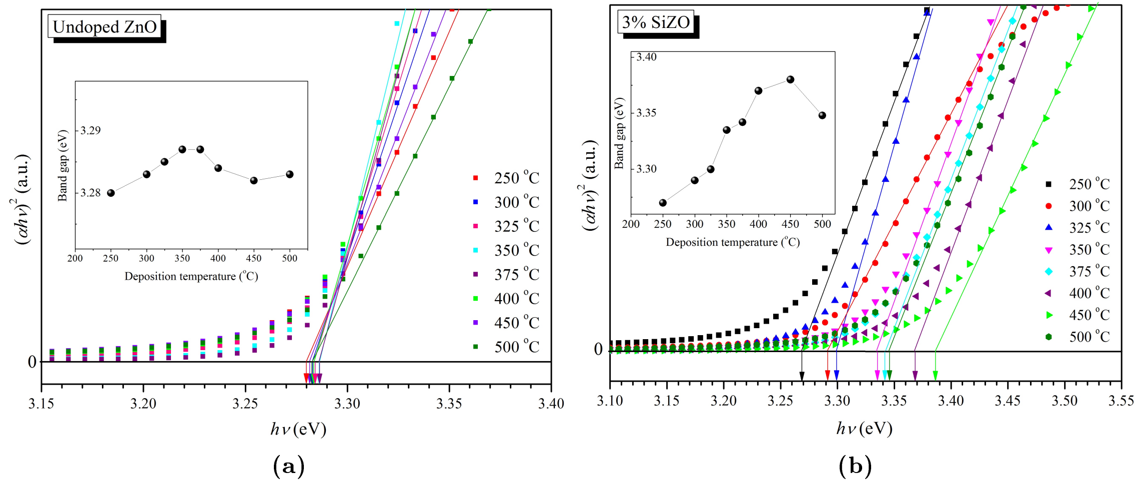

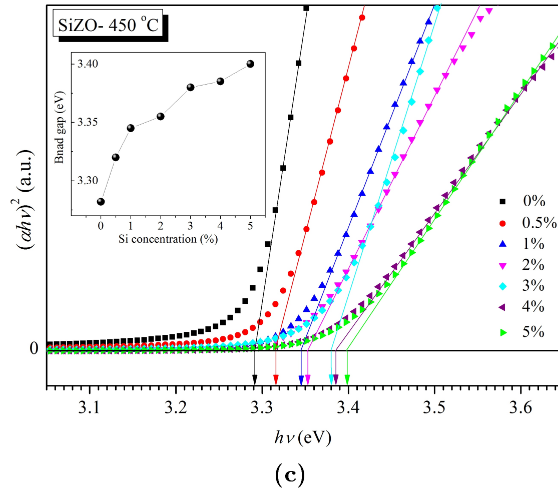

(c)

Figure 4.12: Plot of $(\alpha h\nu)^2$ as a function of photon energy, $h\nu$, for (a) ZnO and (b) 3% SiZO thin films deposited at different temperatures, and (c) SiZO thin films with different Si concentration deposited at 450 °C. Insets show the variation of the derived ZnO and SiZO band gap as a function of deposition temperature and Si concentration

The observed widening of the band gap in SiZO thin films with increasing deposition temperature and Si doping level (insets in Figure 4.12) correlates well with the variations in carrier concentration values determined for both series of thin films, which will be discussed in more detail in Section 4.3.4. The optical band gap of undoped ZnO thin films is almost independent of deposition temperature and is in the range of 3.284 ± 0.004 eV, implying that the carrier concentration in these films is not high enough to cause a Burstein-Moss shift in ZnO band gap and that the Fermi level is located within the band gap. [273]

4.3.4 Electrical transport properties of ZnO and SiZO thin films

The room temperature electrical properties of undoped and Si-doped ZnO thin films as a function of deposition temperature and Si concentration are shown in Figures 4.13 and 4.14, respectively. Increasing deposition temperature induces a steep rise in both carrier concentration and carrier mobility, which occurs for both undoped and SiZO thin films. The increase in electron concentration for undoped films deposited in the range of 250 - 350 °C (Figure 4.13) can be attributed to the higher concentration of intrinsic donor defects i.e.

oxygen vacancies or zinc interstitial atoms generated at the higher deposition temperatures.

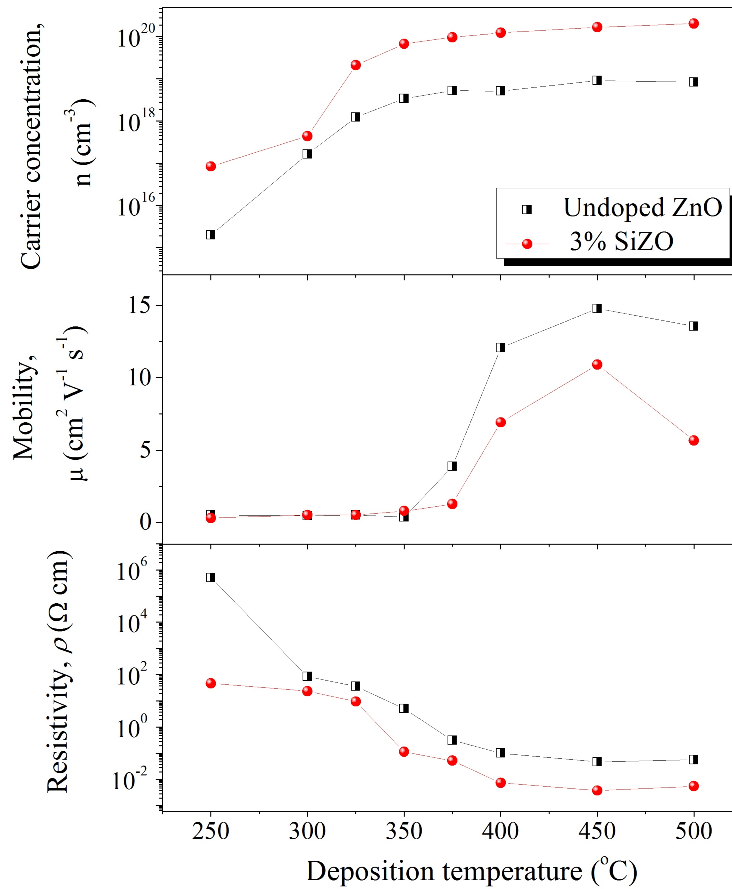

Figure 4.13: Room-temperature variations of electron concentration (n), mobility (μ), and electrical resistivity (ρ) of pure ZnO and 3% SiZO thin films as a function of deposition temperature

Significant changes in particle orientation and morphology of the films as a function of deposition temperature observed above in AFM and SEM images should also influence significantly the electrical transport in the films. It can be proposed that low carrier mobilities in both undoped ZnO and SiZO films deposited at temperatures below 350 °C are caused by a hindered carrier transport across the grain boundaries and poor electrical contacts between the wedge-like particles (Figure 4.10 (a)). A steep increase in carrier mobility at 350 - 450 °C (Figure 4.13) coincides with a rise in the intensity of (002) reflection in XRD spectra (Figure 4.3). The enhanced alignment of particles with c-axis oriented

perpendicular to the substrate surface is also clearly visible in SEM images (Figure 4.10 (c)) and can lead to improved intra-particle electrical contacts and increased mobility for films deposited at temperatures above 350 °C. Importantly, over the whole range of deposition temperatures studied, the carrier concentration in SiZO films remains more than an order of magnitude larger than that in undoped ZnO films. This fact, as well as a rise in electron density with increasing Si content in thin films deposited at 450 °C (Figure 4.14), strongly suggests that in the ZnO thin films grown by spray pyrolysis, Si acts as an effective n-type dopant, presumably due to the substitution of Si for Zn in the crystal structure. Effective Si doping results in carrier concentration of 1.7×10^{20} cm^{-3} and electrical resistivity of 3.7×10^{-3} Ω cm for 3% SiZO thin films obtained at 450 °C. Importantly, SiZO films deposited at this temperature demonstrate a lower electrical resistivity and higher carrier concentration in comparison with 3% Al-doped ZnO films prepared by spray pyrolysis at 475 °C. [274] A drop in carrier mobility for 3% SiZO films deposited at 500 °C (Figure 4.13) might be caused by a possible formation and segregation of low concentration of small clusters of a Zn_2SiO_4 or SiO_2 phases, which act as additional scattering centres for charge carriers.

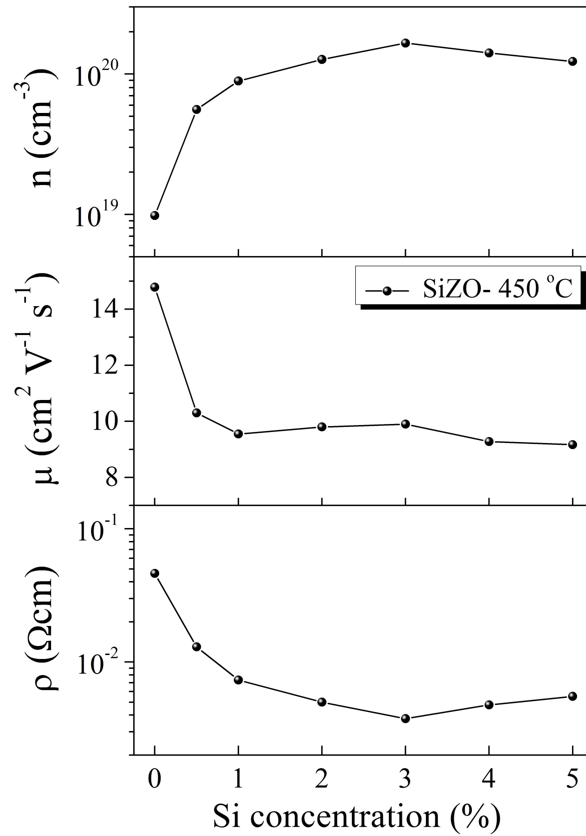

Figure 4.14: Variations in electron concentration (n), mobility (μ), and electrical resistivity (ρ) of SiZO thin films deposited at 450 °C as a function of Si dopant concentration

It is seen in Figure 4.14 that the carrier concentration in the SiZO films reaches a maximum value at around 2 - 3% Si indicating that above this concentration, the addition of more Si atoms does not contribute to the generation of mobile charge carriers. This limiting behaviour corresponds well to that reported for other efficient n-type dopants in ZnO films. [275] Solid solubility limit of Si in the host (ZnO) matrix might be a possible cause of the this observed limiting behaviour.

4.4 The conduction mechanism and the insulator-conductor transition in ZnO, SiZO and FSZO polycrystalline thin films

Oxides of the chemical elements of the periodic table show the most diverse range of electrical behaviour of any class of materials. They include some of the very best insulators, other highly conducting, genuinely metallic conductors, and highest transition-temperature superconductors (Figure 4.15). [276] However, there are many examples in nature where metals can be transformed into highly resistive insulators, and there are many cases where high resistivity materials transition into the metallic state. [277–280]

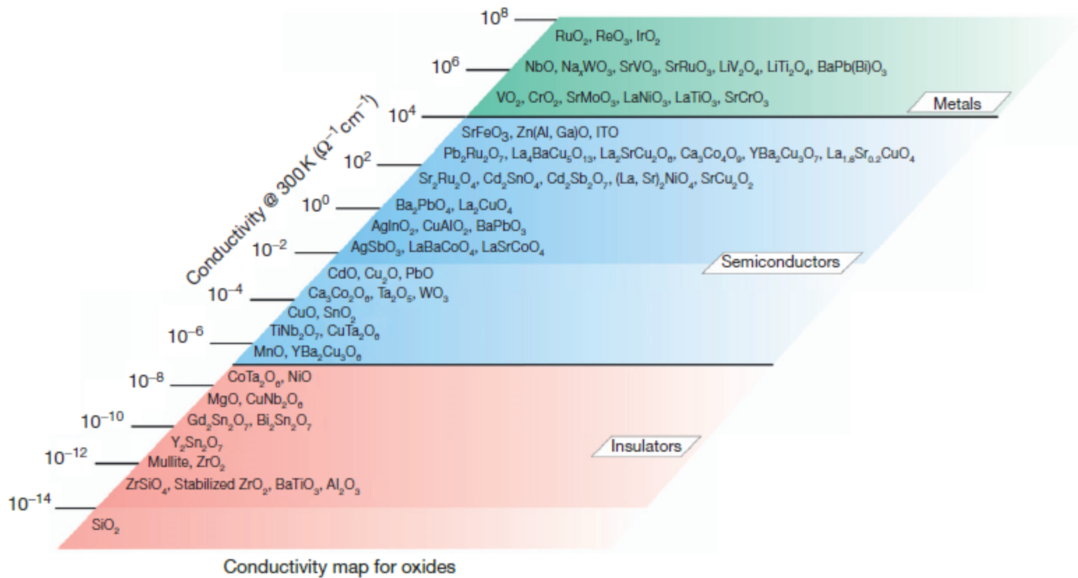

Figure 4.15: The room temperature electrical conductivities of oxides (adapted from [276])

In order to understand semiconductor-metallic state transition in TCOs, it is important to define the ways in which electricity can flow in n-type doped ZnO polycrystalline thin films and different conduction mechanism which can affect the electronic transport in these types of semiconductor materials. Several parameters such as the impurity (dopant) level

concentration and temperature can change the conduction mechanisms. [281] Not taking into account of the role of grain boundaries in electronic transport through the sample, in general, two different conduction mechanisms of the charge carrier transport can be considered; (1) The first conduction process occurs when temperature is high enough to thermally excite the carriers from impurity states into the conduction band of the host (ZnO). In this mechanism, conductivity is approximately proportional to the impurity concentration, therefore, If donor-to-conduction band excitation is the dominant conduction process, a substantial change in n with temperature should be observed. (2) The second mechanism happens when the temperature is low and free carriers can not be thermally excited into the conduction band, and electronic transport arises only from conduction within an impurity band, due to the wavefunction overlap between impurities. This process enables carriers to quantum-mechanically tunnel from an occupied to an energetically similar unoccupied impurity centre. These two processes are characterised by activation energies E_1 and E_2, respectively. Figure 4.16 shows a schematic representation of the stated energy level structure in n-doped ZnO.

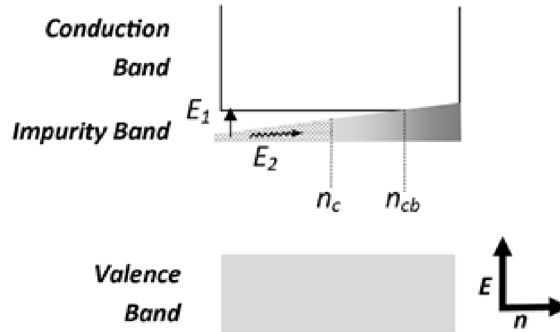

Figure 4.16: Schematic of impurity band conduction in ZnO at various carrier concentrations in the absence of grain boundaries. E_1 and E_2 are the average energy required for thermal excitation of an electron from the impurity band into the conduction band, and the activation energy associated with electron hopping in an impurity band, respectively (adapted from [281])

Since n-type doped ZnO thin films are polycrystalline, grain boundaries between and within individual crystallites can also strongly influence their overall electronic properties.

The grain boundary scattering in polycrystalline semiconductor thin films has often been analysed using a charge-trapping model. [205, 282] This model assumes that the film consists of small grains joined together by grain boundaries with a small thickness. Due to incomplete atomic bonding, grain boundaries typically contain a high density of defects that can also trap impurity atoms, oxygen and hydroxide groups. These acceptor impurity states trap free electrons from the bulk of the particles thus becoming electrically charged and creating a potential energy barrier for electron transport across grain boundaries. As a result, the electrical transport properties in polycrystalline films are often governed by carrier trapping at grain boundaries. The formation of potential barriers due to oxygen chemisorption on a single crystal ZnO surface has been confirmed experimentally. [283] It has been found that oxygen chemisorbed on the ZnO surface can cause the formation of strong surface depletion layers because oxygen atoms capture electrons from the bulk areas forming O^{2-} ions. The formation of the potential barriers due to impurity trapping might be particularly significant for thin films prepared by solution-based routes which could result in a high concentration of hydroxide groups at grain boundaries, thus increasing the electrical resistance of grain boundary regions. The electrical transport across such insulating grain boundaries can occur either by thermionic emission (TE) due to carriers with energy sufficiently high to surmount the potential barrier of height V_b, or by quantum-mechanical tunnelling (T) through the barrier for carriers with energy much less than the barrier height (Figure 4.17 (a)). Of these two conduction mechanisms, only thermionic emission can give rise to an activated temperature dependence of Hall mobility.

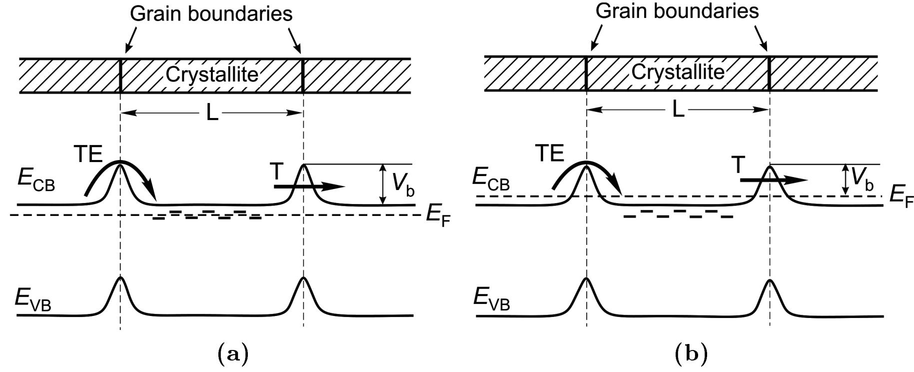

Figure 4.17: Schematic band diagram of (a) a polycrystalline n-type doped semiconductor and (b) a degenerate n-type semiconductor (adapted from [281])

The potential energy barriers can reduce electron mobility, as electrons with energies less than V_b are confined to the potential barriers and therefore, can not take part in charge transport. By increasing carrier concentration, Fermi level shifts to higher energies and into the conduction band. As a result, the height of the energy barriers reduces, and more electron can move across the barriers (Figure 4.17 (b)).

As mentioned earlier, at low temperatures, the critical carrier concentration for a non-metallic to metallic impurity conduction transition, depends on overlap of wavefunctions of impurity states. Mott established the idea that at high impurity densities, overlapping of the impurity wavefunctions occurs to such an extent that free carriers become completely delocalised within the impurity band. The Mott criterion [284] describes the critical carrier concentration for non-metallic to metallic transition as:

$$n_c^{1/3} a_H^* \approx 0.26 \tag{4.3}$$

where n_c is the critical carrier density for the metal-insulator transition (MIT) transition to occur, [285] and a_H^* is the effective Bohr radius of the isolated impurity state at low concentrations, ranging from approximately 1.4 nm for undoped ZnO to 0.67 nm for Al or Si doped ZnO, which correspond to an n_c between 6.4×10^{18} cm^{-3} and 6.0×10^{19} cm^{-3},

respectively. [286, 287] At higher carrier concentrations, n_{cb}, the impurity band which is metallic now, merges with the host conduction band (Figure 4.16), and as a result, the Fermi level shifts to above the conduction band edge and the system will show a metallic-type conduction. $n_{cb} \approx 3n_c$ for a prototypical MIT system such as phosphorous-doped silicon. [288] Using the Mott criterion, Edwards and Sienko demonstrated that the MIT locations of various set of TCOs, including doped ZnO systems, range from $n = 10^{18}$ to 10^{20} cm^{-3}. [279]

The electrical transport properties of undoped ZnO, SiZO films with different Si concentration, and 3%Si - 30%F FSZO film deposited at 450 °C are presented as a function of measurement temperature in Figure 4.18 (variable temperature Hall effect measurement of FSZO thin film was kindly carried out by Alex Vai). In general, samples show a decrease in resistivity with increasing temperature, and this change in resistivity is larger for films with lower carrier concentration. For all of the films, the carrier concentration remains practically constant and is independent of temperature across the entire temperature range studied, indicating that the films are degenerate semiconductors and the Fermi energy is above the bottom of conduction band. Instead, we found that the resistivity change at higher temperatures is driven mostly by a change in mobility. This suggests that that another factor - namely, the effect of grain boundaries - must also be considered. The invariance of n with temperature has previously been taken as a strong indication that an impurity band formed from shallow donor states has now merged with the host (ZnO) conduction band. [289] The films with room temperature carrier concentrations of about 10^{19} cm^{-3} and lower display clear thermally-activated behaviour of n in the higher temperature ranges. These results are in agreement with the critical electron concentration value (n_c) for metal-insulator transition (MIT) obtained using the Mott criterion. The calculated n_c value of 6.4×10^{18} cm^{-3} implies that all undoped ZnO films deposited at temperatures below 450 °C (black line+symbol plot in Figure 4.13) are on the insulating side of the transition. This conclusion also agrees with optical measurements showing a

constant optical band gap value in undoped ZnO films. On the other hand, all of the films presented in Figure 4.18 should be on the metallic side of MIT.

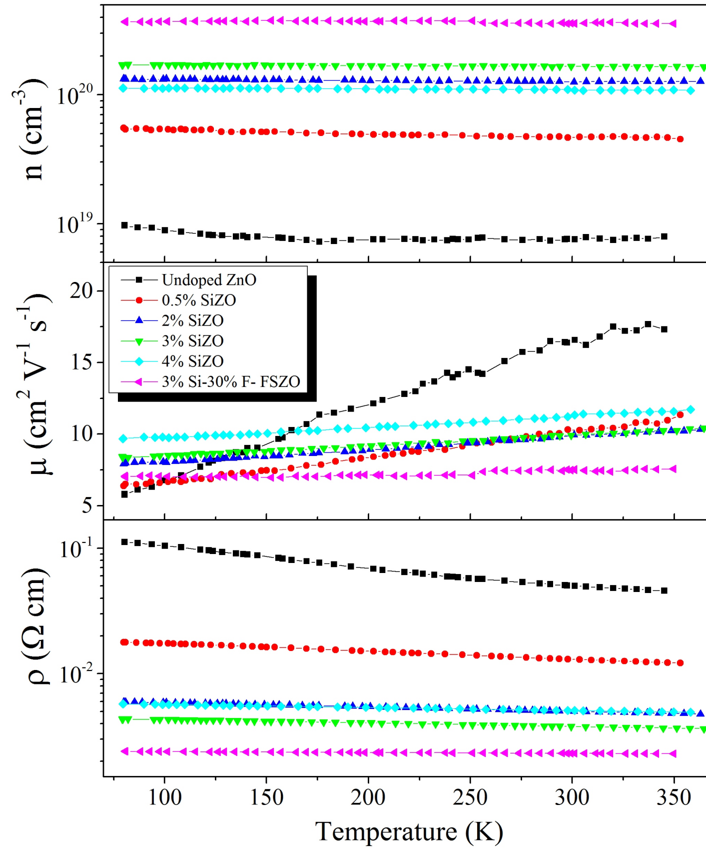

Figure 4.18: Temperature dependence of Hall carrier concentration (n), mobility (μ), and resistivity (ρ) of undoped ZnO, SiZO, and FSZO thin films with different doping levels deposited at 450 °C

As seen in Figure 4.18 the measured Hall carrier mobility at room temperature is around 16.0 cm^2 V^{-1} s^{-1} for the lowest carrier concentration film (undoped ZnO), and initially decreases sharply as the carrier concentration is increased, and finally levelling in the range of 6 - 10 cm^2 V^{-1} s^{-1} for films with $n \geq 1.0 \times 10^{19}$ cm^{-3}. The carrier mobility also displays a positive temperature dependence that becomes less pronounced with increasing carrier concentration. Such behaviour is indicative of an additional thermally-activated electrical conduction process present in the films. The weaker temperature dependence of mobil-

ity at low temperatures which has been observed in many systems has been attributed to the dominant effect of thermally-assisted quantum mechanical tunnelling. [138, 205] A thermally-activated carrier mobility is often explained by either a hopping mechanism, percolation conduction, or grain boundary scattering. Conduction occurs by the “hopping” of electrons between localized impurity states, in a material with a low spatial density of impurities. A variable-range hopping mechanism is unlikely to dominate the carrier transport in the system since, for all samples, a well-defined Hall voltage was observed without the anomalous behaviour usually found in strongly disordered or amorphous materials with an electron mean free path below the Ioffe-Regel limit. [290] Ioffe and Regel argued that mean free path of the free carriers (l_e) can never become shorter than the interatomic spacing a, since at that point the concept of carrier velocity is lost. Therefore, electrical conduction has to break down when the mean free path of carriers approaches the interatomic distance. Similar arguments were later proposed by Mott (1972) and the notion of a minimum metallic conductivity compatible with a minimum mean free path $l_e = a$ became known as the Mott-Ioffe-Regel (MIR) limit. [291] A MIT will occur when $k_F \mathrm{l}_e \approx 1$ (the “Ioffe-Regel criterion”), where k_F is the Fermi wavenumber. When $k_F l_e \ll 1$, the electronic states are localized. Given that,

$$k_F l_e = \frac{h(3\pi^2)^{2/3}}{e^2 \rho n^{1/3}} \tag{4.4}$$

where n is the carrier concentration, ρ is the resistivity (at a given temperature), e is the electronic charge, the value of n that gives $k_F l_e = 1$ can be assigned as the approximate location of the MIT. Equation 4.4 is only valid at low temperatures.

The percolation conduction model often applied to amorphous and disordered conductors also fails to explain the observed trend in carrier mobility as a function of electron density. In the percolation conduction, the carrier mobility should increase with increasing carrier concentration, [292] but such a variation is not observed in these SiZO and FSZO films (Figure 4.18). This suggests that thermally-activated Hall mobility in SiZO and FSZO films can be attributed to grain boundary scattering, as noted earlier. It is often

assumed that grain boundaries do not disturb the transport of free carriers in polycrystalline materials with a carrier concentration above 10^{19} cm^{-3}, because the mean free path of carriers in such systems is much smaller that the crystallite size. However, it has been found that grain boundary scattering of free carriers can have a pronounced effect even in heavily doped (degenerate) microcrystalline ZnO films with carrier concentration as high as 10^{21} cm^{-3}. [196, 293, 294] This has been confirmed by comparing the optical carrier mobility, which is a characteristic of intra-grain scattering, and Hall mobility limited by both intra-grain and grain boundary scattering processes.

Under the conditions that grain interior mobility is much larger than mobility across grain boundaries, the thermally activated Hall mobility, μ_H, for a degenerate semiconductor, due to thermionic emission over the grain boundary can be expressed as: [295]

$$\mu_H = LB \exp\left(-\frac{V_a}{kT}\right) \tag{4.5}$$

where L is an effective grain size, and B is a material specific constant and given by:

$$B = e(\frac{1}{2\pi m_e^* kT})^{1/2} \tag{4.6}$$

m_e^* is the effective electron mass, k is the Boltzmann constant, and V_a is the activation energy related to the grain boundary barrier, defined as $V_a = V_b - (E_F - E_c)$, where V_b is the potential barrier height at grain boundaries and $E_F - E_c$ is the energy separation between the Fermi level and the bottom of the conduction band for the material inside the particles. According to Equation 4.5, a plot of $ln(\mu_H T^{1/2})$ values against $1/T$ should yield a line with slope and intercept from which the parameters V_a and L can be extracted, respectively. Using experimental Hall mobility data presented in Figure 4.18, the room temperature activation energy V_a obtained by plotting $\ln(\mu_H T^{1/2})$ values against $1/T$ ranges and fitting the linear part of the curves for the gradient of room temperature μ_H data point, as shown in Figure 4.19. Only data for T $>$ 160 K was used, because data from below this threshold

show non-linear behaviour (Figure 4.19) which could indicate a transition to a regime with another conduction mechanism, most likely, the thermally-assisted electron tunnelling that dominates charge transport across grain boundaries at low temperatures. [205, 296]

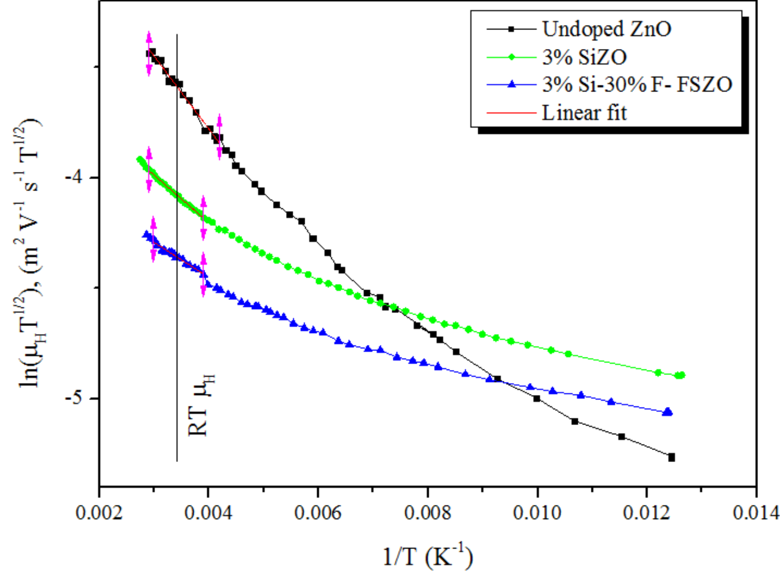

Figure 4.19: Plot of $\ln(\mu_H T^{1/2})$ values against $1/T$ for undoped ZnO, 3% SiZO, and 3%Si - 30%F FSZO films. V_a and L values can be extracted from slope and intercepts of the curves, respectively

The activation energy, V_a, derived from Equation 4.5 is decreasing from 28.4 meV for undoped ZnO films to 18.5 meV for 3% SiZO, and 13.7 meV for 3%Si - 30%F FSZO films deposited at 450 °C. These activation energies are comparable to kT at room temperature (kT_{300K} =25 meV), indicating that grain boundary scattering might play a significant role in electron charge transport. The effective grain size, L, derived from Equation 4.5, decreases as the carrier concentration increases, accounting for the decrease in room temperature mobility in these films as a function of n. It is also seen from Figure 4.18 that the temperature dependence of carrier mobility becomes weaker with increasing carrier concentration in the films. This indicates that at high doping levels the grain boundary potential barrier becomes less significant as a result of a decreasing depletion layer width due to the entry of Fermi level energy into the conduction band.

If the height of the potential barrier at grain boundaries is high and the depletion width is very narrow, thermally-assisted quantum-mechanical tunnelling of electrons through the barriers can become the main charge transport mechanism. The width of the depletion region, *d,* at grain boundaries can be estimated using: [297]

$$d = \left(\frac{2\varepsilon_0 \varepsilon_{ZnO} V_b}{eN_D}\right)^{1/2} \tag{4.7}$$

where N_D is the donor concentration in the depletion layer, ε_0 is the permittivity of free space and ε_{ZnO} = 8.5 is the static dielectric constant of ZnO. [298] The potential barrier height V_b can be estimated using obtained V_a values and the calculated Burstein-Moss shift $\triangle E_{BM}$ in degenerate semiconductors with parabolic bands:

$$\triangle E_{BM} = E_F - E_c = \frac{h^2}{8m_e^*}\left(\frac{3n}{\pi}\right)^{2/3} \tag{4.8}$$

where h is the Planck constant and m_e^* is the electron effective mass. Taking into account the dependence of m_e^* on carrier concentration in doped ZnO films, [299] and assuming that the charge density N_D in the depletion layer is equal to the bulk carrier concentration, the estimated depletion layer width is around 3.1 nm and 1.3 nm for undoped and 3% SiZO films deposited at 450 °C, respectively. A significant decrease in the depletion layer width with rising carrier concentration facilitates the tunnelling current between grains, which becomes a dominant conduction mechanism in heavily doped ZnO films. The width and height of the depletion layer at grain boundaries in solution-processed thin films is affected by the preparation conditions, in particular, by the deposition temperature.

As seen in Figure 4.13, the electrical transport in films prepared at temperatures below 400 °C is significantly hindered, presumably as a result of a large potential barrier formed at grain boundaries due to a significant amount of chemisorbed oxygen and hydroxide groups. With increasing deposition temperature, the density of interface defects decreases due to desorption of the electrically active oxygen-based species from the inter-grain surface during

thin film growth, thus reducing the potential barrier height and width. This model would be consistent with an observed rise in electron mobility with increasing deposition temperature from 350 °C to 450 °C. It is clear that the electrical transport in polycrystalline ZnO films is significantly affected by the film morphology, grain size and grain barrier trap densities of interfacial defects and chemisorbed impurities. The electron mobility in SiZO and FSZO thin films prepared by spray pyrolysis technique is limited by both thermionic emission and electron tunnelling across the grain boundaries. Further efforts are required to study the effect of inter-grain scattering on electron mobility of polycrystalline ZnO films in order to improve their electrical transport performance.

4.5 Conclusions

Highly conducting and optically transparent Si-doped ZnO thin films were prepared on glass substrates at a temperature of 450 °C using a low-cost spray pyrolysis technique. The films deposited at temperatures lower than 350 °C have the (100) preferred crystallographic orientation, whereas films prepared at higher deposition temperatures have the (002) preferred orientation and show flake-like structure which we propose to be responsible for the lower electrical resistivity of the films. At optimum doping concentration of 3% Si and a deposition temperature of 450 °C, the thin films exhibit an electrical resistivity of 3.7×10^{-3} Ω cm, a carrier concentration of 1.7×10^{20} cm^{-3}, and an optical transmittance of around 80 - 85% in the visible region. The temperature dependence of the electrical transport properties of undoped ZnO, SiZO, and FSZO thin films have been measured for the first time over the range of 77 - 350 K. A model of grain boundary scattering is invoked to explain the thermally-activated electron mobility. This work illustrates the great potential of spray pyrolysis for the fabrication of good-quality TCO thin films. The studied SiZO thin films have revealed excellent performance levels in both optical transparency and electrical conductivity.

Chapter 5

Preparation and Characterisation of Fluorine-doped ZnO (FZO) and Chlorine-doped ZnO (ZnO:Cl) Thin Films

5.1 Introduction and overview

Among recent investigations of suitable dopants for ZnO, most researchers have used impurity-doped ZnO transparent conducting thin films with metal cation dopants, while there have been comparatively few studies on the optoelectronic properties of ZnO doped with halogen anions (i.e. F^-, Cl^-). In F-doped ZnO (ZnO:F or FZO) films, as compared with metallic-cation-doped ZnO films, electronic perturbation is largely confined to the filled valence band when F^- is substituted for O^{2-}. Thus, as compared to more typical cation doping, the scattering of conduction electrons is reduced, leading to high mobility and low resistivity for ZnO:F films. [151] F^- ions are also about the same size as O^{2-} ions ($r_{F^-} = 1.31$ Å and $r_{O^{2-}} = 1.38$ Å [150]), and thus F would be predicted to substitute

readily for O^{2-} with minimal lattice distortion, maintaining high mobility. [223] Other potential advantages of FZO films include the reduction in the number of O_s^{2-}/O_s^{-} surface states, leading to increase in carrier mobility, [224] resulting in a higher doping efficiency of the F dopant than for a metallic cation dopant in ZnO for the optimisation of electrical conductivity. [300] At present, the best reported result regarding fluorine doping of ZnO was resistivity as low as $\rho = 4.0 \times 10^{-4}$ Ω cm. [151]

Even though doping with F in ZnO films is difficult, the fabrication of FZO films has been attempted using several deposition techniques including chemical spray pyrolysis, [301–304] sol-gel spin-coating, [148] chemical vapour deposition (CVD), [151] electron beam evaporation, [224] pulsed laser deposition (PLD), [153] atomic layer deposition (ALD), [152] and radio frequency (RF) magnetron sputtering. [305] Most investigations into anionic doping of ZnO films using fabrication method relying on solution-based spray pyrolysis result in resistivity values ranging from 10^{-1} to 10^{-2} Ω cm. Sanchez-Juarez *et al.* reported on the role of [F] / [Zn] ratio in the starting solution and substrate temperature on the structural and optical properties of ZnO thin films prepared using chemical spray pyrolysis technique. [301] They used ammonium fluoride (NH_4F) as fluorine precursor. Their thin films deposited at substrate temperature of 425 °C, showed electrical resistivity of 1.1×10^{-1} Ω cm, Hall mobility of ~ 10 cm^2 V^{-1} s^{-1} and effective carrier concentration of ~ 4.0×10^{19} cm^{-3}. Olvera *et al.* studied the effects of fluorine concentration, substrate temperature and acidity of the spray solution on structural, electrical and optical properties of ZnO films. [304, 306] They used zinc acetylacetonate and ammonium fluoride in the precursor solution. They also observed that ageing of the solution had significant effect on the resistivity of the resulting thin films. Under the optimum conditions, resistivity of 1.5×10^{-2} Ω cm, mobility of 6.0 cm^2 V^{-1} s^{-1} and carrier concentration of 2.0×10^{19} cm^{-3} were obtained. Maldonado *et al.* studied the effect of aged and fresh solution of precursors on the physical properties of the FZO films. [307] They observed that aged solutions could produce less resistive films. The lowest resistivity values of as-deposited films prepared at 500 °C using

a starting solution aged for two days, were 1.4×10^{-2} and 1.8×10^{-2} Ω cm for of zinc acetate and zinc acetylacetonate precursors, respectively.

The chemical spray method allows a relatively easy fabrication of FZO films, but the electrical properties of FZO films made using this method have been far from satisfactory. Therefore, F-doping of ZnO thin films deposited by chemical spray, has not attracted attention due to the fact that F^- incorporation into the host (ZnO) matrix is deficient and high resistivities are obtained. [308] There have been notable reports on FZO films fabricated using CVD and electron beam evaporation. [151, 224] Resistivity values are as low as 4×10^{-4} and 7.95×10^{-4} Ω cm and mobilities are as high as 40 and 46.2 cm^2 V^{-1} s^{-1} are found in the reports of Hu *et al.* and Xu *et al.*, respectively. A lowest resistivity of 1.87 $\times 10^{-3}$ Ω cm for ZnO thin films doped with 1.0 at.% fluorine when carrier concentration and mobility were 1.37×10^{20} cm^{-3} and 24.20 cm^2 V^{-1} s^{-1}, respectively, was reported by Choi *et al.* for FZO thin films deposited using ALD technique. [152] In spite of the low resistivity and high mobility of the FZO films deposited by the aforementioned techniques, the growth temperature was over 450 °C, and additional post-annealing was necessary.

Apart from studies where fluorine doping of ZnO was studied, doping of ZnO with other anion impurities substituting for oxygen has not been widely used despite a few promising reports identifying chlorine as a n-type doping element. [155–157] It is clear that one of the most important factors in doping is the ionic radius of the dopant atom; being larger or smaller than the substituted host anion radius, can cause various distortions of the lattice. Only few techniques such as metal-organic chemical vapour deposition (MOCVD) [155, 157] and electrodeposition [156] have been applied to deposit ZnO:Cl thin films. To the best of our knowledge, there are no data in the literature for intentional chlorine doping of ZnO using the spray pyrolysis technique. One of the first reports on properties of chlorine doping in spray pyrolysed ZnO thin films was demonstrated by Aranovich *et al.* and it was believed that Cl would act as n-type dopant. [59] They observed that when zinc acetate was used as precursor, resistivity value was higher than that of the sample prepared with $ZnCl_2$. They

attributed this difference as due to the possible doping with Cl in the film.

5.2 Experimental

Several series of fluorine and chlorine doped ZnO thin films of thickness of ~ 500 nm were prepared using the spray pyrolysis technique. A more detailed description of procedures for deposition of ZnO thin films using spray pyrolysis is available in Chapter 4. However, process parameters used in this chapter are discussed here for clarity.

The effect of the fluorine or chlorine doping was investigated by adding different amounts of ammonium fluoride (NH_4F, [F] / [Zn]= 5, 10, 15, 20, 30 and 40 mol%), or zinc chloride ($ZnCl_2$, [Cl] / [Zn] = 5, 10, and 20 mol%) to the zinc precursor solution, respectively.

NH_4F is an amphiprotic salt and on dissolving this salt in water containing solution the following dissociation reaction will happen: [309]

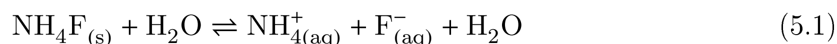

$$NH_4F_{(s)} + H_2O \rightleftharpoons NH^+_{4(aq)} + F^-_{(aq)} + H_2O \tag{5.1}$$

NH_4^+ can donate a proton to solution and F^- can accept a proton. Thus, the two following equilibria can happen, considering that the prediction in the following reactions is for the case of adding the NH_4F to pure water. If strong acid or strong base is also present, the acidity or basicity will be controlled by a limiting reagent condition and any resulting equilibrium:

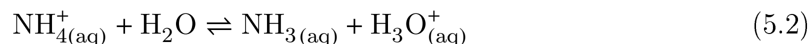

$$NH^+_{4(aq)} + H_2O \rightleftharpoons NH_{3\,(aq)} + H_3O^+_{(aq)} \tag{5.2}$$

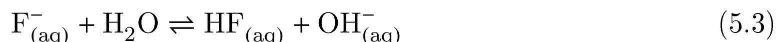

$$F^-_{(aq)} + H_2O \rightleftharpoons HF_{(aq)} + OH^-_{(aq)} \tag{5.3}$$

The K_a of NH_4^+ is 5.69×10^{-10} mol L^{-1} and the K_b of F^- is 1.47×10^{-11} mol L^{-1}. [310] Since $K_a > K_b$, the solution will be made more acidic by addition of NH_4F. Moreover, the precursor solution is slightly acidic as well (pH $\simeq$ 5.5) which will shift the equilibria 5.2

and 5.1 to the left in order to consume the excess amount of acid and NH_4^+, respectively. Consequently the concentration of F^- and HF will decrease, but trace amount of hydrogen fluoride (or hydrofluoric acid, HF) can still be released when ammonium fluoride (or any other fluoride-containing compounds) is combined with water. As HF can react with SiO_2, [311, 312] and glass contains SiO_2, in a different series of experiments, FZO thin films were deposited from precursor solutions prepared in plastic vials (FZO-P, P for plastic) and the data were compared with those deposited from solutions prepared in glass vials (FZO-G, G for glass).

The optical transmission spectra for F-doped and Cl-doped ZnO thin films were recorded at room temperature for wavelengths between 2500 and 200 nm using a PerkinElmer Lambda 19 UV-Vis-NIR spectrometer. The surface morphology of the films was characterised using a JEOL JSM-840F field emission scanning electron microscope at an accelerating voltage of 5 kV. Instrumental parameters for XRD and Hall effect measurements have been explained in Chapter 4.

5.3 Results and discussion

5.3.1 Structural and morphological properties

Figure 5.1 (a) and (b) show the X-ray diffraction patterns for F-doped ZnO thin films, deposited at 450 °C from precursor solutions made in glass vials (FZO-G) and plastic vials (FZO-P), respectively. All samples are polycrystalline. Under our experimental conditions, the preferred orientation of peaks was a mixture of (002) and (101). Some other reflections such as (102) and (103) are also observed with high intensities. No additional phases involving fluorine compounds were observed, even at high [F] / [Zn] content. The intensity of the (002) peak increased slightly with increasing F concentration in FZO-G samples, whereas, this peak is almost unaffected by variation in fluorine concentration in FZO-P samples. Generally, in ZnO thin films the crystal growth and change in the preferential

orientation between (100) and (002) is mainly influenced by deposition temperature or adding impurity atoms as also shown previously in Chapter 4. That an increase in F doping concentration leads to a (002) preferred orientation in ZnO films prepared using various techniques has been reported in the literature. [151, 313, 314] However, our results agree with the structural properties reported for ZnO thin films prepared by some similar deposition processes to spray pyrolysis. [146, 303]

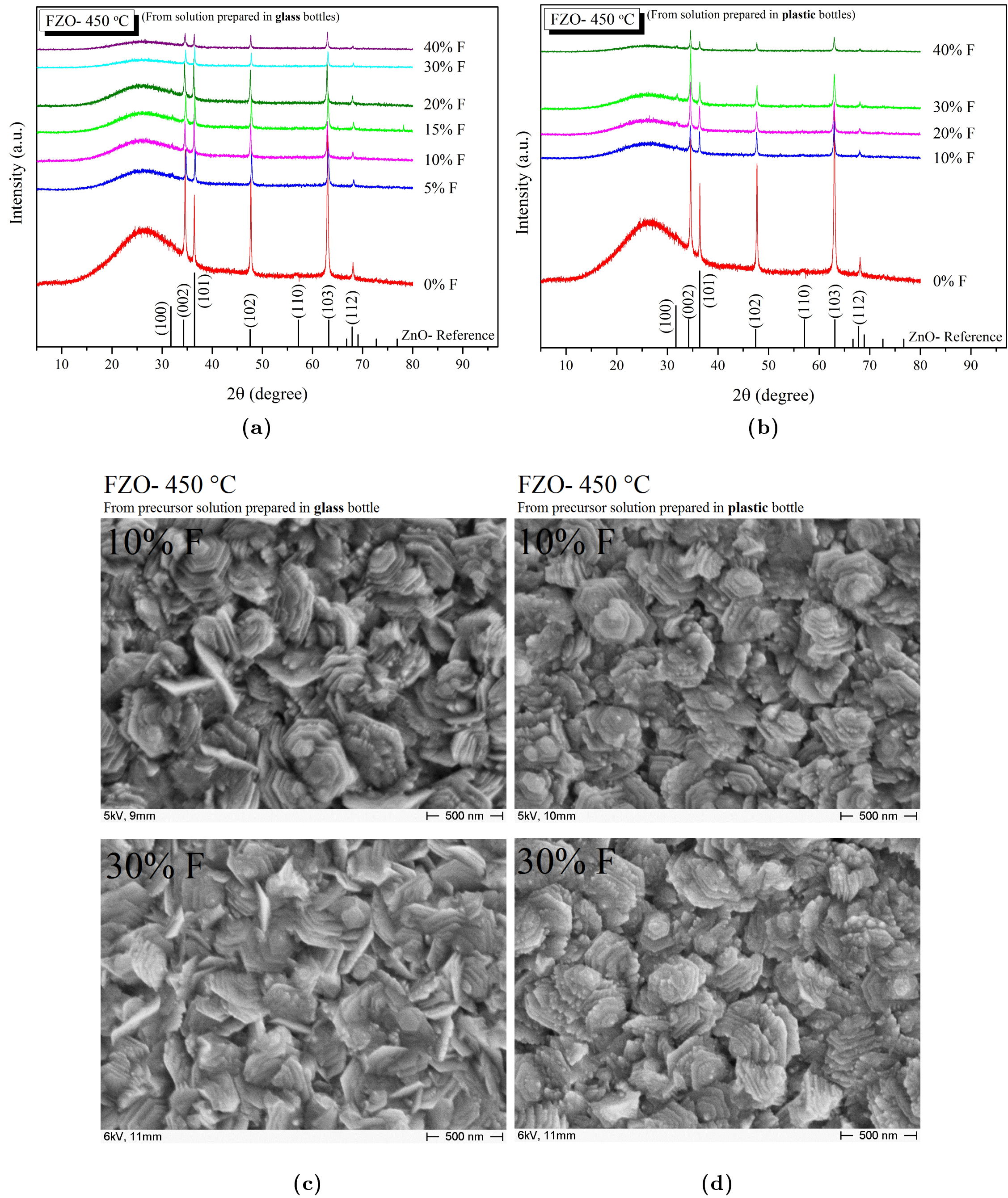

Figure 5.1: XRD patterns of undoped ZnO and FZO thin films with various F contents deposited at a growth temperature of 450 °C on glass substrates from precursor solution prepared (a) in glass vials and (b) in plastic vials. SEM micrographs of 10% and 30% FZO thin films deposited from precursor solution prepared (c) in glass vials and (d) in plastic vials

Figure 5.1 (c) and (d) show SEM images obtained for different FZO thin films. For undoped ZnO (as shown in Chapter 4, Figure 4.10 (c)), the surface morphology consists of hexagonal particles with a particle size of about 50 - 400 nm. In FZO-G films, low F content (~ 10%) in the sample produces no significant change of particle shape and size (Figure 5.1 (c)). Sample with high F content (~ 30%) present a slightly different surface morphology, still composed of hexagonal particles that are a little more randomly oriented on the surface. In FZO-P samples, particle morphology and shape are unchanged by increasing F concentration.

Figure 5.2 (a) depicts XRD patterns of ZnO:Cl samples deposited at 450 °C and with various Cl concentrations. The pure wurtzite structure is maintained for all ZnO:Cl samples grown on glass substrates independent of doping level. The films are highly textured with preferential orientation along the (101) plane. It is revealed from the XRD analysis that the basic crystal structure of ZnO film was modified by the addition of chlorine. Cl doping leads to a different preferred orientation than is seen in undoped films. It is clear from the XRD patterns that the intensity of the peak corresponding to the (100) plane increases gradually at higher chlorine concentrations. It may be noted that the (101) reflection is the most intense in a bulk powder pattern with fully random crystallites. Angappane *et al.* showed that ZnO films grown on Si (111) substrates using pulsed reactive laser ablation technique, were entirely (101) oriented, which is the high density crystal plane as shown in Figure 5.2 (d). [315] They also correlated the preferential growth along (101) plane to the presence of internal stress in the ZnO lattice. Lee *et al.* investigated the changes of crystallographic orientation and microstructural evolution of ZnO films deposited by RF magnetron sputtering. They showed that the (002) preferred orientation was significantly reduced as substrate temperature and/or oxygen partial pressure increased, and the films had rather mixed orientations. Also increasing film thickness changed the preferred orientation from (002) to (101). [316]

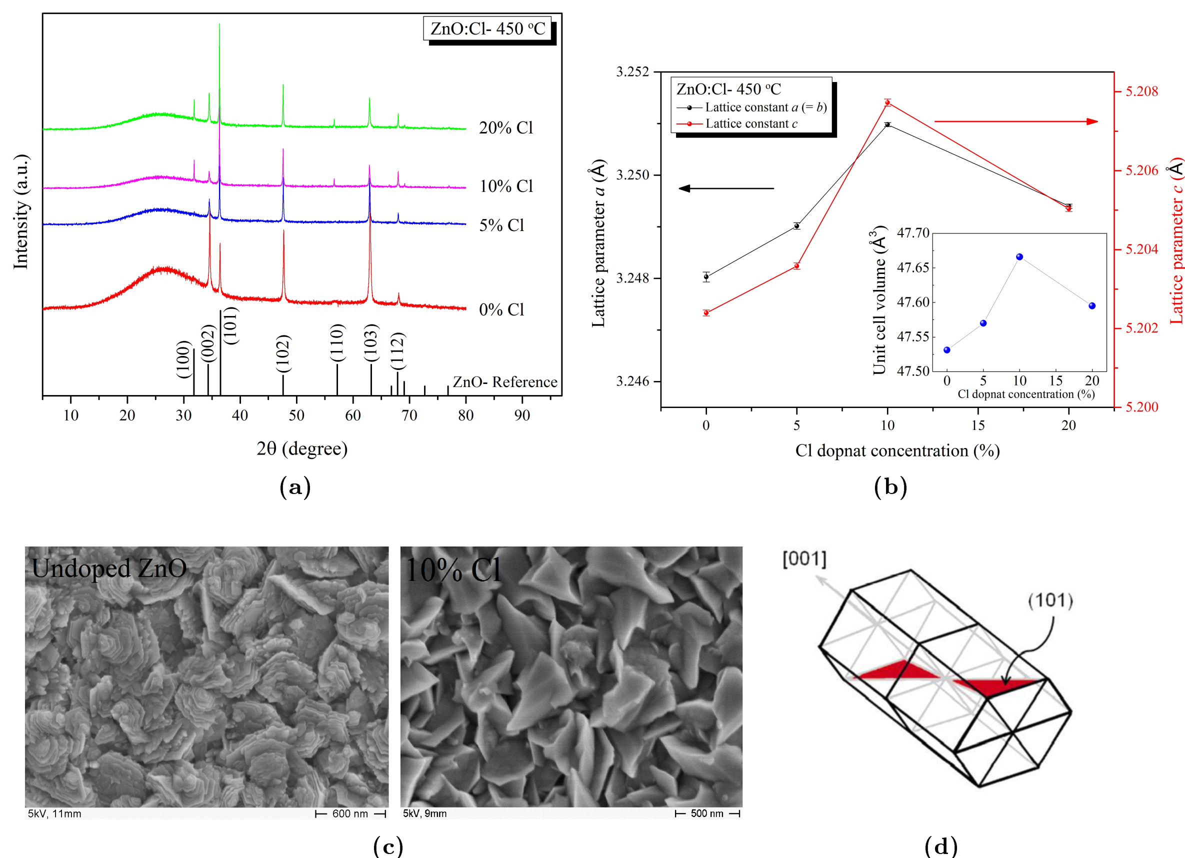

Figure 5.2: (a) XRD patterns of undoped ZnO and ZnO:Cl thin films with various Cl contents deposited at 450 °C, (b) variation in lattice parameters of ZnO:Cl thin films as a function of Cl concentration, (c) SEM micrograph of undoped ZnO and 10% ZnO:Cl thin films deposited at 450 °C and (d) ZnO unit cell showing the (101) plane (adapted from Angappane *et al.* [315])

The variation in lattice parameters of ZnO:Cl thin films as a function of Cl concentration was investigated. Results are shown in Figure 5.2 (b). Both the lattice constant $a = b$ and c found to be dependent on the Cl concentration, with a tendency to increase from 3.248 Å to about 3.251 Å, and from 5.202 Å to 5.208 Å with increasing Cl concentration from 0 to 10%, respectively. The unit cell volume for ZnO:Cl films follows the trend observed for the $a = b$ and c lattice constants and increases from 47.531 Å^3 at 0% Cl to 47.666 Å^3 at 10% Cl concentration. The modest expansion of the ZnO unit cell at Cl concentration of 10% can be attributed to increasing solubility of Cl in the ZnO matrix and substitution of O^{2-} ions in ZnO lattice by the fairly larger Cl^- ions (ionic radii of O^{2-} and Cl^- are 1.38

Å and 1.81 Å, respectively) during the formation of ZnO:Cl films. The Lattice constants $a = b$ and c, and cell volume were decreased with further increment of Cl concentration to 20%.

Grant *et al.* studied the reactivity of Cl_2 with the zinc-terminated ZnO (001) surface. Their results showed that chlorine, which is a strong electron acceptor and can act as a bonding modifier, adsorbed and formed an over-layer on the ZnO (001)-Zn substrates. [317] Zhang *et al.* proposed a growth mechanism for ZnO nanorods in solution with Cl^- ions. [318] They suggested that the common crystal habits in ZnO include a basal polar oxygen-zinc plane (001) and six symmetric non-polar (101) planes parallel to the c-axis. When negatively charged Cl^- ions are added to the solution, they selectively attach to the Zn-terminated surfaces ((002) plane). Therefore, the growth rate along the c-axis decreases while growth along the (101) planes is enhanced. Other anions, such as citrate ($C_6H_5O_7^{3-}$), are also shown to have such a structure-directing or templating effect, which allows fabrication of controlled microstructures and crystal orientations of materials. [319–321]

Figure 5.2 (c) clearly shows that the surface morphology of ZnO material significantly changes by the presence of chlorine. This is in good agreement with earlier observations from the structural analysis that chlorine doping altered the preferrential crystal growth of ZnO. The crystallographic orientation change from (002) to (101) with associated microstructural evolution, seems to be one of the processes that tends to relax the structural stress developed by Cl doping. However, the ZnO (101) surfaces assumed to be unstable and reactive towards organic solvents. [315]

5.3.2 Optical properties

Optical transmittance spectra were recorded in the wavelength range 250 nm to 2500 nm. Optical band gap were determined using the method described in Chapter 2. FZO-G thin films exhibited increased optical transmission in the visible region and band gap values

with increasing F concentration (Figure 5.3 (a) and (b)). However, in FZO-P thins films the transparency and band gap values are almost the same as undoped ZnO thin films. E_g values are in the range of 3.27 eV to 3.28 eV.

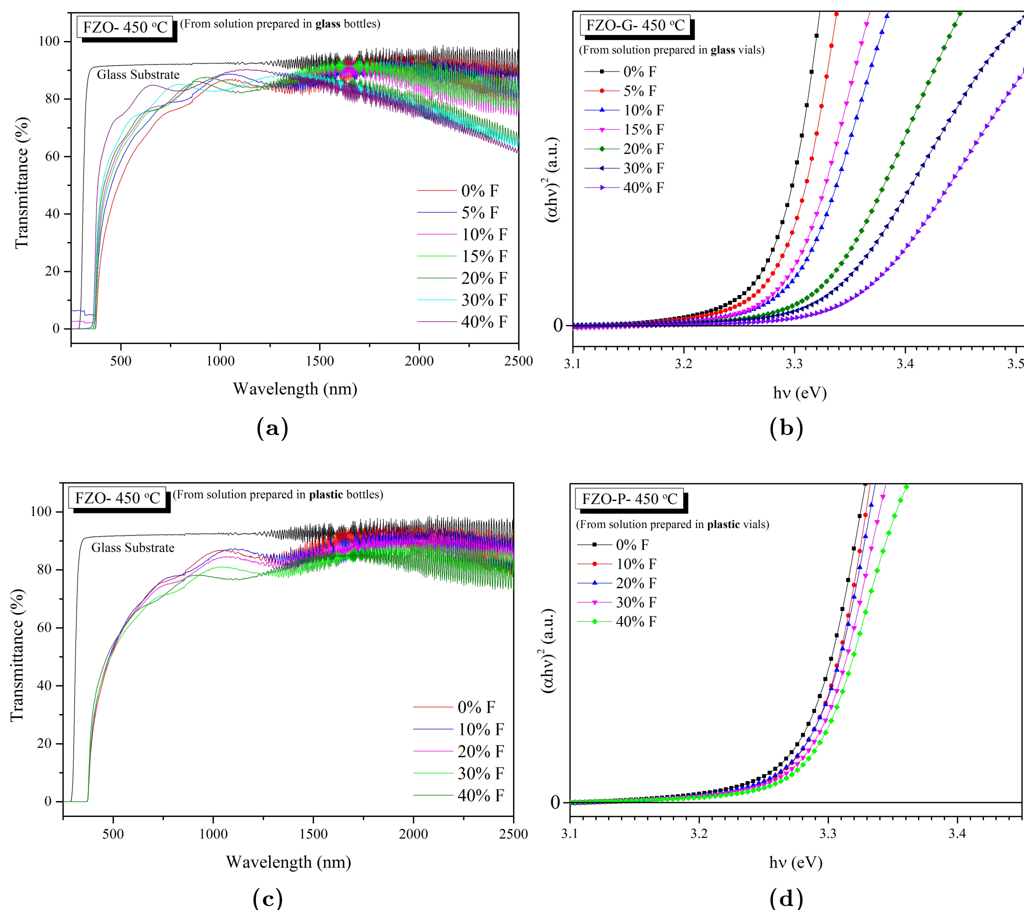

Figure 5.3: Optical transmittance spectra and band gap of FZO thin films deposited at 450 °C from precursor solutions prepared (a, b) in glass vials and (c, d) in plastic vial

It is clear from the Figure 5.4 (a) that visible transmittance decreases due to chlorine doping. The average transparency of ZnO:Cl thin films is very low, about 40 - 50% (uncorrected for glass substrate with transparency of about 92%), and the films had whitish appearance. The lower transmittance of ZnO:Cl samples, might be due to the reduction in the quality of surface of the films and higher scattering loss in the films. It is well known

that rough surfaces cause the light scattering, resulting in reduction of transmittance. This explains the low transmittance measured in films deposited with Cl. This is also consistent with the fact that ZnO:Cl films have a very different surface morphology than undoped ZnO. Band gap values (Figure 5.4 (b)) were nearly same as that of undoped films. The E_g values calculated were in the 3.27 - 3.28 eV range.

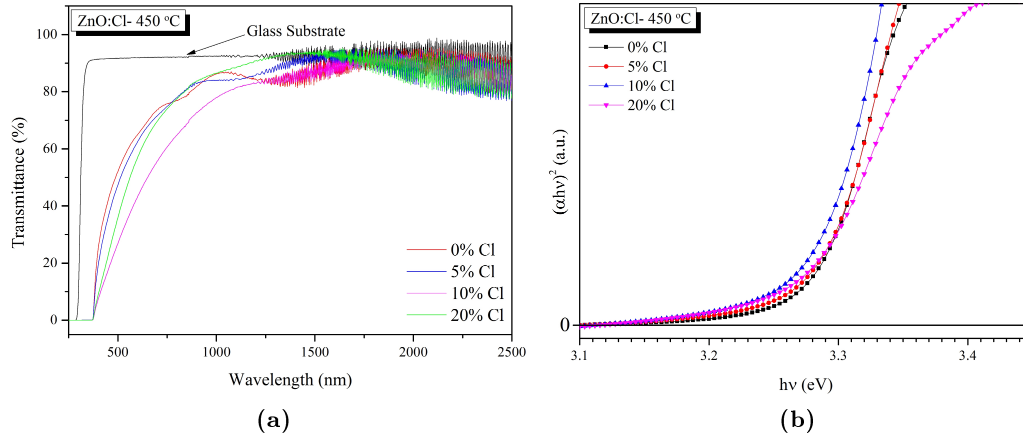

Figure 5.4: Optical transmittance spectra and band gap of ZnO:Cl thin films deposited at 450 °C

5.3.3 Electrical properties

It is important to note that the F and Cl concentrations values are nominal doping concentrations representing the concentrations in the starting spray solution. The real concentrations of the dopants in ZnO lattice are possibly much lower.

Electrical resistivity measurements were carried out at room temperature. The variation in electrical properties with doping concentration is given in Figure 5.5. It was found that resistivity of FZO-G samples (Figure 5.5 (a)) decreased with increasing F concentration in solution From 4.2×10^{-2} Ω cm at 0% F to 6.5×10^{-3} Ω cm at 40% F, whereas the resistivity of FZO-P samples remained almost unchanged with increasing F concentration. Borosilicate glass has chemical composition of about 80.6% SiO_2, 13% B_2O_3, 4% Na_2O and 2.3% Al_2O_3. The decreased resistivity of FZO-G samples might have resulted from

doping with other impurities such as Si or Al released into the spraying solution due to the reaction of HF with borosilicate glass. Although the experimental procedure for spraying solution preparation has not been clearly explained in the work of the other researchers, but the fact that aged the starting solutions enhance the characteristics of the ZnO thin films studied by Biswal *et al.* [308] might be explained by the etching effect of HF on glass vials. Results from FZO-P samples suggest that fluorine incorporation into ZnO thin films under the deposition condition used is not effective. It can be seen from Figure 5.5 (a) that the electrical properties of the films remains almost unaffected by increasing [F] / [Zn] ratio. This can be explained if it is considered that fluorine atoms do not substitute oxygen atoms, instead they probably form a compound such as ZnF_2 which is growing along with ZnO:F. As the concentration of NH_4F in the starting solution increases, a growth competition between ZnO and ZnF_2 might take place, due to the fact that the bonding energy of Zn−F (88 kcal mol^{-1}) is larger than that of the Zn−O bond (67.9 kcal mol^{-1}). [301] However, no extra crystalline phases involving fluoride compounds, such as ZnF_2, were observed in the XRD patterns of FZO-P thin films, even for the highest [F] / [Zn] contents.

The conductivity behaviour of FZO-P might be due to the fact that F atoms are not electrically active due the reaction residues, or considering the polycrystalline nature of the ZnO films, F containing compounds produced in the process might be located at grain boundaries or surfaces but not inside the crystallites. On the other hand, lack of F incorporation into the film, might be due to the high volatility of fluorine, particularly when solution is atomized on the hot substrate. [308]

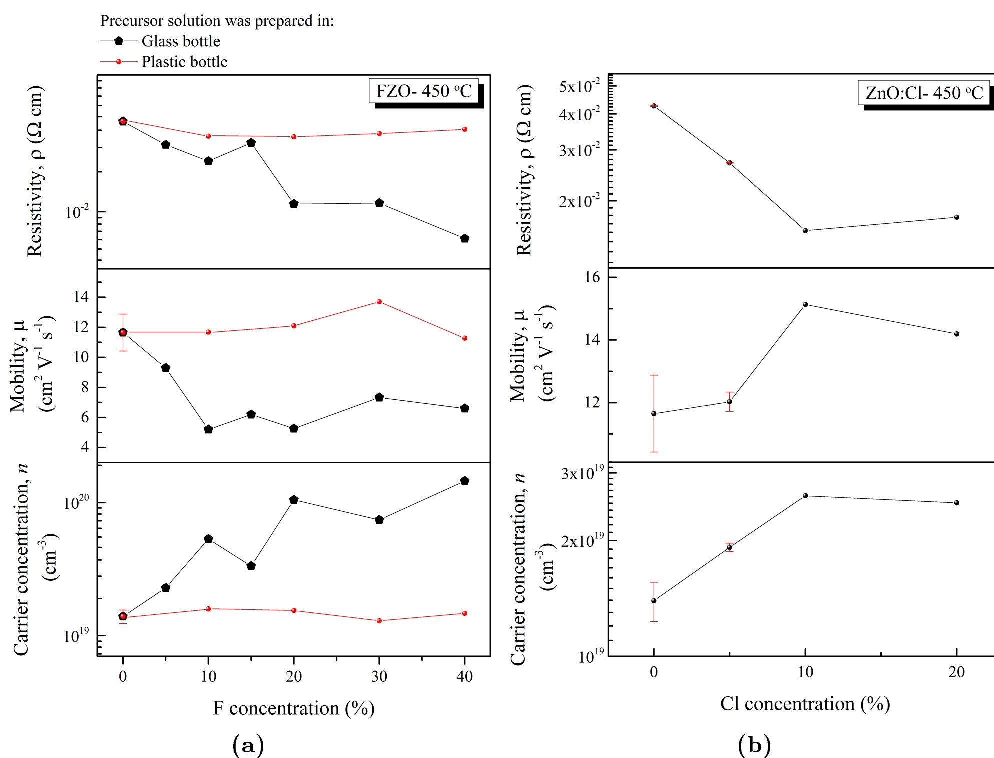

Figure 5.5: Room temperature electrical electrical properties of (a) FZO-G and FZO-P thin films and (b) ZnO:Cl thin films deposited at 450 °C

The variation of electrical resistivity with Cl doping concentration is given in Figure 5.5 (b). The undoped sample had a resistivity of 4.2×10^{-2} Ω cm. As the Cl-doping concentration increased, resistivity decreased and reached to a minimum of 1.5×10^{-2} Ω cm at a Cl concentration of 10%. Generally, in transparent semiconducting oxides, halogen doping reduces resistivity, if the halogen substitutes for oxygen. [155, 156] But, the ionic radius of chlorine (1.81 Å) is much greater than oxygen (1.38 Å) and hence it is very difficult for chloride ion to occupy oxygen sites. However, as shown in Figure 5.2 (b), variation in lattice parameters and cell volume, confirmed incorporation of Cl into ZnO lattice, but perhaps not as effective as expected. At higher doping concentrations, resistivity of the samples increases again. This might be probably due to the clustering or segregation of Cl^- atoms in the grain boundaries. Further experiments are required to prove the presence of Cl^- in the ZnO lattice and the routes cause for observed lower resistivity.

5.4 Conclusions

Two different elements of halogen family (Cl and F) were introduced separately into the ZnO thin films. FZO and ZnO:Cl thin films were deposited on glass substrate at 450 °C by spray pyrolysis. Due to the fact that F^- has comparable ionic radius to O^{2-}, and halogens are assumed to occupy the oxygen sites in ZnO matrix, the F-doping of ZnO therefore, might be an effective route to produce highly conductive and transparent thin films. A decrease in resistivity of FZO thin films was observed when the spraying solution was prepared in glass vials. However, when FZO thin films were deposited from precursor solution prepared in plastic vials, no noticeable change was observed in the electrical and optical properties of the thin films. While the resistivity of undoped ZnO sample was about 4.2×10^{-2} Ω cm, at 40% F concentration, minimum resistivity values of 6.5×10^{-3} Ω cm and 3.7×10^{-2} Ω cm were obtained for FZO thin films deposited from spraying solution in glass vials and plastic vials, respectively. Important consequence is that, F-doping of ZnO under the condiotions used in this work, is not effective. If HF or NH_4F are used as doping agents and the spraying solution is prepared in glasswares, the enhancement in the properties of the samples might not be directly interpreted as doping of FZO with F. In fact, in aqueous solutions HF will react with SiO_2 in glass, so the decreased resistivity of the FZO samples can be attributed to the presence of other impurities (mainly Si) rather than F in the ZnO lattice. The low incorporation of F dopant into ZnO matrix might be due to evaporation or volatility of fluorine-containing compounds. On the other hand, Cl-doping was found to have small effects on the electrical properties of the ZnO thin film. However, the optical transparency of the samples was declined with increasing Cl concentration. Resistivity of the ZnO:Cl thin films deposited at 450 °C reached to a minimum of 1.5×10^{-2} Ω cm at 10% Cl. The preferential growth of the crystallites was changed from along the (002) plane at 0% Cl to a strong (101) at 5% and higher Cl concentrations. This was in good agreement with the significant variation of the surface morphology of the ZnO:Cl thin films.

Chapter 6

Preparation and Characterisation of Fluorine and Silicon Co-doped ZnO (FSZO) Thin Films

6.1 Introduction and overview

The subject of co-doping (two or more dopants) has been widely discussed in the literature over the last two decades and it has been shown to give rise to effects that may be useful in the development of TCOs. Generally, co-doping can be classified into two different types. One type of co-doping method was proposed in order to enhance the optical and electrical properties of p-type wide band gap semiconductors using a method called donor-acceptor co-doping (also called p-type doping - n-type doping). In Chapters 4 and 5, the effect of single doping by Si and F dopants were studied and it was shown that thin films with low resistivities and high optical transparencies can be achieved by adding 3 mol% Si to the Zn precursor solution sprayed at deposition temperatures of 450 °C. In this chapter, in order to understand the effect of co-doping by these dopants, doping of silicon and fluorine into ZnO thin films using spray pyrolysis is explored.

6.1.1 Donor-acceptor dopants

This type of co-doping has been suggested as an effective method for fabricating low resistivity p-type wide-band gap semiconductors. The term co-doping means that, along with the acceptors that are incorporated to produce holes, donors are also incorporated during the crystal growth. [124] The method involves using acceptor and donor dopants simultaneously to both lower the energy levels of the acceptors and raise those of the donors in the band gap, as shown in Figure 6.1. [322]

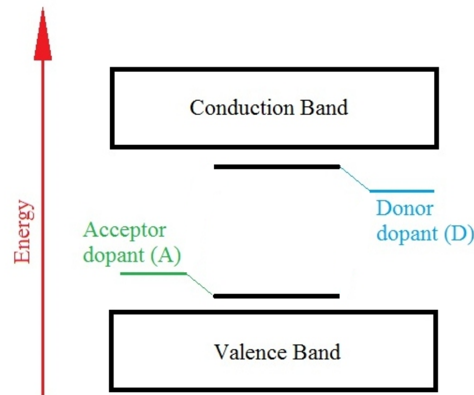

Figure 6.1: Schematic energy diagram for p-type co-doped semiconductors. The acceptor (A) level is lowered and the donor (D) level is raised with the formation of acceptor–donor co-doping (Figure adapted from [322])

There are some notable examples of TCO materials being co-doped with two carrier types at the same time. For example, p-type ZnO was made by Yamamoto *et al.* using either Li or N acceptors with either Al, In or Ga as the donor co-dopants. [323, 324] In another work, Joseph *et al.* doped ZnO with N (in the form of N_2O) as an acceptor and Ga as a donor. An optical transmittance of greater than 85%, but a high resistivity of ~ 2.0 Ω cm were achieved for these thin films deposited by the pulsed laser deposition technique. [161]

Due to the fact that ZnO is naturally only n-type because of the presence of native n-type defects associated with deviations from perfect stoichiometry, such as zinc interstitials

and oxygen vacancies, the acceptor doping of ZnO is difficult. Most of the work on co-doping of p-type TCOs is still theoretical and the experimental results for this type co-doping in ZnO have not been reproduced. This type of co-doping is not in the scope of this thesis and will not be discussed further here.

6.1.2 Two donor dopants

Another type of co-doping method which is only used in n-type TCOs involves using two donor dopants at the same time in order to increase the number of carriers in the semiconductor material. This type of co-doping occurs in two different classes:

1.1.2.1 Class I. Cation-cation co-doping; in which the metal atom in TCO material is substituted by two different n-type dopants. For example, in ZnO, replacement of Zn atom occurs using two different dopants such as Al, Ga, In or Si, giving rise to n-type conductivity. There have been a few reports on cation-cation co-doping of ZnO. Jong-Pil Kim *et al.* reported preparation of ZnO thin films co-doped with Al and Ga using the RF sputtering method. They determined the lowest resistivity values to be in the range of 3.0×10^{-2} to 4.0×10^{-2} Ω cm for films deposited at total working pressure of 5.0×10^{-3} – 5.0×10^{-2} Torr. [167] In another report, a resistivity of 1.1×10^{-3} Ω cm was observed for 1.5% Al - 2.7% Ga co-doped ZnO films deposited on silica substrates by RF magnetron co-sputtering and annealed in vacuum at 450 °C. [168] Nomoto *et al.* used RF magnetron sputtering to prepare Si+Al co-doped ZnO thin films on glass substrates at about 200 °C. In that paper they studied the effect of various Si contents in targets as the Al content was held constant at about 3 at.%. The resistivity of deposited thin films was reported to be enhanced as the Si content was increased to about 1 at.%. Their AZO:Si thin films exhibited an average transmittance above 80% and resistivity of about 8.0×10^{-4} Ω cm. [169]

1.1.2.2 Class II. Cation-anion co-doping; It is commonly accepted that in this type of co-doping of a TCO material a cation is incorporated into the lattice by substituting for

the metal ions, while an anion substitutes for the oxygen. Based on this assumption, the simultaneous doping of TCO materials with both cation and anion can be an interesting way to decrease the electrical resistivity values even more than single doping with either of them. Co-doping with Al+F in ZnO thin films deposited by sol-gel [170] or RF magnetron sputtering, [171] with In+F in ZnO thin films prepared by the chemical spray pyrolysis, [172–174] spin coating, [325] or sol-gel, [175] and with Al+Cl in ZnO thin films grown by the spray pyrolysis technique [176] have been previously studied. As an example, A. Maldonado *et al.* achieved an electrical resistivity of 3.4×10^{-3} Ω cm for In+F co-doped thin films deposited on glass substrate at 475 °C using the spray pyrolysis technique. The [In] / [Zn] = 3 at.% and [F] / [Zn] = 20 at.% were reported as the best doping levels. [172] One reason why co-doping with two donor dopants (D-D) compared to acceptor-donor (A-D) co-doping has high efficiency is because, contrary to Coulomb binding that exists in charged acceptor-donor complexes in the donor-donor co-doping approach, the binding between the two donors results from the level repulsion between the two donor states. The level repulsion significantly reduces the energy of the fully occupied lower level, stabilizing the donor-donor pair, while it increases the energy of the partially occupied upper level, thus reducing the ionization energy. [326] Fluoride ion has a radius close to that of oxygen ($r_{F^-} = 1.31$ Å and $r_{O^{2-}} = 1.38$ Å [150]), which can theoretically substitute oxygen with small crystal lattice distortions, and thus could be an appropriate anion n-type doping candidate. [151] On the other hand, if silicon ions occupy zinc lattice sites ($r_{Si^{4+}} = 0.26$ Å and $r_{Zn^{2+}} = 0.60$ Å [150]), it will act as a donor, but tangible changes may occur in the ZnO lattice. [143]

To the best of our knowledge, there is one published patent on silicon and fluorine co-doping of ZnO films deposited by the spray pyrolysis technique [145] and one published article by Thimont *et al.* on preparation of Si and F co-doped ZnO thin films using pulsed laser deposition (PLD). [327] Resistivities as low as 7.2×10^{-4} Ω cm for thin films deposited from a ZnO (87 at.%)- ZnF_2 (10 at.%)- SiO_2 (3 at.%) target at 150 °C were achieved.

The preparation of silicon and fluorine co-doped ZnO thin films using other deposition techniques has not been reported. Therefore, effect of several parameters such as deposition temperature, F dopant concentration, and Si dopant concentration etc. needs to be thoroughly investigated.

The effect of deposition temperature and Si and F dopants concentrations on the structural, optical, electrical and morphological characteristics of the FSZO co-doped films were studied and compared to those of the Si-doped ZnO thin films in Chapter 4.

6.2 Experimental

Co-doped ZnO thin films were prepared using the spray pyrolysis technique. A more detailed description of procedures for deposition of ZnO thin films using spray pyrolysis is available in Chapter 4. However, some process parameters specific to this chapter are discussed here for clarity.

To study the effect of deposition temperature, 3% Si - 10% F co-doped ZnO thin films were deposited at various heater temperatures of 350 °C, 400 °C, 450 °C, 500 °C and 550 °C.

The effect of the silicon and fluorine co-doping was investigated by adding different amounts of ammonium fluoride (NH_4F, [F] / [Zn]= 5 - 40 mol%) and silicon tetraacetate ($Si(ac)_4$, [Si] / [Zn]= 1 - 5 mol%) to the zinc precursor solution. It is important to note that the Si and F concentration values represent the concentration in the starting spray solution and the real concentrations of the dopants in ZnO lattice are different. To determine an optimum F concentration, a range of co-doped ZnO films at constant Si concentration of 3% were deposited at 450 °C by adding NH_4F with [F] / [Zn]= 5, 10, 15, 20, 30 and 40 mol% to the precursor solution.

To determine the optimum Si dopant concentration, the F concentration was kept constant at 30% (its optimum for 3% Si) and the Si+F co-doped ZnO thin films were deposited at 450 °C from precursor solutions containing $Si(ac)_4$ concentrations of [Si] / [Zn]= 1, 2, 3,

4, and 5 mol%.

A clear change was noted in the properties of the F-doped ZnO (FZO) thin films depending on the material of the container in which the precursor solutions containing ammonium fluoride were prepared, as previously discussed in Chapter 5. Briefly, the thin films deposited from a solution prepared in glass container showed enhanced electrical properties which might be due to the presence of additional Si (or other elements such as Al and B) from glass as dopants in the ZnO lattice. A variety of reagents including hydrofluoric acid (HF) or, under suitably acidic conditions, fluoride or bi-fluoride salts are known to react with glass and used for fluoride-based wet chemical glass etching. The dissolution of silicate glasses by HF results in the formation of the stable hexafluorosilicate (SiF_6^{2-}) anion. [328, 329] NH_4F on dissolving in aqueous acidic solutions forms HF and as glass is mainly made up of SiO_2, in the presence of water the following reaction will happen: [330]

$$6HF + SiO_2 \rightarrow H_2SiF_6 + 2H_2O \tag{6.1}$$

Fluosilicic acid (H_2SiF_6) is generally believed to exist only in the solution phase. It decomposes into hydrofluoric acid and silicon tetrafluoride upon vaporizing in anhydrous solution ($H_2SiF_6 \rightarrow SiF_4 + 2HF$). In aqueous solution ($H_2SiF_6 + 2H_2O \rightarrow 2H_3O^+ + SiF_6^{2-}$), on the other hand, no noticeable amount of HF occurs, and the resulting solution does not etch glass any more. However, an additional series of the same precursor solutions was prepared in plastic vials (FSZO-P) and the data were compared with those from solutions prepared in glass vials.

Various properties of the prepared thin films were characterised by X-ray diffraction (XRD), UV-Vis-NIR spectroscopy, Hall effect measurement, scanning electron microscopy (SEM), and X-ray photoelectron spectroscopy (XPS). Details of the instrumental analyses can be found in the Experimental section in Chapter 4. The optical transmission spectra for Si+F co-doped ZnO thin films were recorded at room temperature for wavelengths between

2500 and 200 nm using a PerkinElmer Lambda 19 UV-Vis-NIR spectrometer. The surface morphology of the films was characterised using a JEOL JSM-840F field emission scanning electron microscope at an accelerating voltage of 5 kV. Samples were observed in the SEM with sputter coating with platinum. XPS spectra were collected on an AXIS Nova using a monochromatic Al-K_α X-ray source (1486.6 eV) operating with an anode voltage of 15 kV and emission current of 15 mA. The spectrometer was calibrated using standard silver, copper and gold reference materials. Cleaning of the surface of the samples was achieved *in-situ* via a 15 second ion etch by argon ions at 5 keV.

6.3 Results and discussion

6.3.1 Effect of deposition temperature

6.3.1.1 Structural characterisation

Figure 6.2 shows XRD patterns obtained for 3%Si - 10%F co-doped ZnO films deposited at various deposition temperatures between 350 °C and 550 °C. The reference XRD stick pattern for pure ZnO powder is also included.

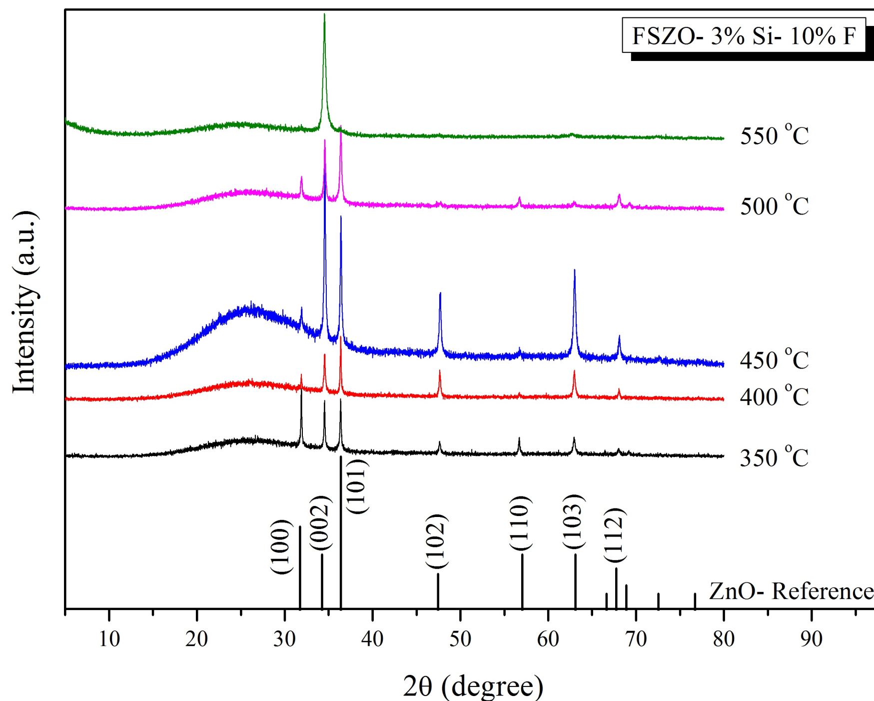

Figure 6.2: XRD patterns of 3%Si - 10%F FSZO thin films deposited from 350 °C to 550 °C

All samples exhibit XRD patterns consistent with a polycrystalline hexagonal wurtzite ZnO structure; no phase corresponding to crystalline SiO_2 (silicon oxide, quartz), Zn_2SiO_4 (zinc silicate), ZnF_2 (zinc fluoride), or SiF_4 (silicon tetrafluoride) phases were observed in the XRD patterns. Reference stick charts for ZnO, SiO_2, [331] Zn_2SiO_4, [332] ZnF_2 [333] powders are shown in Figure 6.3.

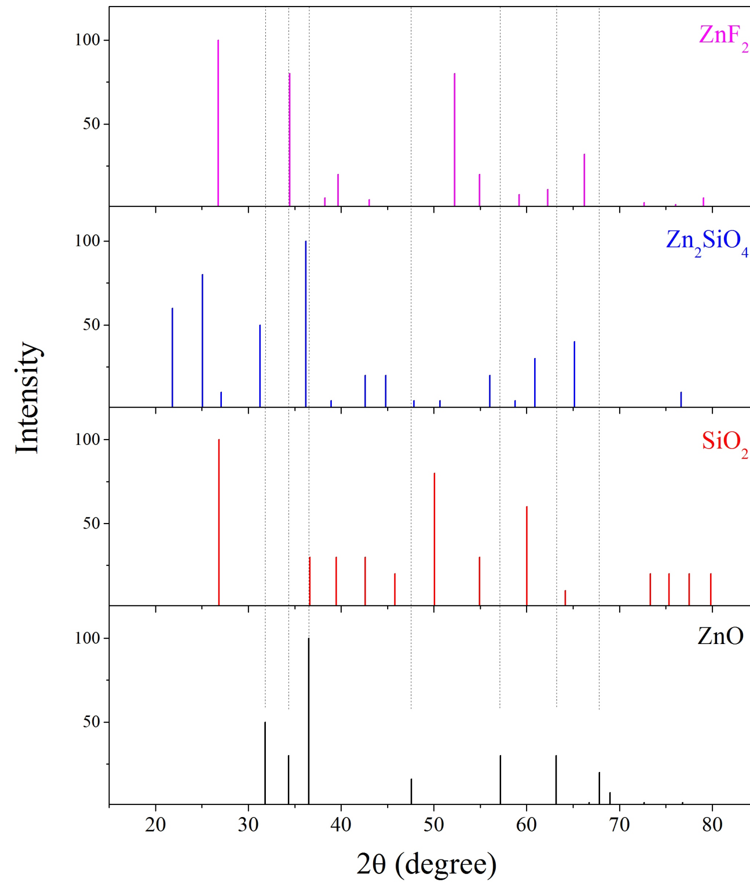

Figure 6.3: Reference XRD spectra of ZnO, SiO_2, Zn_2SiO_4, and ZnF_2 powders. Vertical lines show the diffraction peaks of powdered compounds

Compared with the XRD patterns of powder samples which contain randomly oriented crystallites, there is a tendency to develop a non-random (preferred) orientation for thin film samples which will cause a change in the intensity distribution of X-ray reflections. In such a case, the sample is called "textured". Highly preferred orientation in a sample will result in missing or invisible diffraction peaks, but in the majority of samples, where preferred orientation is mild to moderate, all of the diffraction peaks will be seen but their intensities will differ from that of a randomly oriented sample. ZnO crystals tend to grow predominantly in two different directions: with the *c*-axis normal (90°) to the plane of the substrate (the (002) orientation), or with the *c*-axis parallel to the plane of the substrate

(either the (100) or the (101) orientation). The crystal structure and growth direction of different planes in wurtzite ZnO structure are shown in Figure 6.4.

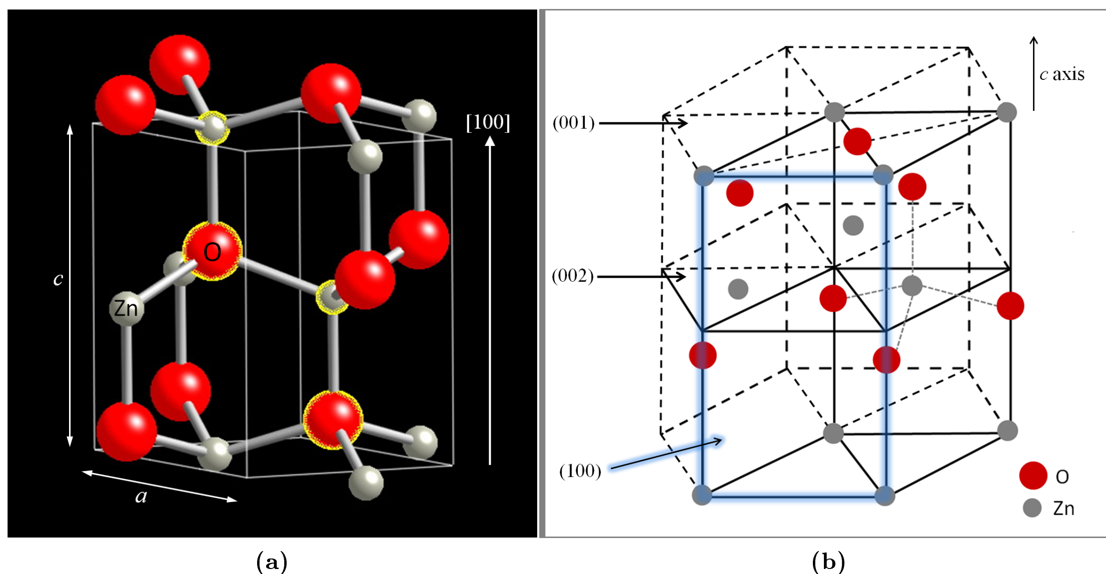

Figure 6.4: (a) The unit cell of the wurtzite ZnO crystal structure. The tetrahedral-coordination between Zn and its neighbouring O is shown. [265] (b) (001), (002) and (100) planes. [334] The hexagonal unit cell is highlighted with bold lines and adjacent atoms are included to show the overall hexagonal nature of the structure. Blue highlight shows (100) plane

The relative intensity of the peaks varies with increasing deposition temperature. At a deposition temperature of 350 °C, the (100), (002) and (101) peaks have similar intensities and the peak intensity ratios are very close to those of powder (shown as ZnO reference), which suggests a nearly random orientation of the crystallites on the surface of the substrate. From 400 °C to 500 °C the (100) peak intensity is diminished, while the (002) and (101) peaks are enhanced. The equivalent intensities of the peaks suggests that crystallites are not purely oriented in one direction. At 550 °C all peaks disappear and only (002) peak is observed. This indicates that crystallites are predominantly oriented with their c-axis perpendicular to the the surface of the substrate. The broad nature of the this peak confirms that the ZnO species grown has very small crystallite size. These results show a clear dependence of crystal growth orientation on the deposition temperature. It can be

seen in Figure 6.2 that at lower temperatures the (100) is the dominant reflection, but as the temperature is increased the preferred orientation shifts to (002). The (101) peak also grows with increasing temperature and becomes predominant at 500 °C.

Preferred orientation can lead to anisotropic distribution of properties such as strength, thermal expansion, electrical conductivity, etc. [335] Therefore, it is important to investigate changes in the texture. The preferred orientation of growth of thin films can be determined by the texture coefficient of the (*hkl*) plane, $TC_{(hkl)}$, using Equation 4.1. Figure 6.5 shows the $TC_{(hkl)}$ variations as a function of deposition temperature. As $TC_{(hkl)}$ increases, the preferential growth of the crystallites in the direction perpendicular to the (*hkl*) plane is increasing.

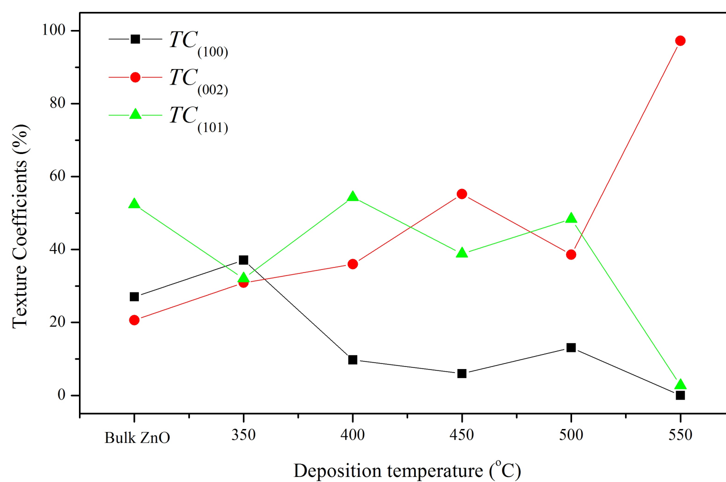

Figure 6.5: Variation of texture coefficient $TC_{(100)}$, $TC_{(002)}$, and $TC_{(101)}$ of FSZO thin films as a function of deposition temperature

The preferential growth of crystallites can be influenced by factors such as defects, impurities, heating conditions and substrate choice, as they all can influence the growth rate in different crystallographic directions. [64] Recently, some explanations have suggested that the change in preferential growth of different planes with increasing temperature can be explained by kinetic or thermodynamic control of the film growth. It is usually supposed that at low substrate temperature growth will occur along the least kinetically hindered

directions and as the substrate temperature increases the influence of thermodynamic stability increases. [336, 337] It is also known that all systems tend to reduce their free energy as they are reaching the equilibrium state and for the same reason, thin films grow along a particular direction in order to minimise their surface free energy ($\gamma = (\frac{\partial G}{\partial A})_{T,P}$, where γ is surface energy, G is Gibbs free energy and A is the surface area). So during film growth, atoms arrange themselves into the crystalline plane with the lowest surface energy. The surface energy of different planes in ZnO were calculated and follows the sequence: γ (002) : 0.099 eVÅ^{-2} > γ (110) : 0.123 eVÅ^{-2} > γ (100) : 0.209 eVÅ^{-2}. [200] Since the surface energy of hexagonal closed packed structure is theoretically minimal in (002) planes, the surface energy of ZnO should also be minimal along the (002) faces. [338] In addition, under conditions which promote tetrahedral coordination, crystal growth along (002) can be obtained, whereas, in the conditions which inhibits the formation of tetrahedral coordination, growth along (100), (101) or (110) planes is amplified and these planes could be obtained when the deposition is performed in the non-equilibrium state. [200] In our FSZO thin films, a competitive growth between the fastest growing orientations ((100) and (101)) and the (002) orientation which produces the maximum packing density and therefore, gives rise to the lowest surface energy, was observed at the moderate deposition temperature of 350 °C. However, all these assumption-based explanations may have some flaws, and might not be able to define the exact mechanisms of the observed variations in the preferential growth of the crystallites.

The crystallite size of the thin films were calculated from X-ray patterns using Scherrer equation (Equation 2.9) as discussed in Chapter 2. The calculated crystallite size remains almost constant as the deposition temperature increases, up to 500 °C, and then decreases with further increase in deposition temperature to 550 °C.

Deposition temperature (°C)	Mean crystallite size (nm)
350	62.2 ± 6.5
400	58.0 ± 5.1
450	61.8 ± 1.6
500	53.1 ± 5.5
550	21.7 ± 0.1

Table 6.1: Crystallite size of FSZO thin films deposited at different temperatures calculated using Scherrer equation

6.3.1.2 XPS Analysis

XPS measurements were carried out to determine the chemical states of the component elements on the surface of the samples. It is important to note that XPS results are more based on the study of the surface of the samples, and on their own, are not enough to make a definite conclusion about the efficiency and mechanism of co-doping of ZnO. The charge shifted spectra were calibrated by using the C 1s signal at 284.6 eV. The XPS survey spectrum of the FSZO film deposited at 450 °C (Figure 6.6) is dominated by two photoelectron peaks, corresponding to electrons originating in the 1s orbitals of the oxygen and 2p orbitals of the zinc atoms in the thin film surface.

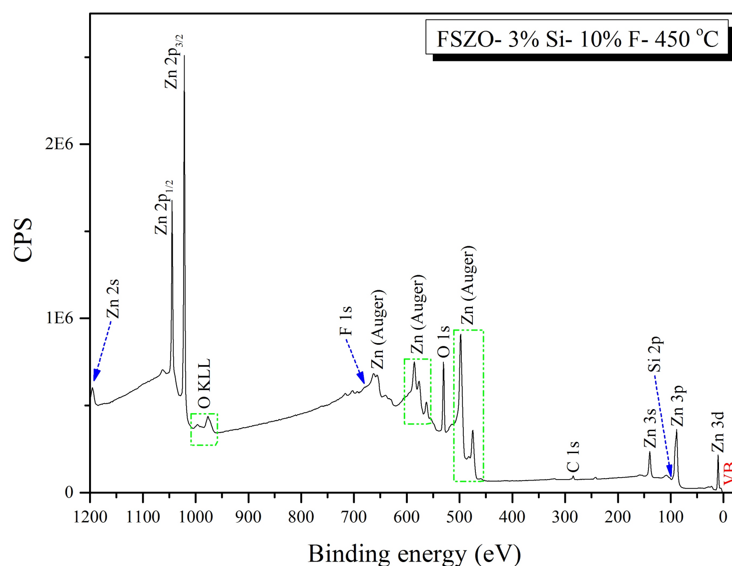

Figure 6.6: Survey XPS spectrum of FSZO thin film with 3% Si and 10% F deposited at 450 °C

The high resolution XPS spectra for FSZO films deposited at various temperatures are shown in Figure 6.7. Zn $2p_{3/2}$ peak (Figure 6.7 (a)) observed at 1021.7 eV exhibits no significant change in the position by increasing deposition temperature. Although the Zn $2p_{3/2}$ peak for ZnO is free from multiplet splitting and other complicating effects, but suffers from an overlap with the Zn metal peak and, therefore, it is difficult to distinguish between Zn^0 (Zn $2p_{3/2}$ binding energy for Zn metal is 1021.4 eV [339, 340]) and Zn^{2+} (binding energy 1021.8 eV [341, 342]) by XPS. [343, 344] However, metals are often characterized by an asymmetric line shape, with the peak tailing to higher binding energy, while metal oxides give rise to a more symmetric peak profile. So, as the Zn $2p_{3/2}$ peaks look quite symmetrical, they can be assigned to ZnO, rather than metallic Zn.

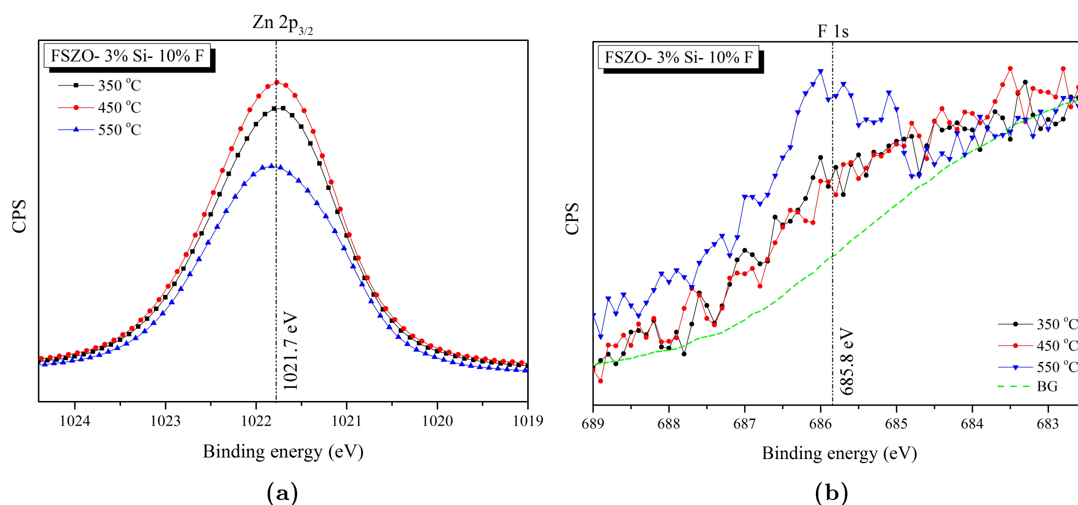

Figure 6.7: (a) Zn $2p_{3/2}$ and (b) F 1s high resolution XPS spectra of FSZO samples deposited at 350 °C, 450 °C and 550 °C (dashed green line is the background)

The broad peak at a binding energy of ~ 685.8 eV is attributed to the F 1s core level (Figure 6.7 (b)). It can be noticed that the intensity of the F 1s peak increases with increasing deposition temperature to 550 °C. Although the F 1s peaks intensity for the FSZO film deposited at 350 °C and 450 °C seem to be smaller, but they have similar peak area to sample deposited at 550 °C. The F 1s peak, theoretically, can be resolved into two components; a peak at lower binding which presumably corresponds to F^- ions surrounded

by Zn^{2+} in the ZnO structure, and a peak at higher binding energy which is related to hydrated F^{-} species on the surface. Curve fitting of the F 1s peak in the data collected for the FSZO films, was not feasible due to the very low intensity of the peaks. It can be inferred from the very low intensity of the F 1s peaks that the concentration of F on the surface of the samples is much less than the amount of F atoms added to the spraying solution (nominal concentration, [F] / [Zn] = 10 mol% = 10 at.%). This suggests that most of the F atoms did not incorporate into the ZnO matrix. The concentration of the F the surface might increase by increasing the concentration of F in the spraying solution. This subject will be studied later in section 6.3.2.

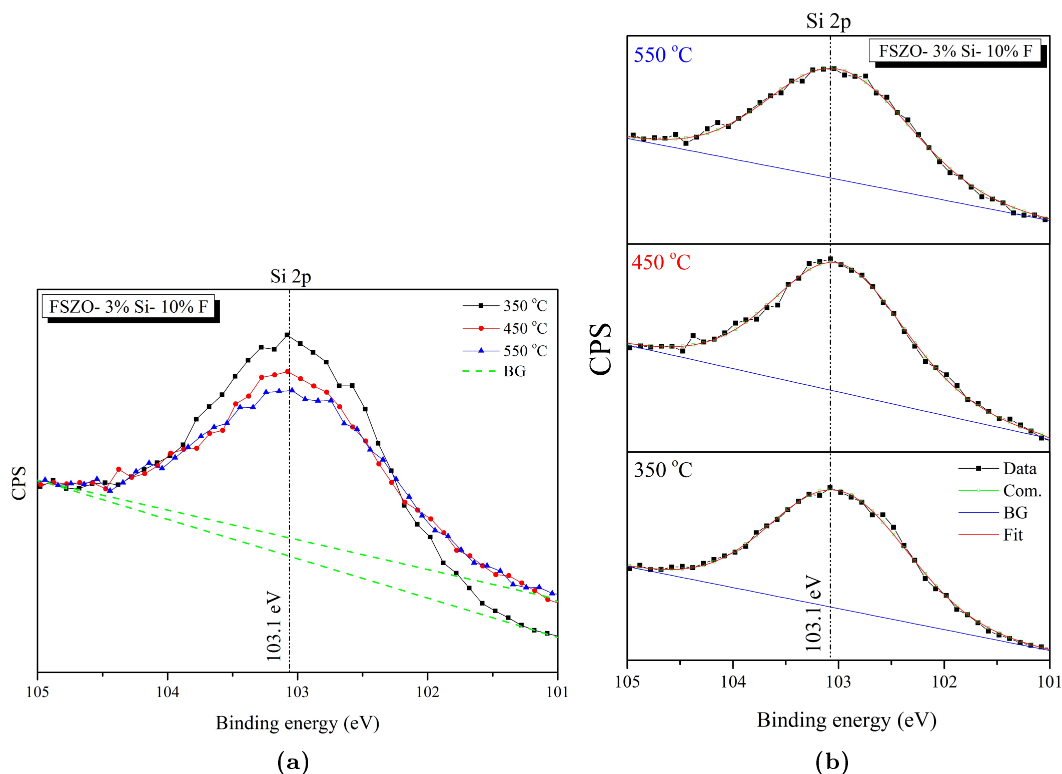

Figure 6.8: (a) Variation in the intensity of Si 2p XPS peaks with temperature and (b) fitted XPS spectra of the Si 2p core level of FSZO thin films as a function of deposition temperature (green dashed lines show the background)

The XPS spectra of the Si 2p core level of FSZO thin films deposited at 350 °C, 450 °C

and 550 °C are shown in Figure 6.8 (a). A slight decrease in the Si 2p peak intensity on the surface with increasing deposition temperature is observed (Figure 6.8 (a)), however, the areas of the peaks are more or less equivalent.

The results of a research work on amorphous SiO_x materials carried out by Philipp in 1972, indicated that amorphous substances of all intermediate compositions between Si and SiO_2 can be formed and that these materials are not simple mixtures of particles of Si and SiO_2 but rather the two atom species are blended on an atomic scale. Based on this model which is called random bonding model, the basic units of this structure are composed of Si tetrahedral of the type $Si{-}(Si_yO_{4-y})$ in which the distribution of atoms for all $y = 0, 1, 2, 3, 4$ is determined by simple statistics. [345] Therefore, assuming validity of this bonding model, the Si 2p peak could be resolved into five different chemical states namely, Si^{4+}, Si^{3+}, Si^{2+}, Si^{1+} and Si^0, corresponding to no Si−Si bond, one Si−Si bond, two Si−Si bonds, three Si−Si bonds, or all four Si−Si bonds had been replaced by Si−O bonds. The possible candidates for these silicon states might be SiO_2 (103.0 - 103.5 eV), Si_2O_3, SiO (or Si_2O_2, 101.2 - 102.5 eV), Si_2O and Si (99.8 eV), respectively. [346, 347] However, due to the fact that the most Si compounds with Si^{3+}, Si^{2+} and Si^{1+} oxidation states are unstable under spray pyrolysis deposition conditions, even if they are formed, they will be oxidised again to the compounds with the most stable Si^{4+} or Si^0 states. Therefore, presence of 3+, 2+, and 1+ oxidation states seems to be very unlikely.

In our FSZO samples, the Si 2p peak can be fitted using only one component, providing evidence for only one chemical state of silicon in the samples. The addition of further components did not significantly improve the quality of the fit. The binding energy (~ 103.1 eV) of the silicon component in the films is consistent with the Si 2p peak for SiO_2 which usually appears at binding energies around 103.0 - 103.5 eV. [339, 348] The presence of the Si^{4+} oxidation state indicates that Si in the FSZO thin films is either replacing Zn^{2+} sites in the Si^{4+} state and thus, will contribute two carrier electrons, or forming a secondary phase like SiO_2 which can reduce the doping efficiency. [141, 143] XRD (Figure 6.2) doesn't

show any evidence for a distinct SiO_2 phase.

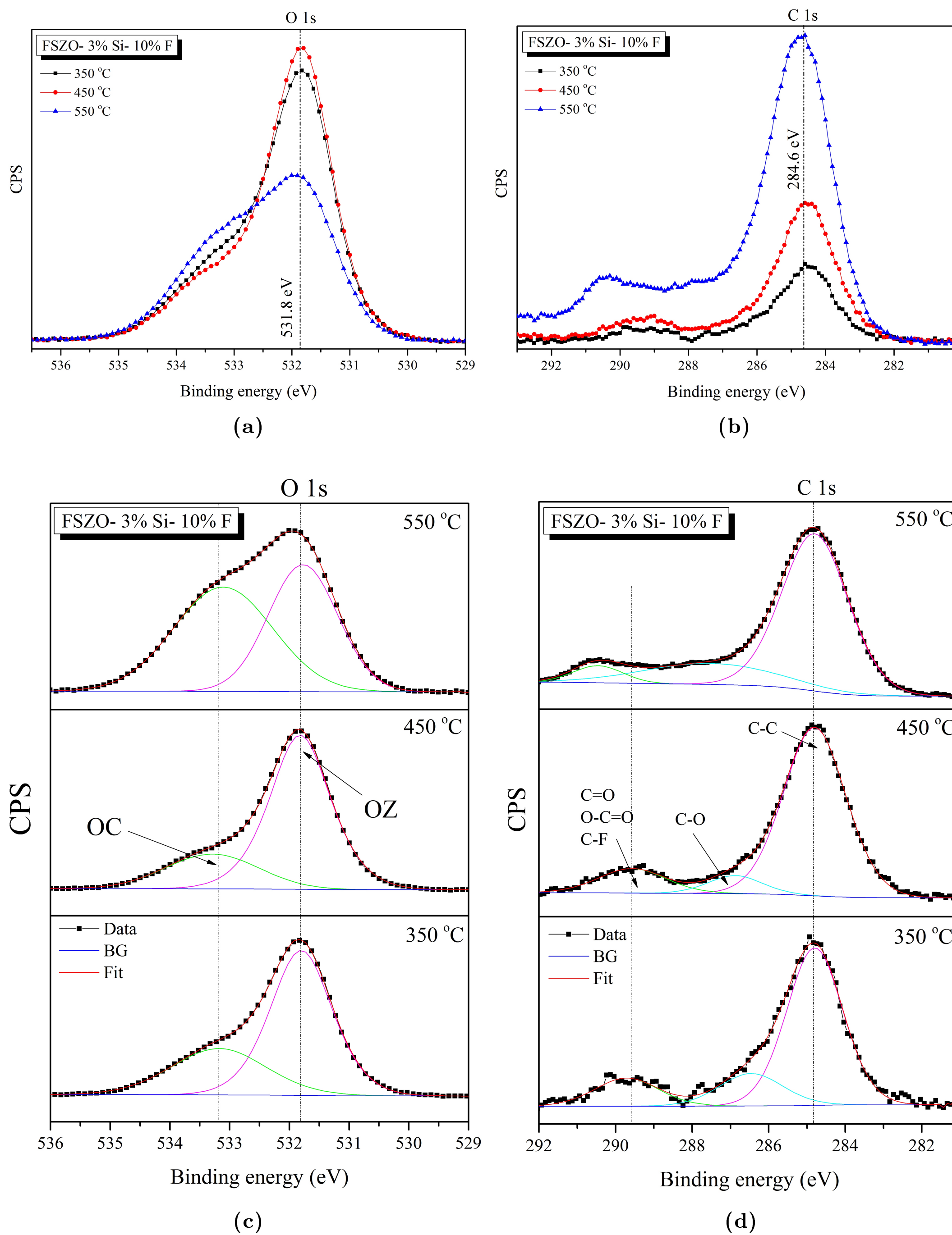

Figure 6.9: (a) O 1s, (b) C 1s, (c) resolved O 1s, and (d) resolved C 1s high resolution XPS spectra of FSZO thin films deposited at 350 °C, 450 °C and 550 °C

In addition, an O 1s signal centred at the binding energy typical for oxygen in bulk zinc oxide is observed in the XPS spectra of FSZO thin films (Figure 6.9 (a)). [339] In general, for many of metal oxide samples, the O 1s peak can be curve fitted into at least two (usually three) components which are attributed to contributions from different oxygen species as shown in Figure 6.9 (c). The lower binding energy peak (~ 531.8 eV) can be assigned to O^{2-} ions bound to Zn^{2+} ions (substitutional oxygen) in the ZnO structure. The second higher binding energy peak (~ 533.2 eV) is associated with surface (or near-surface) species such as hydroxide, hydrated oxygen or organic oxygen (carbon contamination, C−O / C=O bonds). [142, 143, 343] Most likely the 533.2 eV peak is due to C−O contaminations on the surface of the samples, as C content is also higher in 550 °C film (Figure 6.9 (b)).

Peak OC usually contributes between 20% and 40% of the total O 1s signal based on other metal oxides such as nickel oxide and chromium oxide. [349, 350] The relative intensities of OZ and OC components are summarised in Table 6.2 (b).

FSZO- 3% Si - 10% F	OZ (531.8 eV)	OC (533.2 eV)	OZ/OC
350 °C	67.6%	32.4%	2.0
450 °C	75.2%	24.7%	3.0
550 °C	49.6%	50.4%	0.9

Table 6.2: Relative percentage of OZ and OC curve areas in O 1s peak in FSZO samples deposited at different deposition temperatures

It can be found that the intensity of OC component for FSZO film deposited at 450 °C was lower than that of film deposited at other deposition temperature, indicating that the surface of the FSZO films grown at 450 °C has lowest concentration of hydrated or carbon contaminated oxygen species. The film deposited at 550 °C has the smallest OZ/OC value. This may suggest that this film has the highest concentration of hydrated or organic oxygen on the surface. The higher carbon concentration detected on the surface of this film along with higher resistivity and dark colour of this film confirms the presence of more carbon contaminated oxygen species on the surface of this film.

Figure 6.9 (b) shows the C 1s XPS spectra of FSZO samples deposited at different

temperatures. Carbon-containing organic contaminants always exist on the surfaces of samples even when the surface of the samples were ablated by argon ions before XPS measurements. As expected strong C 1s peaks were observed due to the C contaminants at about 284.6 eV and 289.9 eV for the FSZO films. These spectra show higher concentration of carbon on the surface of the samples with increasing deposition temperature. The brown colour, as well as the lower transparency observed for the FSZO film deposited at 550 °C are consistent with the increased intensity of the C 1s spectra for this film. This might be due to higher growth rate of the thin films than the decomposition of the organic ligands, as will be discussed further in section 6.3.1.4.

The C 1s signal (Figure 6.9 (d)) can be modelled by three different components. The peak at a binding energy of 289.9 ± 0.4 eV is usually assigned to the carbon of carbonyl groups (C=O bond), fluorinated organic groups (C−F bond) or carboxyl groups (O=C−O bond), the one at about 286.9 ± 0.3 eV to species with carbon-oxygen single bonds (C−O bond), and the peak with lowest binding energy (~ 284.6 ± 0.1 eV) is assigned to the the tertiary carbon (C−C bond). [339, 348]

The determination of the surface composition of a sample using XPS data is quite complicated. Using the high resolution XPS data the relative atomic concentration, C_x, of the element x in a multi-element surface layer can be calculated from the Equation 2.12 described in Chapter 2. Since only the elements Zn, O and C are clearly observed on the surface of FSZO films, the atomic concentration of Zn, C_{Zn}, for example, with RSF=28.7 will be calculated from equation:

$$C_{Zn} = \frac{\frac{I_{Zn}}{28.7}}{\frac{I_{Zn}}{28.7} + \frac{I_O}{2.93} + \frac{I_C}{1}}$$

The surface relative atomic compositions in the depth range probed by XPS were determined from the Zn 2p (Zn $2p_{1/2}$ + Zn $2p_{3/2}$), O 1s and C 1s core line intensities corrected with the relative sensitivity factors (RSF) after the subtraction of the background. The

rule for selecting a transition is to choose the transition for a given element for which the peak area is the largest, subject to the peak being free from other interfering peaks. The peak areas were obtained and the relative atomic concentration of different elements on the surface of the samples were calculated using Equation 2.12. The results were plotted against the deposition temperature and displayed in Figure 6.10. An accuracy of ± 10% is typically quoted for routinely performed XPS atomic concentrations. [351]

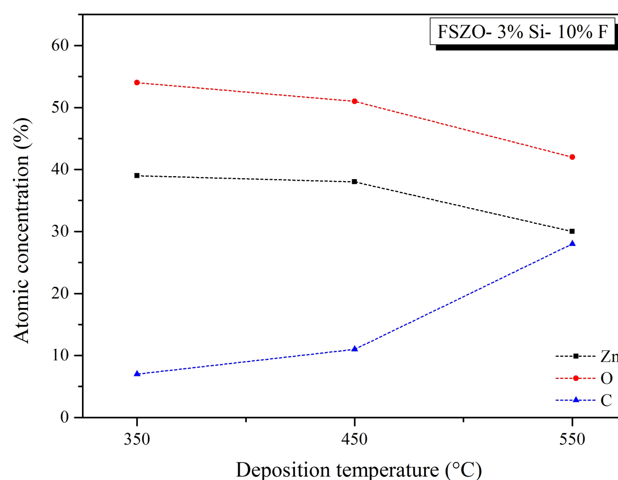

Figure 6.10: Atomic concentrations of Zn, O, and C derived from the area of the peaks in XPS spectra

The changes in relative at.% of Zn, O and C are shown in Figures 6.10. The Zn/O atomic concentration ratio in FSZO films remains more or less unchanged at about 0.72 ± 0.02.

The Si:Zn ratio in these samples was determined by examining high resolution scans with a binding energy range of 110 to 75 eV, which includes the Si 2p and Zn 3p signals. Using the CasaXPS software package, the peak areas were integrated using a linear baseline and normalized by the relative sensitivity factors (0.817 for Si 2p and 2.83 for Zn 3p) to calculate the Si:Zn ratio (Figure 6.11).

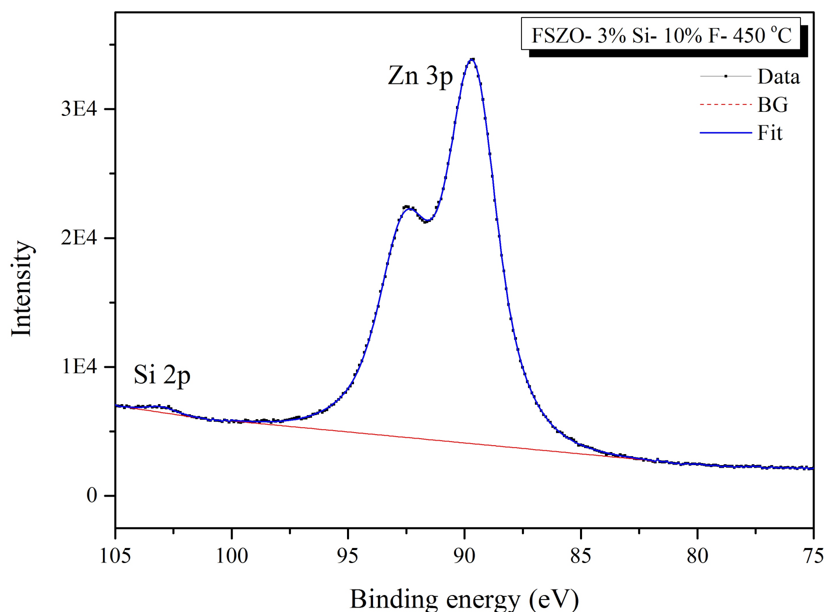

Figure 6.11: Representative experimental XPS spectrum of a FSZO film prepared from a precursor solution containing 3% Si and 10% F in a region containing Si 2p and Zn 3p peaks (square symbols). The fits to the data (blue solid line) and linear backgrounds (dashed line) used to integrate each peak are also shown.

Using precursor solutions with a fixed silicon and fluorine concentration, increasing the deposition temperature resulted in a decrease in silicon concentration from 2.6 at.% for the film deposited at 350 °C to 1.7 at.% for the film deposited at 450 °C, and an increase to 7.1 at.% for the film deposited at 550 °C. The lower concentration of Si on the surface of the thin film deposited at 450 °C might be due to the increase in silicon incorporation into the films at optimum deposition temperature, so Si ions are homogeneously distributed into the ZnO matrix. The greater amount of the silicon in the films is the most straightforward explanation for increased carrier concentration (Figure 6.18). On the other hand, the higher concentration of the dopant at the surface of the oxide thin films than the solution is attributed to the segregation (enrichment) phenomenon. High deposition or thermal treatment temperatures are generally required to obtain crystalline metal oxides. However, they can critically affect their structural properties, such as particle size and surface area, as well as their stoichiometry and dopant distribution. Very high temperatures can lead to

a surface composition that is significantly different from that of the bulk. This phenomenon has been reported for Sb-doped SnO_2 oxides where dopant surface enrichment took place to an extent that was dependent upon bulk composition and calcination temperature or time. [352]

In practice, calculating accurate atomic concentrations from XPS spectra is not an easy task even when the peaks areas are reasonably large. In particular, background correction is not a straightforward procedure. Therefore, calculation of at.% of F was not feasible due to the fact that the backgrounds could not be reliably determined for the very small and broad F peaks.

6.3.1.3 Morphology

In order to investigate the influence of temperature on the surface morphology of FSZO thin films, AFM and SEM images were recorded. Figure 6.12 depicts the AFM micrographs of FSZO films with 3% Si and 10% F concentration deposited at different deposition temperatures, taken over a scan area of $5.0 \times 5.0\ \mu m^2$. AFM micrographs show that all films have dense polycrystalline morphology, with a clear tendency for increasing homogeneity and particle size as the substrate temperature increases to 450 °C. A significant change in particle shape and size can be observed in the AFM images.

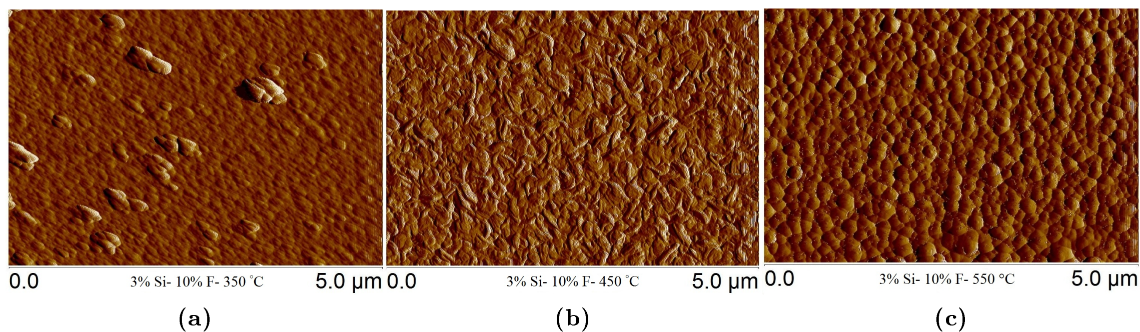

Figure 6.12: AFM images of FSZO thin films deposited at (a) 350 °C, (b) 450 °C, and (c) 550 °C

AFM characterisation of the film surfaces revealed that the mean particle size seems to

slightly increase from 119 ± 57 nm at 350 °C to 171 ± 87 nm as the deposition temperature increases to 450 °C. The particle size did not change significantly with further increase of deposition temperature to 550 °C. The grain size obtained from SEM is larger by about a factor of 4 as compared with that determined from XRD. The estimates of particle size from AFM are considerably larger (by about a factor of 2) as compared with crystallite sizes determined from XRD (by the Scherrer equation, 2.9). The different values of the mean crystallite sizes measured by XRD and the average particle sizes estimated by AFM (or SEM) analysis are not in contradiction. In fact, the particle size is usually greater than the crystallite size because the crystallites are assumed to be the building blocks of the particles. [353] Moreover, the particle size from AFM/SEM is based on the measurement of agglomerated particles on the surface. On the other hand, this difference might be due to the different grain size criteria, underlying the different methods. Fore example, the SEM particle sizes are measured by the distances between the visible grain boundaries, whereas the XRD method determines the extension of the crystalline that diffracts the X-rays coherently, which is a more precise criteria, and thus leading to smaller grain sizes. [354] Different particle and crystallite sizes from AFM/SEM and XRD analyses have also been observed for ZnO thin films by many other researchers, for example, in Al-doped ZnO thin films prepared by Dghoughi *et al.* [272]

Quantitative surface studies show that the mean surface roughness of FSZO thin films follows the same trend observed for particle size. Surface roughness is expressed mathematically by:

$$R_a = \frac{1}{n}\sum_{i=1}^{n}|y_i| \tag{6.2}$$

where n is the total number of data points used in the calculation and y is the average surface height. Therefore, particle size is one of the important parameters in the measurement of roughness. The FSZO films became rougher with increasing deposition temperature to 450 °C and with increasing particle size. Smoother surface was observed again with further increase of the deposition temperature to 550 °C and smaller particles. The mean rough-

ness of the FSZO films deposited at 350 °C, 450 °C and 550 °C found to be about 9.0 nm, 20.4 nm and 9.3 nm, respectively. Observed decrease in the roughness with increase of deposition temperature to 550 °C suggests more uniform distribution of the particle sizes on the surface and this is clearly evident from the AFM image of sample deposited at 550 °C. Smoother morphology and smaller particle size of the high temperature (550 °C) film could be due to the smaller diameters of the spray droplets at higher deposition temperatures. The incorporation of smaller decomposed precursor particles would lead to more uniform growth of the film. Moreover, creation of more nucleation site on the surface at higher temperatures might lead to a more uniform texture.

In Figure 6.13 SEM micrographs show the surface morphology obtained for FSZO films deposited at 350 °C, 450 °C and 550 °C.

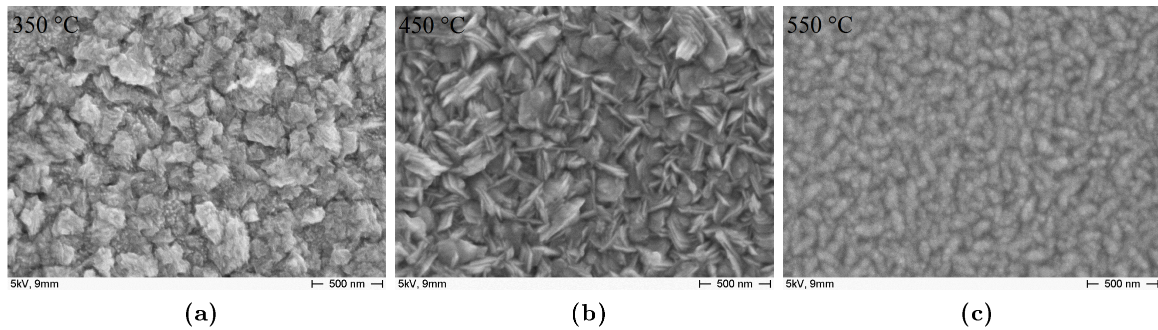

Figure 6.13: SEM images of FSZO thin films with constant Si concentration of 3% and F concentration of 10% deposited at (a) 350 °C, (b) 450 °C, and (c) 550 °C

The FSZO thin film deposited at 350 °C shows a porous structure consisting of particles randomly oriented to the substrate surface. This correlates well with XRD data (Figure 6.2) which show (100), (002) and (101) peaks with similar intensities and thus, confirms a mixed orientation of the particles. On the other hand, a hexagonal flake-like structure with preferential orientation of two-dimensional particle sheets oriented perpendicular to the substrate surface is seen in the SEM image of the film deposited at 450 °C, in agreement with the XRD result which exhibits high intensity of (002) and (101) planes simultaneously.

This film shows very similar surface morphology to that observed in the 3% Si-doped ZnO film prepared at 450 °C (Figure 6.27 (b)) but with a more random orientation of the particles. The FSZO film deposited at 550 °C has a relatively less porous structure composed of smaller particles.

6.3.1.4 Optical properties

The effect of deposition temperature on the optical properties of FSZO thin films is illustrated in Figure 6.14. The average transparency is calculated in the visible range of 400 - 750 nm. The solution-grown Si+F co-doped ZnO thin films show significantly improved optical transparency (comparing to undoped and Si-doped ZnO thin film) as high as about 88% (corrected for glass) as the deposition temperature increases to 400 °C, as shown in Figure 6.14 (b), but drops off thereafter.

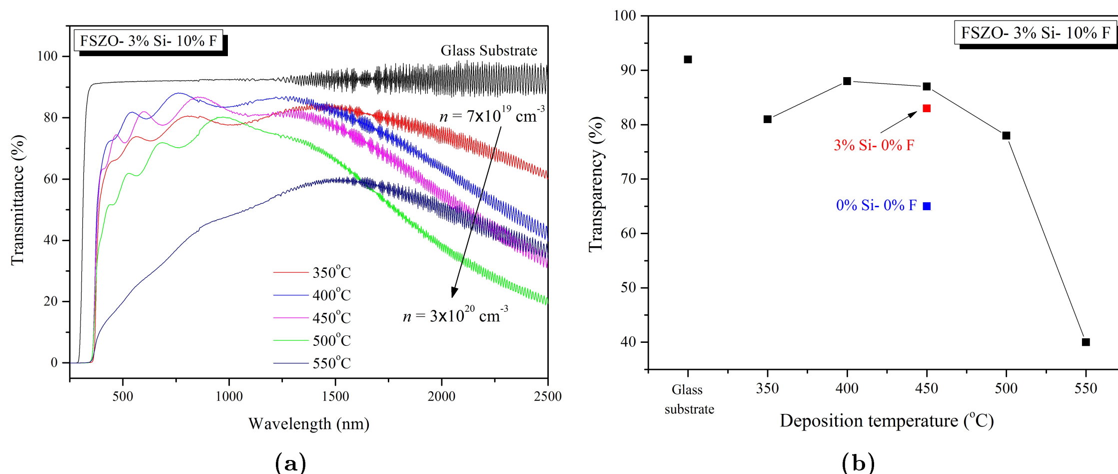

Figure 6.14: (a) UV-Vis-NIR spectra of FSZO thin films deposited at 350 °C to 550 °C and (b) transparency variation of FSZO thin films as a function of deposition temperature compared to glass substrate

The interference fringes observed at longer wavelengths (in the IR region) correspond to multiple reflections in the thin (0.13 mm - 0.17 mm) glass substrates. The wider fringes at shorter wavelengths are related to reflections within the ZnO thin film itself.

As seen in Figure 6.14, FSZO thin films exhibit a decrease in IR transmittance with increasing deposition temperature. This is caused by the dependence of plasma reflectivity on free carrier concentration in the films due to a coherent oscillation of conduction electrons with incident electromagnetic radiation as discussed in Chapter 4 (4.3.3).

The sharp decrease of transmittance at about 380 nm observed for all of the films arises from the intrinsic band gap transitions in ZnO. A direct optical band gap, E_g, can be determined from the transmittance data using the Tauc relation, $(\alpha h\nu)^2 \propto (h\nu - E_g)$. [236] For direct band gap semiconductors the optical band gap can be determined by extrapolating the linear portion of plot of $(\alpha h\nu)^2$ *vs* $h\nu$ to where $\alpha h\nu = 0$. The results of this procedure, shown in Figure 6.15, clearly indicate the expected increase in band gap with higher carrier concentrations.

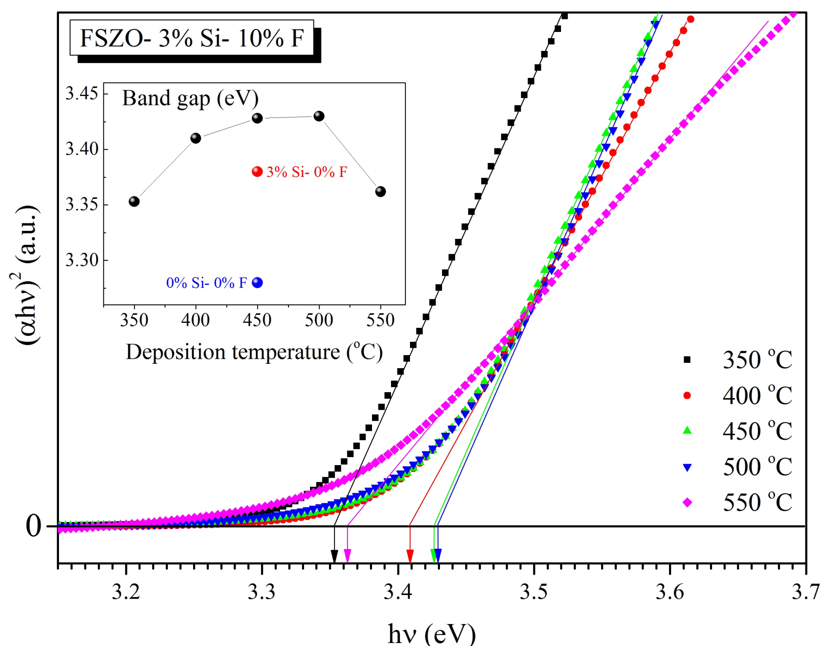

Figure 6.15: Band gap calculation of FSZO thin films deposited from 350 °C to 550 °C and band gap variation of FSZO thin films as a function of deposition temperature (inset: respective values from band gap calculation)

Inset in Figure 6.15 shows the band gap changes (as estimated from the UV-Vis spectrum) for FSZO co-doped ZnO thin films as deposition temperature varies. A sharp increase

in the band gap as the deposition temperature rises is observed due to the Burstein-Moss shift. [192, 193] The shift arises because the Fermi energy (E_F) lies in the conduction band for heavy n-type doped TCOs. As the doping level (carrier concentration) increases more energy states above the conduction band edge become occupied and the filled states block thermal or optical excitation. Consequently, the measured band gap determined from the onset of interband absorption moves to higher energy. The magnitude of the shift ($\triangle_{BM}$), under free-electron theory, is described as:

$$\Delta_{BM} = \frac{\hbar^2}{2m_e^*}[3\pi^2 n]^{2/3} \tag{6.3}$$

where $\hbar$ is the reduced Planck constant, m_e^* is the electron reduced effective mass and n is the electron carrier concentration. [355] However, the band gap shift was obtained for these doped films did not exactly follow above equation as shown in Figure 6.16. Therefore, only BM shift is not sufficient for account in the band gap shift for heavily doped semiconductor like ZnO. [356]

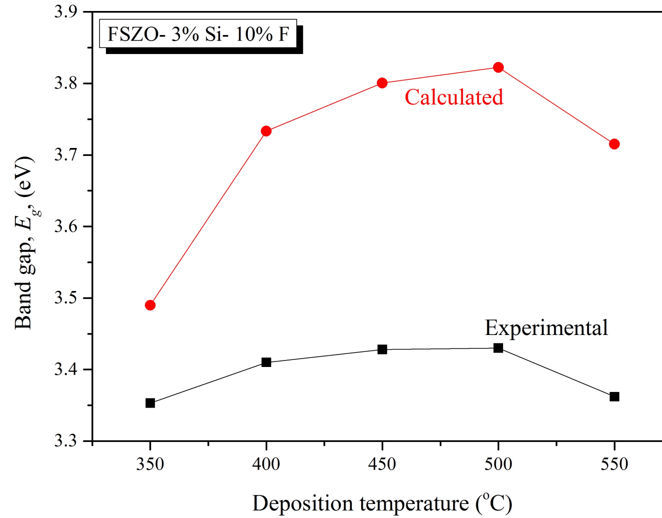

Figure 6.16: Experimental and calculated band gap for FSZO thin films deposited at various temperatures

To account for this discrepancy, a band gap renormalization model was proposed, where

the band gap shrinkage ($\triangle_{RN}$) is considered as a result of mutual exchange and Coulomb interactions between the added free electrons in the conduction band and electron-impurity scattering. In other words, $\triangle_{RN}$ arises from shrinkage or renormalization of the separation between the top of the valence band and the bottom of the conduction band as a result of the degenerate doping itself. [357, 358] This leads to an increase in the energy of the valence-band maximum (VBM) and decrease in the energy of the conduction-band minimum (CBM). The net change in E_g can therefore be taken as a difference of the two contributions, i.e., $\triangle E_g = \triangle_{BM} - \triangle_{RN}$. The total change ($\triangle E_g$) can be experimentally derived from optical-absorption measurements, but decomposition into $\triangle_{BM}$ and $\triangle_{RN}$ component terms is difficult due to uncertainty in the determination of the absolute Fermi level and band-edge positions. [355]

A sharp decrease in transmittance in visible region and also band gap, was observed for the FSZO thin film deposited at 550 °C. These results along with dark (brown-ish) colour of the film deposited at 550 °C suggest that growth rate of the ZnO thin films increases with increasing synthesis temperature, which can lead to a faster decomposition of Zn and dopant precursors than the fragmentation and evaporation of organic ligands. Therefore, the products of the decomposition of precursors have less time to leave the surface of the sample and more impurities such as carbon species might become trapped in the growing layer ZnO. This correlates well with C 1s XPS spectra showing much higher carbon content in high temperature deposited films (Figure 6.9 (b)). These carbon fragment atoms or molecules can create deep donor or acceptor levels (depending on the position of the E_F) below the conduction band. [359] Strong reduction of the transmittance could also be attributed to absorption via extra states within the band gap, associated to the impurities.

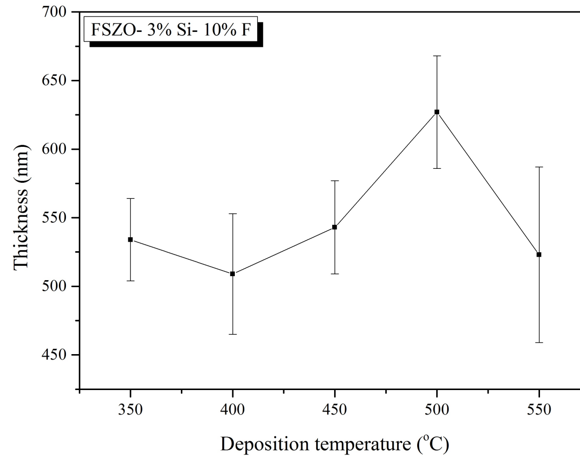

Figure 6.17: Thickness of 3% Si - 10% F FSZO thin films deposited at various deposition temperatures

Figure 6.17 shows thickness of the FSZO samples as a function of deposition temperature calculated using Equations 2.20, 2.21, and 2.22 from optical data. The thickness values for FSZO films deposited at temperatures between 350 °C and 550 °C are nearly equivalent, independent of deposition temperature and in the range of 547 ± 46 nm.

6.3.1.5 Electrical properties

The room temperature electrical properties of 3% Si - 10% F co-doped ZnO thin films as a function of deposition temperature are shown in Figure 6.18. All samples exhibit n-type conductivity and it can be noticed that upon increasing deposition temperature the electrical properties improved. Carrier concentration, mobility and resistivity of about 7.2 $\times$ 10^{19} cm^{-3}, 0.3 cm^2 V^{-1} s^{-1} and 2.7 $\times$ 10^{-1} Ω cm, respectively, were achieved for the FSZO film deposited at 350 °C. Increasing the deposition temperature raised both carrier concentration and mobility. Since the resistivity of a semiconductor material is given by $\rho = 1/ne\mu$, where μ refers to the mobility of the electrons, and n refers to the density of electrons, the resistivity of FSZO films found to decrease by increasing temperature and along with increasing mobility and carrier concentration in thin films. A deposition temperature of 350 °C is presumably too low to successfully integrate the Si and F dopant

atoms into the ZnO lattice and to provide good electrical contact between ZnO grains. A minimum resistivity of about 2.9×10^{-3} Ω cm was achieved for the film deposited at 450 °C. This may be due to the incorporation of more electrically active dopants into the ZnO structure as the deposition temperature increases. The mobility increases with deposition temperature mainly because the particles are larger and thus, there are fewer grain boundaries in the films deposited at higher temperatures.

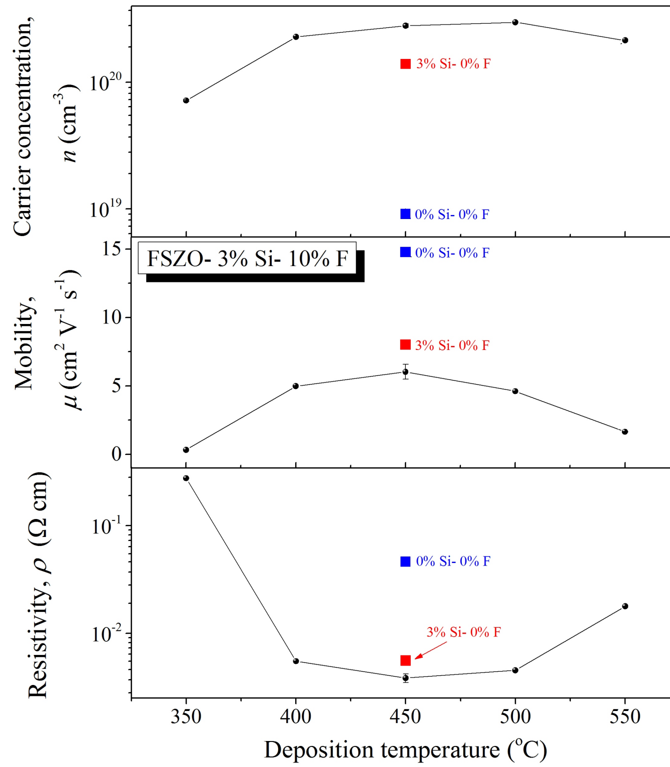

Figure 6.18: Carrier concentration, mobility, and resistivity of FSZO thin films with 3% Si - 10% F concentration, as a function of deposition temperature. Blue and red points show the electrical properties of undoped ZnO and 3% Si-doped ZnO, respectively

However, at higher deposition temperatures (> 500 °C), presumably higher film deposition rate than dopant incorporation rate leads to a lower carrier concentration in the films. Typically, many factors including the grain boundary scattering, the ionized impurity scattering, and structure defects scattering can affect the carrier mobility. In the case of polycrystalline films, the grain boundaries may be considered to be the most dominant

factor affecting carrier mobility. Grain boundaries often contain a large population of distorted or dangling bonds, chemisorbed species, and other defects. Many surface defects generally include oxygen-containing species, which can accept and trap electrons and thus, form a high potential barrier on the surface and at the grain boundary that inhibits electron transport across the grain boundaries. [360] However, F with its surface passivation effect can saturate these dangling bonds and prevent oxygen adsorption, thus, increasing mobility. [224, 361]

Reduction in mobility at high temperatures can be explained by the observed smaller particle size, and the associated increased density of grain boundaries (Table 6.1). Moreover, significant changes in crystallites orientation and morphology of the films as a function of deposition temperature observed above in the XRD spectra (Figure 6.2) and SEM images (Figure 6.13) should also influence significantly the electrical transport in the films. A steep decrease in carrier mobility at 550 °C coincides with a rise in the intensity of (002) reflection and vanishing of other reflections in XRD spectra and smaller particle size as seen in SEM image. From the XPS analysis, a significant decrease in Zn and O at.% on the surface of FSZO film deposited at 550 °C (Figure 6.10), also reflects the considerable carbon content on the ZnO surface leads to the decline of optical and electrical properties. In addition, when thin films are deposited on glass, for example borosilicate glass (with chemical composition of about 80.6% SiO_2, 13% B_2O_3, 4% Na_2O and 2.3% Al_2O_3), boron or sodium might diffuse into the film and increase the resistivity. Contamination by alkali ions from substrate of sheet glass may have a marked effect on electrical conductivity, especially for layers deposited at substrate temperatures greater than 500 °C, as the strain and annealing points of borosilicate glass are 510 and 560 °C, respectively. [187, 362]

More importantly, the carrier concentration in FSZO film deposited at 450 °C is more than two times larger than that in 3% Si-doped ZnO film, and the observed mobility is reasonably high for such high carrier concentration. This fact strongly suggests that in the FSZO thin films grown by spray pyrolysis Si and F act as effective n-type dopants.

6.3.2 Effect of F concentration

6.3.2.1 Structural characterisation

To determine an optimum F concentration, several FSZO thin film samples with 3% Si and different F dopant concentration were prepared at 450 °C. Figure 6.19 shows the XRD patterns of these samples.

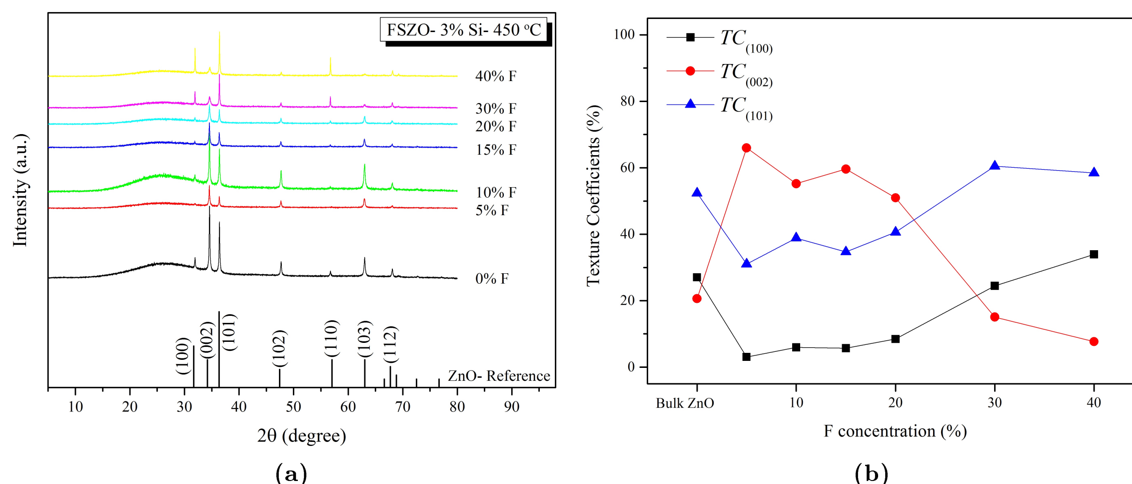

Figure 6.19: (a) XRD patterns of FSZO thin films with 3% Si concentration and various F concentration deposited at 450 °C. The XRD pattern of single doped 3% SiZO (0% F) is also shown. (b) $TC_{(100)}$, $TC_{(002)}$, and $TC_{(101)}$ variations as a function of nominal F concentration

After increasing the concentration of F in the precursor solution, no crystalline phase corresponding to any Zn, Si and F compounds besides ZnO were observed in the XRD patterns of the thin film samples. XRD patterns indicate that Si-doped ZnO (0% F) and 5% F- FSZO films show a slight preferred orientation of crystallites along the (002) plane (c-axis) on the substrate. In the F concentration range from 10 to 20%, the intensity of the (101) diffraction peak was comparable to that of the (002), but because the intensity of the (002) reflection is higher than that of the bulk ZnO, thus the crystallites may still show a little preferential growth along this plane. However, as the F doping level increases to 30%, while the (002) diffraction peak diminishes, the (110) reflection starts increasing, and the growth orientation changes significantly such that in-plane peaks such as (100),

(101) and (110) become predominant in the XRD patterns. At highest F concentration of 40%, growth direction is mainly along (100), (101) and even (110) planes. As previously illustrated in Chapters 4 and 5, a slight preferential orientation along the (002) direction is observed when each dopant is used individually. The observations show that the F concentration has a strong influence on the film texture. The XRD patterns of the FSZO films with high concentration of F (30 and 40%) resemble the XRD pattern of ZnO powder, suggests samples consist of nearly randomly oriented crystallites.

The variation of $TC_{(hkl)}$ values by increasing F dopant concentration is illustrated in Figure 6.19 (b). A clear decrease in the contribution of (002) and increases in the contributions of (100) and (101) phases are observed. This result suggests that the growth orientation is dominated by the [F] / [Zn] ratio when the ZnO films are simultaneously doped with Si and F. Maldonado, *et al.* observed similar effect in ZnO thin films co-doped with In and F. [172] In another work, Altamirano-Juárez, *et al.* reported randomly oriented crystallites for Al+F co-doped ZnO films prepared using sol-gel technique. [170]

The wet chemical growth of horizontally aligned (parallel to the substrate surface) ZnO nanowires have been widely studied. Discussions on theses results might be extended to the observed trends of crystal growth in FSZO thin films. Generally, the reactions taking place in the aqueous systems are considered to be in a reversible equilibrium, and the driving force is to minimise the free energy of the entire reaction system. In wurtzite-structured ZnO grown along *c*-axis, (002) plane is a polar surface, terminated by either Zn^{2+} or O^{2-}. Owing to the high energy of the polar surfaces, when a ZnO nucleus is forming, the incoming precursor molecules tend to be favourably adsorbed on the polar surfaces to minimise the surface energy, resulting in a preferential growth along the (002) plane. [363, 364] On the other hand, if other impurity ions are adsorbed to the Zn^{2+} or O^{2-} ions on the (002) surfaces, they can inhibit the growth along (002) and compel growth along the (101), (100) and (110) surfaces. [363] Experimental results in the literature show that citrate ions can strongly bind to the Zn^{2+} ions on the (002) surfaces and have a strong hindering effect on

the growth there. [365] Decreased growth along c-axis by increasing dopant concentration suggests similar behaviour might happen when the concentration of Si^{4+}, F^{-} and other organic species is increased in the precursor solution.

The variation in lattice parameters and unit cell volume of FSZO thin films as a function of F concentration was investigated and the results are displayed in Figures 6.20.

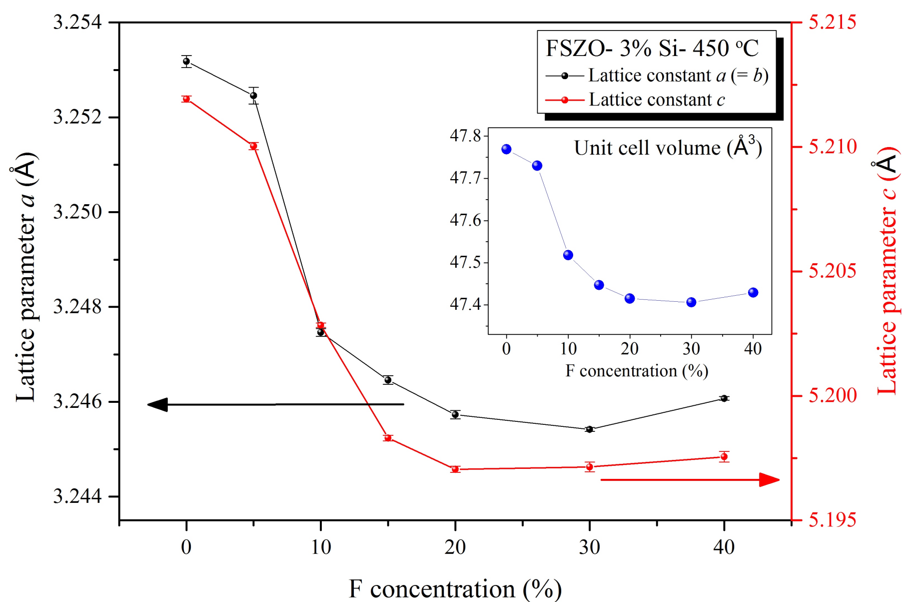

Figure 6.20: Variation of lattice parameters and unit cell volume (inset) of FSZO thin films as a function of F concentration

The ideal ZnO structure is a hexagonal wurtzite structure with two Zn atoms and two O atoms in each primitive cell, and the lattice constants are about $a = b$ =3.249 Å, c =5.206 Å, $\alpha = \beta$ =90° and γ =120°. [123] The lattice constants a and c of FSZO thin films are weakly dependent on the F concentration and were slightly smaller than those of ZnO doped by Si only. A slight reduction in the lattice parameters happens when the diffraction peaks are slightly shifted to the right (higher 2θ). This indicates that small variations in the lattice parameters as increasing F concentration leads to higher defect concentrations in ZnO. Since the unit cell volume of hexagonal structure is given by $V = 3\frac{\sqrt{3}}{2}a^2c$, the unit cell volume follows the trend observed for the a and c lattice constants and decreases

from 47.77 (Å^3) at 0% F concentration to about 47.40 (Å^3) at 20 - 30% F concentration. The contraction of the ZnO unit cell at higher F concentration can be attributed to the substitution of F^- for O^{2-} in ZnO lattice during the formation of FSZO films, and due to the fact that the ionic radius of F^- (1.31 Å) is slightly smaller than that of O^{2-} (1.38 Å). [150]

Using the Scherrer equation (2.9) the average crystallite size of the thin films grown at 450 °C with different F concentration were calculated and presented in Table 6.3. The approximate mean crystallites size reaches a minimum at F concentration of 20 - 30% and increases again as F concentration further increases.

F dopant concentration (%)	Mean crystallite size (nm)
0	65.7 ± 11.2
5	69.8 ± 2.9
10	61.8 ± 1.6
15	62.9 ± 0.8
20	64.0 ± 1.7
30	58.9 ± 6.8
40	78.2 ± 9.1

Table 6.3: Crystallite size of FSZO thin films with different F concentrations deposited at 450 °C calculated using Scherrer equation

6.3.2.2 XPS analysis

Survey XPS spectra of the FSZO thin films with nominal Si and F concentrations of 3% and 30%, respectively, deposited at 450 °C are shown in Figure 6.21. XPS peaks show that the FSZO thin films contain only Zn, O, Si and F elements and a trace amount of C. The following binding energies were studied: Zn $2p_{3/2}$ at ~ 1021 eV, O 1s at ~ 531 eV, Si 2p at ~ 103 eV, F 1s at ~ 685 eV, and C 1s at ~ 284 eV. The XPS survey spectra of other samples are similar.

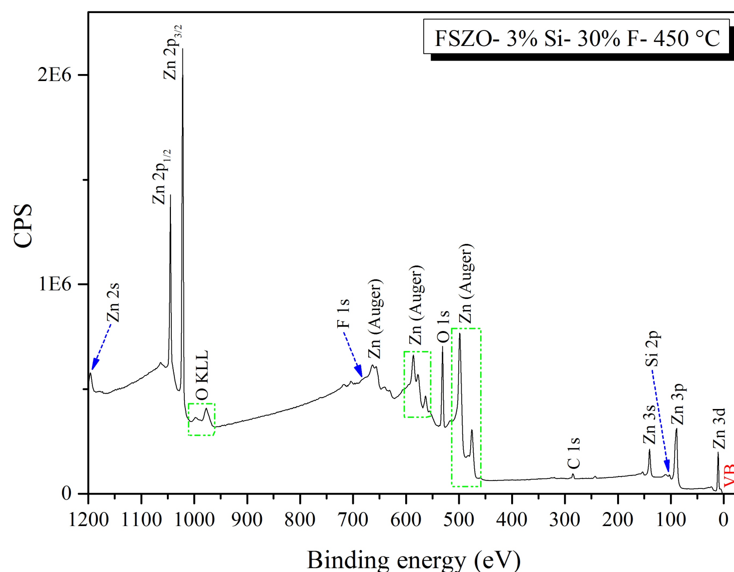

Figure 6.21: XPS survey spectrum of FSZO thin film with 3% Si - 30% F deposited at 450 °C

All spectra were charge corrected by setting the C 1s spectral component binding energy to 284.6 eV. High resolution Zn $2p_{3/2}$ and F 1s core level XPS spectra of FSZO films with different nominal F concentrations are shown in Figure 6.22. Figure 6.22 (a) shows the typical XPS data of Zn $2p_{3/2}$ at a BE of 1021.7 eV in the FSZO films. All peaks are highly symmetric and could be fitted with a single component. Addition of further components did not significantly improve the quality of the fit. Moreover, the binding energy (BE) of the Zn $2p_{3/2}$ peaks remained unchanged by increasing F concentration.

The F 1s peak is usually observed at binding energies between 684.0 eV and 686.0 eV for F^- ion bound to a metal ion and, it lies at higher binding energies of about 689.0 - 690.0 eV for the F^- ion attached to C in organic compounds. [339, 348] The F 1s core level spectra of FSZO films are displayed in Figure 6.22 (b). The observed peaks have binding energy of ~ 685.7 eV and are attributed to the fluoride ions in the ZnO lattice. The intensity of the F 1s peak increases as the F concentration in the solution is increased. The very broad peaks with very low intensities corroborate that the F concentration in the samples is much less than the amount of F added to the starting spraying solution. One possible reason for this

might be a possible reaction of NH_4F and Si^{4+} (for example SiO_2 or $Si(CH_3CO_2)_4$) which occurs in aqueous solutions and described by: [366, 367]

$$Si^{4+} + HF + NH_4F \rightleftharpoons (NH_4)_2SiF_6 \tag{6.4}$$

The ammonium hexafluorosilicate, $(NH_4)_2SiF_6$, decomposes thermally at a temperature of about 300 °C to form gaseous products, according to: [368]

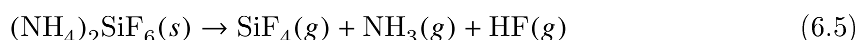

$$(NH_4)_2SiF_6(s) \rightarrow SiF_4(g) + NH_3(g) + HF(g) \tag{6.5}$$

Therefore, it is expected that most of the F^- in the spray solution is volatilized in the hot environment of the spray pyrolysis chamber before arriving to the surface of the substrate. By increasing the concentration of F^- in the solution to 40%, more fluoride ions have the opportunity to reach to the surface of the substrate and be incorporated into the ZnO matrix.

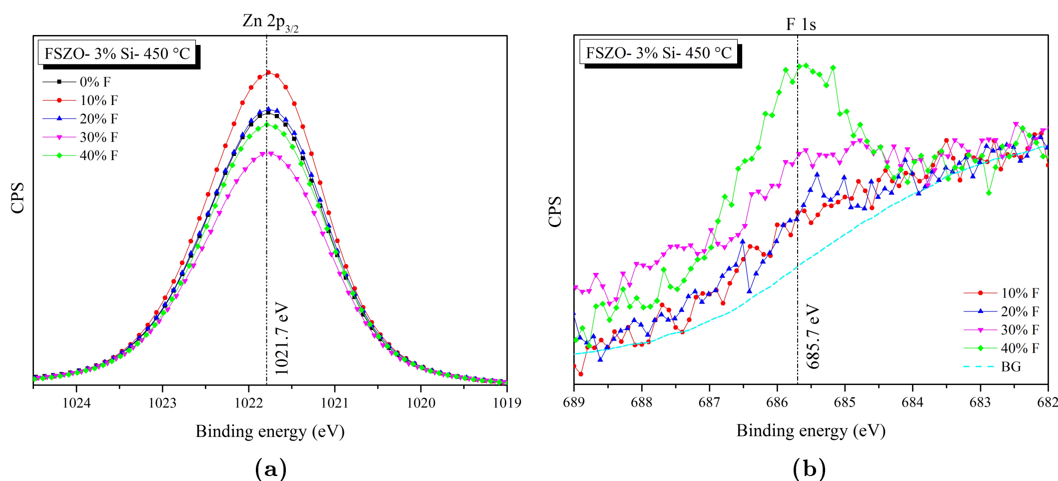

Figure 6.22: (a) Zn $2p_{3/2}$ and (b) F 1s XPS spectra of FSZO films with different nominal F concentration and 3% Si, deposited at 450 °C (blue dashed line in figure (b) shows the background)

Figure 6.23 (a) shows the XPS spectra of the Si 2p core level of FSZO thin films deposited at 450 °C with different F concentrations. Figure 6.23 illustrates an increase in

Si 2p peak intensity on the surface with increasing F concentration in FSZO thin films. The Si 2p peak of FSZO films with different nominal F concentration were fitted using one component, suggesting that only one chemical state of Si is needed to account for the spectra. This silicon state corresponds to Si^{4+} (~ 103.1 eV) and has similar binding energy to Si−O bond in SiO_2 which usually appears at binding energies around 103 - 103.5 eV. [339, 348] The Si^{4+} oxidation state points out that Si in the FSZO thin films will donate two extra electrons to the electrical conduction owing to the fact that it is replacing Zn^{2+} sites in the Si^{4+} state. Si^{4+} state might be assigned to a secondary phase like SiO_2 deposited on grain boundaries, but such a phase was not observed in the XRD spectra of FSZO films (Figure 6.19). [141, 143] More interestingly, Figure 6.23 (a) illustrates an increase in the Si 2p peak intensity on the surface with increasing F concentration in FSZO thin films. This suggest that F not only can act as a n-type dopant contributing electron to the ZnO lattice directly, but also helps Si ions to incorporate more effectively at the substitutional zinc sites in the ZnO lattice.

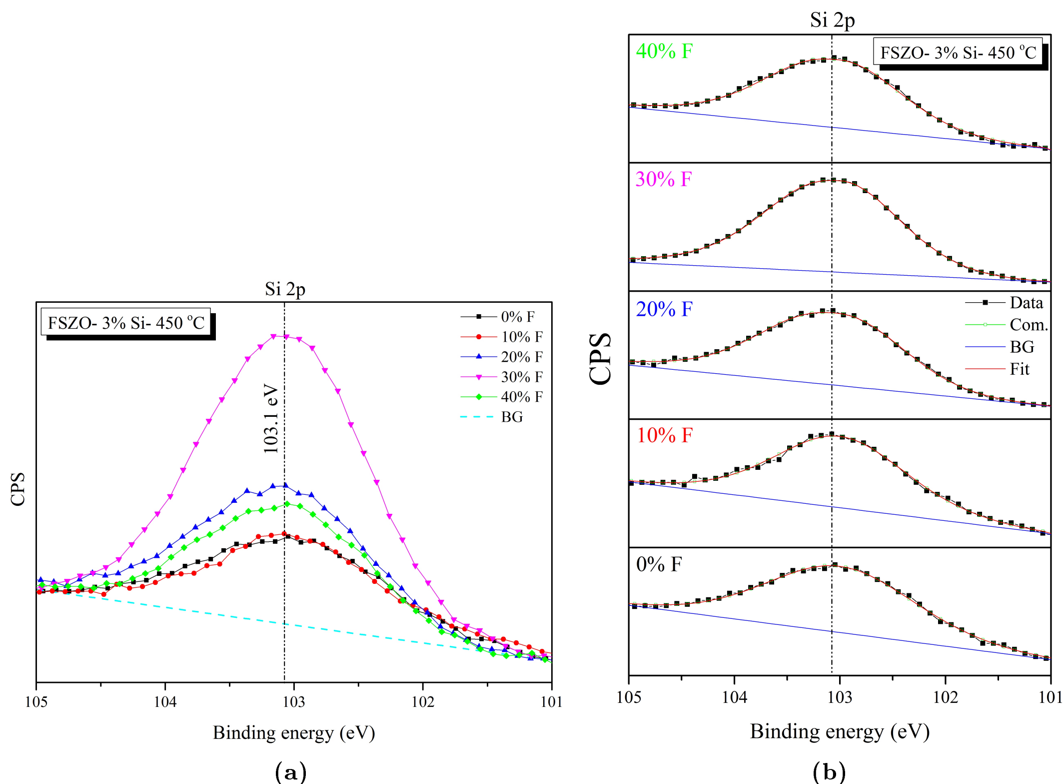

Figure 6.23: High resolution (a) Si 2p and (b) fitted Si 2p XPS spectra of FSZO thin films deposited at 450 °C as a function of F concentration (Blue dashed and solid lines show the background)

The XPS spectra for the O 1s core level are broad and asymmetric indicating the presence of multiple oxygen species (Figure 6.24 (a) and (c)). The O 1s spectra were curve fitted and the peaks are best fitted with two symmetric Gaussian peaks. The two components are centred at about 531.8 and 533.1 eV. The peak with the lowest binding energy (OZ) of the O 1s spectrum is known as the O 1s signal for O^{2-} ions in the hexagonal structure of ZnO lattice surrounded by zinc ions. The higher binding energy peak (OC) is associated with adsorbed hydroxyl (OH), H_2O, or carbon containing groups on the surface of the FSZO thin films. Therefore, changes in the intensity of this component may be related in part to the variations in the concentration of oxygen vacancies.

FSZO- 3% Si - 450 °C	OZ (531.8 eV)	OC (533.1 eV)	OZ/OC
10% F	75.2%	24.8%	3.0
20% F	68.1%	31.9%	2.1
30% F	55.9%	44.1%	1.3
40% F	55.0%	45%	1.2

Table 6.4: Relative area percentage of OZ and OC components in O 1s peak for FSZO samples deposited with different F concentration

Although the area of the O 1s peak is more or less equivalent in FSZO films with various F concentrations, but from the comparative studies, it is found that the integrated peak area for the OC peak gradually increases with the increase in F doping concentration. The calculated content of OC peak in O 1s XPS spectrum changes from 24.8% to 44.1% for the 10% to 30% F in FSZO thin films (Table 6.4). This indicates a gradual increasing of chemisorbed oxygen species on the surface layer with the increase in F doping concentration. Major *et al.* observed that as the In_2O_3 films were etched, the O 1s peak at lower binding energy due to oxygen in In_2O_3 lattice appeared and increased with increasing depth, while the higher binding energy O 1s peak diminished, and at a depth of 1000 Å, only a single O 1s peak at lower binding energy (O^{2-} in In_2O_3) was observed. [369] Similar observation of decreased relative intensity of higher binding energy O 1s component with increasing etching time in Al-doped ZnO films was also reported by Chen *et al.* [370]

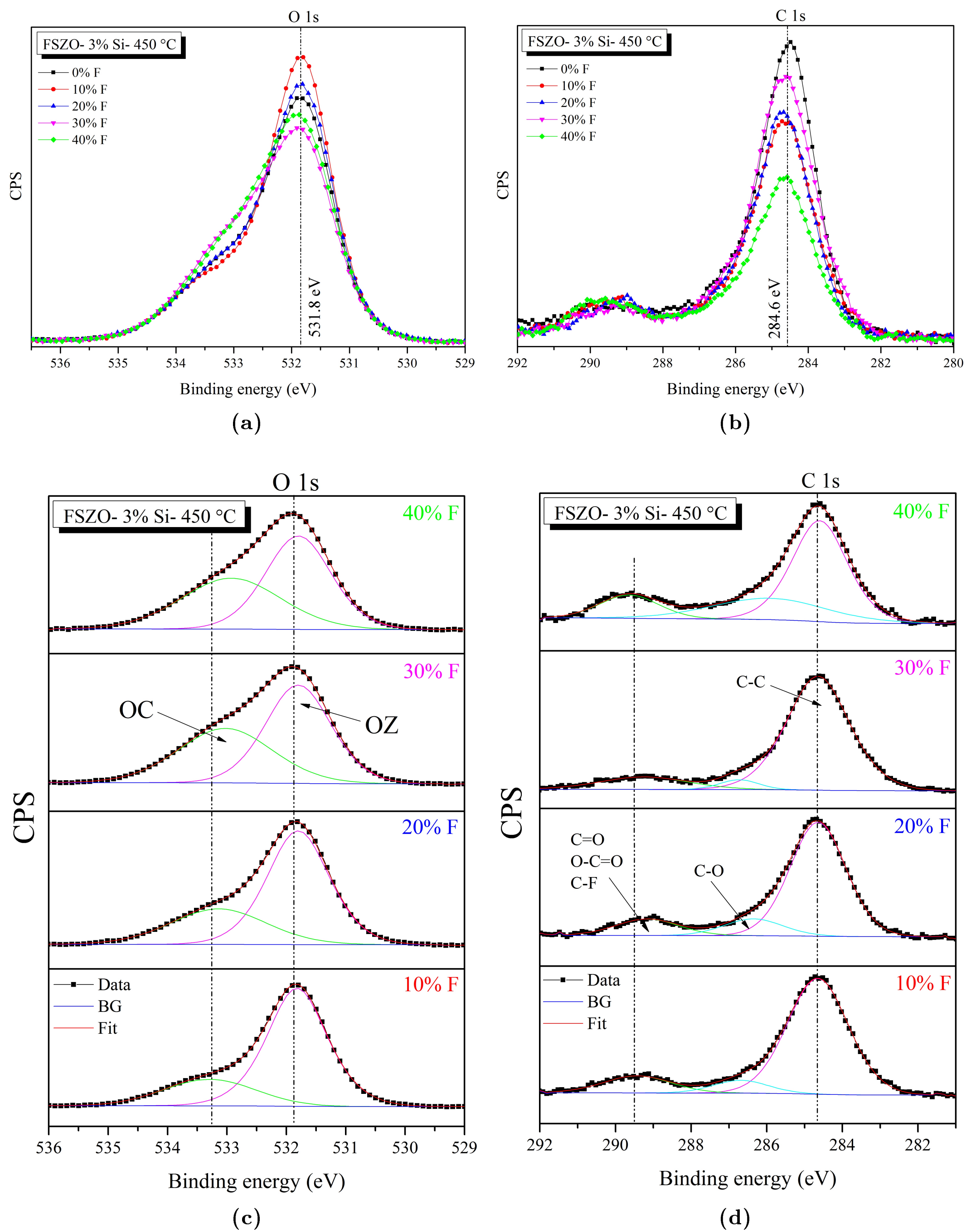

Figure 6.24: High resolution XPS spectra of FSZO thin films with various nominal F concentrations deposited at 450 °C (a) O 1s, (b) C 1s, (c) curve fitted O 1s, and (d) curve fitted C1s

The surface of the samples was etched using Ar to remove the carbon-containing organic

contaminants on the surfaces of samples. The C 1s peaks are still observed at 284.6 eV and 289.5 eV for the FSZO films due to the small amounts of C contaminants remaining on the surface (Figure 6.24 (d)). The 284.6 eV peak of FSZO films is assigned to the binding energy of C in C−C bond. The weak peak at about 286.4 ± 0.3 eV usually comes from C in the C−O single bond. The peak at binding energy of 289.3 ± 0.2 eV is attributed to the contribution of the surface residual C contaminants in the form of C−F, C=O and O=C−O bondings. [339, 371] The area of the peak at binding energy about 289.5 eV is increases as F concentration increases to 40%, which might be because of the higher concentration of organic species containing C−F bonds.

The relative atomic concentration of zinc, oxygen and carbon on the surface of the samples were derived from XPS data using Equation 2.12 and the method explained in Section 6.3.1.2. The O concentration is slightly above 50% for all of the FSZO samples.

High resolution scans of the Si 2p, F 1s, Zn 3p and O 1s signals were used to determine the Si:Zn and F:O ratios in these samples. The F:O ratio in these samples was determined by examining high resolution scans with a binding energy range of 695 to 680 eV, and 540 to 520 eV which includes the F 1s and O 1s signals, respectively. The peak areas were integrated using a linear baseline and normalized by the relative sensitivity factors (4.43 for F 1s and 2.93 for O 1s). As shown in Figure 6.25, using precursor solutions with a fixed silicon concentration, increasing the the concentration of fluorine led to a increase in silicon concentration on the surface of the films deposited at 450 °C, while the fluorine concentration remained almost constant at about 2.0 at.%.

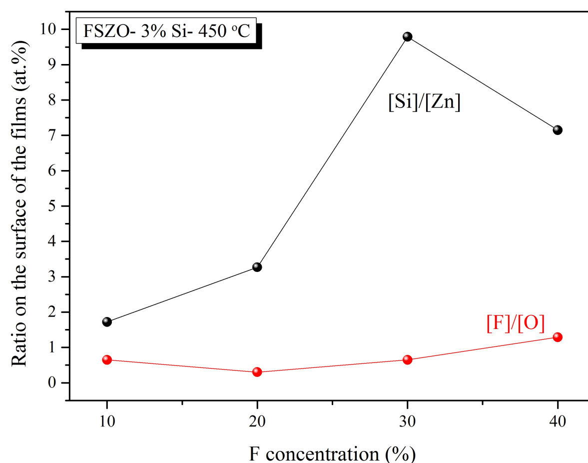

Figure 6.25: Si:Zn and F:O ratios on the surface of the FSZO thin films deposited at 450 °C from precursor solutions with a fixed 3% Si and varying amounts of F

Higher Si:Zn ratio on the surface of the thin films can be attributed to the surface segregation of the dopant atoms. A possible explanation to driving forces to segregation originates from the size mismatch between the dopant and host cations and the associated free surface energy minimization by pushing the larger or smaller dopant to free surfaces or interfaces, and to the charged defect interactions such as a strong association of dopant cations with oxygen vacancies, which can drive the dopants to positively charged interfaces where oxygen vacancies are in abundance as well as with polar surfaces. [372] The greater amount of silicon in the films is the most straightforward explanation for increased carrier concentration (Figure 6.31). However, given the unavoidable presence of adventitious carbon on the ZnO surface, the XPS results are more likely to be quantitative if measurements were carried out on samples which are etched for longer time to minimise carbon presence on the surface.

6.3.2.3 Morphology

The effect of F concentration on the morphology of FSZO thin films was also studied using AFM and SEM. Figure 6.26 displays the surface morphologies of FSZO thin films deposited with 3% Si and various F dopant concentration at a constant temperature of 450 °C as

measured using AFM. The AFM images of FSZO films exhibit smaller particle size with increasing F concentration. The uniformity (of the particle size distribution) appeared to deteriorate as F concentration increases to 30%, as seen from changes in the size and shape of the particles on the surface.

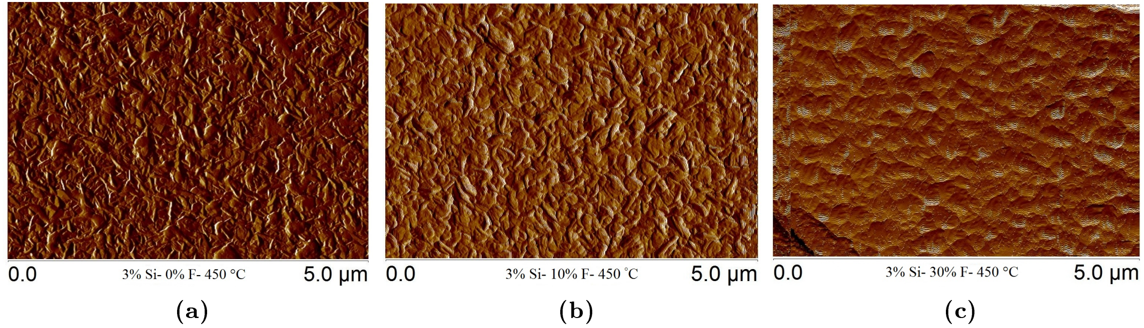

Figure 6.26: AFM images of FSZO thin films deposited at 450 °C with 3% Si and (a) 0%, (b) 10%, and (c) 30% F concentration

The surface roughness of FSZO thin films was found to decrease from 20.4 nm at 10% F concentration to 12.1 nm at 30% F concentration, in consent with the decrease in the mean particle size. The mean particle size for FSZO films with 10% F and 30% F calculated from AFM images was about 171 ± 87 nm and 147 ± 40 nm, respectively. The FSZO film with 10% F concentration exhibited higher roughness owing to larger particle size. However, samples might also exhibit higher roughness despite having smaller particle size, due to the less uniform size distribution of the particles on the surface.

Figure 6.27 shows the microstructures of the FSZO samples with different F concentrations as observed using SEM. In the XRD patterns For the 3% Si (0% F) and 10 - 20% F (3% Si) - FSZO samples both the (002) and (101) reflections are observed (Figure 6.19). These reflections may be correlated to the hexagonal plate and pyramid surface morphologies seen by SEM, respectively (Figure 6.27 (b), (c) and (d)). [373, 374]

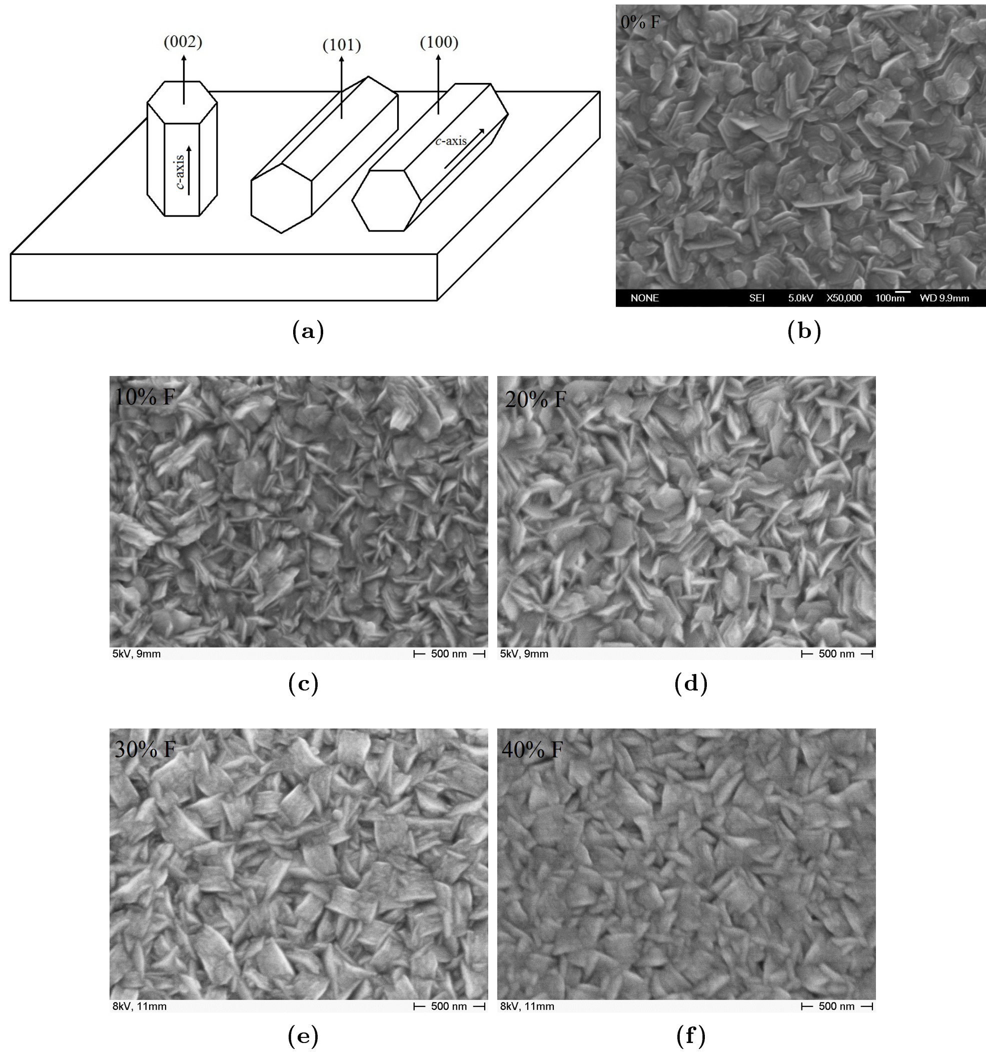

Figure 6.27: (a) ZnO schematic crystallite showing the (002), (101) and (100) planes (Figure adapted form Hu *et al.* [65]), and SEM images of FSZO thin films deposited at 450 °C with Si concentration of 3% and F concentration of (b) 0%, (c) 10%, (d) 20%, (e) 30%, and (f) 40%

Figure 6.27 (a) shows the relationship between microstructure and crystal growth orientations of ZnO films. From this Figure, it is obvious that the *c*-axis is perpendicular to the substrate, leading to columned hexagonal-shape structures in ZnO films with preferential (002) orientation. It can also be seen that the *c*-axis is parallel to the substrate, leading to pyramid-like structures in ZnO films with (101) and (110) oriented crystallites. A significant change in the surface morphology of the FSZO thin films is observed when the

concentration of F is $\geq$ 30%. These films show a well-textured morphology with pyramid-shape particles on the surface, which is consistent with the higher intensity of (101) and (110) reflections in the XRD patterns. Similar XRD and SEM results were reported for B-doped ZnO thin films by Soo-Lee *et al.* [373] and Shah *et al.* [375, 376] They also observed that their doped ZnO thin films exhibited a marked preferred orientation along the (110) crystallographic plane. From these results, we can confirm that the incorporation of F into ZnO lattice will modify the crystal growth and particle orientation on the surface of the films.

The size of the pyramidal shaped particles on the surface is a few hundred nanometres as shown in Figure 6.27 (f). Again, the crystallite size which calculated from the Scherrer equation (2.9) is less than 100 nm. This discrepancy was well explained in section 6.3.1.3. Besides, we can also suggest that the microstructure of FSZO films consists of small crystallites at the bottom of the film, followed by the growth of larger crystallites which emerged with (101) and (110) crystallographic orientations.

6.3.2.4 Optical properties

Figure 6.28 (a) shows the transmittance spectra of FSZO thin films with constant Si concentration of 3% and various F concentrations, all deposited at 450 °C. Thin films with F concentration between 5 and 30% exhibit an average transmittance of over 85% in the visible wavelength region as compared to the transparency of the glass which is around 92%. However, the transparency of the films with F concentration of 40% drops to lower than 80% as illustrated in Figure 6.28 (b). The optical transmission for the thin films decreases in the NIR wavelength range as the F concentration increases. Generally, increasing carrier concentration induces a decrease of transmittance in the NIR wavelength range due to the plasma reflection, as explained in Section 6.3.1.4. Accordingly, the transmittance decrease in the NIR wavelength range is more pronounced for the FSZO thin films with higher carrier concentration.

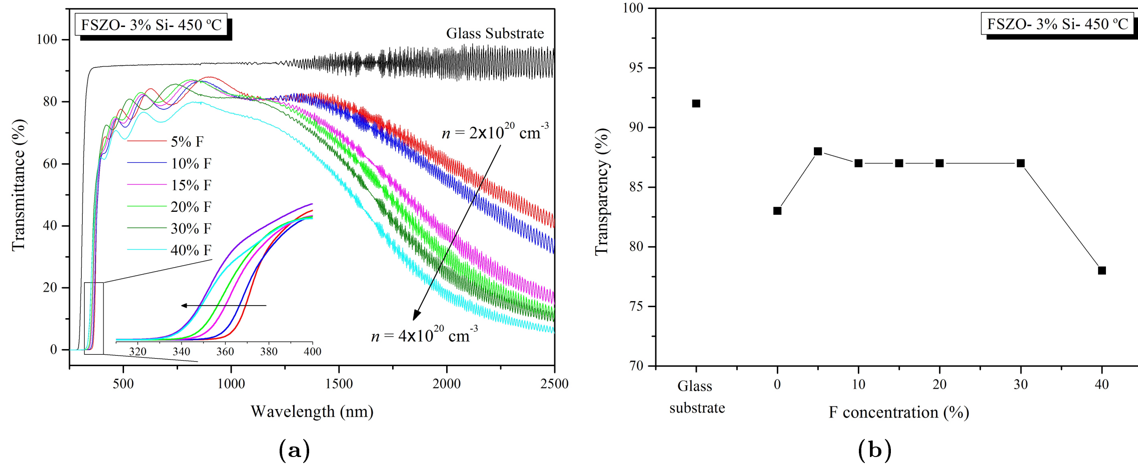

Figure 6.28: Variation of (a) UV-Vis-NIR transmittance spectra and blue shift of the absorption edge (inset), and (b) transparency of FSZO thin films as a function of F concentration

A blue shift of the fundamental absorption edge for FSZO thin films with increasing F concentration is observed in inset in Figure 6.28 (a). This blue-shift is mainly attributed to the Burstein-Moss effect, [192, 193] which implies that the increase of the electron concentration results in a shift of the Fermi level, thereby causing widening of the band gap resulting in the blue-shift of the absorption tail (Section 6.3.1.4). Moreover, the shift in plasma frequency in the NIR region is larger than the Burstein-Moss shift in the near-UV region. Thus, the transmission window becomes narrower as the carrier concentration increases. This means that both the conductivity and the transmittance are interconnected since the conductivity is also related to the carrier concentration, as discussed in Section 6.3.1.5.

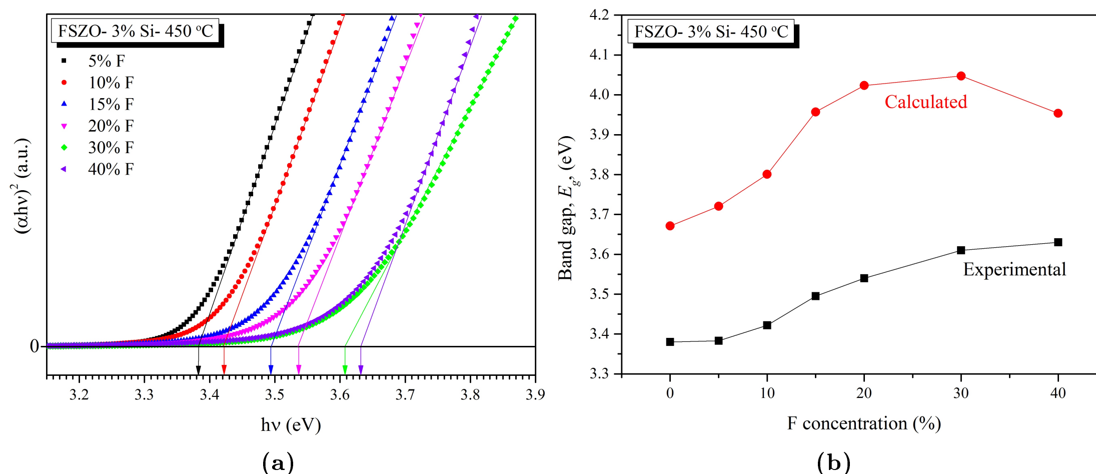

Figure 6.29: (a) Optical band gap calculation and (b) experimental and calculated band gap of FSZO thin films deposited at 450 °C with different F concentration

The optical band gap of the FSZO thin films were higher than that of the Si-doped ZnO thin film and increased from about 3.38 eV at 3% Si - 0% F doping concentration to about 3.61 eV at 3% Si - 30% F (Figure 6.29 (b)). The increase of carrier concentration as the F concentration increases (Figure 6.31 (a)) supports the fact that the band gap widening is dependent on the carrier concentration and F content. The calculated band gap value (calculated from Equation 6.3) is nearly 0.6 ± 0.2 eV higher than the experimental value for all samples and the evident difference may be due to two reasons: (1) the band narrowing (BN) effect, which results from the many-body interactions between the free carriers and ionized impurities in the doped ZnO films, and (2) the nonparabolic effect of the conduction band as further discussed in Section 6.3.1.4. [355, 377]

The variation of the thickness of the FSZO films with increasing F concentration was investigated using the method explained in Section 6.3.1.4. The thickness of the FSZO thin films with F dopant concentration of 0% to 20% is more or less equal and about 570 ± 30 nm. However, a decrease in thickness is observed as the F concentration increases to 30% and higher (Figure 6.30). Considering the ideal axial ratio for a hexagonal close-pack crystal structure (c/a =1.633), under exact same conditions, crystal growth along c-axis

should result in higher thickness. This correlates very well with the increased crystal growth along *a*-axis and other in-plane orientations with increasing F concentration for FSZO thin films (Figures 6.19 and 6.19 (b)), which can lead to decrease in the film thickness.

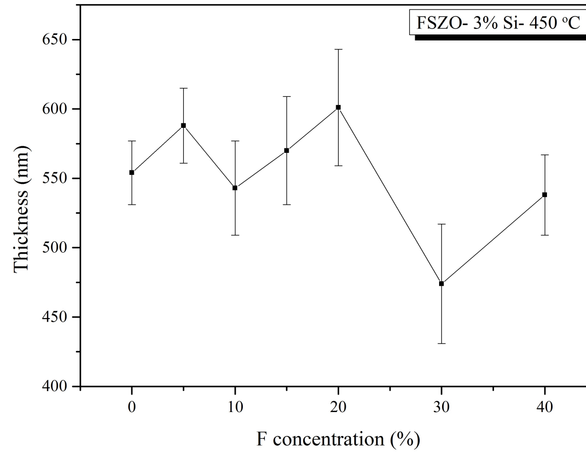

Figure 6.30: Variation of thickness as a function of F concentration in FSZO thin films with constant 3% Si concentration deposited at 450 °C

6.3.2.5 Electrical properties

Figures 6.31 shows the variation of room temperature carrier concentration, mobility and resistivity, respectively, of FSZO films with constant Si concentration of 3% deposited at 450 °C as a function of F concentration. For the purpose of comparison, the electrical properties of 3% Si-doped ZnO deposited at 450 °C are also included in the graphs. The resistivity of FSZO films was found to decrease gradually with increasing F concentration from 5.4×10^{-3} Ω cm at 0% F to 1.8×10^{-3} Ω cm at 40% F. For films with $<$ 20% F, it can be observed that the resistivity reduction in the FSZO films is mainly attributed to the higher carrier concentration. The decrease in mobility in this region is likely due to the increase in the carrier density and the resulting electron-electron scattering, as well as some deterioration in the crystalline quality and formation of concentrated dopant atoms at the grain boundaries. On the other hand, further decreases in resistivity at F concentrations of 30 and 40% are due to the higher mobility rather than carrier concentration.

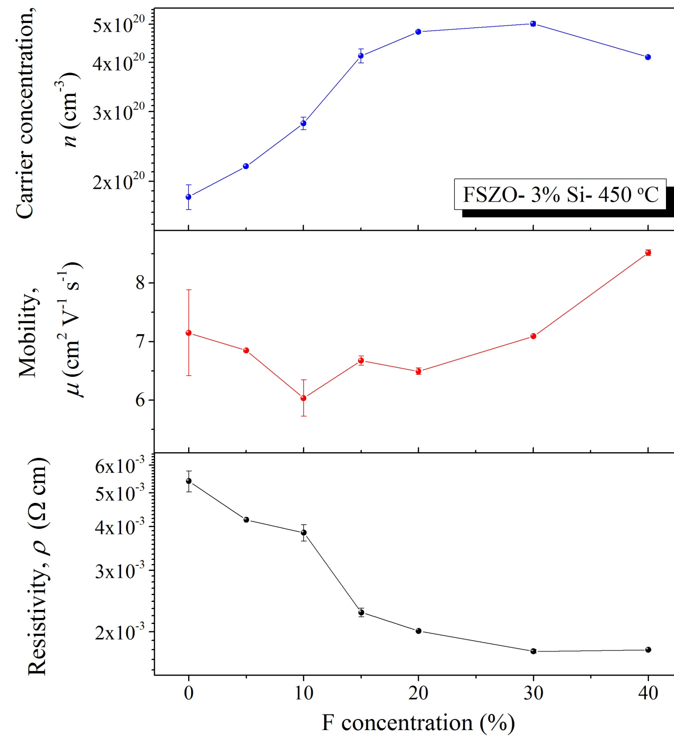

Figure 6.31: Dependence of carrier concentration (blue), mobility (red), and resistivity (black) on concentration of F for FSZO thin films with constant 3% Si concentration, deposited at 450 °C

In order to determine the validity of the observed electrical properties, several series of FSZO films were deposited under the same conditions. Very small error bars confirms that production of Si+F co-doped ZnO thin films by spray pyrolysis is a reproducible process and that the presented results are reliable.

Through a combination of improvement to carrier concentration and mobility, the optimal resistivity reached a minimum value of about 1.8×10^{-3} Ω cm for F concentration of 30 - 40%, when average carrier concentration and mobility were ~ 4.5×10^{20} cm^{-3} and ~ 7.5 cm^2 V^{-1} s^{-1}, respectively. The increase in carrier concentration might originate from the substitution of F^- at O^{2-} sites, which would release one extra free electron per substitution and enhance conductivity. Density functional theory (DFT) calculations by Liu *et. al.* showed that under the oxygen-free conditions (as used for the FSZO thin films deposition) it is energetically more favourable for F^- ions to enter into the O^{2-} sites considering the

similar ionic radii of the two anions and due to the lower formation energy of oxygen vacancies. [223] At higher F concentrations F^- may also form interstitial defects. Thus, F^- can act as a donor dopant and provide free carriers. For hexagonal ZnO the conduction band mainly originates from the metal orbitals, namely the empty 4s orbitals of Zn^{2+}, while the valence band derives from the filled 2p orbitals of O^{2-}. [378] Therefore, dopants such as Al, In or Si which substitute for Zn will mostly perturb the conduction band, whereas, substitution for O would principally cause valence band perturbation. The former will result in a strong scattering of the electrons in the conduction band, and consequently reduce the mobility. On the other hand, the latter effect leaves the conduction band fairly free of scattering and either leaves the mobility unchanged, or leads to an increase in electron mobility. [151, 152] The lower mobility values observed for the FSZO samples comparing to undoped ZnO, may be ascribed to the polycrystalline nature of the thin films and due to the fact that the carriers undergo scattering by grain boundaries, as well as Si doping which causes perturbation to the conduction band, and thus an extra strong ionised impurity scattering of the electrons.

6.3.3 Effect of silicon concentration

6.3.3.1 Structural characterisation

As mentioned in the Experimental section, to find the optimum silicon dopant concentration for FSZO, a range of FSZO thin films with a constant F dopant concentration of 30% and various Si concentrations were deposited at 450 °C. XRD patterns of the samples are shown in Figure 6.32 (a). The diffraction patterns correspond to hexagonal wurtzite structure.

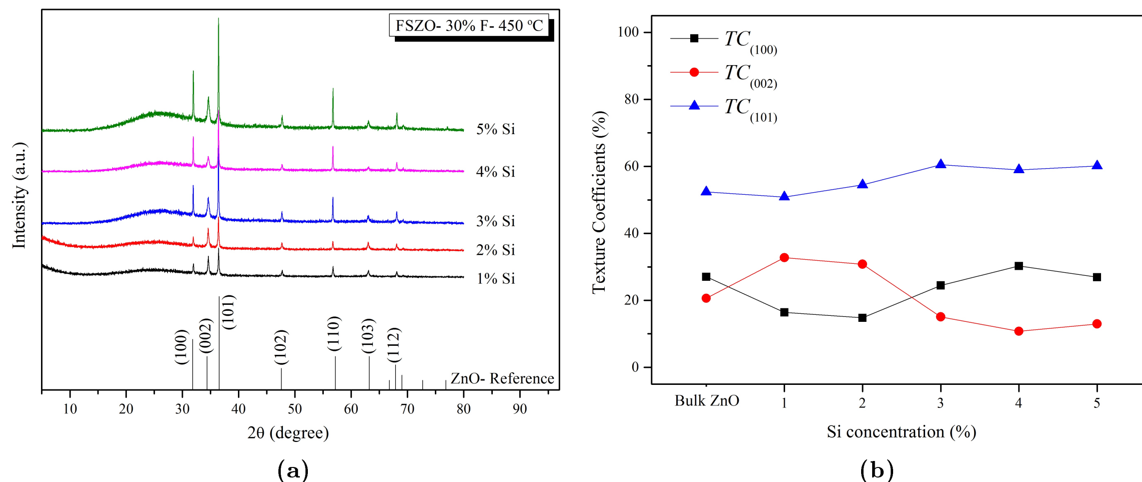

Figure 6.32: (a) XRD spectra and (b) variation of $TC_{(100)}$, $TC_{(002)}$, and $TC_{(101)}$ of FSZO thin films with 30% F concentration and various Si concentration deposited at 450 °C

As expected the thin films show changes in crystallite orientation with changes in dopant concentration. It was observed that by increasing the F doping level to 30%, at 3% Si, the preferred orientation changed from (002) to mainly (101) and (100) (Figure 6.19). As all these samples were deposited with constant F concentration of 30%, the fact that the (002) reflection does not dominate, even at a low Si concentration of 1%, is predictable. The changes in texture coefficients are shown in Figure 6.32 (b). The crystallite orientation for FSZO thin films with 3% Si and greater, at 30% F, are pretty close to random.

Another interesting point was that the peak positions corresponding to the (100), (002) and (101) planes were slightly shifted to higher 2θ values at higher Si concentration. One of the possible reasons for this might be the difference in ionic radius of Si^{4+} which is much smaller than that of Zn^{2+} ($r_{Si^{4+}} = 0.26$ Å and $r_{Zn^{2+}} = 0.60$ Å [150]). Hence, replacing Zn^{2+} by Si^{4+} in the ZnO lattice leads to a decrease in lattice constants.

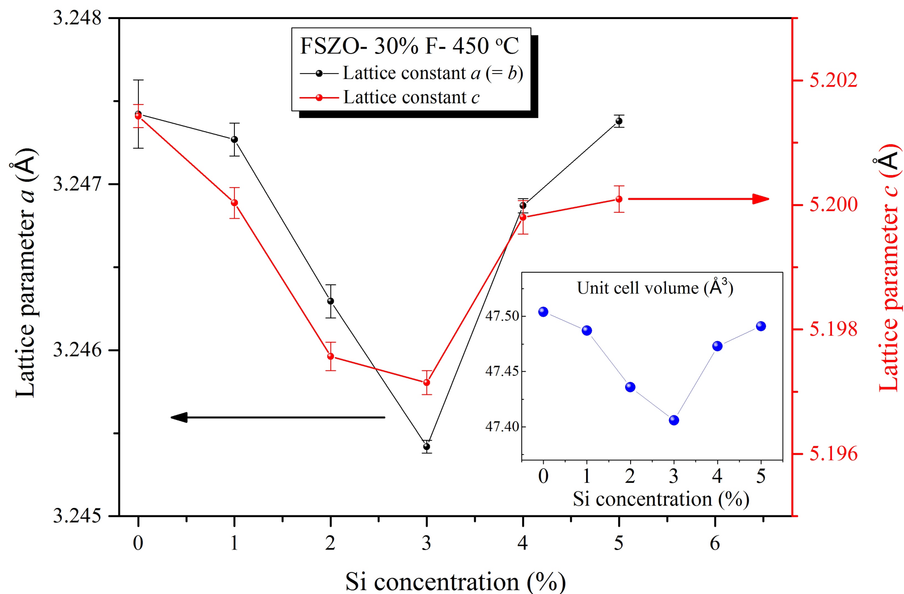

Figure 6.33: Variation of lattice parameters and unit cell volume (inset) of FSZO thin films with 30% F, as a function of Si concentration

Average crystallite sizes were calculated from X-ray diffraction peak widths using the method outlined in Section 6.3.1.1. In all cases, the peaks used for this measurement corresponded to the planes which had the highest intensities. The results are plotted against Si concentration in Figure 6.34. The results show that the mean crystallite sizes in FSZO films grown with various Si concentrations at 450 °C were in the range of 56 - 80 nm. The crystallite size was fairly constant 57.5 ± 1.5 nm up to Si concentration of 3% and grows at Si concentration of 4 and 5%.

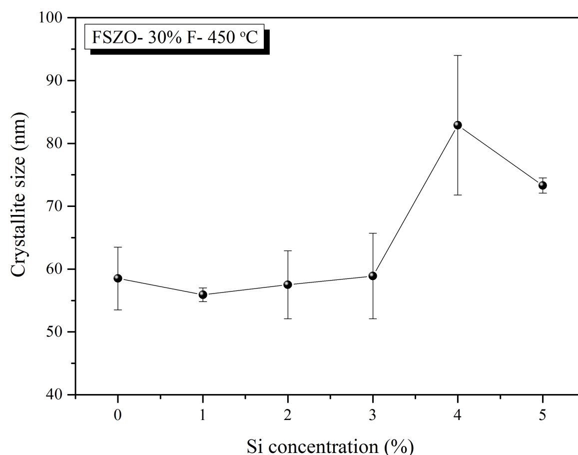

Figure 6.34: Variation of the crystallite size of FSZO films with Si concentration, calculated from XRD data

6.3.3.2 Surface analysis

The surface element composition, oxidation states, and chemical environment of elements in the FSZO thin films with different Si concentration were analysed using XPS. All spectra plotted after they were charge corrected by shifting all peaks to the C 1s spectral component (C–C) binding energy set to 284.8 eV. The Zn 2p spectra are shown in Figure 6.35, where the two strong peaks centred at 1044.8 eV and 1021.7 eV are associated to the core lines of Zn $2p_{1/2}$ and Zn $2p_{3/2}$ in ZnO. Transition metals generally do not show remarkable shifts, [379] which may be the reason why no significant shift of the Zn 2p peaks is observed when the concentration of Si is increased.

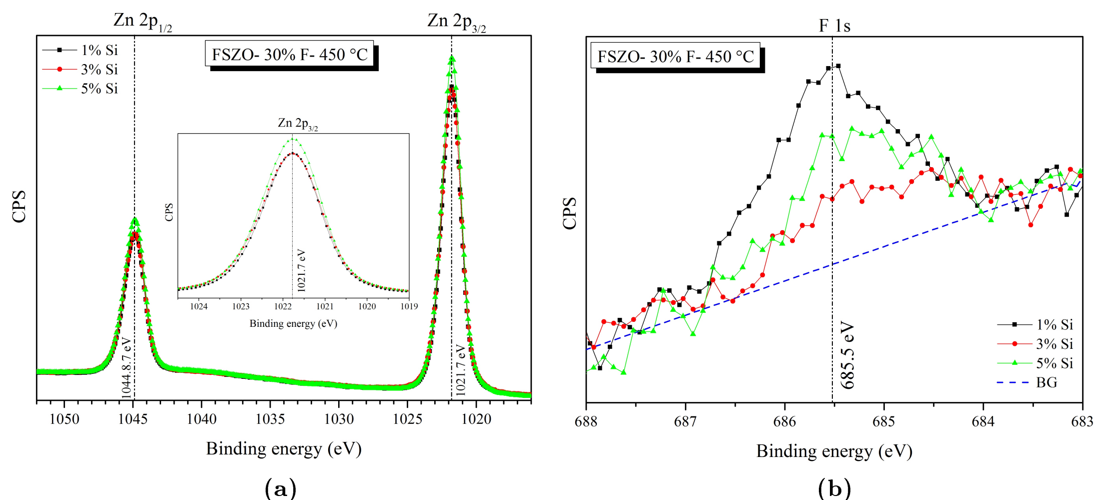

Figure 6.35: (a) Zn 2p and (b) F 1s high resolution XPS core line spectra of FSZO films as a function of Si concentration at constant 30% F

The BE values of F 1s core line (685.5 eV) is consistent with F^- ions bound to metal ions. [339, 348] This supports the hypothesis of F^- substitution for O^{2-} in the ZnO lattice, which results in the formation of Zn–F bonds. The intensity of the F 1s peak was found to slightly decrease with increasing Si concentration.

Figure 6.36 shows the Si 2p spectra of FSZO thin films with Si concentrations of 1, 3, and 5%. The binding energy around 103.1 eV can be assigned to the Si^{4+} since the Si 2p peak associated to the Si–O bond in SiO_2 has a similar binding energy of around 103 - 103.5 eV. [339, 348] The Si 2p peak intensity grows as the Si concentration is increased to 3%, but drops with a further increase of Si concentration to 5%.

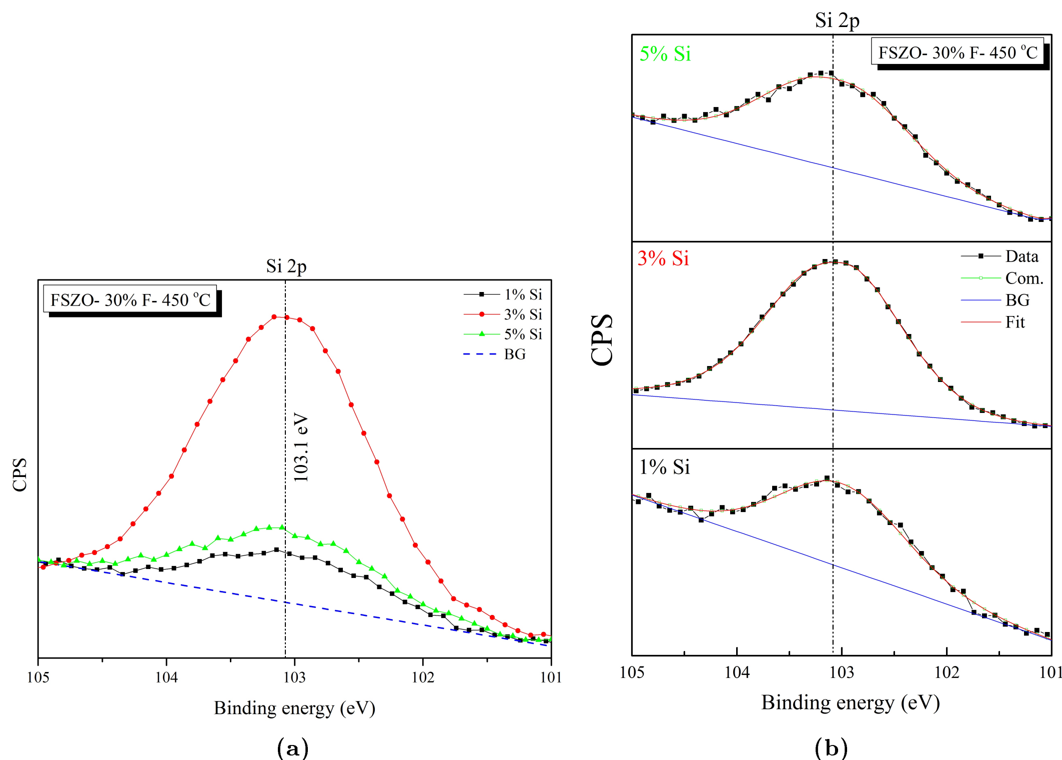

Figure 6.36: High resolution XPS spectra of (a) Si 2p and (b) fitted Si 2p core level for FSZO thin films with various Si doping concentration

The variations of the experimental O 1s spectra of FSZO films with varying Si concentration, and curve fitted into components are presented in Figure 6.37 (a) and (c), respectively. The asymmetric O 1s spectra could be fitted by two components centred at binding energies of around 531.8 eV and 533.0 eV. The fitted peak dominating around 531.8 eV (OZ) is attributed to oxide in a locally stoichiometric ZnO lattice, while another peak around 533.0 eV (OC) is ascribed to O species such as surface adsorbed hydroxyl (OH^-) or organic oxygen groups such as C=O and C−O. The area ratio of these two components (OZ/OC) decreases from 2.1 at 1% Si to about 1.5 at 5% Si.

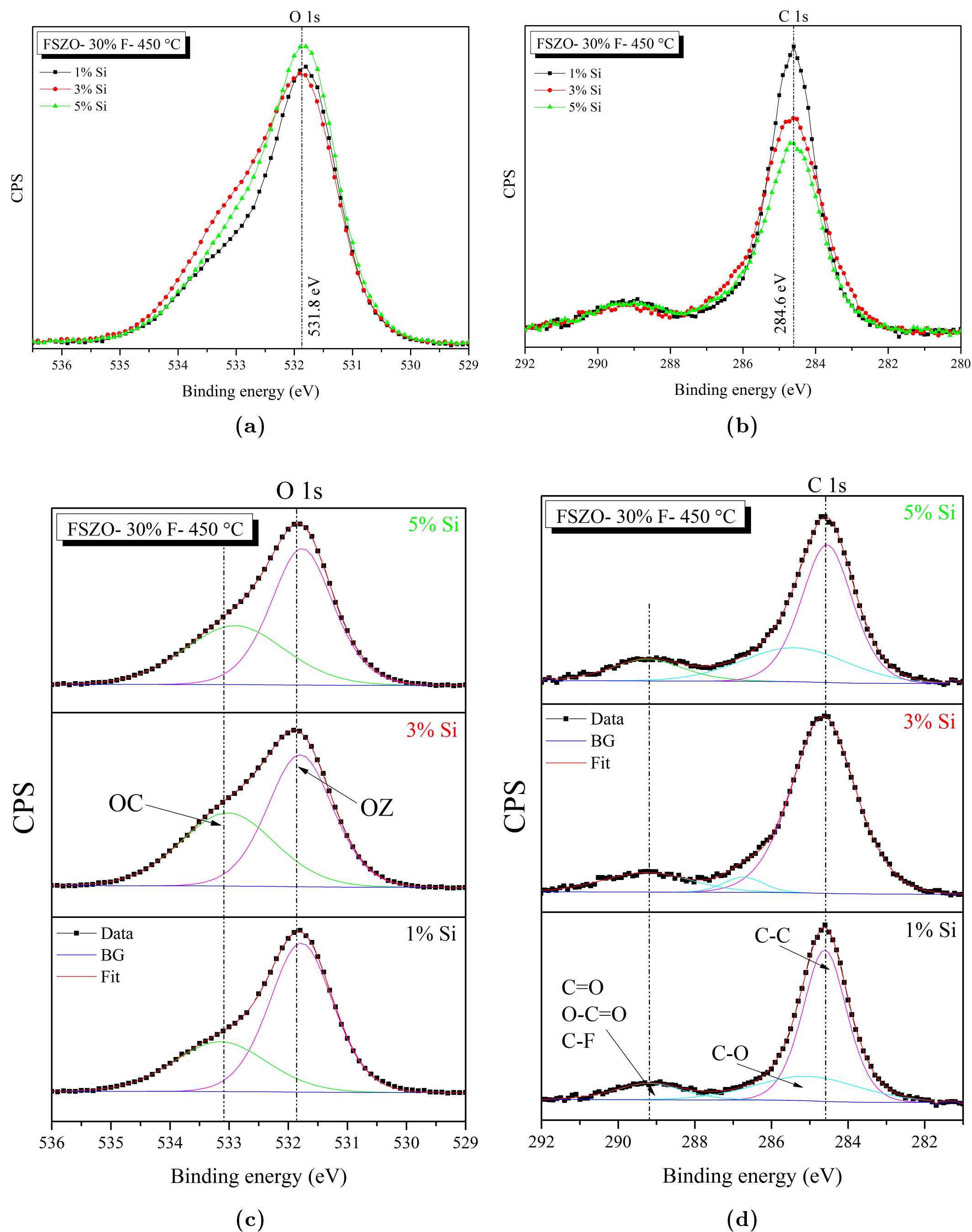

Figure 6.37: The (a), (c) O 1s and (b), (d) C 1s spectra with curve fitting results obtained from FSZO thin films deposited with Si doping concentration of 1%, 3% and 5%, at constant 30% F

Figure 6.37 (b) shows the high resolution C 1s spectra of three FSZO films with various

Si concentrations. The peak intensity of C 1s spectra decreased slightly with an increasing concentration of Si. The curve fitted C 1s spectra show that different C species co-exist on the surface of the samples (Figure 6.37 (d)). The strong peak positioned at 284.6 eV corresponds to species containing single C−C bonds. The fitted component at around 286 eV is assigned to compounds including single C−O bonds. The broad small peak at binding energy centred at 289.1 eV is arisen from double bond C=O or single bond C−F species.

Atomic concentrations of Zn, O, and C were calculated using Equation 2.12. The Zn to O at.% ratio of around 0.7 was achieved for all FSZO samples with various Si concentrations. Si:Zn and F:O ratios were obtained using the method explained in Section 6.3.1.2. The F:O ratio was found to be almost constant at 1.1 ± 0.5 at.% which is in agreement with the fixed concentration of F in the precursor solution. The Si concentration on the surface of the samples does not depend linearly on the [Si] in the solution, and the Si:Zn ratio on the surface of the samples increased from 2.92 at.% for the film deposited from precursor solution with 1% Si concentration to 9.79 at.% for the films deposited from solution with 3% Si. The Si:Zn atomic concentration ratio in the sample decreases to 3.82 at.% with further increase of the [Si] to 5% in the solution.

6.3.3.3 Morphology

Figure 6.38 shows AFM micrographs of the FSZO thin films deposited at 450 °C with different Si concentrations. The samples with Si concentration of 1% and 3% have very uniform surfaces, but the quality of the surface uniformity declines as the Si concentration increases to 5%.

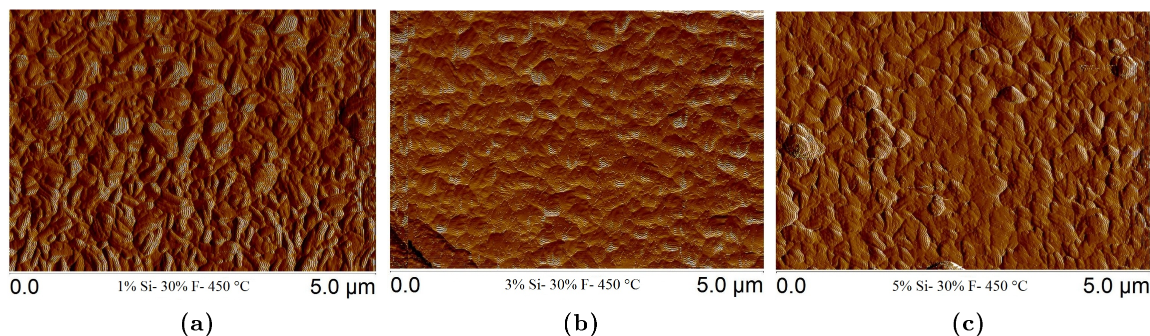

Figure 6.38: AFM images of 30% F - FSZO thin films deposited at 450 °C with: (a) 1%, (b) 3% and (c) 5% Si concentration

The mean particle size was calculated from AFM images and was found to slightly decrease from around 175 ± 67 nm for 1% Si to 147 ± 46 nm for 3% Si and increase to 163 ± 55 nm again as the Si concentration increased to 5%. The mean roughness complied with the changes in particle size. It was higher at Si concentration of 1% (~ 24.9 nm) as it is also evident from the AFM images. The surface of the sample with 3% Si is smoother than other samples with lower and higher Si concentrations, and thus a lower roughness (~ 12.1 nm) can be inferred for this film.

The surface morphology of FSZO thin films with various Si concentrations was also assessed by scanning electron microscopy (SEM). Film grown with the 0% Si concentration at 450 °C showed a flake-like hexagonal-shaped morphology with large particle sizes of mixed orientation on the substrate surface as shown in Figure 6.39 (a). This is consistent with the XRD data for this films (Figure 6.32) with high (002) peak intensity which corresponds to the hexagonal plates parallel to the surface, and the presence of a sharp (101) peak which is responsible for the observed random orientation of the particles.

The effect of increasing Si concentration is shown in Figures 6.39 (b) to (e). The particle shape undergoes a significant change from the hexagonal flake-like to pyramidal-triangle shape as Si concentration increases to 3%. The hexagonal-shape particles can be still observed on the surface of the 1% Si film, but they are more perpendicularly oriented to the surface, so the hexagon shape is not as clearly visible. These changes correspond to the

XRD patterns (Figure 6.32) where a clear shift in predominance from (002) to (100) can be noticed as the Si concentration increases. Moreover, the (110) peak first appeared in the XRD patterns by addition of Si, and a notable increase in the intensity of the (110) peak by increasing Si concentration is discerned. The pyramidal shape of the ZnO particles is considered to be associated to the (101) and (110) peaks. [373, 375, 376] The films with pyramidal-shape particles also appear to have less porous and more compact texture.

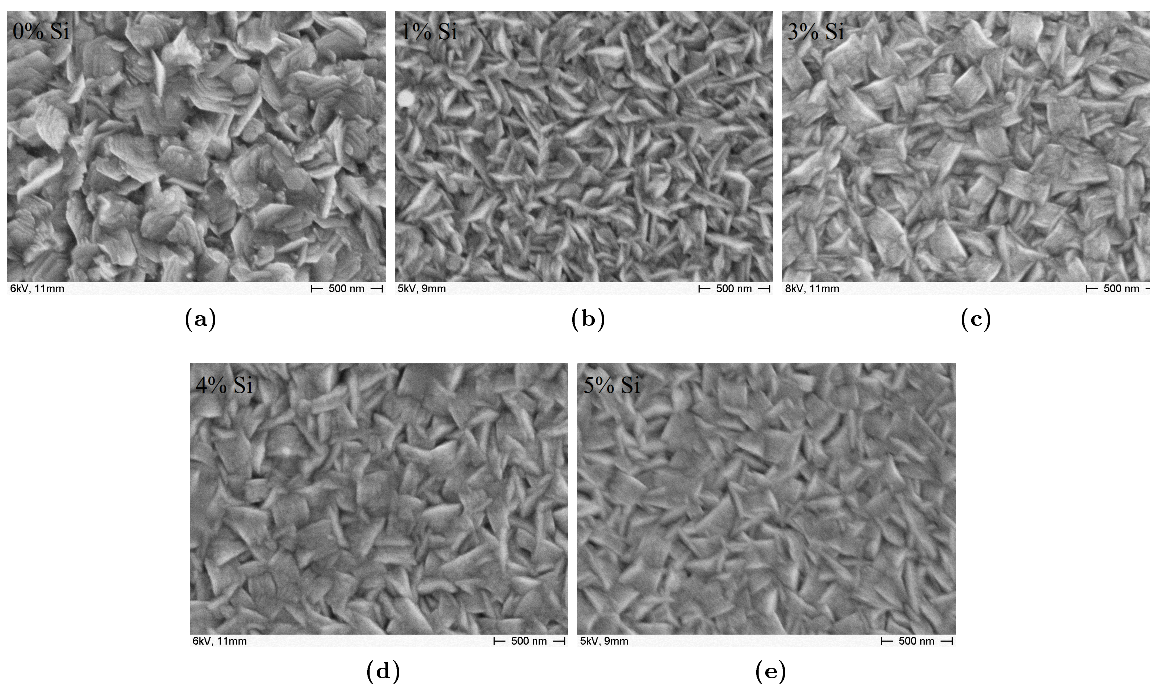

(a) (b) (c)

(d) (e)

Figure 6.39: The SEM micrographs of FSZO thin films deposited at 450 °C with (a) 0%, (b) 1%, (c) 3%, (d) 4%, and (e) 5% Si concentration

6.3.3.4 Optical properties

Figure 6.40 (a) depicts the optical transmittance spectra of FSZO films grown with different Si concentration recorded in the UV-Vis-NIR region (250 - 2500 nm). The UV absorption edge was sharp for all samples. The FSZO films with different Si content are highly transparent (> 85%, corrected for glass substrate) in the visible region. The transmittance in the range 400 nm $< \lambda <$ 750 nm, increases from 85% to 89% as Si content was increased

from 1% to 3%. However, for the heavily doped samples, 4% and 5%, the transmittance was slightly lower at 85%.

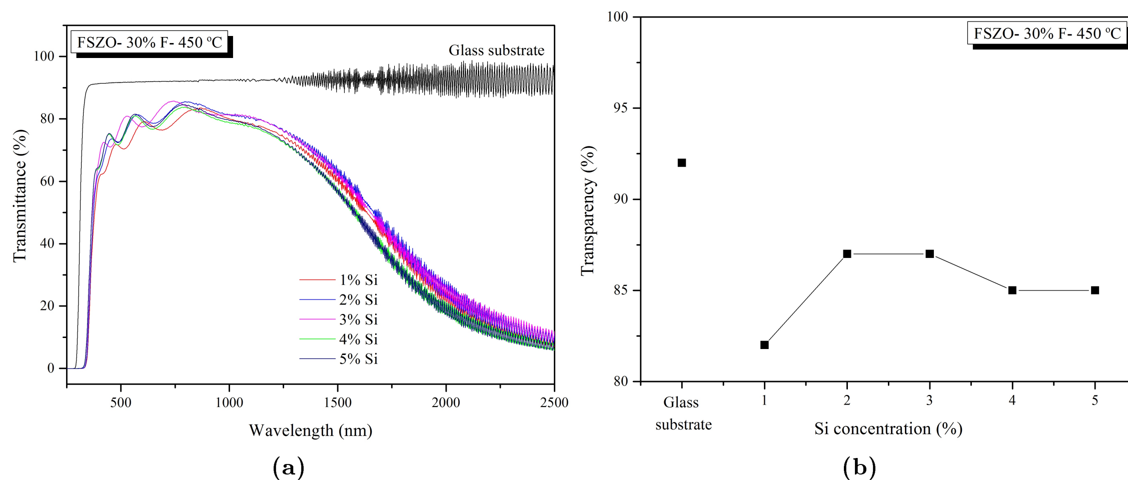

Figure 6.40: (a) Optical transmittance spectra and (b) transparency variation of FSZO thin films deposited with different Si concentration at 450 °C

The optical band gap of the thin films were calculated from the transmission spectra using Equation 2.17. From the graphical form of $(\alpha h\nu)^2$ - $h\nu$ data presented in Figure 6.41, the E_g values were estimated and displayed as inset in Figure 6.41. The optical band gap of the FSZO thin films grown with different Si concentration at substrate temperature of 450 °C was found to increase from 3.57 eV to 3.65 eV as the Si concentration increased from 1% to 4%, and stay unchanged with further increase of Si content. As discussed previously in Section 6.3.1.4, the increase in band gap is attributed to the Burstein-Moss (BM) shift. [192, 193] In the case of heavily n-type doped ZnO films, a donor level is generated at the base of conduction band. According to the Pauli exclusion principle, fermions cannot occupy the same quantum mechanical state, thus, the electrons in valence shell require an additional energy in order to be excited to higher states of conduction band, causing apparent optical band gap widening. Figure 6.43 depicts an increase in the carrier concentration as the Si concentration increases to 3 - 4% which is consistent with the observed widening of the band gap. The calculated band gap energies of our FSZO films

are larger than those of In+F co-doped ZnO films reported elsewhere by other researchers. [172, 175]

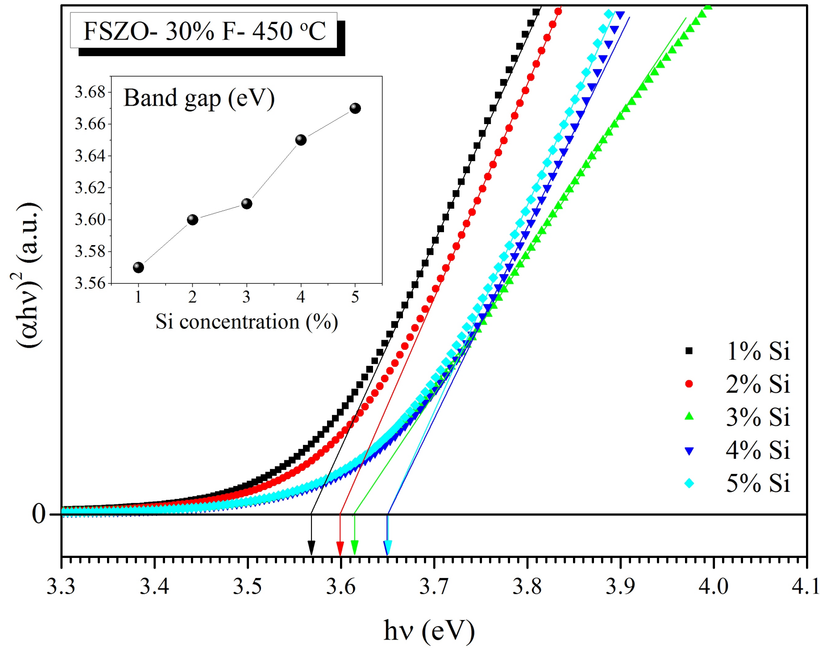

Figure 6.41: Plot of $(\alpha h\nu)^2$ *vs* $h\nu$ for and band gap variation (inset) in FSZO thin film with F concentration of 30% as a function of Si concentrations

Film thicknesses were calculated from optical spectra and plotted for thickness as a function of Si concentration as displayed in Figure 6.42. The general trend is not very stable but, the film thickness decreases slightly from 600 nm to 500 nm with increasing Si concentration.

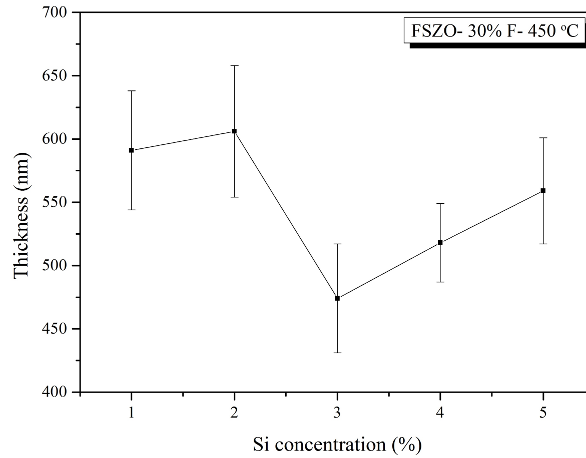

Figure 6.42: Variation of the thickness of the FSZO thin films as a function of Si concentration

The thickness variation seems correlated with the changes of the unit cell volume (Figure 6.33). The film thickness decreases with mean unit cell volume at Si concentration of 3%. Both parameters grow again as the Si concentration increased to 4 - 5%.

6.3.3.5 Electrical properties

Figures 6.43 (a) and (b) show that the carrier concentration, mobility and resistivity of FSZO thin films with varying Si doping level. The trend observed for carrier concentration is an increase as the Si concentration increases up to 4%, and then a drop with further increase of Si content to 5%. A sharp decrease in resistivity for Si concentrations of 3 and 4% arises from the improvements in both the carrier concentration and mobility. However, the fact that the mobility is almost unchanged with increasing Si concentration, indicates that the resistivity is more affected by variations of the carrier concentration.

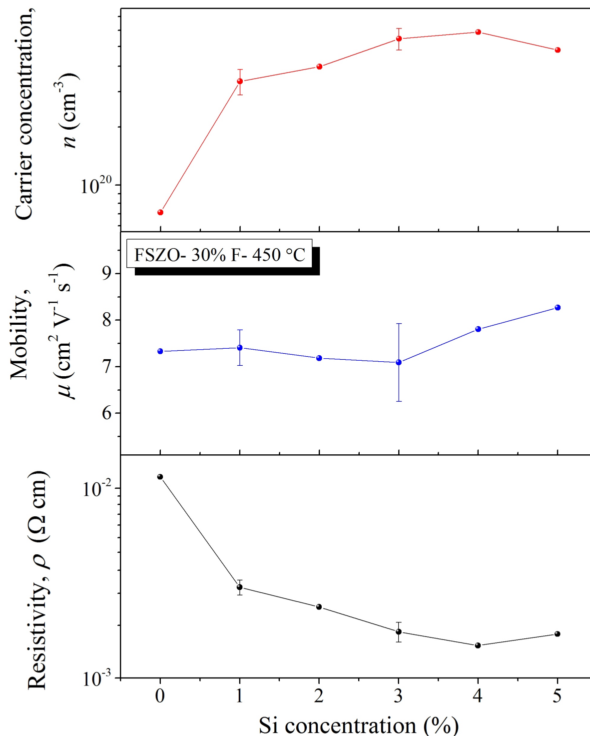

Figure 6.43: Variations of carrier concentration (red), mobility (blue), and resistivity (black) of FSZO films deposited at 450 °C at 30% F, with Si concentration

The observed increase in mobility at Si concentration of ≥ 4% might be because of larger crystallite size (Figure 6.34) and a better particle compactness as seen in SEM images (Figure 6.39). The room temperature electrical resistivity of as-deposited FSZO films reached its minimum value of 1.5×10^{-3} Ω cm for the film deposited with 4% Si and 30% F concentrations at 450 °C. This results from carrier concentration and mobility values of about 5.4×10^{20} cm^{-3} and 7.8 cm^2 V^{-1} s^{-1}, respectively. These significant results for an indium free spray pyrolysed thin film, are as good, and in some cases even superior to electrical and optical properties of some of the best In-doped ZnO thin films, fabricated under similar conditions. [132, 173, 380, 381]

6.3.4 Effect of type of the precursor solution container

As discussed earlier in the Experimental section, a very common chemical reaction in the acidic aqueous solutions containing F species, is the formation of acidic F^- which can etch glass. In order to eliminate the glass etching effect, which can release impurities such as Si and Al into the solution, in a different series of experiments, samples were deposited from spray solutions prepared in plastic containers, and the properties of FSZO-P (P for plastic container) were compared to those of deposited from spray solution prepared in glasswares.

6.3.4.1 Structural characterisation

Figure 6.44 represents the XRD patterns of FSZO-P thin films with various F concentrations of 10, 20, 30, and 40% and constant Si concentration of 3%, deposited at 450 °C from precursor solutions prepared in plastic vials. Only the characteristic diffraction peaks of hexagonal wurtzite phase, typical for undoped and doped ZnO were observed in the samples. Even at high concentrations of F, no crystalline secondary phases were apparent from the diffraction data (Figure 6.3).

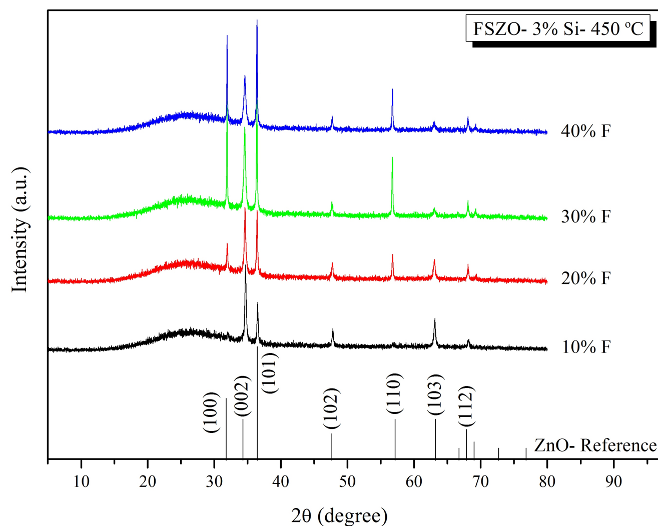

Figure 6.44: XRD patterns of FSZO-P thin films with 3% Si concentration and various F concentration deposited at 450 °C, from solution prepared in plastic vial

The observed XRD patterns in Figure 6.44 are similar, in terms of preferred orientations and peak intensities, to those of FSZO films deposited from precursor solution prepared in glass vials, shown in Figure 6.19, at F concentration of 10% and 20%. By increasing the F doping level, the growth orientation of the crystallines changes from along c-axis ((002) plane perpendicular to the substrate surface) to along a-axis ((100) or (101) planes parallel to the substrate surface). Besides, the (110) plane appears at F concentration of 20% and it's intensity increases with F content. The intensity of the XRD peaks for the FSZO-P film deposited with 40% F is very close to those of ZnO reference (bulk) values. This implies random orientation of the crystallites and lack of texture within the sample.

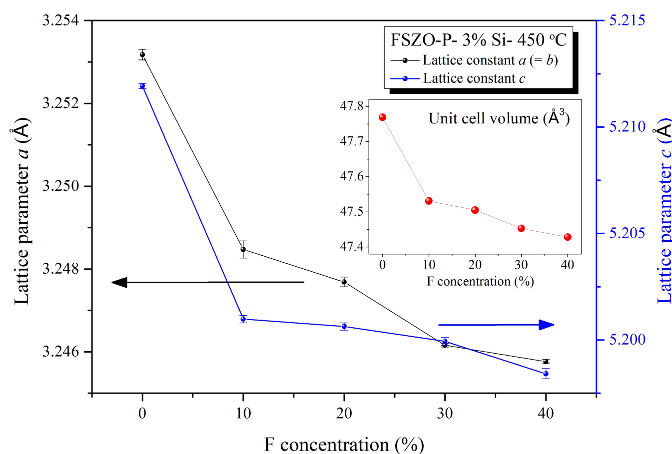

Figure 6.45: Variations of lattice parameters and unit cell volume (inset), as a function of F concentration (for the films deposited from precursor solutions prepared in plastic vial)

As can be seen in Figure 6.45 (b), the lattice parameter a (= b) of FSZO-P thin films was found to slightly decrease with the increasing F doping concentration in solution, while the lattice parameter c is even less affected by increasing F concentration and remains almost constant at about 5.20 ± 0.002 Å. The unit cell volume follows the same trend observed for the a lattice constant, and decreased from 47.7 Å^3 at 0% F to 47.4 Å^3 at 40% F. The decreases in lattice parameters and unit cell volume can be understood by the increasing solubility of Si or F in the ZnO lattice, and radii of Si and F ions which are smaller than that of Zn and O, respectively.

The average crystallite sizes of the FSZO-P thin films were calculated using Scherrer equation (2.9) from the full width at half maximum of the peaks with the highest intensity, and listed in Table 6.5. The overall trend at F concentration of ≥ 10%, is increasing the mean crystallite size of the samples with increasing F concentration.

F dopant concentration (%)	Mean crystallite size (nm)
0	65.7 ± 11.2
10	51.0 ± 4.5
20	64.5 ± 4.3
30	73.5 ± 6.9
40	96.3 ± 6.7

Table 6.5: Mean crystallite size of FSZO-P thin films deposited from solution prepared in plastic vials as a function of F concentrations

6.3.4.2 Surface analysis

Figure 6.46 (a) and (b) show the XPS Si 2p core level peaks and resolved Si 2p peaks for FSZO-P samples with various F concentration, respectively. The Si 2p peak of the Si−O species appears in the 101.0 - 104.0 eV binding energy range. The Si 2p peak is fairly symmetrical and fittable with just a component. The peak position is centred at 101.8 eV, which corresponds to a silicon oxidation degree of 4+. When the sample was deposited from precursor solution with 20% F, the XPS peak of Si 2p reaches to the highest intensity.

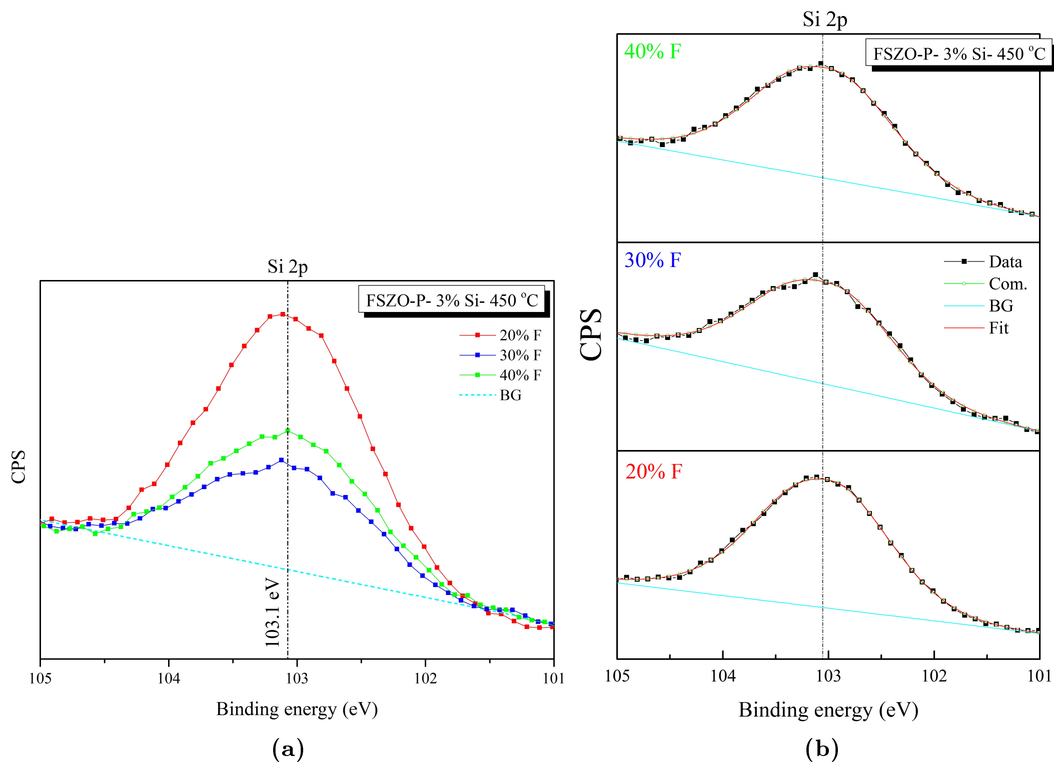

Figure 6.46: (a) Si 2p and (b) fitted Si 2p XPS spectra for FSZO-P thin films deposited with 1%, 3%, and 5% Si concentrations

Figure 6.47 depicts the high resolution F 1s XPS spectra for the surface of the FSZO-P thin films deposited at 450 °C. F 1s peak can usually be fitted by a single component, and binding energies between 684.0 and 685.5 eV are usually correlated to the metal fluorides, whereas, organic fluorine species usually appear in binding energies between 688.0 and 689.0 eV. The position of the F 1s peak confirms that the F^- atoms on the surface of the sample are bound to Zn atoms.

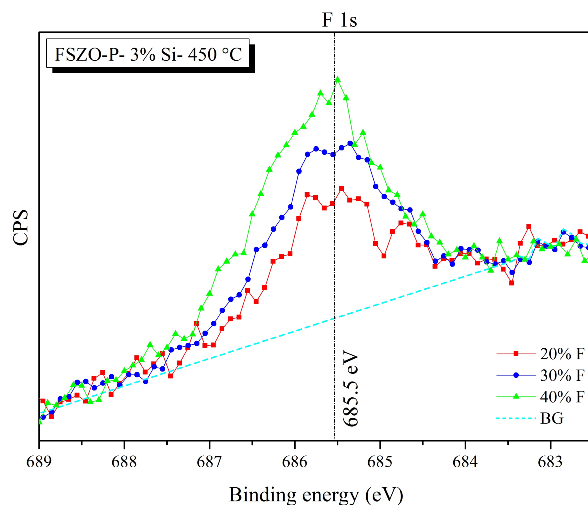

Figure 6.47: F1s high resolution XPS spectra of FSZO-P samples with 20, 30, and 40% F

As indicated in Figure 6.47, the F content on the surface of the FSZO-P thin films grows with increasing F dopant concentration. This suggests that higher concentration of F dopant can probably reinforce the substitution of F^- for O^{2-} in the lattice of ZnO. Table 6.6 summarizes the results for the atomic concentration ratios of the dopants (Si and F) to the parent atoms (Zn and O) on the surface of the samples.

Deposition temperature (°C)	F concentration in solution (%)	Si concentration in solution (%)	[F]/ [O] from XPS (at.%)	[Si]/ [Zn] from XPS (at.%)
450	20.0	3.0	1.13	6.38
450	30.0	3.0	1.64	4.78
450	40.0	3.0	2.02	5.74

Table 6.6: [Si]/[Zn] and [F]/[O] atomic concentration ratios on the surface of FSZO-P thin films prepared from precursor solutions with a fixed Si concentration and varying F concentration

The [F]/[O] ratio slightly increases with the [F] in the solution. The [Si]/[Zn] is almost constant (5.6 ± 0.8 at.%) in agreement with the fixed concentration of Si in the spraying solution. The higher concentration of Si on the surface of the thin films than in the spraying solution is usually ascribed to the segregation phenomenon as explained in Section 6.3.2.2. On the other hand, the lower concentration of F on the surface of the samples compared to

its concentration in the solution might be due to the evaporation of F containing species at high temperature of the substrate during the deposition process, as further discussed in Section 6.3.2.2.

6.3.4.3 Morphology

The morphologies of FSZO-P thin films were evaluated by the SEM micrographs. Figure 6.48 displays the surface SEM images of samples prepared with nominal F contents of 10, 20, 30, and 40% in spraying solution. The undoped ZnO film (Figure 6.27 (b)) consists of closed-packed and hexagonally shaped microcrystallites arrayed regularly on the substrate with a narrow distribution of grain sizes. The morphology of the FSZO-P thin film undergoes a significant change as the F concentration increases to 20% and higher.

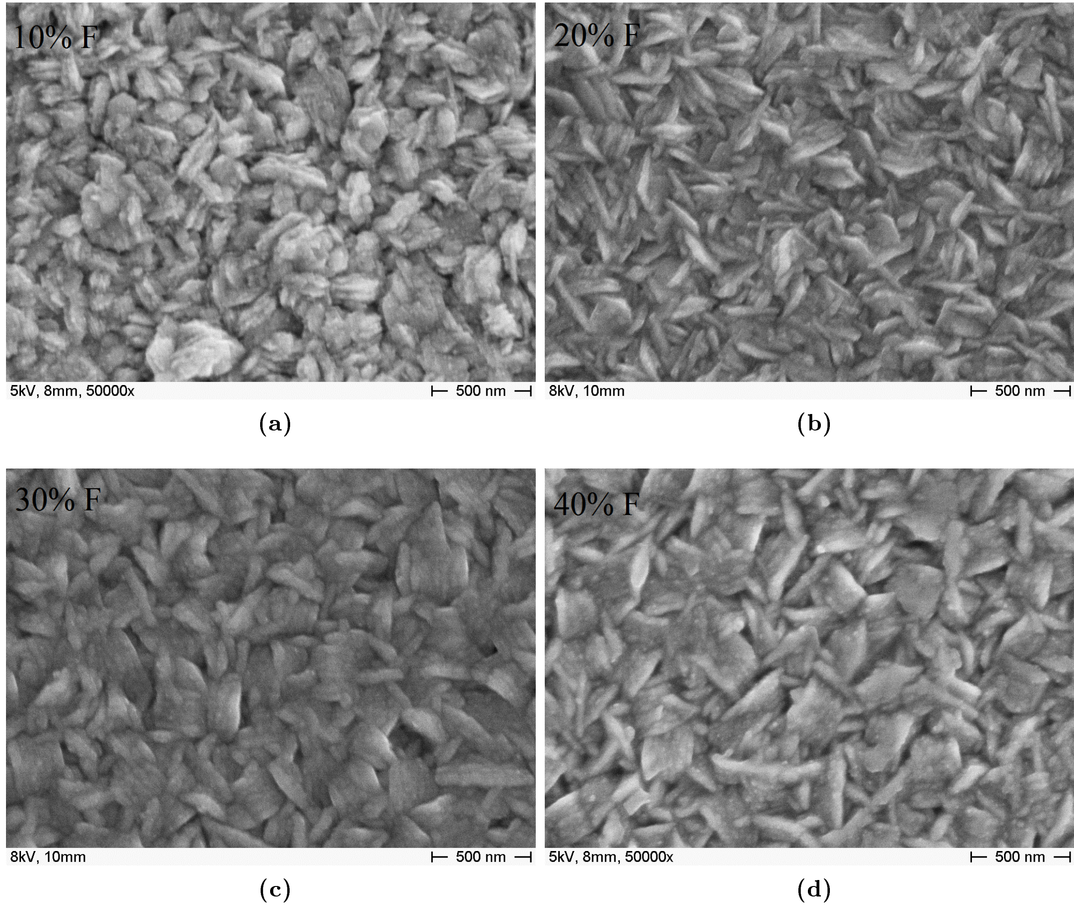

Figure 6.48: SEM micrographs of FSZO-P thin films deposited from solution prepared in plastic at 450 °C with (a) 10%, (b) 20%, (c) 30%, and (d) 40% F concentration

The transformation of particle shape displayed by SEM correlates well with XRD results, which showed noticeable variation in preferential growth of crystallites, most likely caused by the incorporation of F into ZnO lattice.

6.3.4.4 Optical properties

All optical properties of the samples, including the UV-Vis-NIR transmittance spectra, transparency, band gap and thickness values as a function of F concentration are presented in Figure 6.49. Figure 6.49 (a) shows the effect of the F concentration in the starting solution on the optical transmittance of FSZO-P thin films deposited at 450 °C, in a wavelength

interval of 250 - 2500 nm. The fluctuation in the spectra is due to the interference effect owing to the reflection at interfaces. Sharp fundamental absorption edges corresponding the band gap of ZnO, are observed in all the spectra. It can be observed that the optical transmittance is around 80% (not corrected for glass substrate) and decreases as the fluorine concentration increases from 10% to 40%. Based on these results and the results from morphology studies we can conclude that the diminishing the optical transmission obtained in the FSZO-P films by increasing F concentration, might be a result of the film quality, determined by the structural and morphological characteristics. Film transparency can be decreased by the increased scattering induced by irregularly shaped or randomly oriented particles.

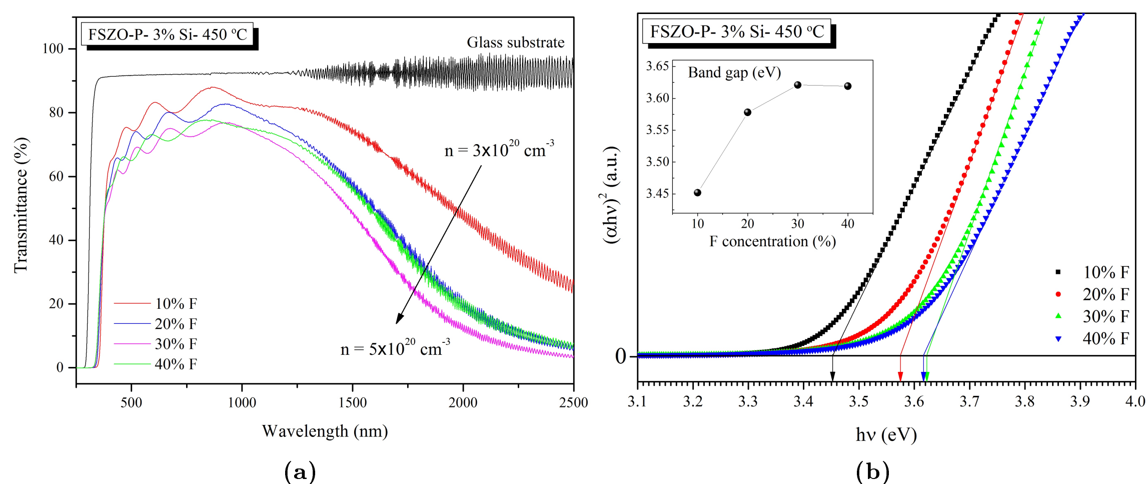

Figure 6.49: Variations of (a) optical transmittance and (b) $(\alpha h\nu)^2$ *vs* $h\nu$ (inset: band gap) of FSZO-P thin films prepared from solution in plastic vial as a function of F concentration

As was expected the concentration of the doping elements also affected the band gap, E_g. A shift towards higher energy is observed when the dopant concentration in the solution is increased, as is shown in Figure 6.49 (b). The E_g values ranged from 3.44 to 3.60 eV. The lowest E_g value corresponds to film deposited with the lowest F doapnt concentration ratio, namely [F] / [Zn] = 10% (inset in Figure 6.49 (b)), where it is expected a lower contribution to the carrier concentration. The variation of E_g under these circumstances

is attributed to the Burstein-Moss effect. [192, 193]

6.3.4.5 Electrical properties

The variation of resistivity, carrier concentration and Hall mobility of FSZO-P thin films as a function of F concentration are presented in Figure 6.50. There is a maximum carrier density achieved at 40% F. It can be seen from Figure 6.50 (b) that resistivity of FSZO-P film is strongly influenced by the F doping concentration. As the F concentration in the spraying solution increases from 0 to 40%, the resistivity of the films decreases rapidly from 5.4×10^{-3} Ω cm to the minimum value of 2.0×10^{-3} Ω cm, with a carrier concentration of 4.8×10^{20} cm^{-3} and a mobility of 6.3 cm^2 V^{-1} s^{-1}. In FSZO-P samples, it can be inferred that the conductivity of the film is mainly attributed to its carrier concentration rather than mobility. As the concentration of Si in the spraying solution is constant is all sample, the initial decrease in resistivity might originate from substituting F^- for O^{2-} sites to release extra free electron that contributes to the conductivity. Small amounts of F doping, if it is successful, can introduce large numbers of free electrons in the films, and therefore increases the conductivity. However, the conductivity of FSZO films is not increasing with increase of F concentration as expected. It can be explained by the fact that excess F atoms cannot be accommodated into ZnO lattice and might form amorphous oxide in the grain boundaries, which act as carrier traps in the lattice rather than electron donors. [305] The mobility of FSZO-P films remains almost unaffected by increasing the F concentration, between 6.0 to 7.0 cm^2 V^{-1} s^{-1}.

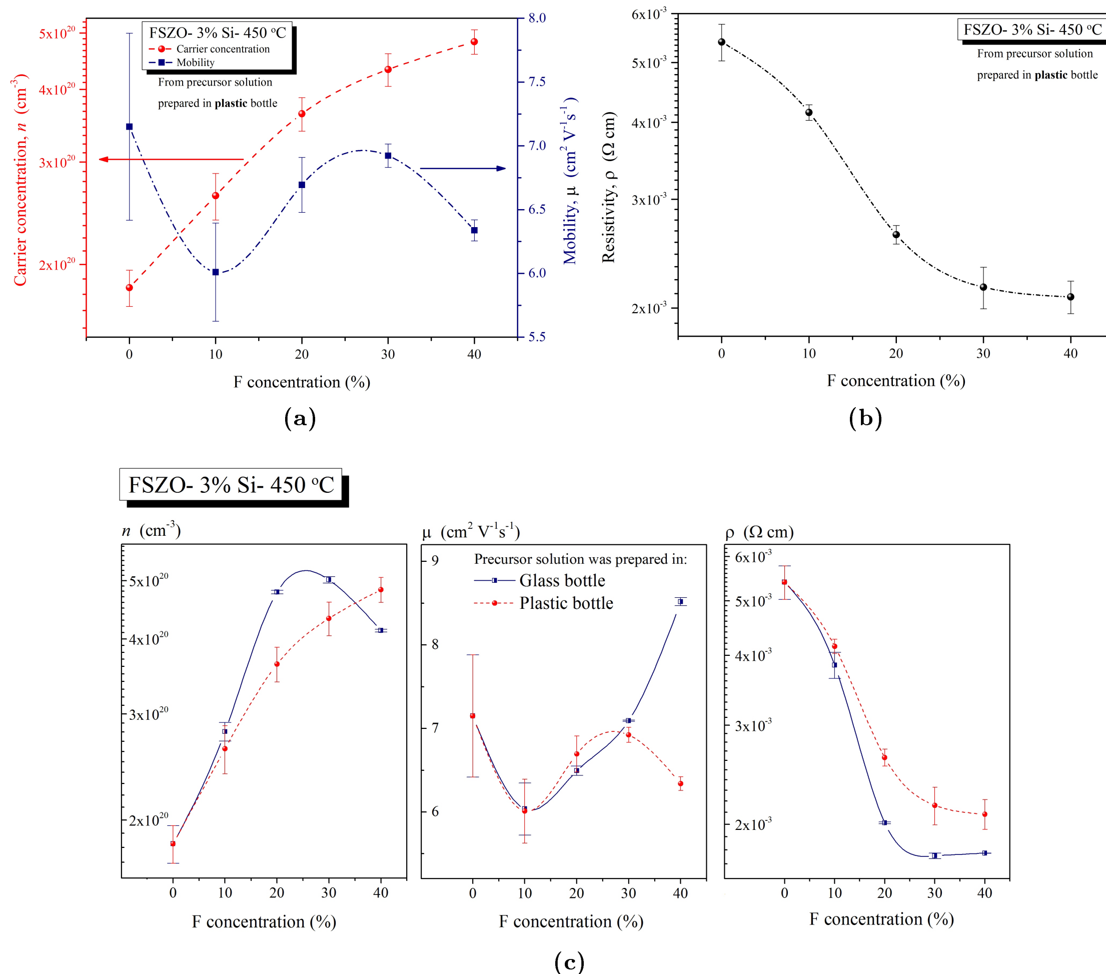

Figure 6.50: (a) Carrier concentration and mobility, and (b) resistivity values as a function of F concentration, for thin films from precursor solution prepared in plastic vial (c) comparison of electrical properties of FSZO samples from solution in glass *vs* plastic vials, as a function of F concentration

Despite the initial uncertainties about the observed optical and, in particular, electrical properties of FSZO thin films, the optimal electrical properties of FSZO-P were comparable to the reported values for FSZO films deposited from solution prepared in glass vials. We also showed in Chapters 4 and 5 that single doping of ZnO with Si or F did not reproduce the results observed in this chapter. These suggest that Si+F co-doping is an effective route to enhance the optical and electrical properties of ZnO thin films. Although the real

mechanism of co-doping needs to be thoroughly investigated, based on the results presented in this chapter, we can propose two mechanisms for the effectiveness of Si+F co-doping in producing high conductivity and transparency in FSZO thin films;

1) First mechanism involves both dopant atoms incorporating into ZnO lattice simultaneously and donating extra electrons to raise the number of free carriers. This approach considers substituting Si^{4+} for Zn^{2+}, and F^{-} for O^{2-} in ZnO matrix. XPS measurements (Figures 6.22, 6.23, 6.35, 6.36) detected both Si and F peaks on the surface of the samples. However, the detected F content was much lower than the amount of F added to the spraying solution. On the other hand, other studies on F-doping of ZnO show that even very small concentration of F can make a huge enhancement in optical and electrical properties of ZnO thin films. Choi and Park, for example, reported resistivity value as low as 1.8×10^{-3} Ω cm, and high optical transparency of about 83% for ZnO thin films doped with only 1.2 at.% F, deposited at 140 °C by ALD. [152]

2) Second mechanism is a little more difficult to prove, and involves only Si incorporating into ZnO, but with higher concentrations in the presence of F. We propose this mechanism based on the results in Chapter 5, in which we showed F doping of ZnO is not successful under our experimental conditions, and based on the XPS results which indicated higher concentration of Si on the surface of the samples with increasing F concentration (Figure 6.23). In this unconfirmed hypothesis, we claim that the solubility of Si in the spraying solution and as a result into ZnO matrix, is increased by formation of highly soluble compound such as fluosilicic acid (H_2SiF_6), due to the fact that solubility of silicon tetraacetate ($Si(OCOCH_3)_4$) in solution is a limiting factor in optimum incorporation of Si into ZnO lattice during deposition process.

While XPS is a surface sensitive technique, a depth profile measurement of a sample can be obtained by combining a sequence of ion gun etch cycles interleaved with XPS measurements from the current surface. Depth profile XPS measurements and Energy Dispersive X-Ray analysis (EDX, which is an X-ray technique used to identify the elemental

composition of materials), on series of samples are in progress, in order to analyse the composition of subsurface layers and determine the concentration of various elements in the samples.

6.4 Conclusions

Co-doped ZnO thin films offer a promising alternative to indium tin oxide (ITO) as transparent conductive layers. Although the electrical properties of our FSZO thin films are still not high enough to replace the ITO in high-end TCO applications such as organic light emitting diodes (OLEDs) and photovoltaic panels, but they can provide an alternative to ITO layers used as transparent electrodes in devices such as liquid crystal and touch screen displays.

Fluorine and silicon co-doped (FSZO) thin films were successfully deposited at substrate temperature of 450 °C using low-cost solution-based spray pyrolysis deposition technique. For the first time, the effect of deposition temperature, F concentration, Si concentration, and the type of the vials in which the precursor solutions were prepared, on the structural, optical, and electrical properties of the thin films were thoroughly investigated. The effect of preparing spraying solution in plastic vials was investigated due to the fact that in water-soluble F containing compounds, F^- can from HF in the solution, and HF will react with SiO_2 in glass, which might also introduce silicon impurities into the solution and thin films.

FSZO thin films deposited on glass substrates at 450 °C with 3% Si and 30 - 40% F exhibited very promising resistivities of $\sim 2.0 \times 10^{-3}$ Ω cm, both from spraying solution prepared in glass and plastic vials. The carrier concentration and mobility values were about 4.8×10^{20} cm^{-3} and 7.0 cm^2 V^{-1} s^{-1}, respectively. However, these results are still far from the best values presented in the only other report on FSZO thin films fabricated by pulsed laser deposition (PLD), in which resistivities as low as 7.2×10^{-4} Ω cm for the films deposited at 150 °C were obtained. [327]

The associated optical transmittance of FSZO was above 85% in the whole visible range.

The band gap value was found to increase from 3.28 eV for undoped ZnO to about 3.65 eV for FSZO thin film doped with 3% Si - 40% F deposited at 450 °C. The XRD patterns and SEM results of FSZO samples revealed that the preferential growth of the crystallites and the structural morphology of these polycrystalline thin films is dependent upon the substrate temperature, and F and Si concentration. The preferential orientation of the crystallites changed from parallel to the c-axis to parallel to the a-axis, with increasing F concentration. The experimental carrier concentration values do not correspond to the presence of the whole amount of F added to the spraying solution. XPS measurements also show much lower F concentration on the surface of the samples comparing to F concentration in spraying solution. Most likely, this is due to the evaporation of F at high temperatures of deposition process.

Chapter 7

Summary and Conclusions

7.1 Conclusions

This thesis demonstrates novel findings into the growth and characterization of n-type ZnO thin films, single-doped with silicon (SiZO), fluorine (FZO), or chlorine (ZnO:Cl), and co-doped with silicon and fluorine (FSZO), and addresses the needs for highly conducting and transparent alternative materials to substitute indium-tin oxide (ITO) for device applications. We obtained n-type ZnO thin films by spray pyrolysis using a range of deposition conditions and dopant sources. The novelty in our approach is in the use of a cost effective solution-based technique and simultaneous doping with Si and F, to fabricate high optically transparent and electrically conductive ZnO-based materials.

In spray pyrolysis technique the substrate temperature is an important parameter, and it strongly affects the decomposition of the zinc compounds to ZnO and almost all properties of the thin films. In Chapter 3, the thermal decomposition of several potential ZnO precursors were studied using thermogravimetric analysis (TGA) and variable temperature X-ray diffraction (VT-XRD). The aim of studying the decomposition temperature of zinc salts was to find a zinc precursor which decomposes to ZnO at relatively low temperatures (lower than 250 °C), in order to develop spray pyrolysis technique for deposition of thin

films on heat-sensitive substrates such as plastics. Our experiments have shown that the deposition temperature has to be sufficiently high (about 400 °C and higher), in order to obtain highly transparent and conductive thin films. However, as the decomposition temperature of the zinc precursor increases, higher deposition temperature might be needed to fabricate films with comparable properties. Results showed that the thermal decomposition of $Zn(acac)_2 \cdot xH_2O$ occurred through a neat two-step process at 220 °C. Decomposition temperature of other zinc salts studied, was much higher and in some cases included several complicated stages.

In Chapter 4, structural, optical, and electrical properties of undoped and Si-doped ZnO (SiZO) thin films were investigated as a function of deposition temperature and Si concentration. With increasing deposition temperature to 350 °C and higher, undoped ZnO and SiZO thin films demonstrated a change in the preferential orientation of the crystallites from along the a-axis to along the c-axis. The optical transparency in the visible range increased to above 80% for the thin films with Si concentration of 3% and higher deposited at 450 °C. The minimum resistivity of 4.6×10^{-2} Ω cm, the highest carrier concentration of 9.1×10^{18} cm^{-3}, and the highest mobility of 14.8 cm^2 V^{-1} s^{-1} were obtained for undoped ZnO films deposited at 450 °C. The resistivity of SiZO thin films decreased to a minimum of 3.7×10^{-3} Ω cm at Si concentration of 3%. The respective carrier concentration and mobility values were 1.7×10^{20} cm^{-3} and 10.9 cm^2 V^{-1} s^{-1}. Improvement in the electrical properties results from the contribution of extra electrons due to the substitution of Si^{4+} for Zn^{2+} in the ZnO lattice, in addition to the native donor defects, such as Zn interstitials and O vacancies. We also presented the results of an investigation into metal-insulator transition (MIT) and conduction mechanism in a set of our polycrystalline ZnO thin films.

In Chapter 5, we studied the anion doping (F and Cl) of ZnO and presented the effect of dopant concentration on the properties of ZnO thin films. Despite large number of publications on successful fabrication of F-doped ZnO thin films using various solution or vacuum-based techniques, we showed that F doping of ZnO can not be easily achieved

using the common F sources and via spray pyrolysis at high temperatures. In fact, the F dopant incorporation into ZnO lattice was very poor. Substitution of Cl^- for O^{2-} sites in the ZnO matrix may not be favourable, as it causes drastic distortion in the lattice due to the greater ionic radius of chloride (1.81 Å) than oxygen (1.38 Å). However, Cl doping was found to have small effects on the electrical properties of the ZnO thin film, although the optical transparency was deteriorated.

In Chapter 6, the effect of various parameters such as deposition temperature, F concentration, Si concentration, and preparation of precursor solutions in plastic vials, on the structural, morphological, optical and electrical properties of Si+F co-doped ZnO thin films were comprehensively studied. The best deposition temperature for the deposition of co-doped ZnO was in the range of 400 - 450 °C in a N_2 atmosphere. The structural parameters, such as preferential orientation and particle shape in the film, depended on the deposition temperature, and the concentration of Si and F in the spraying solution. The XRD diffraction patterns revealed more or less stronger preferential growth along c-axis in the absence of F, and along a-axis with increasing F content in the solution. Three diffraction lines ((100), (002) and (101)), appeared in the XRD patterns of the FSZO films deposited at 450 °C, indicating that the orientation of the crystallites was more random. At optimum doping concentration of 3% Si and 30 - 40% F, and a deposition temperature of 450 °C, the FSZO thin films exhibited electrical resistivity as low as 2.0×10^{-3} Ω cm and the optical transparency of more than 85% in the visible region. These results are as good, and in some cases, even superior to electrical and optical properties of some of the best In-doped ZnO thin films, fabricated under similar conditions. [132, 173, 380, 381]

7.2 Future work

The present work has illustrated some of the uncertainties and unknowns in the growth of undoped and doped ZnO thin films and it is hoped that future work will be carried out in this and the following areas:

(1) The investigation of the fundamental mechanism of Si+F co-doping in ZnO, doping efficiency, and the confirmation of incorporation of Si and/or F into ZnO lattice by means of XPS depth profiling, EDX, or other techniques.

(2) The investigation of the structural crystallographic point defects such as vacancies and interstitials in Si+F co-doped, and single Si or F-doped ZnO in order to find out the lattice-environment of the defects and real arrangement of atoms in the ZnO lattice. Electron microscopy techniques under very high magnification, high resolution X-ray diffraction, extended X-ray absorption fine structure (EXAFS), and neutron diffraction techniques can be used for this purpose.

(3) The study, modelling and understanding the role of parameters such as grain boundaries scattering on limiting electronic transport properties in polycrystalline ZnO films, in order to improve their electrical performance.

(4) The search for other novel combination of dopants (cation+cation or cation+anion) that might be as efficient as Si+F dopants for the production of highly conducting transparent doped ZnO.

(5) The study of other parameters involved in spray pyrolysis process, such as various solvent and pH values on the quality and properties of the thin films.

(6) The use of co-doping method in some other deposition techniques such as magnetron sputtering or PLD to improve the properties of ZnO.

(7) The search for new zinc and dopant precursors, designed for the production of chemically pure and highly conducting ZnO thin films in order to replace established precursors which do not enable a low temperature growth of thin films.

(8) The investigation of the potential application of the thin films with optimised electrical and optical properties in solar energy utilization and optoelectronic devices.

(9) The scale up of the fabrication process to commercial levels, using spray pyrolysis technique which is capable of one-step and cost effective deposition of good quality and large area thin films.

References

[1] Shtereva, K., Tvarozek, V., Sutta, P., Kovac, J. & Novotny, I. Experimental Studies on Doped and Co-Doped ZnO Thin Films Prepared by RF Diode Sputtering. In *Micro Electronic and Mechanical Systems*, December, chap. 14, 211–234 (2009).

[2] Crawford, G. P. (ed.) *Flexible Flat Panel Displays* (John Wiley & Sons, Inc., 2005).

[3] Zhang, K. & Li, D. *Electromagnetic theory for microwaves and optoelectronics* (Springer Berlin Heidelberg, 2008), second edn.

[4] Chen, M. *et al.* Intrinsic limit of electrical properties of transparent conductive oxide films. *Journal of Physics D: Applied Physics* **33**, 2538–2548 (2000).

[5] Ellmer, K. Past achievements and future challenges in the development of optically transparent electrodes. *Nature Photonics* **6**, 809–817 (2012).

[6] Edwards, P. P., Porch, A., Jones, M. O., Morgan, D. V. & Perks, R. M. Basic materials physics of transparent conducting oxides. *Dalton Transactions* 2995–3002 (2004).

[7] Badeker, K. Über die elektrische Leitfähigkeit und die thermoelektrische Kraft einiger Schwermetallverbindungen. *Annalen der Physik* **327**, 749–760 (1907).

[8] Haacke, G. Transparent conducting coatings. *Annual Review of Materials Science* **7**, 73–93 (1977).

[9] Minami, T. Transparent and conductive multicomponent oxide films prepared by magnetron sputtering. *Journal of Vacuum Science and Technology A* **17**, 1765–1772 (1999).

[10] Minami, T., Sato, H., Nanto, H. & Takata, S. Group III impurity doped zinc oxide thin films prepared by RF magnetron sputtering. *Japanese Journal of Applied Physics* **24**, L781–L784 (1985).

[11] Minami, T., Nanto, H. & Takata, S. Highly conductive and transparent Aluminum doped zinc oxide thin films prepared by RF magnetron sputtering. *Japanese Journal of Applied Physics* **23**, L280–L282 (1984).

[12] Minami, T., Sato, H., Nanto, H. & Takata, S. Highty conductive and transparent silicon doped zinc oxide thin films prepared by RF magnetron sputtering. *Japanese Journal of Applied Physics* **25**, L776–L779 (1986).

[13] Gordon, R. G. Preparation and properties of transparent conductors. *Materials Research Society Symposium Proceedings* **426**, 419–429 (1996).

[14] Rupprecht, G. Untersuchungen der elektrischen und lichtelektrischen Leitfähigkeit dünner Indiumoxydschichten. *Zeitschrift für Physik* **139**, 504–517 (1954).

[15] Minami, T. Substitution of transparent conducting oxide thin films for indium tin oxide transparent electrode applications. *Thin Solid Films* **516**, 1314–1321 (2008).

[16] Minami, T. Transparent conducting oxide semiconductors for transparent electrodes. *Semiconductor Science and Technology* **20**, S35–S44 (2005).

[17] Pasquarelli, R. M., Ginley, D. S. & O'Hayre, R. Solution processing of transparent conductors: from flask to film. *Chemical Society reviews* **40**, 5406–5441 (2011).

[18] Facchetti, A. & Marks, T. (eds.) *Transparent Electronics: From Synthesis to Applications* (John Wiley & Sons, Inc., 2010).

[19] Granqvist, C. G. Transparent conductors as solar energy materials: A panoramic review. *Solar Energy Materials and Solar Cells* **91**, 1529–1598 (2007).

[20] Ohta, H. & Hosono, H. Transparent oxide optoelectronics. *Materials Today* **7**, 42–51 (2004).

[21] Lewis, N. S., Crabtree, G., Nozik, A. J., Wasielewsk, M. R. & Alivisatos, P. Basic research needs for solar energy utilization. Tech. Rep., U.S. Department of Energy

(2005).

[22] Bae, S., Kim, S. J., Shin, D., Ahn, J. H. & Hong, B. H. Towards industrial applications of graphene electrodes. *Physica Scripta* **T146**, 014024 (1–8) (2012).

[23] Fortunato, E., Ginley, D., Hosono, H. & Paine, D. C. Transparent conducting oxides for photovoltaics. *MRS Bulletin* **32**, 242–247 (2007).

[24] Granqvist, C. G. Window coatings for the future. *Thin Solid Films* **193-194**, 730–741 (1990).

[25] Mohelnikova, J. Materials for reflective coatings of window glass applications. *Construction and Building Materials* **23**, 1993–1998 (2009).

[26] Bae, J. H. *et al.* Transparent conducting indium zinc tin oxide anode for highly efficient phosphorescent organic light emitting diodes. *Journal of The Electrochemical Society* **155**, J1–J6 (2008).

[27] Jiang, X., Wong, F. L., Fung, M. K. & Lee, S. T. Aluminum-doped zinc oxide films as transparent conductive electrode for organic light-emitting devices. *Applied Physics Letters* **83**, 1875–1877 (2003).

[28] Kamiya, T. & Hosono, H. Material characteristics and applications of transparent amorphous oxide semiconductors. *NPG Asia Materials* **2**, 15–22 (2010).

[29] Wright, M. & Uddin, A. Organic-inorganic hybrid solar cells: A comparative review. *Solar Energy Materials and Solar Cells* **107**, 87–111 (2012).

[30] Razykov, T. M. *et al.* Solar photovoltaic electricity: Current status and future prospects. *Solar Energy* **85**, 1580–1608 (2011).

[31] Lampert, C. M. Heat mirror coatings for energy conserving windows. *Solar Energy Materials* **6**, 1–41 (1981).

[32] Brütting, W., Frischeisen, J., Schmidt, T. D., Scholz, B. J. & Mayr, C. Device efficiency of organic light-emitting diodes: Progress by improved light outcoupling. *Physica Status Solidi (a)* **210**, 44–65 (2013).

[33] Oh, B. Y. *et al.* Transparent conductive Al-doped ZnO films for liquid crystal displays.

Journal of Applied Physics **99**, 124505 (1–4) (2006).

[34] Liu, H., Avrutin, V., Izyumskaya, N., Özgür, U. & Morkoç, H. Transparent conducting oxides for electrode applications in light emitting and absorbing devices. *Superlattices and Microstructures* **48**, 458–484 (2010).

[35] Kim, H. K., Lee, S. & Yun, K. S. Capacitive tactile sensor array for touch screen application. *Sensors and Actuators A* **165**, 2–7 (2011).

[36] Jin, Z. C., Hamberg, L. & Granqvist, C. G. Optical properties of sputter-deposited ZnO:Al thin films. *Journal of Applied Physics* **64**, 5117–5131 (1988).

[37] Choy, K. Chemical vapour deposition of coatings. *Progress in Materials Science* **48**, 57–170 (2003).

[38] Besmann, T. M., Stinton, D. P. & Lowden, R. A. Chemical vapor deposition techniques. *MRS Bulletin* **13**, 45–51 (1988).

[39] Goodman, C. H. L. & Pessa, M. V. Atomic layer epitaxy. *Journal of Applied Physics* **60**, R65–R81 (1986).

[40] Mooney, J. B. & Radding, S. B. Spray pyrolysis processing. *Annual Review of Materials Science* **12**, 81–101 (1982).

[41] Hench, L. L. & West, J. K. The sol-gel process. *Chemical Reviews* **90**, 33–72 (1990).

[42] Aegerter, M. A. & Mennig, M. (eds.) *Sol-Gel Technologies for Glass Producers and Users* (Kluwer Academic Publishers, 2004).

[43] Emslie, A. G., Bonner, F. T. & Peck, L. G. Flow of a viscous liquid on a rotating disk. *Journal of Applied Physics* **29**, 858–862 (1958).

[44] Chopra, K. L., Major, S. & Pandya, D. K. Transparent conductors- A status review. *Thin Solid Films* **102**, 1–46 (1983).

[45] Vossen, J. L. & Kern, W. (eds.) *Thin Film Processes II* (Academic Press, Inc., 1991).

[46] Eason, R. (ed.) *Pulsed laser Deposition of Thin Films* (John Wiley & Sons, Inc., 2006).

[47] Chrisey, D. B. & Hubler, G. K. (eds.) *Pulsed Laser Deposition of Thin Films* (John

Wiley & Sons, Inc., 1994).

[48] Krebs, H. *et al.* Pulsed Laser Deposition (PLD)- A versatile thin film technique. In *Advances in Solid State Physics*, vol. 43, 505–518 (Springer Berlin Heidelberg, 2003).

[49] Wasa, K., Kanno, I. & Kotera, H. (eds.) *Handbook of Sputter Deposition Technology* (Elsevier Inc., 2012), second edn.

[50] Alfonso, E., Olaya, J. & Cubillos, G. Thin film growth through sputtering technique and its applications. In Andreeta, M. R. B. (ed.) *Crystallization - Science and Technology*, chap. 15, 397–432 (InTech, 2012).

[51] Aliofkhazraei, M. (ed.) *Advances in Graphene Science* (InTech, 2013).

[52] George, S. M. Atomic layer deposition: an overview. *Chemical reviews* **110**, 111–131 (2010).

[53] Brinker, C. J., Frye, G. C., Hurd, A. J. & Ashley, C. S. Fundamentals of sol-gel dip coating. *Thin Solid Films* **201**, 97–108 (1991).

[54] Brinker, C. J., Hurd, A. J., Schunk, P. R., Frye, G. C. & Ashley, C. S. Review of sol-gel thin film formation. *Journal of Non-Crystalline Solids* **147-148**, 424–436 (1992).

[55] Oktik, S. Low cost, non-vacuum techniques for the preparation of thin/thick films for photovoltaic applications. *Progress in Crystal Growth and Characterization* **17**, 171–240 (1988).

[56] Chamberlin, R. R. & Skarman, J. S. Chemical spray deposition process for inorganic films. *Journal of The Electrochemical Society* **113**, 86–89 (1966).

[57] Chamberlin, R. R. & Skarman, J. S. Chemically sprayed thin film photovoltaic converters. *Solid-State Electronics* **9**, 819–823 (1966).

[58] Feigelson, R. S., NDiaye, A., Yin, S. Y. & Bube, R. H. II-VI solidsolution films by spray pyrolysis. *Journal of Applied Physics* **48**, 3162–3164 (1977).

[59] Aranovich, J., Ortiz, A. & Bube, R. H. Optical and electrical properties of ZnO films prepared by spray pyrolysis for solar cell applications. *Journal of Vacuum Science*

and Technology **16**, 994–1003 (1979).

[60] Patil, P. S. Versatility of chemical spray pyrolysis technique. *Materials Chemistry and Physics* **59**, 185–198 (1999).

[61] De Merchant, J. & Cocivera, M. Preparation and doping of zinc oxide using spray pyrolysis. *Chemistry of Materials* **7**, 1742–1749 (1995).

[62] Nunes, P., Marques, A., Fortunato, E. & Martins, R. Performances presented by large area ZnO thin films deposited by spray pyrolysis. *MRS Proceedings* **685**, D5.13.1 (2001).

[63] De Waal, H. & Simonis, F. Tin oxide coatings: Physical properties and applications. *Thin Solid Films* **77**, 253–258 (1981).

[64] Ghosh, R., Basak, D. & Fujihara, S. Effect of substrate-induced strain on the structural, electrical, and optical properties of polycrystalline ZnO thin films. *Journal of Applied Physics* **96**, 2689–2692 (2004).

[65] Bae, H. S., Lee, Y. S., Kim, Y. H. & Im, S. Comparison of the optical properties of ZnO thin films grown on various substrates by pulsed laser deposition. *Applied Surface Science* **168**, 332–334 (2000).

[66] Kaneko, H. & Miyake, K. Physical properties of antimony-doped tin oxide thick films. *Journal of Applied Physics* **53**, 3629–3633 (1982).

[67] Kane, J., Schweizer, H. P. & Kern, W. Chemical vapor deposition of antimony-doped tin oxide films formed from dibutyl tin diacetate. *Journal of The Electrochemical Society* **123**, 270–277 (1976).

[68] Mizuhashi, M. Electrical properties of SnO2 films on various glass substrates. *Journal of Non-Crystalline Solids* **38-39**, 329–334 (1980).

[69] Kim, H., Horwitz, J. S., Kushto, G. P., Kafafi, Z. H. & Chrisey, D. B. Indium tin oxide thin films grown on flexible plastic substrates by pulsed-laser deposition for organic light-emitting diodes. *Applied Physics Letters* **79**, 284–286 (2001).

[70] Yang, C. H., Lee, S. C., Lin, T. C. & Chen, S. C. Electrical and optical properties of

indium tin oxide films prepared on plastic substrates by radio frequency magnetron sputtering. *Thin Solid Films* **516**, 1984–1991 (2008).

[71] Banerjee, A. N. *et al.* Low-temperature deposition of ZnO thin films on PET and glass substrates by DC-sputtering technique. *Thin Solid Films* **496**, 112–116 (2006).

[72] Fortunato, E. *et al.* Zinc oxide thin films deposited by RF magnetron sputtering on Mylar substrates at room temperature. *MRS Proceedings* **685**, D5.10.1 (2001).

[73] Ozgur, U., Hofstetter, D. & Morkoc, H. ZnO devices and applications: A review of current status and future prospects. *Proceedings of the IEEE* **98**, 1255–1268 (2010).

[74] Srikant, V. & Clarke, D. R. On the optical band gap of zinc oxide. *Journal of Applied Physics* **83**, 5447–5451 (1998).

[75] Hoffman, R. L., Norris, B. J. & Wager, J. F. ZnO-based transparent thin-film transistors. *Applied Physics Letters* **82**, 733–735 (2003).

[76] Fortunato, E. *et al.* Recent advances in ZnO transparent thin film transistors. *Thin Solid Films* **487**, 205–211 (2005).

[77] Hong, J. S., Jang, K. W., Park, Y. S., Choi, H. W. & Kim, K. H. Preparation of ZnO based thin films for OLED anode by facing targets sputtering system. *Molecular Crystals and Liquid Crystals* **538**, 103–111 (2011).

[78] Yamamoto, N. *et al.* Development of Ga-doped ZnO transparent electrodes for liquid crystal display panels. *Thin Solid Films* **520**, 4131–4138 (2012).

[79] Jin, Z. C., Hamberg, I. & Granqvist, C. G. Reactively sputtered ZnO:Al films for energy-efficient windows. *Thin Solid Films* **164**, 381–386 (1988).

[80] Illy, B. N. *et al.* Electrodeposition of ZnO layers for photovoltaic applications: controlling film thickness and orientation. *Journal of Materials Chemistry* **21**, 12949–12957 (2011).

[81] Ramanathan, K. *et al.* Properties of 19.2% efficiency ZnO/CdS/CuInGaSe2 thin-film solar cells. *Progress in Photovoltaics: Research and Applications* **11**, 225–230 (2003).

[82] Katsuki, T., Nakazawa, F., Sano, S., Takahashi, Y. & Satoh, Y. A compact and high

optical transmission SAW touch screen with ZnO thin-film piezoelectric transducers. In *IEEE Ultrasonics Symposium*, vol. 00, 821–824 (2003).

[83] Guziewicz, E. *et al.* ZnO grown by atomic layer deposition: A material for transparent electronics and organic heterojunctions. *Journal of Applied Physics* **105**, 122413 (1–5) (2009).

[84] Godlewski, M. *et al.* Zinc oxide for electronic, photovoltaic and optoelectronic applications. *Low Temperature Physics* **37**, 235–240 (2011).

[85] Hou, W. C., Lin, B. W., Chang, L., Lin, T. S. & Lin, C. W. Chemical vapor deposition of epitaxial zinc oxide thin films on gallium nitride/sapphire substrates. *Physica Status Solidi (c)* **1**, 856–859 (2004).

[86] Sun, S. *et al.* Metal organic chemical vapor deposition and investigation of ZnO thin films grown on sapphire. *Thin Solid Films* **516**, 5571–5576 (2008).

[87] Kim, D. C., Kong, B. H., Cho, H. K., Lee, J. Y. & Park, D. J. Low temperature growth of ZnO thin film by metalorganic chemical vapor deposition. *Physica Status Solidi (b)* **244**, 1512–1516 (2007).

[88] Dikovska, A. O., Atanasov, P. A., Vasilev, C., Dimitrov, I. G. & Stoyanchov, T. R. Thin ZnO films produced by pulsed laser deposition. *Journal of Optoelectronics and Advanced Materials* **7**, 1329–1334 (2005).

[89] Minami, T., Yamamoto, T. & Miyata, T. Highly transparent and conductive rare earth-doped ZnO thin films prepared by magnetron sputtering. *Thin Solid Films* **366**, 63–68 (2000).

[90] Agashe, C. *et al.* Efforts to improve carrier mobility in radio frequency sputtered aluminum doped zinc oxide films. *Journal of Applied Physics* **95**, 1911–1917 (2004).

[91] Pung, S. Y., Choy, K. L., Hou, X. & Shan, C. Preferential growth of ZnO thin films by the atomic layer deposition technique. *Nanotechnology* **19**, 435609 (1–8) (2008).

[92] Znaidi, L. Sol-gel-deposited ZnO thin films: A review. *Materials Science and Engineering B* **174**, 18–30 (2010).

[93] Choi, B. K., Chang, D. H., Yoon, Y. S. & Kang, S. J. Optical characterization of ZnO thin films deposited by Sol-gel method. *Journal of Materials Science: Materials in Electronics* **17**, 1011–1015 (2006).

[94] Patil, S. L. *et al.* New process for synthesis of ZnO thin films: Microstructural, optical and electrical characterization. *Journal of Alloys and Compounds* **509**, 10055–10061 (2011).

[95] Hasuike, N. *et al.* Low temperature synthesis of ZnO thin films by spin-coating technique. *Physica Status Solidi (c)* **8**, 506–508 (2011).

[96] Paraguay, F. D., Estrada, W. L., Acosta, D. R. N., Andrade, E. & Miki-yoshida, M. Growth, structure and optical characterization of high quality ZnO thin films obtained by spray pyrolysis. *Thin Solid Films* **350**, 192–202 (1999).

[97] Joseph, B., Gopchandran, K. G., Thomas, P. V., Koshy, P. & Vaidyan, V. K. A study on the chemical spray deposition of zinc oxide thin films and their structural and electrical properties. *Materials Chemistry and Physics* **58**, 71–77 (1999).

[98] Perez, L. M., Aguilar-Frutis, M., Zelaya-Angel, O. & Munoz Aguirre, N. Improved electrical, optical, and structural properties of undoped ZnO thin films grown by water-mist-assisted spray pyrolysis. *Physica Status Solidi (a)* **203**, 2411–2417 (2006).

[99] Fiddes, A. J. C. *et al.* Preparation of ZnO films by spray pyrolysis. *Journal of Crystal Growth* **159**, 210–213 (1996).

[100] Bahadur, L., Hamdani, M., Koenig, J. F. & Chartier, P. Studies on semiconducting thin films prepared by the spraypyrolysis technique for photoelectrochemical solar cell applications: Preparation and properties of ZnO. *Solar Energy Materials* **14**, 107–120 (1986).

[101] Manouni, A. E. *et al.* Effect of aluminium doping on zinc oxide thin films grown by spray pyrolysis. *Superlattices and Microstructures* **39**, 185–192 (2006).

[102] El Hichou, A., Addou, M., Ebothé, J. & Troyon, M. Influence of deposition temperature (Ts), air flow rate (f) and precursors on cathodoluminescence properties of

ZnO thin films prepared by spray pyrolysis. *Journal of Luminescence* **113**, 183–190 (2005).

[103] Godbole, B., Badera, N., Shrivastava, S., Jain, D. & Ganesan, V. Growth mechanism of ZnO films deposited by spray pyrolysis technique. *Materials Sciences and Applications* **2**, 643–648 (2011).

[104] Afify, H. H., Nasser, S. A. & Demian, S. E. Influence of substrate temperature on the structural, optical and electrical properties of ZnO thin films prepared by spray pyrolysis. *Journal of Materials Science* **2**, 152–156 (1991).

[105] Fiddes, A. J. C. *Deposition of zinc oxide by spray pyrolysis.* Ph.D. thesis, Durham University (1993).

[106] Kim, M. G., Kanatzidis, M. G., Facchetti, A. & Marks, T. J. Low-temperature fabrication of high-performance metal oxide thin-film electronics via combustion processing. *Nature materials* **10**, 382–388 (2011).

[107] Technical Data- Zinc(II) acetylacetonate hydrate. Tech. Rep., MacKenzieCompany, LLC. URL http://www.mackenziechem.com/.

[108] Ambrozic, G., Djerdj, I., Skapin, S. D., Zigon, M. & Orel, Z. C. The double role of p-toluenesulfonic acid in the formation of ZnO particles with different morphologies. *CrystEngComm* **12**, 1862–1868 (2010).

[109] Ambrozic, G., Skapin, S. D., Zigon, M. & Orel, Z. C. The synthesis of zinc oxide nanoparticles from zinc acetylacetonate hydrate and 1-butanol or isobutanol. *Journal of Colloid and Interface Science* **346**, 317–323 (2010).

[110] Adkins, H., Kutz, W. & Coffman, D. D. The Alcoholysis of Certain 1,3-Diketones in The Presence of Hydrogen Chloride. *Journal of The American Chemical Society* **52**, 3212–3221 (1930).

[111] Charles, R. G. & Pawlikowski, A. M. Comparative heat stabilities of some metal acetylacetonate chelates. *The Journal of Physical Chemistry* **62**, 440–444 (1958).

[112] Hoene, J. V., Charles, R. G. & Hickam, W. M. Thermal decomposition of metal

acetylacetonates: Mass spectrometer studies. *The Journal of Physical Chemistry* **62**, 1098–1101 (1958).

[113] Rudolph, G. & Henry, M. C. The thermal decomposition of zinc acetylacetonate hydrate. *Inorganic Chemistry* **3**, 1317–1318 (1964).

[114] Hussien, G. A. M. Characterisation of the thermal genesis course of zinc oxide from zinc acetoacetonate dihydrate. *Thermochimica Acta* **186**, 187–197 (1991).

[115] Arii, T. & Kishi, A. The effect of humidity on thermal decomposition of zinc acetylacetonate monohydrate. *Journal of Thermal Analysis and Calorimetry* **83**, 253–260 (2006).

[116] Ginley, D. S. (ed.) *Handbook of Transparent Conductors* (Springer, 2010).

[117] Robertson, J. Disorder, band offsets and dopability of transparent conducting oxides. *Thin Solid Films* **516**, 1419–1425 (2008).

[118] Falabretti, B. & Robertson, J. Electronic structures and doping of SnO2, CuAlO2, and CuInO2. *Journal of Applied Physics* **102**, 123703 (1–5) (2007).

[119] King, P. *et al.* Surface Electron Accumulation and the Charge Neutrality Level in In2O3. *Physical Review Letters* **101**, 116808 (1–4) (2008).

[120] Nunes, P., Fortunato, E. & Martins, R. Influence of the post-treatment on the properties of ZnO thin films. *Thin Solid Films* **383**, 277–280 (2001).

[121] Bouderbala, M., Hamzaoui, S., Adnane, M., Sahraoui, T. & Zerdali, M. Annealing effect on properties of transparent and conducting ZnO thin films. *Thin Solid Films* **517**, 1572–1576 (2009).

[122] Ozgur, U. *et al.* A comprehensive review of ZnO materials and devices. *Journal of Applied Physics* **98**, 041301 (1–103) (2005).

[123] Klingshirn, C. ZnO: From basics towards applications. *Physica Status Solidi (b)* **244**, 3027–3073 (2007).

[124] Janotti, A. & van de Walle, C. G. Fundamentals of zinc oxide as a semiconductor. *Reports on Progress in Physics* **72**, 126501 (1–29) (2009).

[125] Lee, W. J., Kang, J. & Chang, K. J. p-type doping and compensation in ZnO. *Journal of the Korean Physical Society* **53**, 196–201 (2008).

[126] Liping, Y., Qiqiang, Z., Dayong, F. & Zili, L. Development in p-type Doping of ZnO. *Journal of Wuhan University of Technology-Mater. Sci. Ed.* **27**, 1184–1187 (2012).

[127] Park, C. H., Zhang, S. B. & Wei, S. H. Origin of p-type doping difficulty in ZnO: The impurity perspective. *Physical Review B* **66**, 073202 (1–3) (2002).

[128] Brauer, G., Kuriplach, J., Ling, C. C. & Djurisic, A. B. Activities towards p-type doping of ZnO. *Journal of Physics: Conference Series* **265**, 012002 (1–14) (2011).

[129] Nunes, P. *et al.* Effect of different dopant elements on the properties of ZnO thin films. *Vacuum* **64**, 281–285 (2002).

[130] Lee, J. H. & Park, B. O. Transparent conducting ZnO:Al, In and Sn thin films deposited by the sol-gel method. *Thin Solid Films* **426**, 94–99 (2003).

[131] Aktaruzzaman, A. F., Sharma, G. L. & Malhotra, L. K. Electrical, optical and annealing characteristics of ZnO:Al films prepared by spray pyrolysis. *Thin Solid Films* **198**, 67–74 (1991).

[132] Maldonado, A. *et al.* Characteristics of spray pyrolytic ZnO:In thin films grown from zinc acetate and indium nitrate. *Journal of Vacuum Science and Technology A* **15**, 2905–2907 (1997).

[133] Reddy, K. T. R., Gopalaswamy, H., Reddy, P. J. & Miles, R. W. Effect of gallium incorporation on the physical properties of ZnO films grown by spray pyrolysis. *Journal of Crystal Growth* **210**, 516–520 (2000).

[134] Cheng, C. H. *et al.* Study on optoelectronic characteristics of Sn-doped ZnO thin films on poly(ethylene terephthalate) and indium tin oxide/poly (ethylene terephthalate) flexible substrates. *Japanese Journal of Applied Physics* **52**, 05DA16 (1–4) (2013).

[135] Liu, Y., Li, Y. & Zeng, H. ZnO-based transparent conductive thin films: Doping, performance, and processing. *Journal of Nanomaterials* **2013**, 196521 (1–9) (2013).

[136] Sans, J. A., Sánchez-Royo, J. F., Segura, A., Tobias, G. & Canadell, E. Chemical

effects on the optical band-gap of heavily doped ZnO:MIII (M=Al,Ga,In): An investigation by means of photoelectron spectroscopy, optical measurements under pressure, and band structure calculations. *Physical Review B* **79**, 195105 (1–9) (2009).

[137] Zhao, J. L., Sun, X. W., Ryu, H. & Moon, Y. B. Thermally stable transparent conducting and highly infrared reflective Ga-doped ZnO thin films by metal organic chemical vapor deposition. *Optical Materials* **33**, 768–772 (2011).

[138] Major, S., Banerjee, A. & Chopra, K. L. Highly transparent and conducting indium-doped zinc oxide films by spray pyrolysis. *Thin Solid Films* **108**, 333–340 (1983).

[139] Sato, H., Minami, T. & Takata, S. Highly transparent and conductive group IV impurity-doped ZnO thin films prepared by radio frequency magnetron sputtering. *Journal of Vacuum Science & Technology A* **11**, 2975–2979 (1993).

[140] Kim, H. M. Preparation of transparent metal films, silicon-doped zinc-oxide films (ZnO)100-x(SiO2)x by using a RF magnetron sputtering method. *Journal of the Korean Physical Society* **53**, 3307–3311 (2008).

[141] Das, A. K., Misra, P. & Kukreja, L. M. Effect of Si doping on electrical and optical properties of ZnO thin films grown by sequential pulsed laser deposition. *Journal of Physics D: Applied Physics* **42**, 165405 (1–7) (2009).

[142] Clatot, J. *et al.* Low temperature Si doped ZnO thin films for transparent conducting oxides. *Solar Energy Materials and Solar Cells* **95**, 2357–2362 (2011).

[143] Yuan, H. Structural, electrical and optical properties of Si doped ZnO films grown by atomic layer deposition. *Journal of Materials Science: Materials in Electronics* **23**, 2075–2081 (2012).

[144] Sorar, I., Saygin-Hinczewski, D., Hinczewski, M. & Tepehan, F. Z. Optical and structural properties of Si-doped ZnO thin films. *Applied Surface Science* **257**, 7343–7349 (2011).

[145] Kuznetsov, V. L. & Edwards, P. P. Transparent electrically conducting oxides (2014).

[146] Shinde, S. S. *et al.* Physical properties of transparent and conducting sprayed fluorine

doped zinc oxide thin films. *Solid State Sciences* **10**, 1209–1214 (2008).

[147] Guillen-Santiago, A., Olvera, M. d. L. L., Maldonado, A., Reyes, A. & Asomoza, R. Chemically sprayed fluorine-doped zinc oxide thin films deposited from Zn(C5H7O2)2: Effect of the molarity and substrate temperature on the physical properties. *Physica Status Solidi (a)* **191**, 499–508 (2002).

[148] Nam, G. M. & Kwon, M. S. F-doped ZnO by sol-gel spin-coating as a transparent conducting thin film. *Electronic Materials Letters* **7**, 127–131 (2011).

[149] Pawar, B. N. *et al.* Fluorine-doped zinc oxide transparent and conducting electrode by chemical spray synthesis. *Applied Surface Science* **254**, 6294–6297 (2008).

[150] Shannon, R. D. Revised effective ionic radii and systematic studies of interatomie distances in halides and chaleogenides. *Acta Crystallographica A* **32**, 751–767 (1976).

[151] Hu, J. & Gordon, R. G. Textured fluorine-doped ZnO films by atmospheric pressure chemical vapor deposition and their use in amorphous silicon solar cells. *Solar Cells* **30**, 437–450 (1991).

[152] Choi, Y. J. & Park, H. H. A simple approach to the fabrication of fluorine-doped zinc oxide thin films by atomic layer deposition at low temperatures and an investigation into the growth mode. *Journal of Materials Chemistry C* **2**, 98–108 (2014).

[153] Cao, L. *et al.* Highly transparent and conducting fluorine-doped ZnO thin films prepared by pulsed laser deposition. *Solar Energy Materials and Solar Cells* **95**, 894–898 (2011).

[154] Bhachu, D. S., Sankar, G. & Parkin, I. P. Aerosol assisted chemical vapor deposition of transparent conductive zinc oxide films. *Chemistry of Materials* **24**, 4704–4710 (2012).

[155] Chikoidze, E., Nolan, M., Modreanu, M., Sallet, V. & Galtier, P. Effect of chlorine doping on electrical and optical properties of ZnO thin films. *Thin Solid Films* **516**, 8146–8149 (2008).

[156] Rousset, J., Saucedo, E. & Lincot, D. Extrinsic doping of electrodeposited zinc

oxide films by chlorine for transparent conductive oxide applications. *Chemistry of Materials* **21**, 534–540 (2009).

[157] Chikoidze, E., Modreanu, M., Sallet, V., Gorochov, O. & Galtier, P. Electrical properties of chlorine-doped ZnO thin films grown by MOCVD. *Physica Status Solidi (a)* **205**, 1575–1579 (2008).

[158] Wang, T. *et al.* Low temperature synthesis wide optical band gap Al and (Al, Na) co-doped ZnO thin films. *Applied Surface Science* **257**, 2341–2345 (2011).

[159] Yamamoto, T. & Katayama-Yoshida, H. Solution using a codoping method to unipolarity for the fabrication of p-yype ZnO. *Japanese Journal of Applied Physics* **38**, L166–L169 (1999).

[160] Katayama-Yoshida, H. & Yamamoto, T. Theoretical predictions for codoping properties in wide band-gap semiconductors. *Japanese Journal of Applied Physics* **39**, 229–236 (2000).

[161] Joseph, M., Tabata, H. & Kawai, T. p-Type electrical conduction in ZnO thin films by Ga and N Codoping. *Japanese Journal of Applied Physics* **38**, L1205–L1207 (1999).

[162] Kumar, M., Kim, T. H., Kim, S. S. & Lee, B. T. Growth of epitaxial p-type ZnO thin films by codoping of Ga and N. *Applied Physics Letters* **89**, 112103 (1–3) (2006).

[163] Yun, E. J., Park, H. S., Lee, K. H., Nam, H. G. & Jung, M. Characterization of Al-As codoped p-type ZnO films by magnetron cosputtering deposition. *Journal of Applied Physics* **103**, 073507 (1–4) (2008).

[164] Dutta, M., Ghosh, T. & Basak, D. N doping and Al-N co-doping in sol-gel ZnO films: Studies of their structural, electrical, optical, and photoconductive properties. *Journal of Electronic Materials* **38**, 2335–2342 (2009).

[165] Shet, S. *et al.* Carrier concentration tuning of bandgap-reduced p-type ZnO films by codoping of Cu and Ga for improving photoelectrochemical response. *Journal of Applied Physics* **103**, 073504 (1–5) (2008).

[166] Zhang, Y. Z. *et al.* Effects of growth temperature on Li-N dual-doped p-type ZnO thin

films prepared by pulsed laser deposition. *Applied Surface Science* **254**, 1993–1996 (2008).

[167] Kim, J. P. *et al.* Optical and electrical properties of ZnO films, codoped with Al and Ga deposited at room temperature by an RF sputtering method. *Thin Solid Films* **518**, 6179–6183 (2010).

[168] Lee, W. *et al.* Investigation of electronic and optical properties in Al-Ga codoped ZnO thin films. *Current Applied Physics* **12**, 628–631 (2012).

[169] Nomoto, J., Miyata, T. & Minami, T. Transparent conducting Si-codoped Al-doped ZnO thin films prepared by magnetron sputtering using Al-doped ZnO powder targets containing SiC. *Journal of Vacuum Science & Technology A* **27**, 1001–1005 (2009).

[170] Altamirano-Juarez, D. C., Torres-Degado, G., Jimenez-Sandoval, S., Jimenez-Sandoval, O. & Castanedo-Perez, R. Low-resistivity ZnO:F:Al transparent thin films. *Solar Energy Materials and Solar Cells* **82**, 35–43 (2004).

[171] Choi, B. G. *et al.* Electrical, optical and structural properties of transparent and conducting ZnO thin films doped with Al and F by rf magnetron sputter. *Journal of the European Ceramic Society* **25**, 2161–2165 (2005).

[172] Maldonado, A., Rodrnguez-Baez, J. & Olvera, M. d. l. L. Physical properties of indium and fluorine codoped zinc oxide thin films deposited by chemical spray. *Materials Chemistry and Physics* **129**, 109–115 (2011).

[173] Vimalkumar, T. V., Poornima, N., Jinesh, K. B., Kartha, C. S. & Vijayakumar, K. P. On single doping and co-doping of spray pyrolysed ZnO films: Structural, electrical and optical characterisation. *Applied Surface Science* **257**, 8334–8340 (2011).

[174] Morales-Saavedra, O. G., Castaneda, L., Banuelos, J. G. & Ortega-Martinez, R. Morphological, optical, and nonlinear optical properties of fluorine-indium-doped zinc oxide thin films. *Laser Physics* **18**, 283–291 (2008).

[175] Keskenler, E. F., Turgut, G. & Dogan, S. Investigation of structural and optical properties of ZnO films co-doped with fluorine and indium. *Superlattices and Micro-*

structures **52**, 107–115 (2012).

[176] Gledhill, S. *et al.* Doping induced structural and compositional changes in ZnO spray pyrolysed films and the effects on optical and electrical properties. *Thin Solid Films* **519**, 4293–4298 (2011).

[177] Ingram, B. J., Gonzalez, G. B., Kammler, D. R., Bertoni, M. I. & Mason, T. O. Chemical and structural factors governing transparent conductivity inoxides. *Journal of Electroceramics* **13**, 167–175 (2004).

[178] Pietsch, U. & Unger, K. The influence of free carriers on the equilibrium lattice parameter of semiconductor materials. *Physica Status Solidi (a)* **80**, 165–172 (1983).

[179] Chen, N., Wang, Y., He, H. & Lin, L. Effects of point defects on lattice parameters of semiconductors. *Physical Review B* **54**, 8516–8521 (1996).

[180] Bragg, W. L. The crystalline structure of zinc oxide. *Philosophical Magazine Series 6* **39**, 647–651 (1920).

[181] Morkoc, H. & Ozgur, U. *Zinc Oxide: Fundamentals, Materials and Device Technology* (WILEY-VCH Verlag GmbH & Co. KGaA, Weinheim, 2009).

[182] Jagadish, C. & Pearton, S. (eds.) *Zinc Oxide Bulk, Thin Films and Nanostructures* (Elsevier, 2006).

[183] Desgreniers, S. High-density phases of ZnO: Structural and compressive parameters. *Physical Review B* **58**, 14102–14105 (1998).

[184] Ashrafi, A. B. M. A. *et al.* Growth and characterization of hypothetical zinc-blende ZnO films on GaAs(001) substrates with ZnS buffer layers. *Applied Physics Letters* **76**, 550–552 (2000).

[185] Kim, S. K., Jeong, S. Y. & Cho, C. R. Structural reconstruction of hexagonal to cubic ZnO films on Pt/Ti/SiO2/Si substrate by annealing. *Applied Physics Letters* **82**, 562–564 (2003).

[186] Sze, S. M. & Ng, K. K. *Physics of semiconductor devices* (John Wiley & Sons, Inc., 2007), third edn.

[187] Hartnagel, H. L., Dawar, A. L., Jain, A. K. & Jagadish, C. *Semiconducting Transparent Thin Films* (Institute of Physics Publishing Ltd., 1995).

[188] Dressel, M. & Scheffler, M. Verifying the Drude response. *Annalen der Physik* **15**, 535–544 (2006).

[189] Hu, J. & Gordon, R. G. Atmospheric pressure chemical vapor deposition of gallium doped zinc oxide thin films from diethyl zinc, water, and triethyl gallium. *Journal of Applied Physics* **72**, 5381–5392 (1992).

[190] Bellingham, J. R., Phillips, W. A. & Adkins, C. J. Amorphous indium oxide. *Thin Solid Films* **195**, 23–31 (1991).

[191] Simonis, F., van der Leij, M. & Hoogendoorn, C. J. Physics of doped tin dioxide films for spectral-selective surfaces. *Solar Energy Materials* **1**, 221–231 (1979).

[192] Burstein, E. Anomalous optical absorption limit in InSb. *Physical Review* **93**, 2–632–633 (1954).

[193] Moss, T. S. The interpretation of the properties of indium antimonide. *Proceedings of the Physical Society B* **67**, 775–782 (1954).

[194] Roth, A. P., Webb, J. B. & Williams, D. F. Absorption edge shift in ZnO thin films at high carrier densities. *Solid State Communications* **39**, 1269–1271 (1981).

[195] Roth, A. P., Webb, J. B. & Williams, D. F. Band-gap narrowing in heavily defect-doped ZnO. *Physical Review B* **25**, 7836–7839 (1982).

[196] Yamada, T., Makino, H., Yamamoto, N. & Yamamoto, T. Ingrain and grain boundary scattering effects on electron mobility of transparent conducting polycrystalline Ga-doped ZnO films. *Journal of Applied Physics* **107**, 123534 (1–8) (2010).

[197] Zhang, D. H. & Ma, H. L. Scattering mechanisms of charge carriers in transparent conducting oxide films. *Applied Physics A* **62**, 487–492 (1996).

[198] Minami, T., Suzuki, S. & Miyata, T. Electrical conduction mechanism of highly transparent and conductive ZnO thin films. *Materials Research Society Symposium Proceedings* **666**, F1.3 (1–7) (2001).

[199] Foster, N. F. Crystallographic orientation of zinc oxide films deposited by triode sputtering. *Journal of Vacuum Science and Technology* **6**, 111–114 (1969).

[200] Fujimura, N., Nishihara, T., Goto, S., Xu, J. & Ito, T. Control of preferred orientation for ZnOx films: control of self-texture. *Journal of Crystal Growth* **130**, 269–279 (1993).

[201] Ellmer, K., Klein, A. & Rech, B. (eds.) *Transparent Conductive Zinc Oxide* (Springer Berlin Heidelberg, 2008).

[202] Webb, J. B., Williams, D. F. & Buchanan, M. Transparent and highly conductive films of ZnO prepared by rf reactive magnetron sputtering. *Applied Physics Letters* **39**, 640–642 (1981).

[203] Natsume, Y., Sakata, H., Hirayama, T. & Yanagida, H. Low-temperature conductivity of undoped zinc oxide films by chemical vapour deposition. *Journal of Materials Science Letters* **10**, 810–812 (1991).

[204] Ogawa, M. F., Natsume, Y., Hirayama, T. & Sakata, H. Preparation and electrical properties of undoped zinc oxide films by CVD. *Journal of Materials Science Letters* **9**, 1351–1353 (1990).

[205] Roth, A. P. & Williams, D. F. Properties of zinc oxide films prepared by the oxidation of diethyl zinc. *Journal of Applied Physics* **52**, 6685–6692 (1981).

[206] Major, S., Banerjee, A. & Chopra, K. L. Optical and electronic properties of zinc oxide films prepared by spray pyrolysis. *Thin Solid Films* **125**, 179–185 (1985).

[207] Minami, T., Nanto, H. & Takata, S. Highly conductive and transparent ZnO thin films prepared by R.F. magnetron sputtering in an applied external D.C. magnetic field. *Thin Solid Films* **124**, 43–47 (1985).

[208] Ben Ayadi, Z., El Mir, L., Djessas, K. & Alaya, S. Effect of the annealing temperature on transparency and conductivity of ZnO:Al thin films. *Thin Solid Films* **517**, 6305–6309 (2009).

[209] Nunes, P., Fortunato, E. & Martins, R. Influence of the annealing conditions on

the properties of ZnO thin films. *International Journal of Inorganic Materials* **3**, 1125–1128 (2001).

[210] Lee, J. H., Yeo, B. W. & Park, B. O. Effects of the annealing treatment on electrical and optical properties of ZnO transparent conduction films by ultrasonic spraying pyrolysis. *Thin Solid Films* **457**, 333–337 (2004).

[211] Calnan, S. & Tiwari, A. N. High mobility transparent conducting oxides for thin film solar cells. *Thin Solid Films* **518**, 1839–1849 (2010).

[212] Oba, F., Choi, M., Togo, A. & Tanaka, I. Point defects in ZnO: an approach from first principles. *Science and Technology of Advanced Materials* **12**, 034302 (1–14) (2011).

[213] Janotti, A. & van de Walle, C. G. Native point defects in ZnO. *Physical Review B* **76**, 165202 (1–22) (2007).

[214] Zhang, S., Wei, S. H. & Zunger, A. Intrinsic n-type versus p-type doping asymmetry and the defect physics of ZnO. *Physical Review B* **63**, 075205 (1–7) (2001).

[215] Gsiea, A. M., Goss, J. P., Briddon, P. R., Al-habashi, R. M. & Etmimi, K. M. Native Point Defects in ZnO. *International Journal of Mathematical, Computational, Physical and Quantum Engineering* **8**, 127–132 (2014).

[216] Kim, Y. S. & Park, C. H. Rich variety of defects in ZnO via an attractive interaction between O vacancies and Zn interstitials: Origin of n-type doping. *Physical Review Letters* **102**, 086403 (1–4) (2009).

[217] Kohan, A., Ceder, G., Morgan, D. & Van de Walle, C. G. First-principles study of native point defects in ZnO. *Physical Review B* **61**, 15019–15027 (2000).

[218] Janotti, A., Varley, J. B., Lyons, J. L. & van de Walle, C. G. Controlling the conductivity in oxide semiconductors. In *Functional Metal Oxide Nanostructures*, vol. 149 of *Springer Series in Materials Science*, 23–35 (Springer, New York, NY, 2012).

[219] Jokela, S. & McCluskey, M. Structure and stability of O-H donors in ZnO from high-pressure and infrared spectroscopy. *Physical Review B* **72**, 113201 (1–4) (2005).

[220] Shi, G. A. *et al.* Hydrogen local modes and shallow donors in ZnO. *Physical Review B* **72**, 195211 (1–8) (2005).

[221] Wu, H. C., Peng, Y. C. & Shen, T. P. Electronic and Optical Properties of Substitutional and Interstitial Si-Doped ZnO. *Materials* **5**, 2088–2100 (2012).

[222] Korner, W. & Elsasser, C. Density functional theory study for polycrystalline ZnO doped with Si or Nb. *Physical Review B* **83**, 205306 (1–6) (2011).

[223] Liu, B., Gu, M., Liu, X., Huang, S. & Ni, C. First-principles study of fluorine-doped zinc oxide. *Applied Physics Letters* **97**, 122101 (1–3) (2010).

[224] Xu, H. Y. *et al.* F-doping effects on electrical and optical properties of ZnO nanocrystalline films. *Applied Physics Letters* **86**, 123107 (1–3) (2005).

[225] Liu, B., Gu, M., Liu, X., Huang, S. & Ni, C. Defect formation in chlorine-doped zinc oxide. *Solid State Communications* **171**, 30–33 (2013).

[226] Kaufmann, E. N. (ed.) *Characterization of Materials* (John Wiley & Sons, Inc., 2003), first edn.

[227] Smart, L. E. & Moore, E. A. *Solid State Chemistry: An Introduction* (Taylor & Francis Group (CRC Press), 2005), third edn.

[228] Kniess, C. T., Cardoso de Lima, J. & Prates, P. B. The quantification of crystalline phases in materials: Applications of Rietveld method. In Shatokha, V. (ed.) *Sintering - Methods and Products*, chap. 14, 293–316 (InTech, 2005).

[229] Skoog, D. A., Holler, F. J. & Crouch, S. R. *Principles of Instrumental Analysis* (Thomson Brooks/Cole, 2007), sixth edn.

[230] Vilalta-Clemente, A. & Glyostein, K. Principles of Atomic Force Microscopy (AFM). Tech. Rep. (2008).

[231] Wilson, R. A. & Bullen, H. A. Basic theory of Atomic Force Microscopy (AFM). Tech. Rep. (2006).

[232] Hercules, D. M. Electron spectroscopy: Applications for chemical analysis. *Journal of Chemical Education* **81**, 1751–1766 (2004).

[233] Nebesny, K. W., Maschhoff, B. L. & Armstrong, N. R. Quantification of Auger and X-ray photoelectron spectroscopies. *Analytical Chemistry* **61**, 696A–480A (1989).

[234] Grant, J. T. Methods for Qquantitative analysis in XPS and AES. *Surface and Interface Analysis* **14**, 271–283 (1989).

[235] Silvestein, R. M., Bassler, G. C. & Morrill, T. C. *Spectrometric Identification of Organic Compounds* (John Wiley & Sons, Inc., 1991).

[236] Tauc, J., Grigorovici, R. & Vancu, A. Optical properties and electronic structure of amorphous germanium. *Physica Status Solidi (b)* **15**, 627–637 (1966).

[237] Chopra, N., Mansingh, A. & Chadha, G. K. Electrical, optical and structural properties of amorphous V2O5-TeO2 blown films. *Journal of Non-Crystalline Solids* **126**, 194–201 (1990).

[238] Manifacier, J. C., Gasiot, J. & Fillard, J. P. A simple method for the determination of the optical constants n, k and the thickness of a weakly absorbing thin film. *Journal of Physics E: Scientific Instruments* **9**, 1002–1004 (1976).

[239] Swanepoel, R. Determination of the thickness and optical constants of amorphous silicon. *Journal of Physics E: Scientific Instruments* **16**, 1214–1222 (1983).

[240] van der Pauw, L. J. Method of measuring specific resistivity and Hall effect of discs of arbitrary shape. *Philips Research Reports* **13**, 1–9 (1958).

[241] Smits, F. M. Measurement of sheet resistivities with the four-point probe. *The Bell System Technical Journal* **37**, 711–718 (1958).

[242] van der Pauw, L. J. A method of measuring the resistivity and Hall coefficient on lamellae of arbitrary shape. *Philips Technical Review* **20**, 220–224.

[243] Matsumura, T. & Sato, Y. A Theoretical study on Van Der Pauw measurement values of inhomogeneous compound semiconductor thin films. *Journal of Modern Physics* **01**, 340–347 (2010).

[244] Newbury, D. E. *et al.* *Scanning Electron Microscopy and X-Ray Microanalysis* (Kluwer Academic/Plenum Publishers, 2003), third edn.

[245] Lehraki, N. *et al.* ZnO thin films deposition by spray pyrolysis: Influence of precursor solution properties. *Current Applied Physics* **12**, 1283–1287 (2012).

[246] Bacaksiz, E. *et al.* The effects of zinc nitrate, zinc acetate and zinc chloride precursors on investigation of structural and optical properties of ZnO thin films. *Journal of Alloys and Compounds* **466**, 447–450 (2008).

[247] Arca, E., Fleischer, K. & Shvets, I. V. Influence of the precursors and chemical composition of the solution on the properties of ZnO thin films grown by spray pyrolysis. *The Journal of Physical Chemistry C* **113**, 21074–21081 (2009).

[248] Achour, Z. B. *et al.* Effect of doping level and spray time on zinc oxide thin films produced by spray pyrolysis for transparent electrodes applications. *Sensors and Actuators A* **134**, 447–451 (2007).

[249] Yoshino, K. *et al.* Low-temperature growth of ZnO films by spray pyrolysis. *Japanese Journal of Applied Physics* **50**, 040207 (1–3) (2011).

[250] Yoshino, K. *et al.* Growth of spin-coated ZnO films using diethylzinc solution. *Japanese Journal of Applied Physics* **50**, 108001 (1–2) (2011).

[251] Arii, T. & Kishi, A. The effect of humidity on thermal process of zinc acetate. *Thermochimica Acta* **400**, 175–185 (2003).

[252] McAdie, H. G. The pyrosynthesis of strontium zincate. *Journal of Inorganic and Nuclear Chemistry* **28**, 2801–2809 (1966).

[253] Duan, Y. *et al.* Kinetic analysis on the non-isothermal dehydration by integral masterplots method and TG-FTIR study of zinc acetate dihydrate. *Journal of Analytical and Applied Pyrolysis* **83**, 1–6 (2008).

[254] Sirina, A. M., Kalinichenko, I. I. & Purtov, A. I. Thermal decomposition of cobalt, zinc, copper, and chromium nitrate hydrates. *Russian Journal of Inorganic Chemistry* **15**, 2430–2433 (1970).

[255] Nikolic, R., Zec, S., Maksimovic, V. & Mentus, S. Physico-chemical characterization of thermal decomposition course in zinc nitrate-copper nitrate hexahydrates. *Journal*

of Thermal Analysis and Calorimetry **86**, 423–428 (2006).

[256] Dumont, H., Marbeuf, A., Bouree, J. E. & Gorochov, O. Mass-spectrometric study of thermal decomposition of diethylzinc and diethyltellurium. *Journal of Materials Chemistry* **2**, 923–930 (1992).

[257] Dumon, H., Marbeuf, A., Bouree, J. E. & Gorochov, O. Pyrolysis pathways and kinetics of thermal decomposition of diethylzinc and diethyltellurium studied by mass spectrometry. *Journal of Materials Chemistry* **3**, 1075–1079 (1993).

[258] Ryabova, L. A. & Savitskaya, Y. S. The preparation of thin films of some oxides by the pyrolysis method. *Thin Solid Films* **2**, 141–148 (1968).

[259] Skorsepa, J., Godocikova, E. & Cernak, J. Comparison on thermal decomposition of propionate, benzoate and their chloroderivative salts of Zn(II). *Journal of Thermal Analysis and Calorimetry* **75**, 773–780 (2004).

[260] Mereu, R. A. *et al.* Synthesis, characterization and thermal decomposition study of zinc propionate as a precursor for ZnO nano-powders and thin films. *Journal of Analytical and Applied Pyrolysis* **104**, 653–659 (2013).

[261] Dollimore, D. & Tonge, K. H. The thermal decomposition of zinc and manganous formates. *Journal of Inorganic and Nuclear Chemistry* **29**, 621–627 (1967).

[262] Zhang, J. *et al.* Thermodynamic properties and thermal stability of the synthetic zinc formate dihydrate. *Journal of Thermal Analysis and Calorimetry* **91**, 861–866 (2008).

[263] Kamata, K., Nishino, J., Ohshio, S. & Maruyama, K. Rapid Formation of Zinc Oxide Films by an Atmospheric-Pressure Chemical Vapor Deposition Method. *Journal of the American Ceramic Society* **77**, 505–508 (1994).

[264] Haga, K., Katahira, F. & Watanabe, H. Preparation of ZnO films by atmospheric pressure chemical-vapor deposition using zinc acetylacetonate and ozone. *Thin Solid Films* **343-344**, 145–147 (1999).

[265] Herng, T. S. *et al.* Investigation of the non-volatile resistance change in noncentrosym-

metric compounds. *Scientific Reports* **2**, 587 (1–9) (2012).

[266] Clatot, J., Campet, G., Jean, M., Nistor, M. & Rougier, A. Influence of dopant nature on the TCO properties of ZnO:M (M=Al, Ga, Sn, Si, Ge) thin films. *MRS Proceedings* **1328**, 1308 (1–10) (2011).

[267] Luo, J. T., Zhu, X. Y., Chen, G., Zeng, F. & Pan, F. The electrical, optical and magnetic properties of Si-doped ZnO films. *Applied Surface Science* **258**, 2177–2181 (2012).

[268] Faure, C. *et al.* Co-sputtered ZnO:Si thin films as transparent conductive oxides. *Thin Solid Films* **524**, 151–156 (2012).

[269] Barrett, C. S. & Massalski, T. B. *Structure of Metals* (Pergamon Press, 1980), third edn.

[270] The International Centre for Diffraction Data. URL `http://www.icdd.com/`.

[271] Solookinejad, G. & Jabbari, M. Extracting structural parameters of nanocrystalline ZnO thin films annealed at different temperatures. *Journal of Applied Sciences* **11**, 2954–2960 (2011).

[272] Dghoughi, L. *et al.* The effect of Al-doping on the structural, optical, electrical and cathodoluminescence properties of ZnO thin films prepared by spray pyrolysis. *Physica B* **405**, 2277–2282 (2010).

[273] Lai, H. H. C. *et al.* Dopant-induced bandgap shift in Al-doped ZnO thin films prepared by spray pyrolysis. *Journal of Applied Physics* **112**, 083708 (1–5) (2012).

[274] Babu, B. J., Maldonado, A., Velumani, S. & Asomoza, R. Electrical and optical properties of ultrasonically sprayed Al-doped zinc oxide thin films. *Materials Science and Engineering B* **174**, 31–37 (2010).

[275] Major, S., Banerjee, A. & Chopra, K. L. Electrical and optical transport in undoped and indium-doped zinc oxide films. *Journal of Materials Research* **1**, 300–310 (1986).

[276] Edwards, P. P., Kuznetsov, V. L., Slocombe, D. & Vijayaraghavan, R. The Electronic Structure and Properties of Solids. In Reedijk, J. & Poeppelmeier, K. (eds.) *Com-*

prehensive Inorganic Chemistry II: From Elements to Applications, vol. 4, 153–176 (Elsevier Ltd., 2013).

[277] Mott, N. F. The transition to the metallic state. *Philosophical Magazine* **62**, 287–309 (1961).

[278] Edwards, P. P., Ramakrishnan, T. V. & Rao, C. N. R. The Metal-Nonmetal Transition: A Global Perspective. *The Journal of Physical Chemistry* **99**, 5228–5239 (1995).

[279] Edwards, P. P. & Sienko, M. J. The Transition to the Metallic State. *Accounts of Chemical Research* **15**, 87–93 (1982).

[280] Edwards, P. P., Lodge, M. T. J., Hensel, F. & Redmer, R. '... a Metal Conducts and a Non-Metal Doesn't'. *Philosophical Transactions of the Royal Society A* **368**, 941–965 (2010).

[281] Vai, A. T. *et al.* The Transition to the Metallic State in Polycrystalline n-type Doped ZnO Thin Films. *Zeitschrift für anorganische und allgemeine Chemie* **640**, 1054–1062 (2014).

[282] Seto, J. Y. W. The electrical properties of polycrystalline silicon films. *Journal of Applied Physics* **46**, 5247–5254 (1975).

[283] Many, A. Relation between physical and chemical processes on semiconductor surfaces. *C R C Critical Reviews in Solid State Sciences* **4**, 515–539 (1973).

[284] Edwards, P. P. & Sienko, M. J. Universality aspects of the metal-nonmetal transition in condensed media. *Physical Review B* **17**, 2575–2581 (1978).

[285] Gil, B. & Kavokin, A. V. Giant exciton-light coupling in ZnO quantum dots. *Applied Physics Letters* **81**, 748–750 (2002).

[286] O'Neil, D. H. *Materials Chemistry and Physics of the Transparent Conducting Oxides.* Ph.D. thesis, University of Oxford (2009).

[287] Danhara, Y., Hirai, T., Harada, Y. & Ohno, N. Exciton luminescence of ZnO fine particles. *Physica Status Solidi (c)* **3**, 3565–3568 (2006).

[288] Fritzsche, H. *Metal Non-metal Transitions in Disordered Solids* (Scottish Universities

Summer School in Physics, Edinburgh, 1978).

[289] Shanthi, E., Dutta, V., Banerjee, A. & Chopra, K. L. Electrical and optical properties of undoped and antimony-doped tin oxide films. *Journal of Applied Physics* **51**, 6243–6251 (1980).

[290] Mott, N. F. & Davis, E. A. *Electronic processes in non-crystalline materials* (Oxford University Press, 1979).

[291] Gurvitch, M. Ioffe-Regel criterion and resistivity of metals. *Physical Review B* **24**, 7404–7407 (1981).

[292] Adler, D., Flora, L. P. & Sentuna, S. D. Electrical conductivity in disordered systems. *Solid State Communications* **12**, 9–12 (1973).

[293] Ellmer, K. & Mientus, R. Carrier transport in polycrystalline transparent conductive oxides: A comparative study of zinc oxide and indium oxide. *Thin Solid Films* **516**, 4620–4627 (2008).

[294] Kuznetsov, V. L., ONeil, D. H., Pepper, M. & Edwards, P. P. Electronic conduction in amorphous and polycrystalline zinc-indium oxide films. *Applied Physics Letters* **97**, 262117 (1–3) (2010).

[295] Bruneaux, J., Cachet, H., Froment, M. & Messad, A. Correlation between structural and electrical properties of sprayed tin oxide films with and without fluorine doping. *Thin Solid Films* **197**, 129–142 (1991).

[296] Orton, J. W. & Powell, M. J. The Hall effect in polycrystalline and powdered semiconductors. *Reports on Progress in Physics* **43**, 1263–1307 (1980).

[297] Vanheusden, K. *et al.* Mechanisms behind green photoluminescence in ZnO phosphor powders. *Journal of Applied Physics* **79**, 7983–7990 (1996).

[298] Ashkenov, N. *et al.* Infrared dielectric functions and phonon modes of high-quality ZnO films. *Journal of Applied Physics* **93**, 126–133 (2003).

[299] Kim, W. M. *et al.* Density-of-state effective mass and non-parabolicity parameter of impurity doped ZnO thin films. *Journal of Physics D: Applied Physics* **41**, 195409

(1–5) (2008).

[300] Ilican, S., Caglar, Y., Caglar, M. & Yakuphanoglu, F. Structural, optical and electrical properties of F-doped ZnO nanorod semiconductor thin films deposited by sol-gel process. *Applied Surface Science* **255**, 2353–2359 (2008).

[301] Sanchez-Juarez, A., Tiburcio-Silver, A. & Ortiz, A. Properties of fluorine-doped ZnO deposited onto glass by spray pyrolysis. *Solar Energy Materials and Solar Cells* **52**, 301–311 (1998).

[302] Sanchez-juarez, A., Tiburcio-silver, A., Ortiz, A., Zironi, E. P. & Rickards, J. Electrical and optical properties of fluorine-doped ZnO thin films prepared by spray pyrolysis. *Thin Solid Films* **333**, 196–202 (1998).

[303] Douayar, A. *et al.* Fluorine-doped ZnO thin films deposited by spray pyrolysis technique. *The European Physical Journal-Applied Physics* **53**, 20501 (1–4) (2011).

[304] Olvera, M. d. l. L., Maldonado, A. & Asomoza, R. ZnO:F thin films deposited by chemical spray: effect of the fluorine concentration in the starting solution. *Solar Energy Materials and Solar Cells* **73**, 425–433 (2002).

[305] Yoon, H. S. *et al.* Properties of fluorine doped ZnO thin films deposited by magnetron sputtering. *Solar Energy Materials and Solar Cells* **92**, 1366–1372 (2008).

[306] Olvera, M. d. l. L., Maldonado, A., Asomoza, R. & Melendez-Lira, M. Effect of the substrate temperature and acidity of the spray solution on the physical properties of F-doped ZnO thin films deposited by chemical spray. *Solar Energy Materials and Solar Cells* **71**, 61–71 (2002).

[307] Maldonado, A., Tirado-Guerra, S., Melendez-Lira, M. & Olvera, M. d. l. L. Physical properties of ZnO:F obtained from a fresh and aged solution of zinc acetate and zinc acetylacetonate. *Solar Energy Materials and Solar Cells* **90**, 742–752 (2006).

[308] Biswal, R. R. *et al.* Fluorine doped zinc oxide thin films deposited by chemical spray, starting from zinc pentanedionate and hydrofluoric acid: Effect of the aging time of the solution. *Materials Science and Engineering B* **174**, 46–49 (2010).

[309] Tissue, B. M. *Basics of Analytical Chemistry and Chemical Equilibria* (John Wiley & Sons, Inc., 2013).

[310] King, E. L. *Chemistry* (Painter Hopkins Publishers, 1979), first edn.

[311] Judge, J. S. A study of the dissolution of SiO2 in acidic fluoride solutions. *Journal of The Electrochemical Society* **118**, 1772–1775 (1971).

[312] Kline, W. E. & Fogler, H. S. Dissolution of silicate minerals by hydrofluoric acid. *Industrial & Engineering Chemistry Fundamentals* **20**, 155–161 (1981).

[313] Olvera, M. d. l. L., Maldonado, A., Asomoza, R., Solorza, O. & Acosta, D. R. Characteristics of ZnO:F thin films obtained by chemical spray: Effect of the molarity and the doping concentration. *Thin Solid Films* **394**, 242–249 (2001).

[314] Wang, F. H., Yang, C. F. & Lee, Y. H. Deposition of F-doped ZnO transparent thin films using ZnF2-doped ZnO target under different sputtering substrate temperatures. *Nanoscale Research Letters* **9**, 97 (1–7) (2014).

[315] Angappane, S., Selvi, N. R. & Kulkarni, G. U. ZnO(101) films by pulsed reactive crossed-beam laser ablation. *Bulletin of Materials Science* **32**, 253–258 (2009).

[316] Lee, Y. E. *et al.* Microstructural evolution and preferred orientation change of radio-frequency-magnetron sputtered ZnO thin films. *Journal of Vacuum Science and Technology A* **14**, 1943–1948 (1996).

[317] Grant, A. W., Jamieson, A. & Campbell, C. T. Adsorption of chlorine on ZnO(0001)-Zn and coadsorption with HCOOH. *Surface Science* **458**, 71–79 (2000).

[318] Zhang, R. H., Slamovich, E. B. & Handwerker, C. A. Controlling growth rate anisotropy for formation of continuous ZnO thin films from seeded substrates. *Nanotechnology* **24**, 195603 (1–11) (2013).

[319] Tian, Z. R. *et al.* Complex and oriented ZnO nanostructures. *Nature materials* **2**, 821–826 (2003).

[320] Wagata, H., Ohashi, N., Katsumata, K., Okada, K. & Matsushita, N. The effect of citric Ion on the spin-sprayed ZnO films: IR and XPS study for the organic impurities.

Key Engineering Materials **485**, 291–294 (2011).

[321] Ichinose, K., Mizuno, T., Schuette White, M. & Yoshida, T. Control of nanostructure and crystallographic orientation in electrodeposited ZnO thin films via structure directing agents. *Journal of The Electrochemical Society* **161**, D195–D201 (2014).

[322] Yamamoto, T. Codoping method for solutions of doping problems in wide-band-gap semiconductors. *Physica Status Solidi (a)* **193**, 423–433 (2002).

[323] Yamamoto, T. & Katayama-Yoshida, H. Physics and control of valence states in ZnO by codoping method. *Physica B* **302-303**, 155–162 (2001).

[324] Yamamoto, T. & Katayama-Yoshida, H. Unipolarity of ZnO with a wide-band gap and its solution using codoping method. *Journal of Crystal Growth* **214-215**, 552–555 (2000).

[325] Seo, J. S. *et al.* Solution-processed flexible fluorine-doped indium zinc oxide thin-film transistors fabricated on plastic film at low temperature. *Scientific reports* **3**, 2085 (1–9) (2013).

[326] Wei, S. H. Overcoming the doping bottleneck in semiconductors. *Computational Materials Science* **30**, 337–348 (2004).

[327] Thimont, Y., Clatot, J., Nistor, M., Labrugère, C. & Rougier, A. From ZnF2 to ZnO thin films using pulsed laser deposition: Optical and electrical properties. *Solar Energy Materials and Solar Cells* **107**, 136–141 (2012).

[328] Wong, L., Suratwala, T., Feit, M. D., Miller, P. E. & Steele, R. The effect of HF/NH4F etching on the morphology of surface fractures on fused silica. *Journal of Non-Crystalline Solids* **355**, 797–810 (2009).

[329] Proksche, H., Nagorsen, G. & Ross, D. The influence of NH4F on the etch rates of undoped SiO2 in buffered oxide Etch. *Journal of The Electrochemical Society* **139**, 521–524 (1992).

[330] Wiberg, N., Holleman, A. F. & Wiberg, E. (eds.) *Inorganic Chemistry* (Academic Press, Inc., 2001), first edn.

[331] Harrington, E. A. X-ray diffraction measurements on some of the pure compounds concerned in the study of Portland cement. *American Journal of Science* **13**, 467–479 (1927).

[332] Taylor, H. F. W. The dehydration of hemimorphite. *The American Mineralogist* **47**, 932–944 (1962).

[333] Kabalkina, S. S., Vereschagin, L. F. & Lityagina, L. M. X-ray diffraction study of ZnF2 at pressures up to 130 kbar and at temperatures of 25 and 300Â°. *Soviet physics Doklady* **12**, 946–949 (1968).

[334] Das, S. & Ghosh, S. Fabrication of different morphologies of ZnO superstructures in presence of synthesized ethylammonium nitrate (EAN) ionic liquid: synthesis, characterization and analysis. *Dalton Transactions* **42**, 1645–1656 (2013).

[335] H&M Analytical Service Literature- Preferred Orientation. URL `http://www.h-and-m-analytical.com/`.

[336] Jain, A., Sagar, P. & Mehra, R. M. Changes of structural, optical and electrical properties of sol-gel derived ZnO films with their thickness. *Materials Science-Poland* **25**, 233–242 (2007).

[337] Knuyt, G., Quaeyhaegens, C., D'Haen, J. & Stals, L. M. A model for thin film texture evolution driven by surface energy effects. *Physica Status Solidi (b)* **195**, 179–193 (1996).

[338] Matysina, Z. A. The relative surface energy of hexagonal close-packed crystals. *Materials Chemistry and Physics* **60**, 70–78 (1999).

[339] Wagner, C. D., Riggs, W. M., Davis, L. E. & Moulder, J. F. *Handbook of X-ray photoelectron spectroscopy* (Perkin-Elmer Corporation, 1979).

[340] Lindsay, R. & Thornton, G. Structure of atomic and molecular adsorbates on low-Miller-index ZnO surfaces using X-ray absorption spectroscopy. *Topics in Catalysis* **18**, 15–19 (2002).

[341] Rössler, N., Kotsis, K. & Staemmler, V. Ab initio calculations for the Zn 2s and

2p core level binding energies in Zn oxo compounds and ZnO. *Physical chemistry chemical physics* **8**, 697–706 (2006).

[342] Rössler, N. & Staemmler, V. Ab initio calculations for the 2s and 2p core level binding energies of atomic Zn, Zn metal, and Zn containing molecules. *Physical Chemistry Chemical Physics* **5**, 3580–3586 (2003).

[343] Biesinger, M. C., Lau, L. W. M., Gerson, A. R. & Smart, R. S. C. Resolving surface chemical states in XPS analysis of first row transition metals, oxides and hydroxides: Sc, Ti, V, Cu and Zn. *Applied Surface Science* **257**, 887–898 (2010).

[344] Woll, C. The chemistry and physics of zinc oxide surfaces. *Progress in Surface Science* **82**, 55–120 (2007).

[345] Philipp, H. R. Optical and bonding model for non-crystalline SiOx and SiOxNy materials. *Journal of Non-Crystalline Solids* **8-10**, 627–632 (1972).

[346] Basic quantification of XPS spectra (2008). URL `www.casaxps.com`.

[347] Zhang, W., Zhang, S., Liu, Y. & Chen, T. Evolution of Si suboxides into Si nanocrystals during rapid thermal annealing as revealed by XPS and Raman studies. *Journal of Crystal Growth* **311**, 1296–1301 (2009).

[348] Wagner, C. D. *The NIST X-ray photoelectron spectroscopy (XPS) database* (U.S. National Institute of Standards and Technology Publications, Washington, 1991).

[349] Biesinger, M. C., Payne, B. P., Lau, L. W. M., Gerson, A. & Smart, R. S. C. X-ray photoelectron spectroscopic chemical state quantification of mixed nickel metal, oxide and hydroxide systems. *Surface and Interface Analysis* **41**, 324–332 (2009).

[350] Biesinger, M. C., Brown, C., Mycroft, J. R., Davidson, R. D. & McIntyre, N. S. X-ray photoelectron spectroscopy studies of chromium compounds. *Surface and Interface Analysis* **36**, 1550–1563 (2004).

[351] XPS Spectra (2013). URL `www.casaxps.com`.

[352] Fabbri, E., Rabis, A., Kötz, R. & Schmidt, T. J. Pt nanoparticles supported on Sb-doped SnO2 porous structures: developments and issues. *Physical chemistry chemical*

physics : PCCP **16**, 13672–13681 (2014).

[353] Yi, J. B., Li, X. P., Ding, J. & Seet, H. L. Study of the grain size, particle size and roughness of substrate in relation to the magnetic properties of electroplated permalloy. *Journal of Alloys and Compounds* **428**, 230–236 (2007).

[354] Lu, J. G. *et al.* Structural, optical, and electrical properties of (Zn,Al)O films over a wide range of compositions. *Journal of Applied Physics* **100**, 073714 (1–11) (2006).

[355] Walsh, A., Da Silva, J. & Wei, S. Origins of band-gap renormalization in degenerately doped semiconductors. *Physical Review B* **78**, 075211 (1–5) (2008).

[356] Sernelius, B. E., Berggren, K. F., Jin, Z. C., Hamberg, I. & Granqvist, C. G. Band-gap tailoring of Zno by means of heavy Al doping. *Physical Review B* **37**, 10244–10248 (1988).

[357] O'Neil, D. H. *et al.* Experimental and density-functional study of the electronic structure of In4Sn3O12. *Physical Review B* **81**, 1–8 (2010).

[358] Kuznetsov, V. L., O'Neil, D. H., Pepper, M. & Edwards, P. P. Electrical and optical properties of transparent conducting In4+xSn3-2xSbxO12 thin films. *Journal of Applied Physics* **110**, 033702 (1–8) (2011).

[359] Sakong, S. & Kratzer, P. Density functional study of carbon doping in ZnO. *Semiconductor Science and Technology* **26**, 014038 (1–5) (2011).

[360] Shapira, Y., McQuistan, R. B. & Lichtman, D. Relationship between photodesorption and surface conductivity in ZnO. *Physical Review B* **15**, 2163–2169 (1977).

[361] Miki, N., Maeno, M., Maruhashi, K., Nakagawa, Y. & Ohmi, T. Fluorine passivation of metal surface for self-cleaning semiconductor equipment. *IEEE Transactions on Semiconductor Manufacturing* **3**, 1–11 (1990).

[362] Points, S. Re-evaluation of glass viscosities at annealing and strain points. *Journal of The American Ceramic Society* **37**, 111–117 (1954).

[363] Xu, S. & Wang, Z. L. One-dimensional ZnO nanostructures: Solution growth and functional properties. *Nano Research* **4**, 1013–1098 (2011).

[364] Xu, S., Shen, Y., Ding, Y. & Wang, Z. L. Growth and transfer of monolithic horizontal ZnO nanowire superstructures onto flexible substrates. *Advanced Functional Materials* **20**, 1493–1497 (2010).

[365] Tian, Z. R., Voigt, J. A., Liu, J., McKenzie, B. & McDermott, M. J. Biomimetic arrays of oriented helical ZnO nanorods and columns. *Journal of The American Chemical Society* **124**, 12954–12955 (2002).

[366] Kikyuama, H. *et al.* Principles of wet chemical processing in ULSI micro fabrication. *IEEE Transactions on Semiconductor Manufacturing* **4**, 26–35 (1991).

[367] Niwano, M., Kurita, K., Takeda, Y. & Miyamoto, N. Formation of hexafluorosilicate on Si surface treated in NH4F investigated by photoemission and surface infrared spectroscopy. *Applied Physics Letters* **62**, 1003–1005 (1993).

[368] Pretorius, C. J., Plessis, W., Nel, J. T. & Crouse, P. L. Kinetics and thermodynamic parameters for the manufacturing of anhydrous zirconium tetrafluoride with ammonium acid fluoride as fluorinating agent. *The Journal of The Southern African Institute of Mining and Metallurgy* **7A**, 601–604 (2012).

[369] Major, S., Kumar, S., Bhatnagar, M. & Chopra, K. L. Effect of hydrogen plasma treatment on transparent conducting oxides. *Applied Physics Letters* **49**, 394–396 (1986).

[370] Chen, M. *et al.* X-ray photoelectron spectroscopy and auger electron spectroscopy studies of Al-doped ZnO films. *Applied Surface Science* **158**, 134–140 (2000).

[371] Park, J. W., Kim, D. H., Choi, S. H., Lee, M. & Lim, D. The Role of Carbon Doping in ZnO. *Journal of the Korean Physical Society* **57**, 1482–1485 (2010).

[372] Lee, W., Han, J. W., Chen, Y., Cai, Z. & Yildiz, B. Cation size mismatch and charge interactions drive dopant segregation at the surfaces of manganite perovskites. *Journal of the American Chemical Society* **135**, 7909–7925 (2013).

[373] Lee, C. S., Yoon, K. H. & Ahn, B. T. Improved optical transmittance of boron doped ZnO thin films by low pressure chemical vapor deposition with pulse boron doping.

Journal of The Electrochemical Society **158**, H482–H486 (2011).

[374] Hu, Y. H. *et al.* Texture ZnO thin-films and their application as front electrode in solar cells. *Engineering* **02**, 973–978 (2010).

[375] Fay, S., Kroll, U., Bucher, C., Vallat-Sauvain, E. & Shah, A. Low pressure chemical vapour deposition of ZnO layers for thin-film solar cells: temperature-induced morphological changes. *Solar Energy Materials and Solar Cells* **86**, 385–397 (2005).

[376] Fay, S. *et al.* Rough ZnO layers by LP-CVD process and their effect in improving performances of amorphous and microcrystalline silicon solar cells. *Solar Energy Materials and Solar Cells* **90**, 2960–2967 (2006).

[377] Jia, J., Takasaki, A., Oka, N. & Shigesato, Y. Experimental observation on the Fermi level shift in polycrystalline Al-doped ZnO films. *Journal of Applied Physics* **112**, 013718 (1–7) (2012).

[378] Rossler, U. Energy bands of hexagonal II-VI semiconductors. *Physical Review* **184**, 733–738 (1969).

[379] Sekine, T., Ikeo, N. & Nagasawa, Y. Comparison of AES chemical shifts with XPS chemical shifts. *Applied Physics Letters* **100-101**, 30–35 (1996).

[380] Lee, C., Lim, K. & Song, J. Highly textured ZnO thin films doped with indium prepared by the pyrosol method. *Solar Energy Materials and Solar Cells* **43**, 37–45 (1996).

[381] Olvera, M. d. l. L., Maldonado, A., Asomoza, R., Konagai, M. & Asomoza, M. Growth of textured ZnO:In thin films by chemical spray deposition. *Thin Solid Films* **229**, 196–200 (1993).